ALMA MATER STUDIORUM
UNIVERSITA' DI BOLOGNA

Dottorato di ricerca in Astrofisica

Ciclo XXXI

RR Lyrae stars as standard candles and stellar population tracers with *Gaia*

Presentata da: **Alessia Garofalo**

Supervisore:
Chair.mo Prof. Luca Ciotti

Coordinatore Dottorato:
Chair.mo Prof.
Francesco Rosario Ferraro

Co-Supervisori:
Dr. Gisella Clementini
Dr. Felice Cusano
Dr. Tatiana Muraveva

Esame finale anno 2019

Settore Concorsuale: 02/C1 – Astronomia, Astrofisica, Fisica della Terra e dei Pianeti Settore Scientifico Disciplinare: FIS/05 – Astronomia e Astrofisica

"Quello che vedi davanti a te, amico mio, è il risultato di una vita di cioccolato."

Katharine Hepburn

Abstract

As creatively argued by Sarajedini (2011), the RR Lyrae stars (RRLs) are the "swiss knife" of Astronomy.

Easily identified thanks to the characteristic light variation, RRLs are primary distance indicators as well as tracers of the oldest stellar component (t>10 Gyr) in their hosts. Their pulsation characteristics (periods, amplitudes, shape of the light curve, etc.) are unaffected by distance and reddening and directly related to intrinsic stellar parameters (e.g. mass, luminosity, effective temperature and chemical composition).

RRLs have been found in all Local Group (LG) galaxies where they have been searched for, irrespective of morphological type.

The main goal of this thesis is to exploit the dual role of RRLs as stellar population tracers in our Galaxy and its LG companions, and primary standard candles for the definition of the cosmic distance ladder, to (i) investigate the stellar populations in a number of new stellar satellites recently discovered around the Milky Way (MW) and Andromeda (M31) spiral galaxies; and (ii) study the luminosity - metallicity and period - luminosity - (metallicity) relations that RRLs conform to, based on the unprecedented astrometric and photometric dataset that is being collected by the European Space Agency (ESA) mission *Gaia*.

The thesis is organized in 5 Chapters and 3 Appendices.

In Chapter 1 we provide a general, brief description of the RRL properties and characteristics from both stellar evolution and observational perspectives. We then focus on their potential as distance indicators and old stellar population tracers in the light of the *Gaia* mission.

In Chapter 2 we present results from our study of the MW ultra-faint dwarf galaxy Pisces II and of two dwarf spheroidal satellites of M31: Andromeda XXV and Andromeda XXVII, that we have observed with the Large Binocular Telescope. We present our datasets, the procedures for the photometric reduction and the identification of variable sources. We describe how the RRLs (and anomalous Cepheids - ACs) we have identified along with the colour magnitude diagrams allowed us to measure the distance, characterise the resolved stellar populations and study the structure of these systems in the context of the tidal interaction with the giant spirals they orbit around, the MW and M31.

In Chapter 3, after a general presentation of the *Gaia* mission (spacecraft, payload and scientific goals) and the content of the first and second data releases (*Gaia* DR1

and DR2, respectively), we describe our strategy and approaches to test the *Gaia* DR1 parallaxes for Galactic RRLs and Cepheids and the DR2 parallaxes for RRLs. We also briefly describe our validation of the DR2 catalogue of RRLs with variable stars in the MW globular clusters and dwarf satellites.

In Chapter 4, exploiting *Gaia* DR1 and 2 parallax data, we present results on the distance to the Large Magellanic Cloud globular cluster Reticulum and the Sculptor dwarf spheroidal galaxy, obtained in two complementary projects, the Carnegie RRL Project (CRRP; Freedman et al. 2012) and the *Spitzer* Merger History And Shape of the Galactic Halo (SMHASH; Johnston et al. 2013).

In Summary and Future Developments (Chapter 5) we summarize and briefly describe future developments of the work presented in this PhD thesis. Finally, Appendix A contains tables which are too long to be inserted in the main text of the thesis and Appendices B and C contain additional figures and a short description of the main properties and characteristics of other pulsation variables (classical, anomalous and Type II Cepheids) recalled/used in this thesis.

Contents

List of Figures

List of Tables

Abbreviations

ABL	**A**strometric **B**ased **L**uminosity
AC	**A**nomalous **C**epheid
And XXV	**And**romeda XXV
And XXVII	**And**romeda XXVII
BA	**B**ayesian **A**pproach
CC	**C**lassical **C**epheid
CMD	**C**olour **M**agnitude **D**iagram
CU	**C**oordination **U**nit
dSph	**d**warf **Sph**eroidal galaxy
DPAC	**D**ata **P**rocessing and **A**nalisis **C**onsortium
DR1	**D**ata **R**elease 1
DR2	**D**ata **R**elease 2
FoV	**F**ield **o**f **V**iew
GC	**G**lobular **C**luster
GGC	**G**alactic **G**lobular **C**luster
GPoA	**G**reat **P**lane **o**f **A**ndromeda
HB	**H**orizontal **B**ranch
HJD	**H**eliocentric **J**ulian**D**ay
HST	**H**ubble **S**pace **T**elescope
IS	**I**nstability **S**trip
LBC	**L**arge **B**inocular **C**amera
LBT	**L**arge **B**inocular **T**elescope
LG	**L**ocal **G**roup
LPV	**L**ong **P**eriod **V**ariable
LSQ	**L**east **SQ**uares fit

LSST	**L**arge **S**ynoptic **S**urvey **T**elescope
MIR	**M**id **I**nfra-**R**ed
MSTO	**M**ain **S**equence **T**urn **O**ff
MW	**M**ilky **W**ay
M31	Andromeda Galaxy
NIR	**N**ear **I**nfra-**R**ed
Peg III	**Peg**asus III
P	**P**eriod
PL	**P**eriod **L**uminosity
PLZ	**P**eriod **L**uminosity metallicity
Psc II	**P**isces II
PW	**P**eriod **W**esenheit
RGB	**R**ed **G**iant **B**ranch
RRLs	**RR L**yrae **s**tars
S	**S**pecific frequency
SOS	**S**pecific **O**bject **S**tudies
T2C/T2Cep	**T**ype II **C**epheid
UFD	**U**ltra **F**aint **D**warf
VPOS	**V**ast **PO**lar **S**tructure
ZAHB	**Z**ero **A**ge **H**orizontal **B**ranch

Chapter 1

RR Lyrae stars, a multi-purpose tool

1.1 Astrophysical context

As creatively argued by Sarajedini (2011), the RR Lyrae stars (RRLs) are the "swiss knife" of Astronomy. They are well known as distance indicators, their presence testifies the existence of a stellar population with an age older than ∼10 Gyr, their periods and amplitudes are unaffected by distance and reddening and directly related to intrinsic stellar parameters such as the stellar mass (M), luminosity (L), effective temperature (T_{eff}) and chemical composition (Y,Z), hence, they can be used to estimate the metal abundance of the stellar system (e.g. star cluster or galaxy) in which they reside, while their light curves and colours can be used to measure the interstellar reddening. We refer the reader to Smith (1995) and Catelan & Smith (2015) for a detailed description of virtues and shortcomings of RRLs. But, before being overwhelmed by their countless applications, first things first.

From the point of view of stellar evolution, the RRLs are low-mass stars (0.6-0.8 $M_{\odot}$) which are going through the evolutionary phase of core helium burning. Hence, they are Horizontal Branch (HB) giants with typical luminosities of $\log(L/L_{\odot}) \sim$ 1.5-1.8, radii of 5-6 $R_{\odot}$, effective temperatures between 7400 and 6100 K and observed metallicities between $Z=10^{-4}$ and $Z=10^{-2}$. The RRL progenitors are low-mass stars, of about ~ 0.8 $M_{\odot}$ which spend most of their lifetime on the Main Sequence (MS) evolutionary stage.

When hydrogen in their cores becomes exhausted the cores start to contract and become electron degenerate. This contraction is slowed by down by the additional pressure of the increased core degeneracy, but proceeds gradually, together with envelope expansion. At the time the star reaches the base of the Red Giant Branch (RGB), the core is fully electron degenerate, and the central temperature is too low to ignite helium. Then, the star has no alternative than to burn hydrogen in a shell, while the core grows in mass, which characterizes the entire RGB phase. Only when the star reaches the RGB tip, with a core mass of ~ 0.47 $M_{\odot}$, the core temperature increase enough to trigger the so-called helium flash, the process that activates the helium burning in the core and removes the electron degeneracy carrying the star on the Zero Age HB (ZAHB), which represents the initial stage of the HB evolutionary phase. If the star falls on the ZAHB inside the magnitude and colour ranges of the classical instability strip (IS), it starts pulsating as an RRL. The location of a star on the ZAHB depends on its total mass, on the core mass and on the star chemical composition. Since stars on the ZAHB have similar core masses their position depends mainly on the envelope mass, hence, moving from the theoretical to the observational plane, the HB sequence in colour reflects primarily a mass sequence. Stellar evolution theory tells us that RRLs are Population II stars with ages no younger than 10 Gyr and sub-solar metal abundances. Therefore, their detection in a galaxy or stellar system traces the presence of a corresponding Population II stellar component and demonstrates that the system started forming stars at an early epoch. RRLs are very common: they have been found in globular clusters (GCs), galactic halos, spiral galaxies like the Milky Way (MW) and Andromeda (M31), in their dwarf satellites and in all Local Group galaxies where they have been searched for (see Section 1.3), thus showing that all nearby galaxies contain a very ancient stellar component and must have started forming stars just after they were formed.
RRLs pulsate with periods in the range from ~ 0.2 to ~ 1 day. The amplitude of their light variation depends on the observed passband, decreasing from around 1.8 mag at blue to less than 0.1 mag at mid-infrared passbands.

According to the pulsation mode and the shape of the light curve, RRLs are divided in three different types:

* Fundamental mode RRLs exhibit light curves with an asymmetric shape and a rapid ascent to maximum light (sawtooth-like). Their periods are between $\sim$0.4 and $\sim$1 day and their amplitude in the visual band (Amp_V) steadily decreases as

the period increases but is generally larger than 0.7 mag. They are referred to as ab-type (RRab) or RR0 variables.

* First overtone RRLs show sinusoidal-shaped light curves, have periods ranging from ∼0.2 to∼ 0.4 day and lower amplitudes than the RRab variables, from 0.2 to 0.6 mag. They are referred to as c-type (RRc) or RR1 variables.

* Lastly, RRLs that pulsate in both the fundamental and first overtone modes simultaneously are named double-mode RRLs, d-type (RRd) or RR10 variables. For RRd stars the period ratio between first overtone and fundamental pulsation mode is in the range between 0.74 and 0.75.

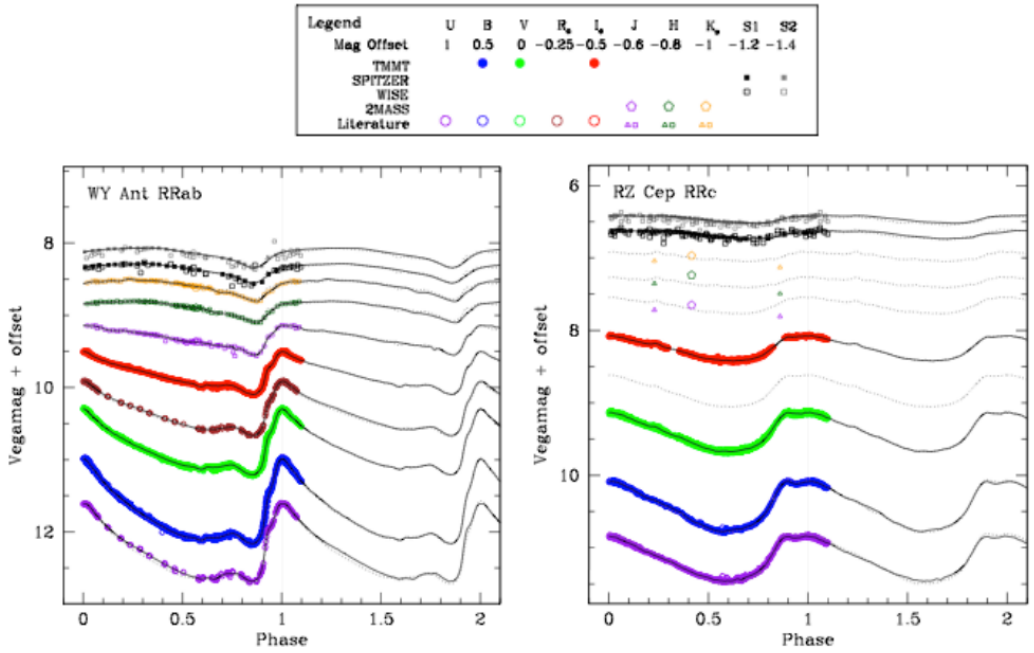

FIGURE 1.1: Multi-band light curves for the RRab star WY Ant (left) and the RRc star RZ Cep (right). From top to bottom in each panel, the bands are S2 (gray), S1 (black), K_s (orange), H (dark green), J (purple), I_C (red), RC (brown), V (light green), B (blue), and U (purple). Figure from Monson et al. (2017).

Figure 1.1 shows examples of multi-band light curves for the RRab WY Ant (left) and the RRc type RZ Cep (right), two of the brightest RRLs located in the Galactic field.

RRab and RRc stars, having different period and amplitude of the light variation, occupy two different and well-defined regions on the so-called Bailey (Bailey , 1902; Bailey & Pickering, 1913; Bailey et al., 1919) or period versus amplitude diagram. Oosterhoff (1939) noticed that the GGCs divide into two distinct groups according to the mean period of their RRab stars ($< P_{ab} >$) and the number of RRab and RRc stars they host.

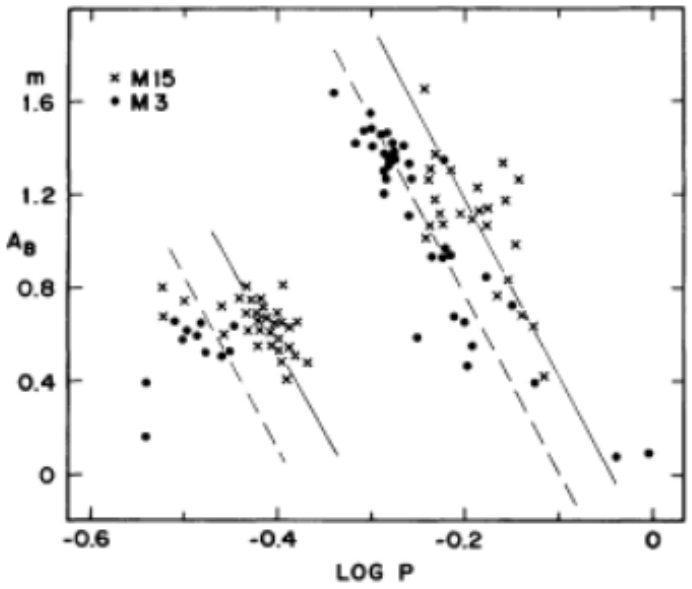

FIGURE 1.2: Period-amplitude diagram in the B-band of RRLs in M3 and M15. Figure from Sandage et al. (1981). Solid and dashed lines show the loci of Oo II and Oo I GGCs, respectively.

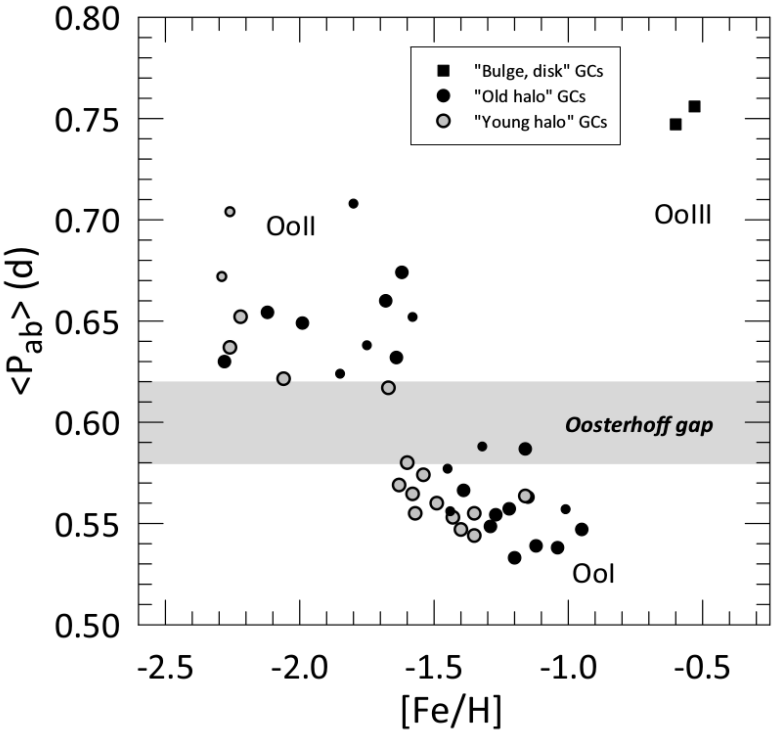

FIGURE 1.3: $< P_{ab} >$ of RRLs versus [Fe/H] for MW GCs. The clusters are separated into "bulge/ disk" (squares), "young halo" (filled gray circles) and "old halo" (filled black circles) subsystems, according to the Makovoz & Khan (2005)'s classification (based on the GCs' positions in the HB morphology-metallicity plane). Figure from Catelan (2009).

This phenomenon is known in the literature as the Oosterhoff dichotomy (see Figure 1.2). GCs with $< P_{ab} > \sim 0.55$ day and $fc = N_{RRc}/(N_{RRab} + N_{RRc}) \sim 0.44$ belong to the Oosterhoff I type (Oo I) while GCs with $< P_{ab} > \sim 0.65$ day and $fc \sim 0.17$ are Oosterhoff II type (Oo II; Clement et al. 2001). Differences in the mean periods of the RRc stars are also found between the two groups, with the Oo I GCs having $< P_c > \sim 0.32$ d and the Oo II GCs having $< P_c > \sim 0.37$ d (see, e.g., Catelan 2009). It was later discovered that a number of MW GCs do not conform to the Oosterhoff dichotomy and have $< P_{ab} >$ between about 0.58 and 0.62 d. They are named Oosterhoff-Intermediate (Oo-Int) GCs. As shown in Figure 1.3 the Oosterhoff dichotomy reflects also a bimodality in metal abundance, since Oo II GCs are generally more metal-poor ([Fe/H]$\sim$ -2.0 dex) and tend to have bluer HBs than the Oo I GCs which typically have [Fe/H]$\sim$ -1.4 dex and redder HBs. The Oosterhoff dichotomy is clearly observed in the period-amplitude diagram, where the RRab stars belonging to Oo I GGCs are well separated from the RRab of Oo I GGCs (traditionally called the Sandage period-shift effect).

The different pulsation mode does not affect the magnitude of RRab and RRc stars, that is, the typical mean magnitude of an RRL star does not change between different types (they all lie on the HB level). However, during a pulsation cycle, the different pulsation mode has an effect on the stellar radius and effective temperature, hence on the colour and position within the IS. RRc stars have slightly higher mean and minimum light effective temperatures than RRab stars. Thus, the cooler (redder) portion of the RRL IS tends to be populated by RRab stars, while the hotter (bluer) portion is populated by RRc stars, with RRd stars located in between RRab and RRc variables.

As mentioned above, besides being tracers of old stellar populations, a main virtue of RRLs is that they are primary distance indicators, because their mean intrinsic brightness follows a specific absolute magnitude-metallicity relation ($M_V - $[Fe/H]) in the visual band, and period-luminosity (PL) and period-luminosity-metallicity (PLZ) relations in the near- and mid-infrared passbands (see Section 1.2).

In sections 1.2 and 1.3 we will discuss the dual role of RRLs as distance indicators and fundamental tracers of an old stellar population to introduce the astrophysical context and aims of this thesis. However, before we briefly describe a number of methods based on the RRL pulsation properties, that allowed us to estimate a photometric metallicity and the interstellar reddening for the RRL populations we have analysed in this thesis work.

1.1.1 Photometric metallicities from RR Lyrae stars

Although spectroscopic metallicities are always to be preferred because more reliable and accurate, photometric metallicities represent an acceptable alternative when spectroscopy is not available or is unfeasible, for instance, because sources are too faint. Jurcsik & Kovacs (1996) developed a method to estimate the metal abundance of RRab stars from the ϕ_{31} parameter of the Fourier decomposition of their V-band light curves. In Jurcsik & Kovacs (1996) formulation the V-band light curve of an RRL is fitted by a Fourier function of the form:

$$V(t) = A_0 + \sum_{i=1}^{N} A_i cos(i\omega_0(t - t_0) + \phi_i), \tag{1.1}$$

where V(t) is the observed magnitude at time t, A_0 is the star mean magnitude, A_i and ϕ_i are, respectively, the amplitude and the phase coefficients of the i^{th} Fourier term, which corresponds to the i-1 harmonic, ω_0 is the angular pulsation frequency of the star, t the time of observation and t_0 the time of the maximum light. The shape of the light curves can be quantified by the low order coefficients of the fit: $R_{i1} = A_i/A_1$ and $\phi_{i1} = 1\phi_i$-iϕ_1 and the A_1, ϕ_{21} and the ϕ_{31} parameters of the Fourier decomposition can be used to classify RRLs in type and pulsation mode (see e.g., Simon & Teays 1982 and Cacciari et al. 2005). Indeed it was shown that one can characterise the shape of the light curve (and hence the pulsation mode) by R_{21} ϕ_{21} or R_{31} and ϕ_{31} Fourier parameters which can be used to distinguish RRLs in pulsation modes, hence in types. The Fourier decomposition terms depend on the number of harmonics used to fit the light curve. Jurcsik & Kovacs (1996) used the first six Fourier components of the light curve to define their method, hence at least six harmonics are necessary to apply this method. They also introduced the so-called compatibility condition and defined a deviation parameter $D_F = |F_{obs} - F_{calc}|/\sigma_F$, where F_{obs} is the observed value of the given Fourier parameter, F_{calc} is its predicted value from the other observed parameters and σ_F is the corresponding standard deviation. D_m is the maximum value of the deviation parameters (D_F) and measures the regularity of the light curve. According to the compatibility condition, this method can produce reliable results only for light curves satisfying the condition, $D_m < 3$. For RRab stars with V-band light curves satisfying the regularity conditions described above, it is possible to apply the Jurcsik & Kovacs (1996) linear relation existing between metallicity ([Fe/H]), pulsation period

(P) and ϕ_{31} Fourier parameter[1]:

$$[Fe/H] = -5.038 - 5.394P + 1.345\phi_{31} \tag{1.2}$$

Later Cacciari et al. (2005) showed that a less stringent condition of $D_m < 5$ is also acceptable, as it does not affect significantly the reliability of the method and improves considerably the statistics. However, Kapakos et al. (2011) found that the condition $D_m < 3$ it not enough to select a robust sample of RRab stars without taking into consideration the σ_{D_m}. Thus, in their analysis, they applied the following condition: σ_{D_m} <3 and $D_m - \sigma_{D_m}$ <3. Jurcsik & Kovacs (1996) calibrated their method using accurate light curves for a large sample of RRab stars belonging to various Galactic globular clusters (GGCs) whose metallicity was known from spectroscopic studies[2].
A less solid, but still useful relation to infer the mean metallicity of a statistically significant RRL sample, is that found among metal abundance, pulsation period and amplitude of the V-band light variation (Amp_V) by Alcock et al. (2000), who defined their relation using RRab stars in three GGCs, namely, M3, M5 and M15. This relation is described by the following formula:

$$[Fe/H] = -8.85 \times (logP + 0.15Amp_V) - 2.60 \tag{1.3}$$

Alcock et al. (2000) verified their relation on the RRab sample of Jurcsik & Kovacs (1996) and found that the two methods provide consistent results within $\sigma_{[Fe/H]} = 0.31$ dex/star.

1.1.2 Interstellar reddening from RR Lyrae stars

RRLs can be used to estimate the interstellar reddening by exploiting the relations existing between their intrinsic colours and the pulsation parameters. Techniques frequently used are Sturch (1966)'s method applied to RRab stars at minimum light; Walker (1992)'s method which is based on the comparison of observed and intrinsic colour of

[1]Similarly Morgan et al. (2007) found a relation that connects [F/H], P and ϕ_{31} for RRc stars. These expressions are derived on the Jurcsik (1995) metallicity scale, specifically used for RRLs. This scale is based on both spectroscopic cluster abundances and ΔS index measurements of cluster variables. The spectroscopic index ΔS is defined by Preston (1959) as ΔS = 10[Sp(H)-Sp(K)] where Sp(H) and Sp(K) are based on the strength of the Balmer lines and K line of Calcium II respectively.

[2]A new calibration of the relation between metallicity ([Fe/H]), Period and ϕ_{31} Fourier parameter has recently been derived by Nemec et al. (2013) using RRLs observed by the Kepler mission (Koch et al. 2010).

the blue edge of the RRL IS; the model fitting of the RRL light curve with theoretical pulsation models (e.g. Marconi & Clementini 2005); and the Piersimoni et al. (2002) method which provides individual reddening values via the following empirical relation:

$$(B-V)_0 = 0.0507(\pm0.0149) - 0.052(\pm0.007)Amp_B + 0.223(\pm0.039)logP + 0.036(\pm0.005)[Fe/H] \quad (1.4)$$

with σ=0.014, which connects the intrinsic colour $(B-V)_0$ of an RRab star to its pulsation period (P), the metal abundance ([Fe/H]) and the amplitude of the light variation in the B-band (Amp_B). Obviously, how reliable the reddening estimated for a stellar system is using this relation depends on how representative of the entire stellar population is the sample of RRLs to which Eq. 1.4 is applied. On the other hand, the strengths of the Piersimoni et al. (2002) method are at least two: (i) it depends on stellar parameters that are not directly affected by reddening and, (ii) it can be used to estimate the reddening of RRLs in different regions of our Galaxy, from the halo to the bulge, providing precise estimates of intrinsic colours across the IS and for a wide range of metallicities.

1.2 RR Lyrae stars as primary distance indicators

RRLs are the primary distance indicators for Population II stellar systems, widely used to measure distances within our own Galaxy and its nearest neighbours up to about 1 Mpc in distance. Recently, the RRLs have also become the Population II standard candle used to define an alternative route to determine the Hubble constant H_0, independently from Classical Cepheids (CCs), the Population I primary standard candle (Beaton et al. 2016). Different relations from the optical to the mid-infrared (MIR) bands make RRLs distance indicators. The most widely used at optical passbands is the relation linking the metallicity to the absolute visual magnitude of RRLs, traditionally known as Luminosity - Metallicity (LZ) relation, M_V-[Fe/H]. At the end of the eighties Longmore et al. (1986, 1990) with their seminal work empirically showed that RRLs also follow a well-defined PL relation in the K-band. Following in quick succession several theoretical and empirical studies explored and verified the existence of such a relation up to MIR passbands (Bono et al. 2001, 2003; Catelan et al. 2004; Dall'Ora et al. 2004; Sollima et al. 2006; Coppola et al. 2011; Madore et al. 2013; Braga et al. 2015; Marconi et al. 2015; Muraveva et al. 2015, 2018a,b). In the following we discuss these fundamental relations the RRLs conform to in more detail.

1.2.1 M_V − [Fe/H] relation of RR Lyrae stars

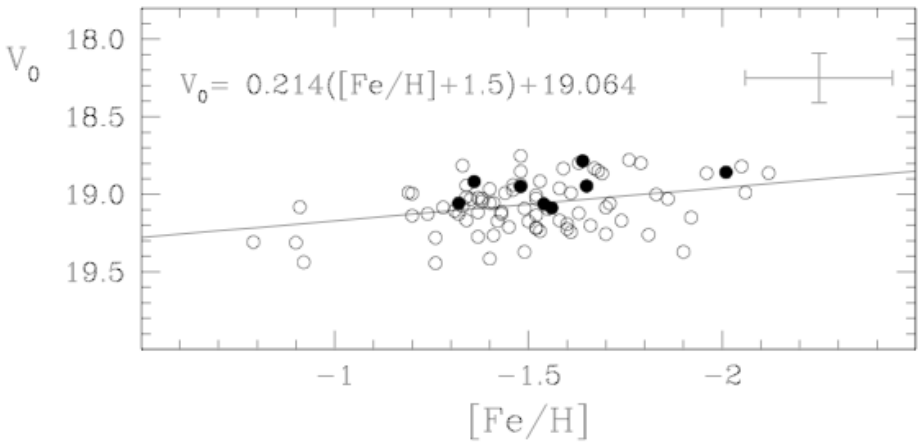

FIGURE 1.4: Luminosity-metallicity relation of RRLs in the LMC. The filled circles mark the RRd stars. Figure from Clementini et al. (2003).

The M_V − [Fe/H] relation of RRLs is, in first approximation, assumed to be linear and universal, and it is usually described in the form $M_V = \alpha[Fe/H] + \beta$ (Sandage et al. 1981). Current determinations of the slope α and zero-point β of this relation span a wide range of values (see e.g. Clementini et al. 2003; Cacciari & Clementini 2003; Marconi et al. 2015 and references therein). An often adopted slope of the metallicity term is $\alpha = 0.214 \pm 0.047$ mag/dex (Clementini et al. 2003; Gratton et al. 2004) which is based on a combined spectroscopic and photometric study of about 100 RRLs in the LMC (Figure 1.4):

$$V_0 = (0.214 \pm 0.047)([Fe/H] + 1.5) + (19.064 \pm 0.017), \tag{1.5}$$

where V_0 is the apparent dereddened average magnitude. However, in the literature for α there are values ranging from 0.30 - 0.37 (Sandage 1993; Feast 1997) to 0.13 (Fusi Pecci et al. 1996). Theoretical studies based on evolutionary (Catelan et al. 2004) and pulsation models (Di Criscienzo et al. 2004) also suggest a change in the slope that becomes significantly steeper, $\alpha = 0.359 \pm 0.027$ mag/dex at [Fe/H]≈ -1.5 dex (see e.g. Caputo et al., 2000; Cassisi et al., 1998; Lee et al., 1990; Bono et al., 2003), therefore a quadratic form of this relation has been proposed over the whole metallicity range covered by the MW RRLs (almost 3 dex for MW field variables).

The zero-point, β, of the $M_V - [\mathrm{Fe/H}]$ relation has been inferred with a number of different techniques, among which: i) the parallax measured by the Hubble Space Telescope (HST) for a few RRLs in the MW (Benedict et al. 2011; see Section 3.5.2.2); ii) the calibration via GCs with distances estimated by main sequence fitting with subdwarfs whose parallaxes were measured by the *Hipparcos* satellite (e.g., Gratton et al. 1997, 1999; Carretta et al. 2000 such absolute magnitudes are known within ± 0.1 mag); (iii) various theoretical and empirical assumptions, such as the adoption of a value for the distance to the Large Magellanic Cloud (LMC; for instance that of Pietrzynski et al. 2013). Despite its simplicity, this relation is also affected by a number of uncertainties, among which the most significant are: i) a poor knowledge of the evolutionary status of the RRL populations; ii) errors in the metallicity measurements, which includes both systematic differences between metallicity scales (calibrations) and methodologies (e.g., what elemental abundance is actually being measured); iii) lack of information about the α-element enhancement.

1.2.2 RR Lyrae NIR and MIR PL and PLZ relations

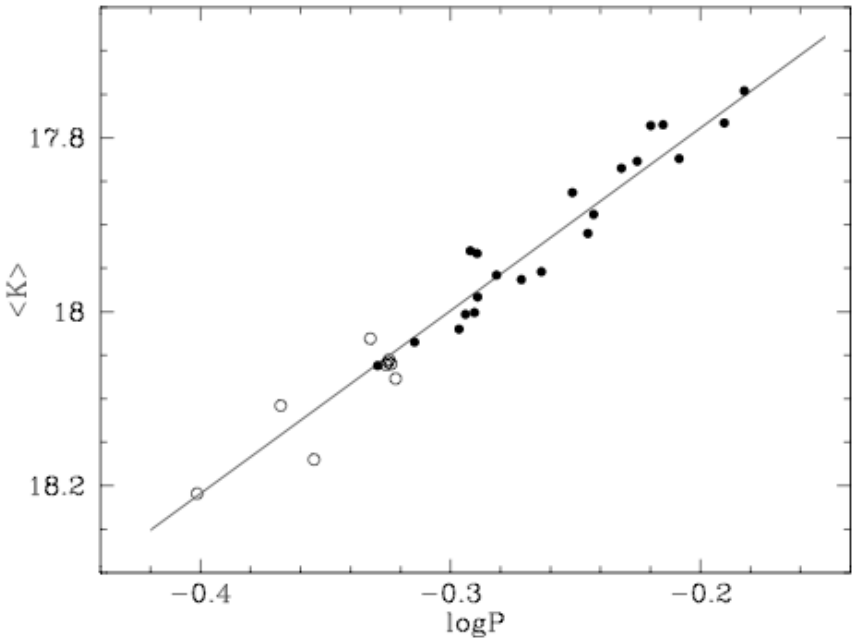

FIGURE 1.5: Period-luminosity relation in the K-band for RRLs in the Reticulum GC. Open and filled circles are RRc and RRab stars, respectively. Figure from Dall'Ora et al. (2004).

The near-infrared (NIR) and mid-infrared (MIR) PL and PLZ relations of RRLs have several advantages in comparison with the visual M_V – [Fe/H] relation, and primarily a smaller dependence of the luminosity on interstellar extinction, metallicity and evolutionary effects. The latter cause an intrinsic spread of the M_V – [Fe/H] relation on the order of $\sim$ 0.2 mag. For comparison, the intrinsic dispersion of the PLZ relation due to evolutionary effects is only 0.04 mag in the K band (Marconi et al. 2015). The effect of extinction is less pronounced in the infrared, particularly in the MIR bands. For instance, the extinction in the Wide-field Infrared Survey Explorer (WISE) W1 (3.4 μm) passband is roughly 15 times smaller than in the V band ($A_{W1} = 0.065A_V$, Madore et al. 2013). Furthermore, the NIR and MIR light curves of RRLs have smaller amplitudes, hence, determination of the mean magnitudes is easier and more precise than in visual bands, thus further reducing the dispersion of their fundamental relations.

A number of studies on the RRL NIR PL and PLZ relations exist in the literature both from the empirical and the theoretical sides. The PLZ relation in the K-band (hereinafter, PM_KZ) is generally assumed of the form:

$$M_K = \alpha \times logP + \beta \times [\mathrm{Fe/H}] + ZP. \tag{1.6}$$

In the literature, the coefficients (α, β) and zero point (ZP) of the PM_KZ relation differ significantly from one study to the other (see e.g. Marconi et al. 2015, for a summary).

Bono et al. (2003) and Catelan et al. (2004) analysed the PM_KZ from the semi-theoretical and theoretical points of view and found a non-negligible dependence of the RRLs K-band absolute magnitude M_K on metallicity, β= 0.231 ($\pm$ 0.012) and 0.17, respectively.

Conversely, in empirical studies, the dependence of the M_K on metallicity is generally much shallower (Del Principe et al. 2006) or even negligible (Sollima et al. 2006, 2008, Borissova et al. 2009, Muraveva et al. 2015). The slope of the period term (α) in the literature varies from -2.101 (Bono et al. 2003) to -2.73 (Muraveva et al. 2015; for a detailed compilation see table 3 in Muraveva et al. 2015).

The RRL MIR relations, although appeared only recently in the literature, have been studied by many different authors both empirically (e.g. Dambis et al. 2014; Sesar et al. 2017) and theoretically (e.g Neeley et al. 2017) at the W1 band of WISE (PMW_1 and PMW_1Z) and almost at the same wavelength (3.6 μm) using the IRAC camera

on board the *Spitzer* space telescope. While Neeley et al. (2017) find a non-negligible dependence on metallicity of 0.180±0.003 mag/dex, Dambis et al. (2014) derived for the PMW_1Z relation a dependence on metallicity of 0.096±0.021 mag/dex, based on a sample of RRLs in 15 globular clusters (covering a metallicity range from −0.99 to −2.37 dex). Recently Sesar et al. (2017) derived instead a metallicity slope $0.15\pm^{0.09}_{0.08}$ mag/dex using the Thyco-*Gaia* Astrometric Solution (TGAS) parallaxes published with the first *Gaia* data release (see Chapter 3) for a sample of about 100 MW RRLs. The literature values of the period slope vary from -2.15 ± 0.23 (3.6μm passband; Muraveva et al. 2018a) to -2.47 ± 0.74 (Sesar et al. 2017).

Accurate trigonometric parallaxes (ϖ) for a significantly large sample of RRLs are needed to firmly calibrate the M_V − [Fe/H] and NIR and MIR $(PL)Z$ relations. This is a main goal of the European Space Agency (ESA) mission *Gaia* (see Section 1.4 and Chapters 3, 4).

1.3 RR Lyrae stars as stellar population tracers

RRLs have been identified in all Local Group (LG) galaxies, irrespective of morphological types and trace the oldest stellar component of these systems. In particular, RRLs are abundant in the LG dwarf spheroidal galaxies (dSphs), which all are known to be characterized by a predominantly old stellar component (t$\sim$ 10−13 Gyr; see, e.g. Tolstoy et al. 2009). A detailed compilation of RRLs in the MW and M31 dSphs is provided by table 3 of Clementini (2010), table 6 of Martínez-Vázquez et al. (2017) and table 4 of Cusano et al. (2017).

The processes driving the formation and evolution of the MW and M31 spirals and, in particular, the connection with their dSph satellites are still open issues. Under the current ΛCDM paradigm, these old satellites could be witnesses/survivors of the accretion events that led to the formation of the stellar halos of the large galaxies they orbit around (Bullock & Johnston 2005; Sales et al. 2007; Stierwalt et al. 2017). Therefore, the MW and M31 dSphs are invaluable laboratories, contributing to our understanding of the Universe on both local and cosmological scales. The LG dSphs are close enough to be resolved in stars, thus allowing to study the building up of the MW and M31 halos by exploiting the information arising from the stars by which they are composed.

The RRLs, along with other types of pulsating variables tracing respectively young and intermediate ages (classical and anomalous Cepheids, respectively, see Appendix C), allow to characterise the different stellar generations occurred in the satellite galaxies, hence, are an essential tool to investigate the formation, evolution and structure of these stellar systems. The information provided by the RRLs becomes even more relevant in the case of the M31 satellites, whose large distance precludes the direct observation of the main sequence turn-off (MSTO) even with the largest ground-based telescopes available so far and requires tens of orbits with the HST.

In the last few years, observations carried out by wide-field surveys like the Sloan Digital Sky Survey (SDSS; York et al. 2000) have increased extraordinarily the numbers of know satellites around the MW and M31. The latest census of the M31 companions currently counts 31 dSphs, whose luminosities range from 10^4 to 10^8 $L_{\odot}$. They were discovered thanks to the systematic imaging of the M31 halo by the Pan-Andromeda Archaeological Survey (PAndAS; Richardson et al. 2011 and references therein), the SDSS (Bell et al. 2011 and references therein), and, more recently, the Panoramic Survey Telescope and Rapid Response System 1 survey (Pan-STARRS1; Martin et al. 2013). Since 2005 the SDSS has revealed the presence around the MW of a new class of satellites, the *ultra-faint dwarf* (UFD) galaxies, which have such low stellar densities to make them very hard to detect unless specific techniques are applied to very large datasets as those provided by the SDSS. This survey in first place and then following imaging surveys like the Dark Energy Survey (DES; The Dark Energy Survey Collaboration 2005), Pan-STARRS1 3π (Chambers et al., 2016) and ATLAS (Shanks et al., 2015) have increased so far the number of new MW satellites (UFDs and globular clusters) up to 46 (Drlica-Wagner et al. 2015; Laevens et al. 2015; Torrealba et al. 2016, and references therein). The UFDs are characterised by the following properties: (i) they have surface brightness $\mu_V \geq 28$ mag arcsec^{-2} and luminosities $-8 \leq M_V \leq -1.5$ (Martin et al., 2008), hence resulting fainter than all previously known dSphs (hereafter, classical dSphs) and GCs. On the absolute visual magnitude versus half-light radius (M_V-r_h) plane, they populate the extension to lower luminosities of the Classical dSphs (see, e.g., figure 1 in Clementini et al. 2012); (ii) they typically host metal poor ([Fe/H] $\leq -$ 2 dex) populations older than 10 Gyr as revealed by accurate spectroscopic studies of their stellar content (see e.g. Simon & Geha 2007, Kirby et al. 2008, Norris et al. 2010, Simon et al. 2011), making them very similar to the stars of the MW's outer halo. Their metallicities are lower than

those of the classical dSphs and similar to the metal abundance of the most metal-poor GGCs; (iii) they display significant spreads in metallicity spanning [Fe/H] values down to −4 dex (see Tolstoy et al. 2009 and references therein); (iv) all UFDs, but Leo T (see e.g. Clementini et al. 2012), have no signature of ongoing star formation activity; (v) these systems are believed to be strongly dark matter dominated, as their mass-to-light ratios and velocity dispersions are much higher than for the classical MW satellites (Strigari et al. 2008); (vi) UFDs often have an irregular shape as they were tidally distorted by the interaction with the MW. A further interesting feature of the MW and M31 dSph satellites, is that they seem to lie on planes surrounding their giant parent galaxies: the Vast Polar Structure of the MW dSphs (VPOS; Pawlowski et al. 2013; Pawlowski 2016) which hosts about a half of the MW satellites and the Great plane of Andromeda (GPoA; Ibata et al. 2013) on which lays about a half of the M31 dSphs. The existence of the VPOS and GPoA is not consistent with the predictions of the standard ΛCDM cosmology where the spatial distribution of the satellites is expected to be isotropic. So far, theory and simulations have not been able to explain the existence of these planes in the framework of the ΛCDM cosmological model.

Photometric studies carried out in the last decade to define the pulsation properties of the RRLs in the MW satellites have revealed that the classical dSphs generally do not show the dichotomy and, with the exception of Sagittarius (Sgr) and Ursa Minor (UMi) are all classified as Oosterhoff-Intermediate (Mateo 1998). On the contrary, although the 12 UFDs studied for variability contain only very few RRLs hence, a robust Oosterhoff classification is not possible, nevertheless they mainly tend to host RRLs with Oo II properties (Clementini 2010).The number of M31 GCs and dSphs studied so far for variability is relatively small when compared with the MW satellites, and results are more controversial. The RRL population has been characterized only in two M31 GCs: B514 which has Oo-Int properties (Clementini et al. 2009) and G11 which has been classified as an Oo II GC (Contreras Ramos et al. 2013). Regarding the M31 field, Brown et al. (2004) used the HST/Advanced Camera for Surveys (ACS) to study the pulsating properties of a sample of 55 RRLs located in a $3.5' \times 3.7'$ field along the south-east minor axis of Andromeda and concluded that, unlike in the MW, the old population in the M31 halo has Oo-Int properties. However, Sarajedini et al. (2009) using the same instrumental set-up observed two fields near M32 at a few kpc from the M31 centre. They identified more than 600 RRLs and concluded that these M31 fields have Oo I properties. Finally, Jeffery et al. (2011) observed about 100 RRLs distributed over six

HST/ACS ultra-deep fields located in the disk, stream and halo of M31, and found that the RRLs appear mostly to be of the Oo I and Oo-Int types. Nine of the M31 dSphs have been analysed for variability up to now and RRLs were identified in all of them (Pritzl et al. 2002, 2004, 2005; Mancone & Sarajedini 2008; Yang & Sarajedini 2012; Cusano et al. 2013, 2015, 2016, 2017 and Martínez-Vázquez et al. 2017). According to these studies all three Oosterhoff types (Oo I, Oo II, and Oo-Int) seem to be present among the M31 satellites.

The properties of the RRLs and the Oosterhoff dichotomy observed in the MW and M31 halos (dSphs, GCs and field) can put constrains on the sub-structures that have contributed in the past to the formation of the MW and M31 halos. However, the question of whether an Oosterhoff dichotomy exists outside the MW remains at present without an answer. Answering this question may help to clarify the processes leading to the formation of the two large spiral galaxies.

1.4 RR Lyrae stars and *Gaia*

Gaia, a European Space Agency (ESA) cornerstone mission in scientific operations since July 2014, is repeatedly monitoring the whole sky by measuring positions, trigonometric parallaxes, proper motions and time-series photometry in 3 pass-bands for over a billion sources, down to a faint limit of $V \sim 21.0$ mag. Among them are hundreds of thousands of RRLs.

Trigonometric parallaxes provide the most direct method of measuring distances in Astronomy. They are needed to transform observed quantities, such as fluxes, into their absolute values. Until recently, accurate parallax measurements were available for only a handful RRLs (Benedict et al. 2011). *Gaia* is expected to provide parallax measurements with end-of-mission errors of about 10 microarcsec (μas) for all RRLs brighter than V ~12-13 mag (see Chapter 3), thus allowing an accurate zero-point re-calibration of the fundamental relations that make RRLs primary standard candles of the cosmic distance ladder, a quantitative re-assessment of their dependence on the chemical composition, and a stringent test of their linearity and universality.

In addition, at the end of the *Gaia* mission, each source will have on average 70 photometric measurements, over 200 observations for sources at |DEC|=45±10 deg and about 40 spectroscopic measurements. Therefore *Gaia* not only will provide accurate distance estimations for known RRLs but will also discover large numbers of new RRLs, increasing the sample of these primary calibrators and, at the same time, offering a fresh view of the systems and structures that host these classical pulsators.

By setting on solid grounds the RRL M_V − [Fe/H] and the $PL(Z)$ relations, as well as the fundamental relations of other standard candles such as the classical, Type II and anomalous Cepheids (see Appendix C), it will thus be possible to re-calibrate secondary distance indicators reaching cosmological distances and probe the value of the Hubble constant H_0 which is still the subject of a very hot debate (Beaton et al. 2016, Riess et al. 2018, etc.).

The *Gaia* Data Release 2, on 25 April 2018, published a catalogue of more than ∼500,000 variables of different types (Holl et al. 2018) and a first census of full-sky RRLs containing more than 140,000 sources among which about 50,000 are new discoveries (Clementini et al. 2018 and Chapter 3). The *revolution* that *Gaia* is carrying in the field of RRLs not only involves their role as distance indicators but also their use as old stellar population tracers. Besides the parallaxes, *Gaia* provides proper motion (PM) measurements that, along with line-of-sight velocities, allow to determine the orbits of the MW satellites, thus revealing the process by which a giant galaxy acquires its satellite and whether the orbits of satellites are consistent with expectations from the concordance cosmological model. At the same time, the RRL pulsation properties (Section 1.3) along with their PMs and parallaxes (hence distances) from *Gaia* allow us to better trace the ancient stellar populations contained in the MW satellites, as well as to identify new systems, stellar streams and debris of destroyed satellites giving us a more complete picture of our Galaxy as a whole.

As stated by Casertano et al. (2016) "[...]This is the start of an exciting phase of measurement and perhaps discovery in the long-lived field of parallax measurement, with the best yet to come.".

Chapter 2

Study of the variable stars and resolved stellar populations in Pisces II, Andromeda XXV and Andromeda XXVII

In this Chapter we present results on the study of the UFD MW satellite Pisces II and the M31 dSph satellites Andromeda XXV and Andromeda XXVII. The main goal was to study the stellar populations hosted by these dwarf galaxies and identify RRLs and other variables which allowed us to measure the distance, trace the dominant stellar population(s) and derive main properties (age, metallicity and Oosterhoff type) to compare with the properties of the MW and M31 stellar halos in order to get hints on the galactic formation process. The studies presented in this Chapter are part of a larger project (PI: G. Clementini) being carried out with the Large Binocular Cameras (LBCs; LBC-blue and LBC-red, respectively) of the Large Binocular Telescope (LBT; Hill et al. 2010). Besides the three systems discussed here the project includes two further dSphs of the M31 complex: Andromeda XIX and Andromeda XXI, for which results were published in Cusano et al. (2013, 2015).

2.1 Pisces II: the member of a pair?

2.1.1 Background

The Pisces II UFD galaxy [Psc II, R.A.(J2000) = 22h58m31s, DEC.(J2000) = 5°57′9″; l = 69.85°, b = −41.83°] was discovered in the southern Galactic portion of the SDSS Segue survey (Yanny et al. 2009) by Belokurov et al. (2010), and later studied in more detail by Sand et al. (2012) and Kirby et al. (2015). Using deep wide-field photometry obtained with Megacam at the Magellan Clay telescope, Sand et al. (2012) estimated the structural and photometric parameters of Psc II. From the mean magnitude of the HB they derived a distance modulus of 21.31 ± 0.17 mag, corresponding to a heliocentric distance of 183 ± 15 kpc. Sand et al. (2012) also estimated a half-light radius of 1.1 ± 0.2 arcmin (that delimitates the region containing the bulk of Psc II stars) which at their estimated heliocentric distance to Psc II corresponds to a linear extension of 58 ± 10 pc, and an absolute magnitude $M_V = -4.1 \pm 0.4$ mag. From the comparison of the galaxy colour-magnitude diagram (CMD) with theoretical isochrones by Girardi et al. (2004), Sand et al. (2012) concluded that Psc II hosts a dominant old (> 10 Gyr) and metal-poor ([Fe/H]∼ -2 dex) stellar population. Kirby et al. (2015) carried out a spectroscopic study of Psc II using the Keck DEIMOS spectrograph. Their radial velocity measurements confirm the membership of seven candidate RGB stars, leading to a systemic velocity $< v_{\odot} > = -226.5 \pm 2.7$ kms^{-1}. They also measured spectroscopic metallicities for four of the seven confirmed members, finding an average value of $<$ [Fe/H] $> = -2.45 \pm 0.07$ dex and a metallicity dispersion on σ[Fe/H]=$0.48\pm^{0.70}_{0.29}$ dex. Finally, Kirby et al. (2015) estimated the velocity dispersion: $\sigma = 5.4^{+3.6}_{-2.4}$ kms^{-1}, the dynamical mass: $\log(M_{1/2}/M_{\odot}) = 6.2^{+0.3}_{-0.2}$ and the mass-to light ratio: $M/L_V = 370^{+310}_{-240}$ $M_{\odot}/L_{\odot}$, hence confirming that Psc II is a dark matter dominated galaxy.

A few years later another new ultra-faint MW satellite, Pegasus III (Peg III) was discovered from analysis of the Sloan Digital Sky Survey (SDSS) Data Release 10 (DR10; Ahn et al. 2014) and then confirmed with deeper Dark Energy Camera (DECam) follow-up observations by Kim et al. (2015). The derived physical properties of Peg III are very similar to those of previously known MW UFDs, and indeed, Peg III perfectly locates in the region populated by UFDs of the size-luminosity diagram. In addition, Kim et al. (2015, 2016) noticed that Peg III is spatially close to Psc II. They are separated by only 8.5° on the sky and have fairly similar distances. The spatial separation of the two

UFDs is ∼43±19 kpc (Kim et al. 2016). If Psc II and Peg III do indeed form a physical pair they would resemble the case of Leo IV and Leo V (de Jong et al. 2010), and this would suggest that each couple of galaxies may be related to the same disrupting or disrupted progenitor.

To study the stellar populations of Psc II and Peg III and investigate their possible physical connection from the comparison of their properties (distance, CMDs and variable star populations) we were granted observing time with the LBT, whose wide-field cameras allowed us to image an area of about 9 half-light radii in the LBT pointing centred on Psc II and about 12 half-light radii of Peg III in the LBT pointing centred on this UFD. The study of Psc II was carried out mainly during the second year of my PhD. Results of this work are discussed in Sects. 2.1.2through 2.1.8. The study of Peg III is reported in the Master Thesis of Maria Tantalo (which I co-tutored and to which we refer for details) and only briefly summarised in Sect. 2.1.9 to allow a comparison between the two systems.
The paper: "Born in a pair (?): Pisces II and Pegasus III" by A. Garofalo, M. Tantalo, F. Cusano et al., presenting results from the analysis of these two MW UFDs, is in advanced stage of preparation.

2.1.2 LBT observations and PSF photometry of Psc II

B,V time-series photometry of Psc II was collected with the Large Binocular Cameras (LBCs) program (PI: G. Clementini) which targeted also the MW UFD Peg III. Each LBC has a field of view (FoV) of $23' \times 23'$ and is equipped with four 2048 × 4608 pixel EEV CCDs resulting in a 6150 × 6650 pixel equivalent detector, with a pixel scale of $0.224''$/pixel. The data collected for Psc II consist of 26 B and 26 V images each with an exposure time of 180s acquired over six nights from October to December, 2015. Most of the observations were obtained with seeing ≤ 1.2 arcsec. This is well suited for our purposes. All images were pre-reduced (bias-subtracted, flat-fielded and astrometrized) by the LBT team through an LBC dedicated pipeline, and then, on each of the four CCDs of the two LBCs, separately, we performed point spread function (PSF) photometry with the `DAOPHOT-ALLSTAR-ALLFRAME` packages (Stetson 1987, 1994). To transform the instrumental magnitudes to the Johnson standard system we used standard stars selected from the SDSS catalogue (available at `https://www.sdss3.org/`

dr8/algorithms/sdssUBVRITransform.php#Lupton2005). We used calibration equations of the form: $B - b = c_B + m_B \times (b - v)$ and $V - v = c_V + m_V \times (b - v)$, where B and V are the standard Johnson magnitudes of the SDSS stars, and b and v are the instrumental magnitudes in our photometric catalogue. The parameters of the calibration were derived by applying a 3σ clipping rejection algorithm to fit the data. The final fit was obtained using a total of 772 stars and provided the following calibration equations: $B - b = 8.229 - 0.1409 \times (b - v)$ and $V - v = 8.139 - 0.0823 \times (b - v)$, with r.m.s. values of 0.034 and 0.024 mag in B and V, respectively. Our final B, V combined catalogue contains more than 28,000 sources observed in the LBT field centred on Psc II.

2.1.3 Variable stars: identification and pulsation properties

To identify variable stars in Psc II we first considered stellar sources having a high value of the variability index computed by `DAOMASTER` (Stetson 1994) both in the V and B passbands. Then we also checked all stars that in the CMD have colours and magnitudes falling within the edges of the classical instability strip (IS). This procedure returned a list of ~ 20 candidate variables with more than 22/24 data points which were inspected visually with the GRaphical Analyzer of TImes Series package (GRATIS, Clementini et al. 2000). GRaTiS uses both the Lomb periodogram (Lomb 1976; Scargle 1982) and then the best fit of the data with a truncated Fourier series in the period interval around the periodicity found by the Lomb algorithm. The final periods adopted to fold the light curves were those that minimize the r.m.s. scatter of the truncated Fourier series best fitting the data. Taking into account the derived period, the shape of the light curve, the position on the CMD and the mean B and V magnitudes, we confirmed the variability of three candidates and classified in type two of them: 1 RRab and 1 SX Phoenicis (SX Phe) star, whereas the classification of the third variable remains uncertain because two alternative periods are equally possible and, correspondingly, this variable may either be a metal poor RRab star or an anomalous Cepheid (AC). Since the available data do not allow us to firmly establish the correct periodicity, hence classification in type, of this variable source, in this work we used both periodicities to fold the star light curves. A fourth source, which is located inside the galaxy r_h, exhibits variability particularly in the B passband. We tentatively classified this source as an SX Phe star, however, this classification remains doubtful because the V light curve of the star shows very little, if any, variability (see Figure 2.1).

The properties of the variable stars identified in Psc II are summarised in the upper portion of Table 2.1. To ease the comparison, the bottom portion of Table 2.1 summarises the properties of the variables identified in Peg III. Column 1 provides the star identifier. This is an increasing number starting from the galaxy centre, for which we have adopted the coordinates of the discovery paper (Belokurov et al. 2010). Columns 2 and 3 give the coordinates, Columns 4, 5 and 6 list respectively the classification in type, the period (P) and the Heliocentric Julian Day (HJD) of maximum light, and Columns 7, 8, 9 and 10 provide the intensity-weighted mean B and V magnitudes and the corresponding amplitudes of the light variation. The B, V light curves of the confirmed (3) and candidate (1) variable stars in Psc II are shown in Figure 2.1. The spatial distribution of all stars measured in our LBT observations of Psc II with respect to the galaxy centre (α_0, δ_0) is shown in Figure 2.2. In the figure we have marked in blue five ellipses representing from once to five times the r_h of Psc II, 1.1 $\pm$ 0.2 arcmin, as estimated by Sand et al. (2012). The bona-fide RRab star (V1; magenta filled square) is located within the Psc II r_h, at a distance from the centre of about 0.3′. The SX Phe star (V3; cyan triangle) and the variable of uncertain type (V4; red filled circle) both are outside the galaxy r_h, at distances of about 2.6′ and 4.5′ from the galaxy centre. In particular, the SX Phe star is within 3 r_h and the uncertain type variable within 5 r_h. The distance from the galaxy centre and the position on the CMD (see Sect. 2.1.7, Figure 2.8) of bona-fide RRab star and SX Phe star suggest that they belong to Psc II; conversely, the membership of V4 remains doubtful (see Section 2.1.6).

TABLE 2.1: Properties of the variable stars identified in Psc II and Peg III

Name	α (J2000)	δ (J2000)	Type	P (days)	Epoch (max) HJD (2457000)	$\langle B \rangle$ (mag)	A_B (mag)	$\langle V \rangle$ (mag)	A_V (mag)
Pisces II									
V1	22:58:29.858	+5:57:10.92	RRab	0.5551	296.71	22.28	0.94	21.89	0.69
V2	22:58:33.535	+5:57:43.63	SXPhe(?)	...	...	...	...	...	...
V3	22:58:40.807	+5:56:23.16	SXPhe	0.06348	333.6245	24.245	1.119	23.935	0.775
$V4_{RRL}$	22:58:44.659	+5:54:16.33	RRab	0.722	335.565	21.98	1.18	21.63	0.93
$V4_{AC}$	22:58:44.659	+5:54:16.33	AC	0.4186	335.612	22.004	1.097	21.635	0.825
Pegasus III									
V1	22:24:18.312	+5:22:17.78	RRab	0.5537	357.560	22.58	1.18	22.13	0.96
$V2_{RRL}$	22:24:01.932	+5:25:45.52	RRab	0.6594	296.771	22.33	1.26	21.80	1.16
$V2_{AC}$	22:24:01.932	+5:25:45.52	AC	0.3972	357.531	22.37	1.03	21.85	0.84

Notes: In Psc II for V4 (as well for V2 in Peg III) GRATIS finds best-fitting Fourier model of the light curve for two different periodicities having similar r.m.s. scatter. On these periodicities GRATIS provides the amplitudes and the corresponding intensity-weighted mean B and V magnitudes.

2.1.4 Distance to Psc II

We measured the distance to Psc II using V1, the RRL with a solid classification and located within the galaxy's r_h. The mean V magnitude of V1 is $< V > = 21.890 \pm 0.038$ mag (see Table 2.1), which we de-reddened using a standard extinction law $A_V = 3.1 \times E(B\text{-}V)$ and the the reddening value from Schlegel et al. (1998), E(B-V)=0.056 ±0.052 mag[1]. We adopted an absolute magnitude of $M_V = 0.54 \pm 0.09$ mag for RRLs with a metallicity of [Fe/H] = -1.5 dex (Clementini et al. 2003) and

[1]An independent estimate of the reddening can be obtained from RRLs using the Piersimoni et al. (2002) method (section 1.1.2). From V1 we obtained a reddening value E(B-V)=0.052±0.023 mag that agrees very well with the reddening from Schlegel et al. (1998). A more recent reddening value is provided by Schlafly & Finkbeiner (2011), this value is ∼0.01 mag higher but still consistent with the Schlegel et al. (1998)'s estimate.

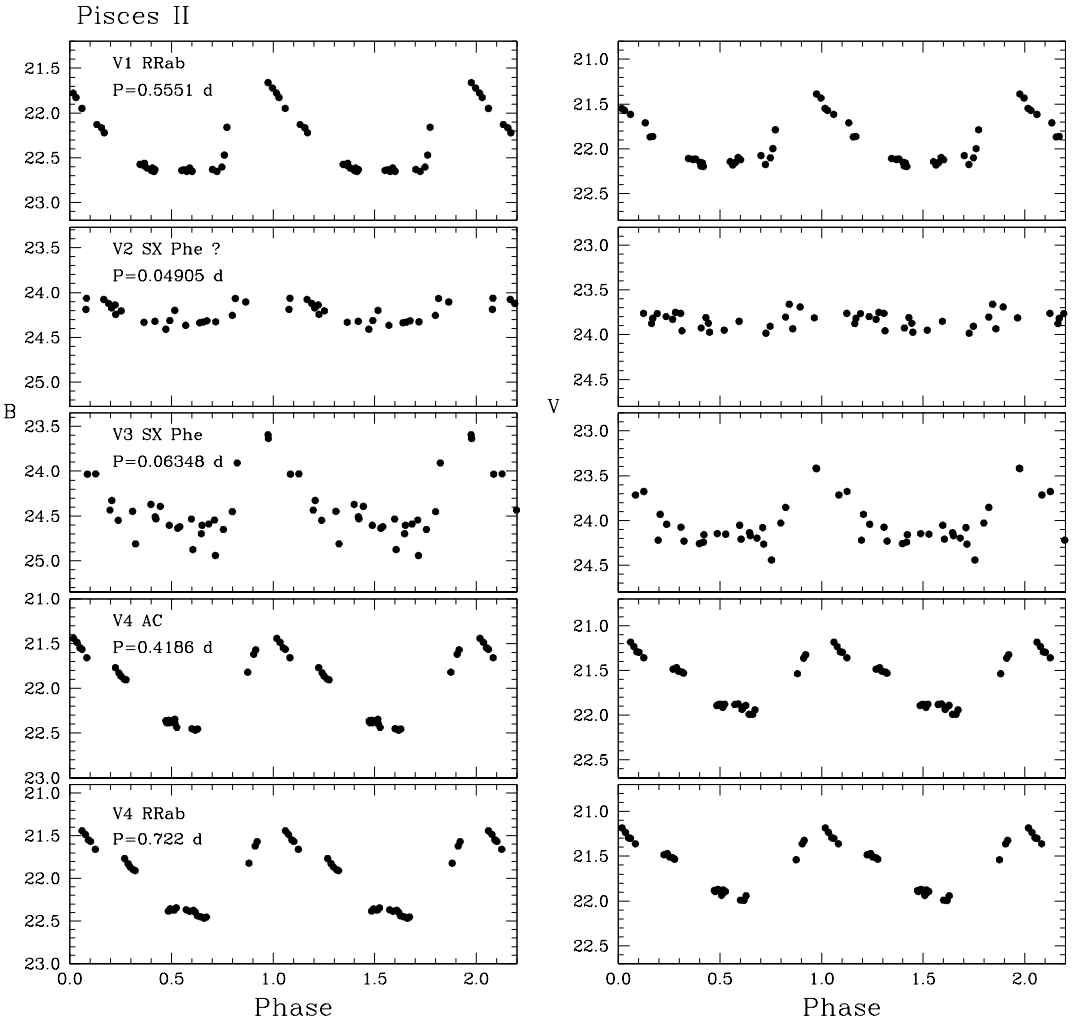

FIGURE 2.1: B (left panels) and V (right panels) light curves of confirmed and candidate variable stars that we have identified in the Psc II galaxy. For V4 the data have been folded according to both periods.

the slope of the luminosity-metallicity relation provided by Clementini et al. (2003) and Gratton et al. (2004), namely $\frac{\Delta M_V}{\Delta[Fe/H]}$=-0.214 ± 0.047 mag dex^{-1} (eq. 1.5, Section 1.2.1). For the metallicity of Psc II we adopt the value [Fe/H]∼ −1.7 ± 0.1 dex according to the theoretical isochrones we overlaid on the CMD (see Figure 2.11, Section 2.1.7) even if the spectroscopic metallicity estimated by Kirby et al. (2015) is much lower ([Fe/H]=−2.45±0.07 dex). The distance modulus we derived for Psc II is (m-M)$_0$= 21.22 ± 0.14 mag, which corresponds to a distance of d = 175 ± 11 kpc. This distance is shorter than the value estimated by Sand et al. (2012) but is consistent with it within the respective errors. If we assumed instead the Kirby et al. (2015) spectroscopic metallicity, the distance modulus would be 0.16 mag fainter, placing Psc II ∼ 14 kpc farther than the previous estimate and in agreement with the literature value.

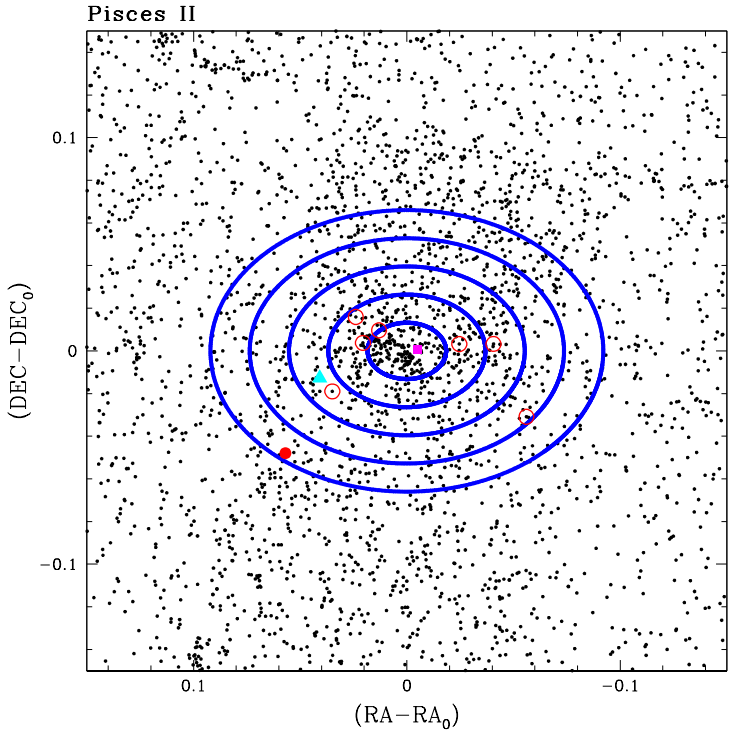

FIGURE 2.2: Map of the sources measured in the LBC FoV of Psc II. Only sources selected according to the cuts described in Sect. 2.1.7 are displayed. Five blue ellipses are drawn showing from one (inner ellipse) to 5 times the galaxy r$_h$ (outer ellipse; that is where V4, the outermost variable of Psc II is located), adopting the position angle, r$_h$, ellipticity, and centre coordinates of Sand et al. (2012). A magenta square marks the fundamental mode RRL (V1), a cyan triangle the confirmed SX Phe star (V3) and a red filled circle the RRab/AC star (V4). Red open circles show 7 members of Psc II spectroscopically confirmed by Kirby et al. (2015).

2.1.5 Bailey diagram and Oosterhoff classification

We have used the amplitude in the V band and the period of V1, the bona-fide RRab star identified in Psc II, to plot the source on the period-amplitude diagram (Figure 2.3) and make a comparison with RRLs in other MW UFD satellites.

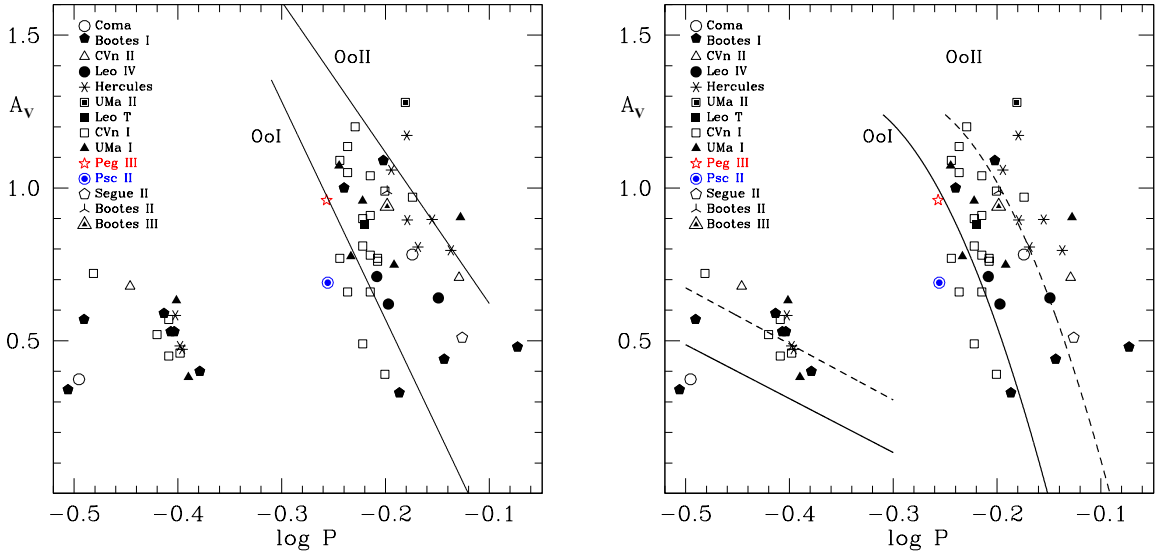

FIGURE 2.3: Period-amplitude (Bailey) diagram: the RRab star inside the r_h of Psc II (star V1) is marked by a blue circle while the bona-fide RRab in Peg III is marked by a red star. Solid lines show the loci of Oo I and Oo II GGCs according to Clement & Rowe (2000, left panel) and Cacciari et al. (2005, right panel). For comparison, we also plotted the RRLs identified in other 12 MW UFD satellites (see text for details).

In left and right panels of Figure 2.3 a blue circle marks the RRab star within the half-light radius of Psc II and a red star shows the bona-fide RRab star in Peg III (from M. Tantalo's Master Thesis). The RRLs detected in other 12 MW UFDs are also plotted in the figure using different symbols: Coma (Musella et al. 2009), Bootes I (Dall'Ora et al. 2006), Bootes II and Bootes III (Sesar et al. 2014), Canes Venatici I (Kuehn et al. 2008), Canes Venatici II (Greco et al. 2008), Leo IV (Moretti et al. 2009), Hercules (Musella et al. 2012), Leo T (Clementini et al. 2012), Segue II (Boettcher et al. 2013), Ursa Major I (Garofalo et al. 2013) and Ursa Major II (Dall'Ora et al. 2012). In the Bailey diagram RRab (fundamental mode) and RRc (first overtone) stars are well separated. As expected for their periods the RRLs we have identified in Psc II and Peg III fall in the region of the fundamental mode pulsators. We have also highlighted with solid

lines the loci of the two Oosterhoff types, Oo I and Oo II (Oosterhoff 1939; Sect. 1.1)[2] . Although based on just two RRLs, the positions of the bona-fide RRab stars in Psc II and Peg III on the Bailey diagram would suggest an Oo I classification for both galaxies. This is in contrast with what is found for other MW UFDs, most of which are classified as Oo II, a few as Oo-Int and none as Oo I. However, this result is consistent with the photometric metallicity we inferred for the two RRab stars, namely, [Fe/H] ~ -1.7 dex for Psc II (using Eqs. 1.2 and 1.3 in Sect.1.1.1) and [Fe/H] $= -1.61 \pm 0.50$ dex for Peg III (from the fit with theoretical isochrones; M.Tantalo's Master Thesis).

2.1.6 The intriguing case of V4

As anticipated in Section 2.1.3, V4 has an uncertain classification. Its B and V data can as well be folded with P $\sim$ 0.72 d and the variable being an RRab star, or with P $\sim$ 0.42 d and the star being a first-overtone AC. We performed a number of tests to investigate the nature of V4 first assuming a classification as AC and then as RRab star. ACs are known to follow specific PL and Period-Wesenheit (PW) relations, which differ from both the classical and the Type II Cepheids relationships (see Appendix C, Section C.3). Therefore, if V4 is an AC it should conform to the PL and PW relations of ACs. We have compared V4 with the PW relations (that are narrower and by definition reddening free, Madore 1982) followed by ACs in the Large Magellanic Cloud (LMC; see Ripepi et al. 2014). These relations are defined in the V and I bands, hence we converted them to the B, V bands[3] using the relation $< W(V,I) >= -0.22(\pm 0.001) + 1.03 < W(B,V) >$ (Eq. 12 of Marconi et al. 2004). The PW relations of the LMC ACs converted into B and V bands are shown as solid lines in the left panel of Figure 2.4, together with their 1σ uncertainties (dotted lines). In the figure the lower line is the PW relation for fundamental mode ACs, while the upper line is for ACs that pulsate in the first-overtone mode. V4 (red filled circle) is plotted according to its period as an AC and the Wesenheit index computed by correcting the $< V >$-band apparent magnitude for the distance modulus (m-M)$_0$ = 21.22 mag as estimated from V1, the RRL inside the r$_h$ of Psc II. V4 lies within the 1σ uncertainty of the PW relation for first-overtone ACs, hence, it could indeed be an AC belonging to Psc I. As a check, in the right panel of Figure 2.4

[2]We show Oo I and Oo II reference loci both linear (left panel), as found by Clement & Rowe (2000), and not linear (right panel), as found by other analyses (Cacciari et al., 2005; Zorotovic et al., 2010; Arellano Ferro et al., 2018).

[3]The Wesenheit index in our case is $W(B,V) = M_V - 3.1 \times (B-V)$, where M$_V$ is the V magnitude corrected for the distance.

we have compared V4 also with the *PW* relations for LMC Classical Cepheids (CCs) by Jacyszyn-Dobrzeniecka et al. (2016). The star appears to be significantly fainter than the Wesenheit index of a fundamental-mode CC with the same period, hence, it is unlikely that it could be a CC of Psc II. Furthermore, in the CMD of Psc II (see Figure 2.8) there is no indication of the presence of a young population (< 300 Myr) as that traced by CCs. Figure 2.4 seems thus to reinforce the hypothesis that V4 might be a first overtone AC belonging to Psc II.

We further checked this hypothesis comparing the star with stellar evolutionary tracks by Pietrinferni et al. (2004, available at `http://basti.oa-teramo.inaf.it/index.html`), for the typical mass and metallicity of ACs ($\sim$1.8-2.2 $M_{\odot}$ according to Caputo et al. 2004 and Z = 0.0004 following Marconi et al. 2004). This is illustrated in the three

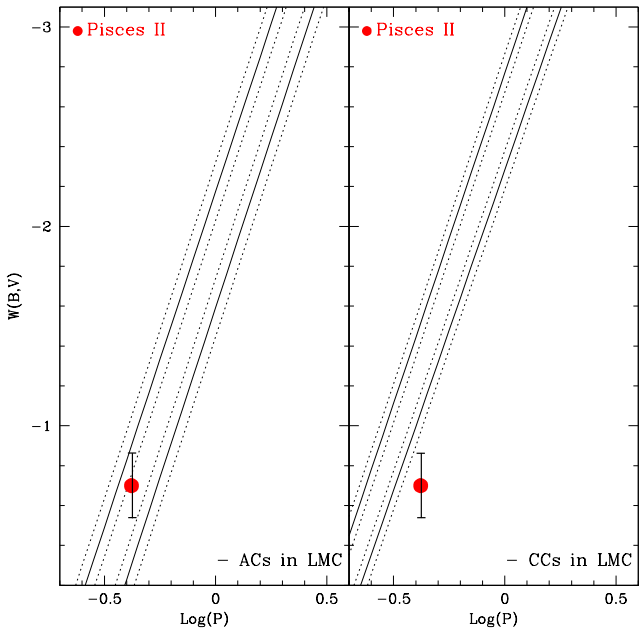

FIGURE 2.4: *PW* relations (solid lines) for ACs (left panel; from Ripepi et al. 2014) and CCs (right panel; from Jacyszyn-Dobrzeniecka et al. 2016) in the LMC, transformed to the B and V bands. Dotted lines represent the 1σ uncertainties, which for the ACs relations correspond to 0.15 and for CCs to 0.10. A red filled circle shows the position of V4, according to the period of $\sim$ 0.42 d and a Wesenheit index calculated for a distance modulus of $(m\text{-}M)_0 = 21.22$ mag as estimated from V1, the RRL inside the half-light radius of Psc II.

panels of Figure 2.5 that show the CMD of Psc II with overlaid evolutionary tracks for metallicity Z = 0.0003 and masses of 1.8, 1.9 and 2.0 $M_{\odot}$, corrected for the Psc II distance modulus and for a reddening of E(B-V) = 0.056 mag according to Schlegel et al. (1998) reddening maps. This comparison shows that if V4 is indeed an AC belonging to Psc II it should be at least 1 mag brighter to lie on the proper region of the evolutionary track: the hook above the HB. On the other hand, since V4 is at about five r_h from Psc II centre, it could be a field AC. We thus shifted the stellar tracks as to fit the luminosity of V4 and found that the hook of the 1.8 $M_{\odot}$ track would fit the luminosity

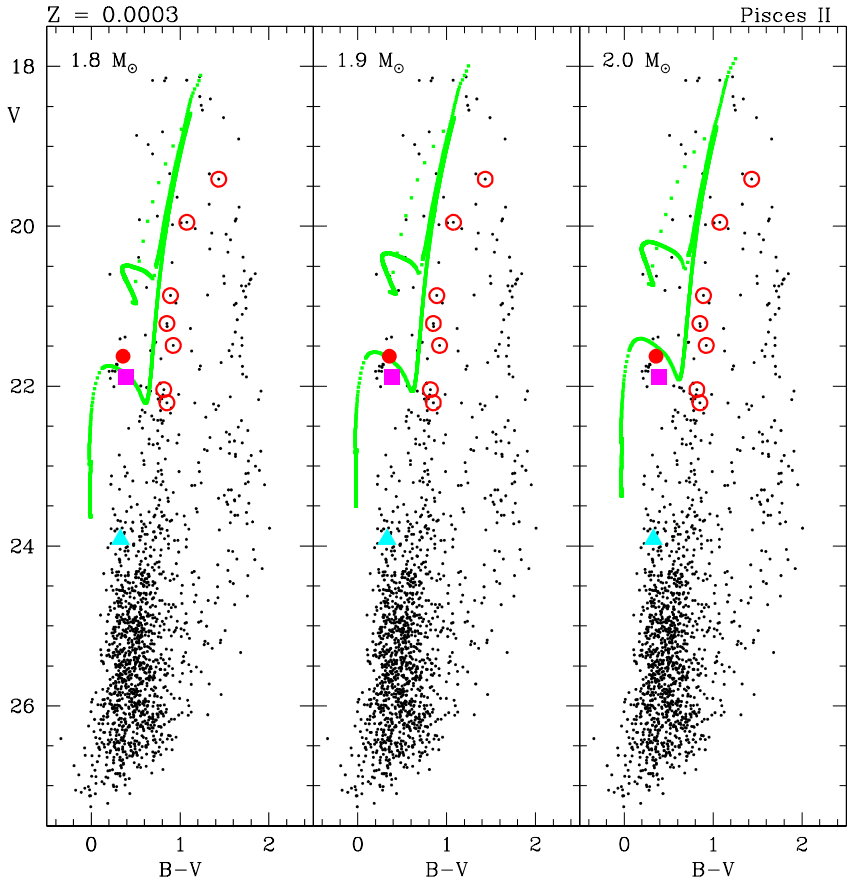

FIGURE 2.5: Stellar evolutionary tracks (BaSTI web interface) for 1.8, 1.9 and 2.0 $M_{\odot}$ (green solid line; left, central and right panels, respectively) and metallicity Z = 0.0003 ([Fe/H] = −1.8 dex) overlaid on the galaxy CMD. The tracks were corrected adopting the distance modulus of Psc II derived from the RRab star [V1; $(m\text{-}M)_0$ =21.22mag] and the reddening E(B-V)=0.056 from Schlegel et al. (1998) maps. V1 is marked by a magenta filled square, the AC/RRab star (V4) by a filled red circle, the SX Phe star (V3) by a cyan triangle and the spectroscopically confirmed members from Kirby et al. (2015) by red open circles.

of V4 for a distance modulus of $(m\text{-}M)_0 \sim 22.4$ mag and for longer moduli in case of larger masses. However, adopting these longer distance moduli, V4 could no longer fit any of the *PW* relations for ACs or CCs, as clearly shown by Figure 2.6. Based on these conflicting results we conclude that the classification of V4 as an AC either belonging to Psc II or to the background field is very unlikely.

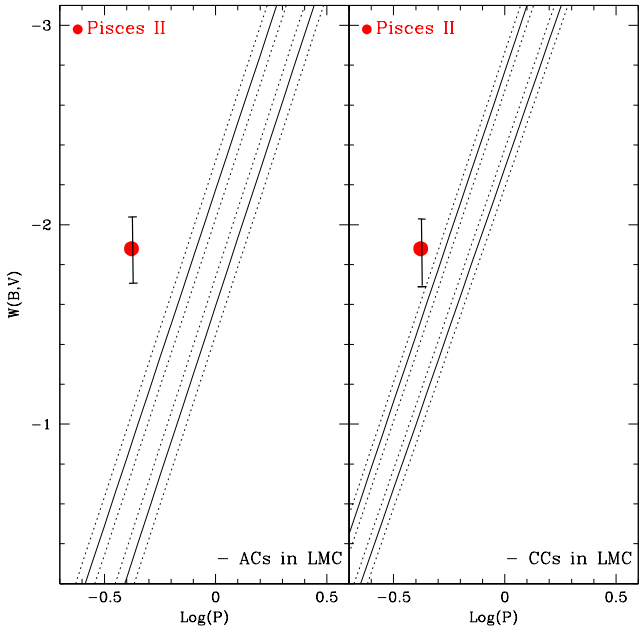

FIGURE 2.6: Same as in Figure 2.4 but adopting for V4 a mass of $1.8M_{\odot}$ and a Wesenheit index calculated for a distance modulus of 22.4 mag.

We now explore the possibility that V4 is an RRab star with P=0.722 d. Left and right panels of Figure 2.7 show the position that V4 (blue filled circle at logP=−0.141) occupies in the period-amplitude diagram. The star falls very close to the Oo II locus and has a higher luminosity and lower metallicity than V1 (blue filled circle at logP=−0.256) which falls instead near the Oo I locus. Variable stars in Oo II clusters have longer periods, higher luminosities and lower metallicities than those in the Oo I clusters (see e.g. Clement & Rowe 2000, and references therein) and are supposed to be evolved off the Zero Age HB (ZAHB; see e.g. Lee et al. 1990) or to contain higher helium abundances (see e.g. VandenBerg et al. 2016). However, even if UFDs exhibit metallicity dispersions

of the member stars that can be as large as 1 dex (see e.g. Tolstoy et al. 2009, and references therein), none of those studied so far has been found to host RRLs belonging to the two different Oosterhoff types. Hence, it is difficult to explain how Psc II is able to host Oo I and Oo II RRLs at the same time.

A further option could be that V4 belongs to a structure/stellar system projected in front of Psc II. However, there is no sign of any overdensity/structure surrounding V4 in the isodensity contour maps (see Figure 2.13). On the other hand, the distance moduli inferred for V1 and V4 are well consistent with one another, within the respective errors, hence, it may be possible that both stars are members of Psc II. Still, it remains unclear how the two stars can belong to the same system although they are about 8 kpc apart in projected distance (if we trust the difference in distance moduli, see Section 2.1.7) and about 5 r_h apart from the centre of Psc II.

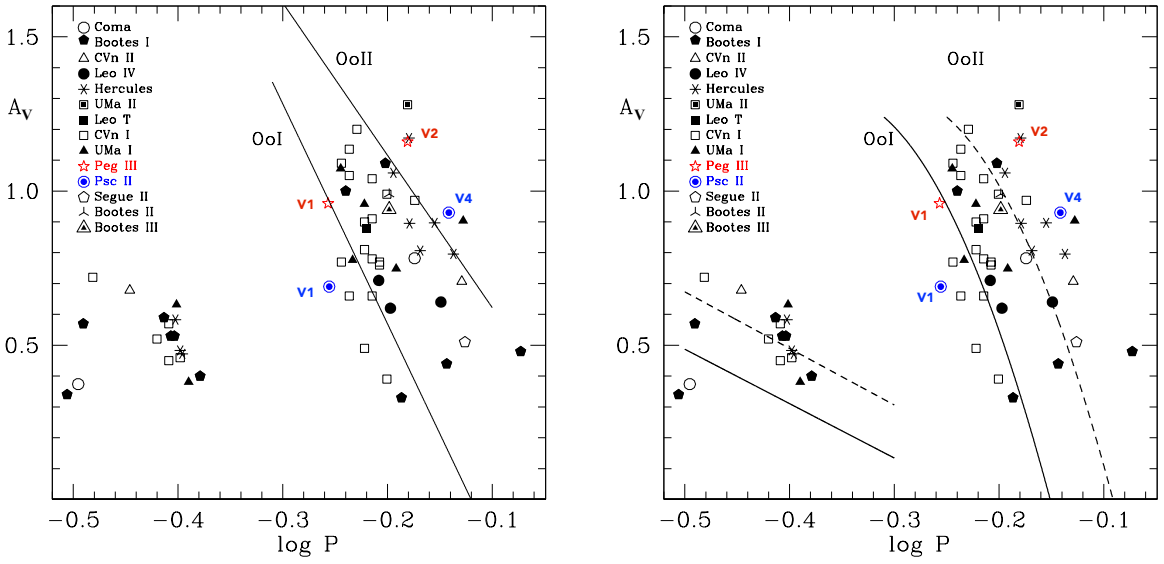

FIGURE 2.7: Same as in Figure 2.3 but with V4 also added (blue filled circle at logP=−0.141). The two red stars are, respectively, the bona-fide RRab star (V1) and the variable star with uncertain classification (V2) in Peg III (from M. Tantalo's Master Thesis).

To conclude, the tests we have made lead us to rule out that V4 is an AC (either belonging to Psc II or to the background field). The most likely hypothesis is that V4 is an RRab star with Oo II characteristics belonging to the Psc II UFD. However, it remains to clarify how Psc II can host two stellar populations of different age and metallicity.

Might two separate star formation episodes have occurred in this small galaxy? This is not quite a common scenario among the MW UFDs. This hence remains an open issue that only with the collection of new observations allowing us to definitively constrain the period and classification in type of V4 may be clarified. Moreover new observations can allow us to better define in Psc II period and amplitude of V1. The V1 maximum light, once perfectly sampled, may also reveal period and amplitude more similar to V4 placing the star closer to Oo II locus, as well the mean V magnitude of V1 may be brighter and hence the difference between V1 and V4 may be less than 0.25 mag.

2.1.7 Colour Magnitude Diagram of Psc II

The V, B-V CMD of Psc II obtained in this study is shown in Figure 2.8. We used the quality information provided by the the `DAOPHOT` quality images parameters χ and *Sharpness*, to clean the list of measured sources selecting for the CMD only the stellar detections satisfying the following quality photometry criteria: -0.4 $\leq$ *Sharpness* $\leq$ 0.4, and $\chi < 2.2$, in both B and V images. This allowed us to reduce the contamination by background galaxies. In Figure 2.9 we have plotted all the stellar detections in the LBT FoV, selected according to the above χ and *Sharpness* values, separated according to the four CCDs of the LBC mosaic. Typical internal errors of the photometry for non-variable stars are shown in the right-hand side of the plots. These errors are, typically, <0.1 mag for $B < 20.0$ mag, <0.15 mag for $20.0 < B < 25$ mag and then steeply increase for $B > 25$ mag. In order to distinguish stars belonging to the Psc II galaxy from the overwhelming population of field stars belonging to the MW halo we have cross-matched our catalogue against the Kirby et al. (2015) list of spectroscopically confirmed Psc II members. All the 7 RGB stars that are Psc II members according to Kirby et al. (2015) have a counterpart in our catalogue, marked as empty red circles in Figs. 2.8 and 2.9. A magenta square marks V1, the bona-fide RRab star, a red filled circle marks the variable with uncertain classification, V4, both plotted according to the intensity-weighted mean magnitudes computed along the pulsation cycle. A cyan filled triangle shows the SX Phe star (V3).

Our CMD of Psc II is rather deep, reaching $V \sim 26.5$ mag, hence allows us to trace the galaxy main sequence (MS) below the turn-off (TO) point, that is located approximately

between 25 and 25.5 mag in V according to the theoretical isochrones overlaid on the CMD (see Figure 2.11, later in this Sect.).

As shown in Figure 2.9, the galaxy is fully contained in CCD2, the central CCD of the LBC configuration, where are located all the Psc II members spectroscopically confirmed plus V1. Only in CCD2 is recognisable a hint of HB and RGB (for the latter, the eye is guided by the presence of the spectroscopic members). The CMD of Psc II within the half-light radius would be very poorly populated; only V1 and one of the spectroscopic member are located in this region, the other six members are all located in the region between 1 and 4 times the galaxy r_h. We tried to build a final CMD reasonably populated, containing all the spectroscopic members and V4, the variable of uncertain classification. This is shown in Figure 2.10 that corresponds to the V, B-V CMD of all stellar sources located within 5 times the r_h of Psc II (hereinafter, in this section, the CMDs we show will all be within 5 r_h). The features most recognisable in the CMD of Psc II are: (i) HB at $V \sim 22$ mag, as also inferred from the mean V magnitude of the bona-fide RRab star ($< V >$=21.89 mag), populated by a few stars

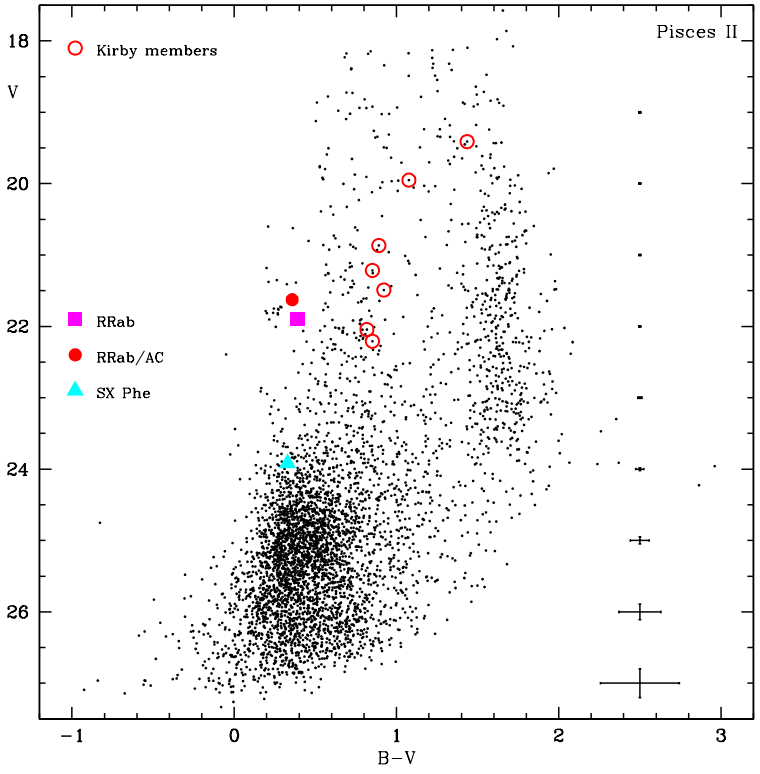

FIGURE 2.8: V , B-V CMD of Psc II obtained after the selections in χ and *Sharpness*. Symbols and colour-coding are the same as in Figure 2.5.

close to the red and blue edges of the IS and roughly ending at $B-V \sim 0.2$ mag; (ii) RGB between$(B-V)\sim$0.7 and $\sim$1.4 mag, reaching as bright as $V \sim$ 19.5-19 mag and recognisable because traced by the RGB member stars by Kirby et al. (2015).

These features are indicative of a stellar population older than 10 Gyr, in agreement with the typical ages of the stellar components observed in the UFDs. In order to estimate the age and metallicity of the Psc II dominant stellar population, we over-plotted on the CMD the PARSEC stellar isochrones from Bressan et al. (2012), available on the CMD 2.9 web interface. Figure 2.11 shows the CMD of Psc II in a region within 5 times the galaxy r_h with overlaid the PARSEC isochrones for a fixed age of 13 Gyr and different metallicities: [Fe/H] = −2.3, −1.9, −1.8, −1.7 and −1.5 dex. The isochrones

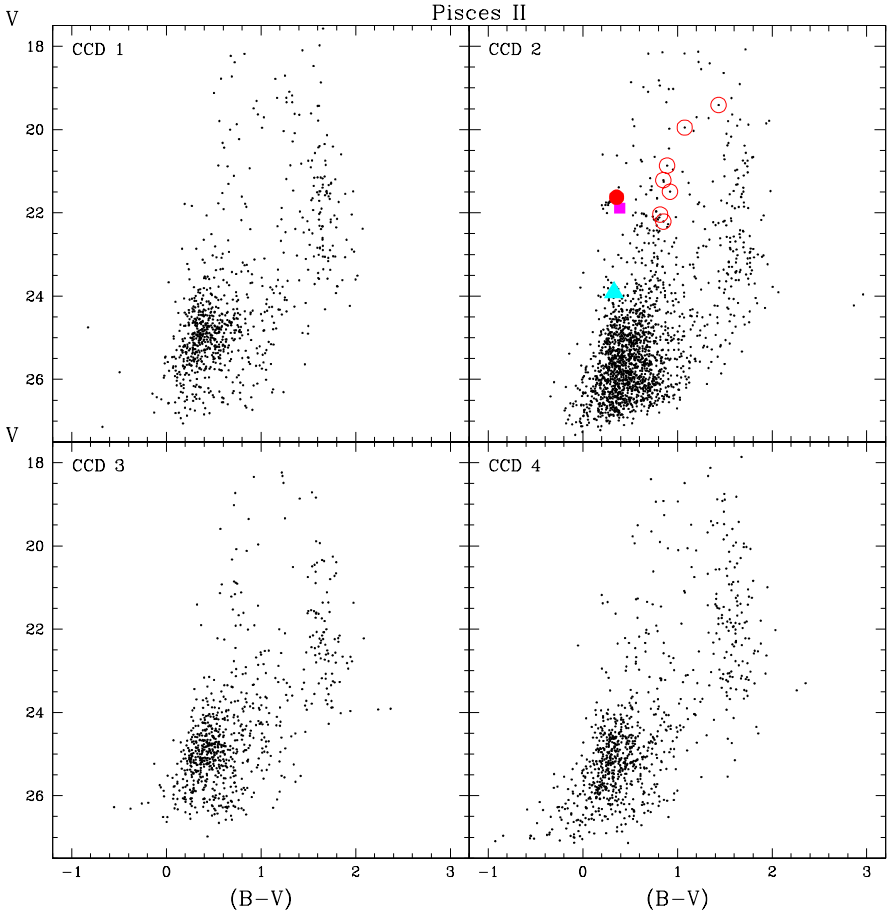

FIGURE 2.9: V, B-V CMDs of Psc II obtained from the data corresponding to the four CCDs of the LBC mosaic, separately. Symbols and colour-coding are the same as in Figure 2.5.

were adjusted to the distance modulus of Psc II (21.22 mag, as inferred by the bona fide RRab star within the half-light radius of Psc II) and a reddening value of E(B-V)= 0.056 mag from Schlegel et al. (1998) maps. The comparison with the stellar isochrones shows that Psc II hosts a dominant ancient stellar population ($\sim$ 13 Gyr) more metal-rich than [Fe/H]$\sim -1.8\pm0.1$ dex, assuming that the bona fide RRab star (magenta square) traces the Psc II HB level and the spectroscopically confirmed members (red empty circles) of Kirby et al. (2015) trace the galaxy RGB.

The comparison with isochrones of different metallicity presented here, the very low metallicity measured for the member stars by Kirby et al. (2015) and the position on the period-amplitude diagram suggest a plausible scenario for V2 of being a very metal-poor ([Fe/H]$\gtrsim -2.4$ dex) RRab star belonging to Psc II. Adopting for V4 the metallicity derived by Kirby et al. (2015) ([Fe/H]=-2.45 ± 0.07 dex) its distance modulus becomes: (m-M)$_0$= 21.12 $\pm$ 0.20 mag) that is consistent within the errors with the distance modulus of V1 (21.22 $\pm$ 0.14 mag). This indicates that Psc II might host a second old (>

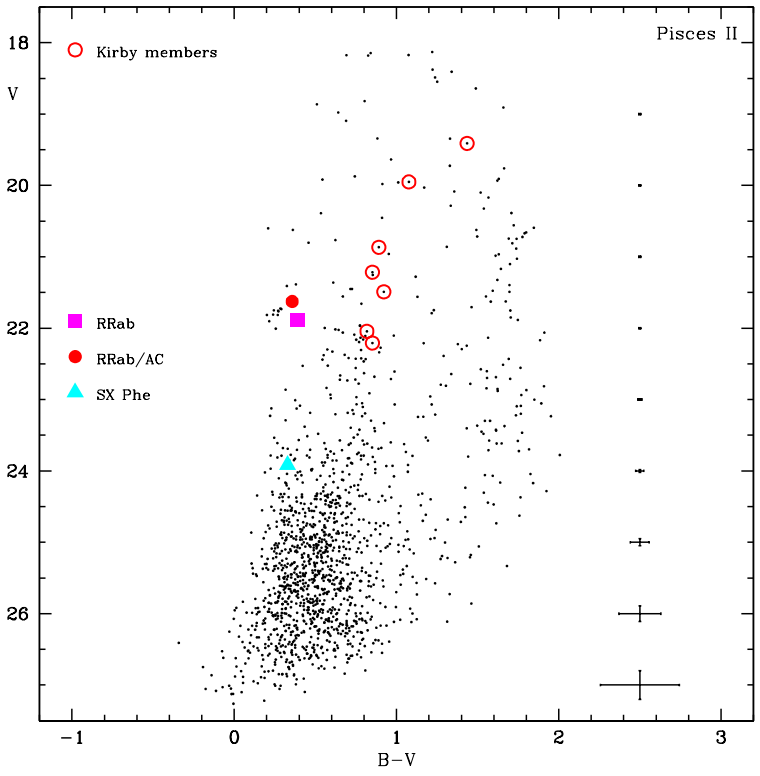

FIGURE 2.10: V, B-V CMD of Psc II showing all the stellar sources located within five times the galaxy half-light radius. Symbols and colour-coding are the same as in Figure 2.5.

10 Gyr) stellar component traced by V4. This further stellar component should be significantly more metal-poor than the dominant one, since the mean V magnitude of V4 is 0.25 mag brighter than the metal-rich HB traced by V1 and its corresponding RGB might be steeper than the metal-rich RGB associated with V1. Unfortunately there are no signs of a steeper, more metal-poor RGB in the CMD.

As both the PARSEC isochrones (CMD 2.9 web interface) and the isochrones by Pietrinferni et al. (2004) (BaSTI web interface) do not reach metallicities lower than [Fe/H]$\sim -2.2/-2.3$ dex, as last check, we compared the CMD to the mean ridge lines of low metallicity GGCs to fit the metal-poor stellar component of Psc II. Figure 2.12 shows

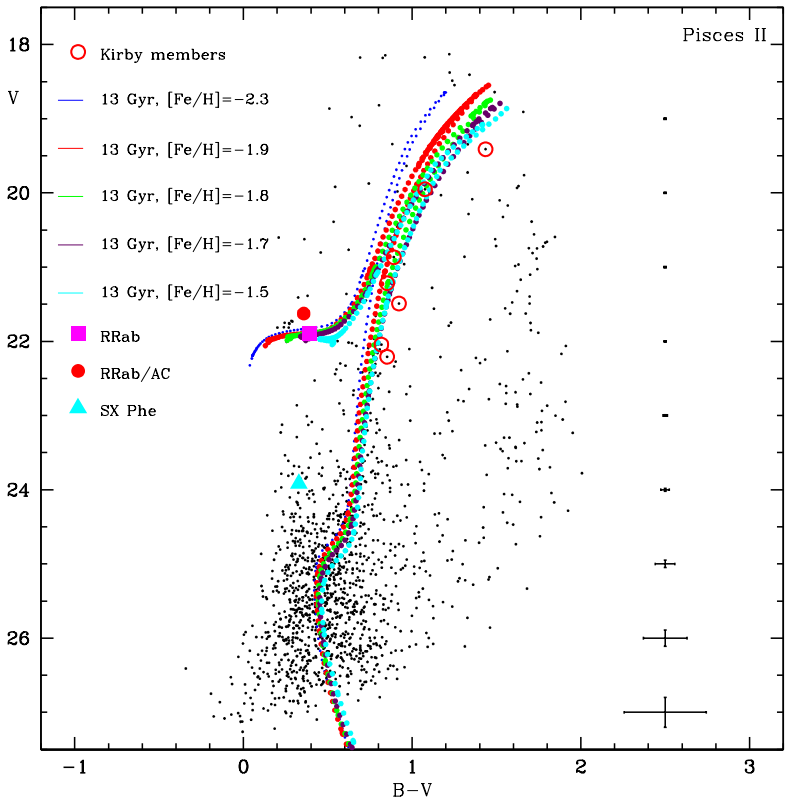

FIGURE 2.11: Same as in Figure 2.10, but with dotted lines showing the PARSEC stellar isochrones (Bressan et al. 2012) for an age of 13 Gyr and metallicities of: [Fe/H] = −2.3 dex, blue; [Fe/H] = −1.9 dex, orange; [Fe/H] = −1.8 dex, green; [Fe/H] = −1.7 dex, purple; and [Fe/H] = −1.5 dex, cyan. They were corrected for a distance modulus of 21.22 mag as derived from the bona fide RRab star (V1) in Psc II and for a foreground reddening of E(B-V) = 0.056 mag, according to the Schlegel et al. (1998) maps.

the GGC mean ridge lines we used to trace the RGB [with V1 and Kirby et al. (2015) members as references] and the HB (with V1 and V4 as references) of the two different populations possibly observed in Psc II. Specifically, we used the fiducial tracks published by Piotto et al. (2002) for the GGCs M15 and NGC 5824, which have metallicities respectively of [Fe/H] = −2.4 and −1.9 dex, to fit the metal-poor component, and the fiducial lines of M13 and M5, with metallicities respectively of [Fe/H] = -1.5 and -1.3 dex, to fit the metal-rich component. The ridge lines were corrected according to the proper reddening and distance modulus of each GGC (Harris 1996[4]): E(B-V) = 0.1 mag and (m-M)$_0$ =15.39 mag for M15, E(B-V)=0.13 mag and (m-M)$_0$ =17.94 mag for NGC 5824, E(B-V) = 0.02 mag and (m-M)$_0$ = 14.33 mag for M13, E(B-V)= 0.03 mag and (m-M)$_0$ = 14.46 mag for M3 and then further shifted to the distance modulus (21.22 ± 0.14 mag) and reddening E(B-V)= 0.056 ± 0.052 mag (Schlegel et al. 1998) of Psc II. The ridge line of NGC5824, corresponding to a metallicity of [Fe/H] = −1.9 dex, well

[4]Revision of December 2010

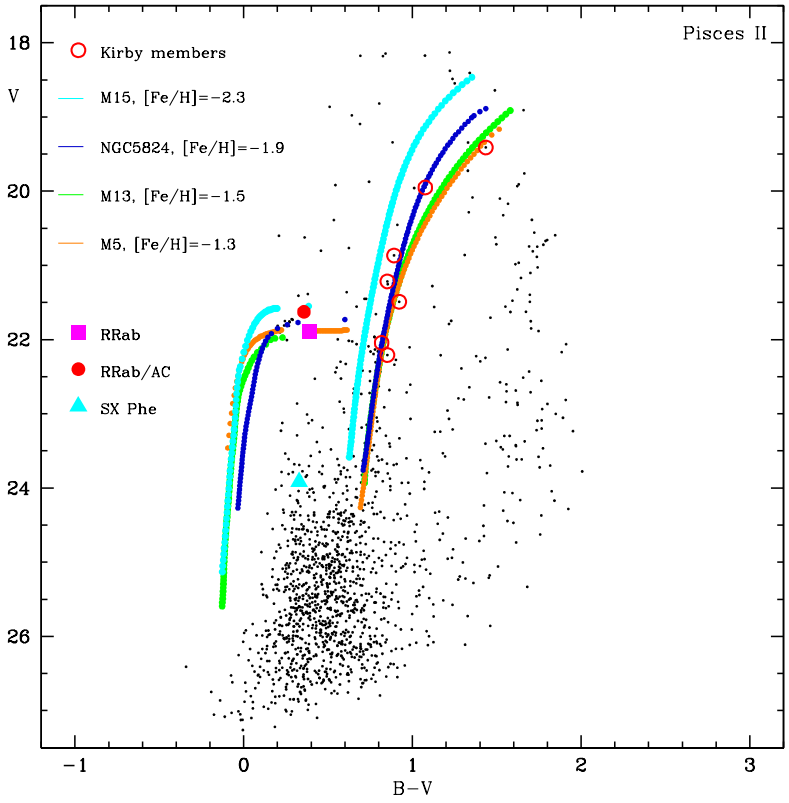

FIGURE 2.12: Same as Figure 2.10 but with solid lines showing the ridge lines of the GGCs: M15 (cyan), NGC 5824 (blue), M13 (green), and M5 (orange).

traces the RGB and the position of V4, while M5 and M13 well reproduce the RGB and the position of V1. We conclude that Psc II might host two old stellar components, a metal-poor component, traced by V4, and a higher metallicity component traced by V1.

2.1.8 Isodensity contour maps

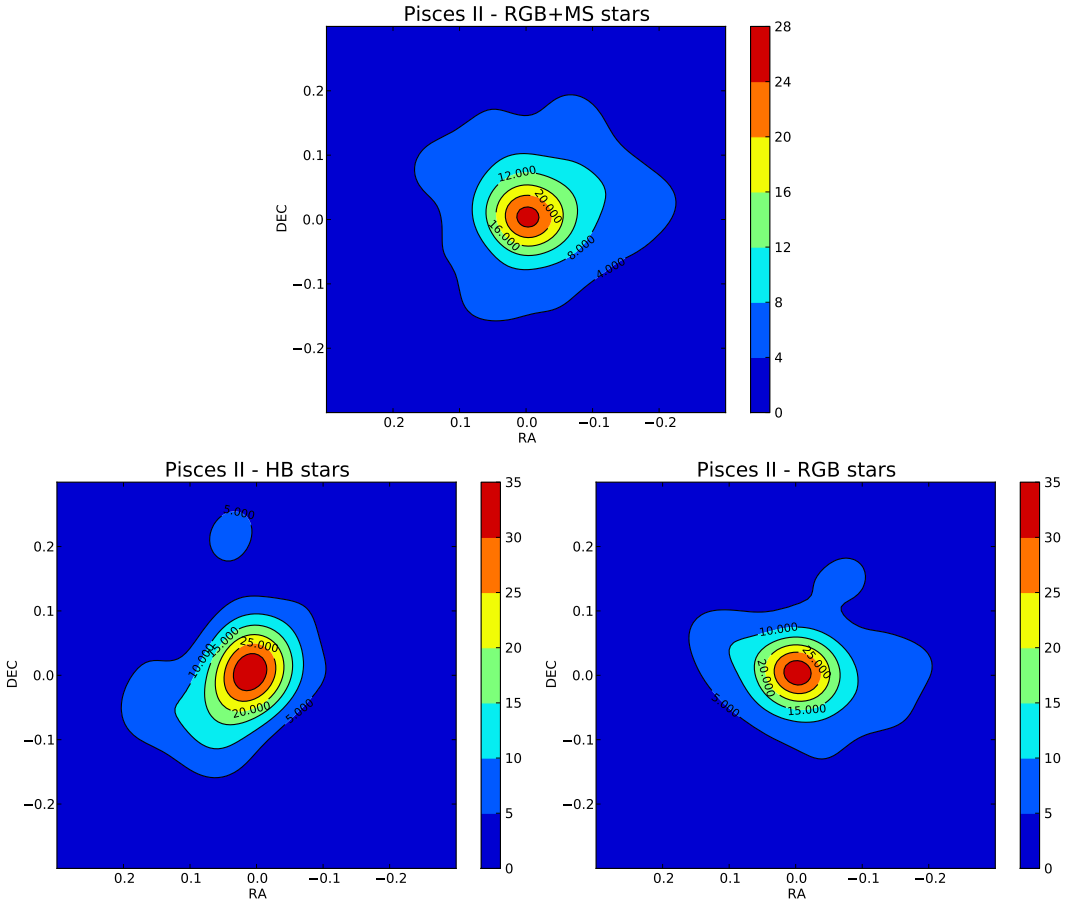

FIGURE 2.13: Isodensity contour maps of Psc II obtained with a bin size of 0.23′. *Upper panel*: isodensity map of Psc II MS and RGB stars, selected by following the theoretical isochrones. *Lower panel*: same as in the upper panel but for the Psc II HB (left) and RGB (right) stars only.

Figure 2.13 shows the isodensity contour map obtained from all stars in our photometric catalogue of Psc II, selected by χ and *Sharpness* using the same limits as for the galaxy CMD. The upper panel of the figure shows the isodensity contour map obtained selecting MS and RGB stars, the lower panels, only the RGB on the right and only HB stars on the left. The selection of RGB, MS and HB stars was made by overlying the theoretical isochrones to the galaxy CMD. The isodensity contours were obtained by setting a bin size of 0.23 arcmin. The isodensity maps confirm the presence of a stellar overdensity

at the center of the map, corresponding to the position of Psc II. The overdensity at the center of the map is clearly seen also in the isodensity maps of the RGB and MS stars, separately. The two isodensity maps do not have an irregular shape as it would be expected if the galaxy was under tidal disruption. For sake of completeness, the position of Peg III in these maps is in the top-left direction. The lack of an irregular shape of the isodensity maps seems to exclude the existence of a link or stream between Psc II and Peg III.

2.1.9 Comparison with Peg III and conclusions

In this section we compare the mean properties of Psc II derived in the previous sections with those of the resolved stellar populations in Peg III, which we also observed with the LBCs at the LBT, in order to further investigate a possible physical connection, between these two galaxies, as suggested in previous studies. For this comparison we have used as main tools (i) the properties of the RRLs identified in these systems, (ii) the features of the observed CMDs and, (iii) the density contour maps.

Results on Peg III are presented in detail in M. Tantalo's Master Thesis and only briefly summarised here. In Peg III we have identified 2 variable stars (lower portion of Table 2.1): an RRab star with P $\sim$ 0.55 days (V1) and one variable (V2, with uncertain type classification). Both variables are located outside the galaxy half-light radius (r_h= 0.85 $\pm$ 0.22 arcmin; Kim et al. 2016), respectively within $4r_h$ and $10r_h$ from Peg III centre. As with Psc II, we classified Peg III as an Oo I system based on the period of the bona-fide RRab star (V1; see Figure 2.3), from which we measured a distance modulus of 21.21 $\pm$ 0.32 mag that puts the galaxy at 174 $\pm$ 26 kpc, in good agreement with the literature value and at the same distance from us as Psc II. The variable star with uncertain classification in Peg III (V2) shares the same issues as V4 in Psc II; it may either be an RRab star with P $\sim$ 0.66 d or an AC with P $\sim$ 0.40 d and is 0.3 mag brighter than the HB level of Peg III. We performed the same tests as done for Psc II and reached very similar conclusions: V2 is very likely an RRab star with Oo II characteristics belonging to Peg III. Hence, Peg III like Psc II seems to contain RRLs with different Oo types. The comparison of the Peg III CMD with stellar isochrones also suggests, in analogy with Psc II, the presence of a dominant old stellar population ($>$ 10 Gyr) with metallicity larger than [Fe/H] ~ -1.8 dex. However, the Peg III RGB

exhibits a non negligible spread in colour that likely is indicative of a metallicity spread. This evidence, along with the likely Oo II nature of V2, could be a hint of the presence in Peg III of an old more metal-poor ([Fe/H] ~ -2.4 dex) stellar component, as suggested also by the comparison with the mean ridge lines of GGCs (see Figure 2.14).

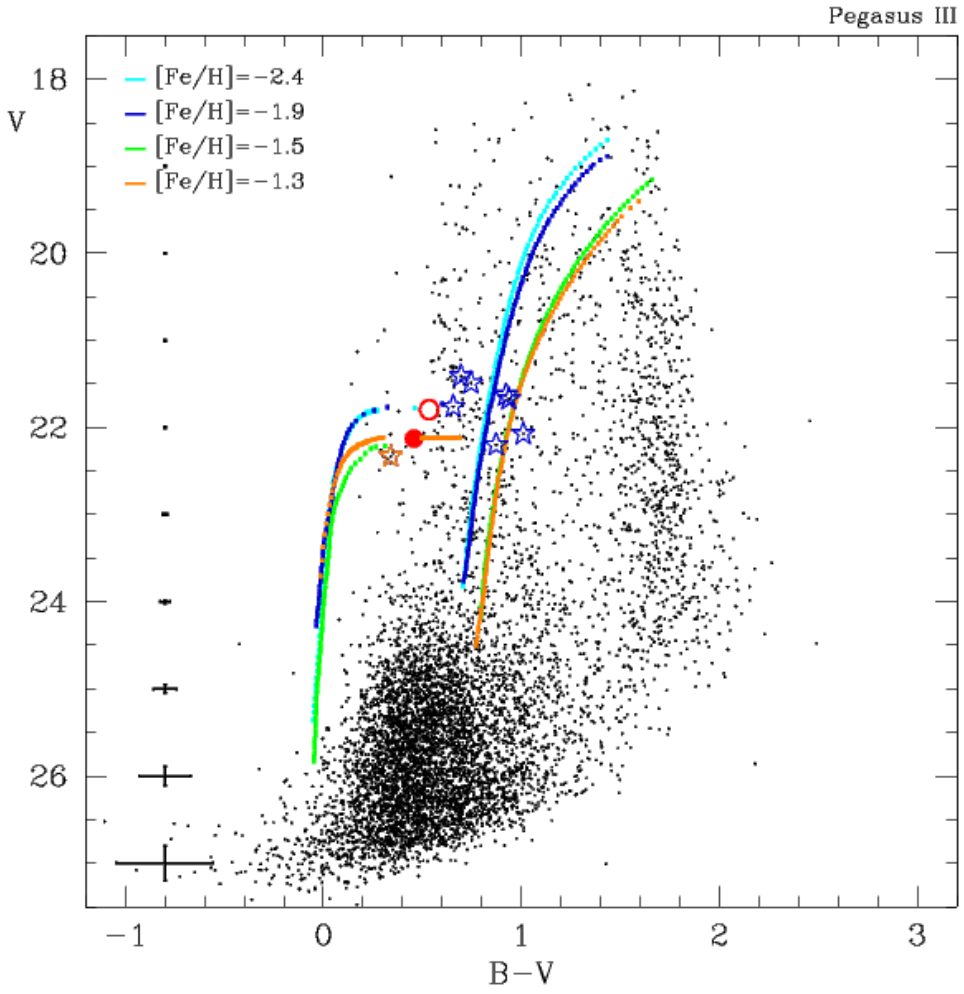

FIGURE 2.14: V , B-V CMD of Peg III showing all stellar sources with $-0.4 \leq$ *Sharpness* ≤ 0.4 and $\chi \leq 2.2$ located within ten times the galaxy r_h (Kim et al. 2016). Blue and orange star symbols represent spectroscopically confirmed and an ambiguous member of Peg III, respectively, according to Kim et al. (2016); red filled and open circles identify, respectively, the bona-fide RRab star (V1) and the variable with uncertain classification (V2) in Peg III. The solid lines are the ridge lines of the GGCs: M15 (cyan), NGC 5824 (blue), M13 (green), and M5 (orange). Figure from M. Tantalo's Master Thesis.

To conclude, Psc II and Peg III share very similar properties and issues:

- The comparison of the CMDs with stellar isochrones suggests the presence in both galaxies of an old stellar population (12-13 Gyr) with a metallicity [Fe/H]> -1.8

dex, higher than the spectroscopic estimates for these two systems and also higher than typically observed in other UFDs;

- Both UFDs are classified as Oo I systems according to the period of their inner bona-fide RRab stars. Even though this is not a statistically firm classification, it differs from the Oo classification of other MW UFD satellites, which mainly tend to be Oo II systems, with only a few of them Oo-Int, but none so far classified as Oo I.

- The occurrence in both galaxies of a likely Oo II RRab star brighter than the HB level seems to indicate that, besides the dominant more metal rich component, an old and more metal-poor component may be present in Psc II and Peg III which would thus share a similarly complex star formation and evolution.

However, in spite of all those similarities and the proximity on the sky, the density contour maps do not reveal signatures of a tidal interaction between Psc II and Peg III. If they were indeed born in a pair, or physically connected in the past, no trace of this physical connection seems to have survived.

Although the analysis we have presented does not allow us to reach firm conclusions, it revealed very intriguing characteristics and similarities of Psc II and Peg III that prompt us to further study these systems. Unfortunately, the HB of these galaxies is at/below the limiting magnitude reached by *Gaia* ($V \sim$ 20.5-21 mag; see Chapters 3 and 4 for details on *Gaia* performances); however, the brighter RGB stars in Psc II and Peg III are well within the reach of *Gaia*, which can in future data releases[5], for instance, tell us whether they share the same relative proper motions. Furthermore, in the near future the Large Synoptic Survey Telescope (LSST), designed to collect deep (5 mag deeper than *Gaia*) ground- based, wide-field imaging from the blue to the near-infrared wavelengths, will be able to provide observations of Psc II and Peg III and the field between them deep enough to shed light on their nature and origin.

[5]Psc II and Peg III are in a region of the sky that is still poorly sampled by the *Gaia* observations released in DR2.

2.2 Andromeda XXV

2.2.1 Background

Andromeda XXV (And XXV) is one of over 20 new dSphs identified in the data of the PAndAS survey of M31 (Martin et al., 2013, and reference therein). It was discovered by Richardson et al. (2011), who measured the galaxy's structural and photometric parameters. In particular they estimated the galaxy distance modulus: $(m\text{-}M)_0 = 24.55 \pm 0.12$ mag from the luminosity of the HB and the half-light radius: $r_h = 3.0'$, corresponding to 732 $\pm$60 pc at the distance of And XXV. The $(m\text{-}M)_0$ value is 1 σ longer than found by Conn et al. (2012) from the luminosity of the galaxy red giant branch tip (TRGB) constrained adopting a Bayesian approach [$(m\text{-}M)_0 = 24.33^{+0.07}_{-0.21}$ mag)]. From the Calcium triplet (CaII) of RGB stars Collins et al. (2013) estimated for And XXV a metallicity [Fe/H]$=-1.9 \pm 0.1$ dex and, from 25 spectroscopically confirmed members and a velocity dispersion of $\sigma = 3.0^{+1.2}_{-1.1}$ kms^{-1}, a rather low value, when compared with the large extension of And XXV. These authors also estimated a mass-to-light ratio, inside one r_h, of $[M/L]_{r_h} = 10.3\ M_{\odot}/L_{\odot}$ that they conclude is consistent with a stellar population without a dark matter component. In a more recent paper using as an argument the circular velocity within the galaxy's r_h Collins et al. (2014) concluded that the mass of And XXV should have been much more prominent in the past than today for the galaxy to be able to form stars. The large distance of the dSphs in the M31 complex prevents the direct observation of their main sequence turn-off (MSTO) with present day ground-based telescopes. The RRLs (and other pulsating variable stars) being about 3 (or more) magnitudes brighter than the MSTO can be much more easily reached from the ground, hence are excellent alternative tools for tracing and characterizing the different stellar generations in these systems (the oldest component in particular). In addition, the ground-based telescopes allow to cover areas significantly larger than the half-light radius of the M31 dSphs, which often is rather extended, thus providing much more complete and statistically significant samples.

We have obtained B, V time-series observations of And XXV, as well as for other 3 M31 dSph satellites, using the LBCs at the LBT (PI: G.Clementini). In the following sections we present results on the study of the variable stars in And XXV based on the LBT data. This study was carried out during the first year of my PhD and its results have been

published in the paper: "Variable stars and stellar populations in Andromeda XXV: III. A central cluster or the galaxy nucleus?" by F. Cusano, A. Garofalo, G. Clementini et al. 2016, ApJ, 829, 26.

2.2.2 Observations, data reduction and identification of the variable stars

The log of the observations of And XXV is provided in Table 2.2. A total of 85 B and 87 V images of 400 s exposure each were obtained with the LBC of a region of $23' \times 23'$ around the centre of And XXV (R.A.=$00^h30^m08.9^s$, decl. =$+46°51'07''$, J2000.0; Richardson et al. 2011) in the week from October 18 to 24, 2011. All images were obtained with seeing $\leq 1\ ''$.

TABLE 2.2: Log of And XXV observations

Dates	Filter	N	Exposure time (s)	Seeing (FWHM) (arcsec)
October 18, 2011	B	1	400	1
October 20-24, 2011	B	84	400	0.8-1
October 18, 2011	V	3	400	1
October 20-24, 2011	V	84	400	0.8-1

Bias, flat fielding and distortion corrections of the raw images were performed with a dedicated pipeline developed at INAF-OAR[6]. The photometric reductions of the And XXV images were carried out following a consolidated procedure described in detail in our papers on And XIX (Cusano et al. 2013) and And XXI (Cusano et al. 2015). As in those previous studies (as well as for the study of Psc II) Point Spread Function (PSF) photometry was performed using the `DAOPHOT-ALLSTAR-ALLFRAME` packages (Stetson 1987, 1994). The Landolt standard fields L92 and SA113 (Landolt 1992), observed during the run, were used to derive calibration equations[7] with an r.m.s.=0.03 mag (this is fully adequate for our purpose of identifying And XXV variable stars) and transform the instrumental magnitudes to the Johnson standard system. We searched for candidate variables using the variability index (VI) computed in `DAOMASTER`, selecting as candidate variables, stars with VI> 1.4. Then their B and V light curves were analysed

[6] http ://lbc.oa- roma.inaf.it/commissioning/index.html

[7] $B - b = 27.696 - 0.113 \times (b - v)$ r.m.s.=0.03, $V - v = 27.542 - 0.060 \times (b - v)$ r.m.s.=0.03

with GRATIS (Clementini et al. 2000); more details on this procedure can be found in Section 2.1.3. We identified, in the B, V photometric catalogues of And XXV, a total of 62 variable stars: 58 RRLs (see Section 2.2.3), 3 anomalous Cepheids (AC), 1 eclipsing binary (ECL) and 1 unclassified variable (see Section 2.2.5). The properties of the confirmed variable stars in And XXV are summarized in Table A.1 (Appendix A). Adopting the coordinates by Richardson et al. (2011), we ordered the variables with an increasing number based on their proximity to the galaxy centre. Examples of light curves for RRLs and other types of variables in And XXV are shown in Figure 2.15.

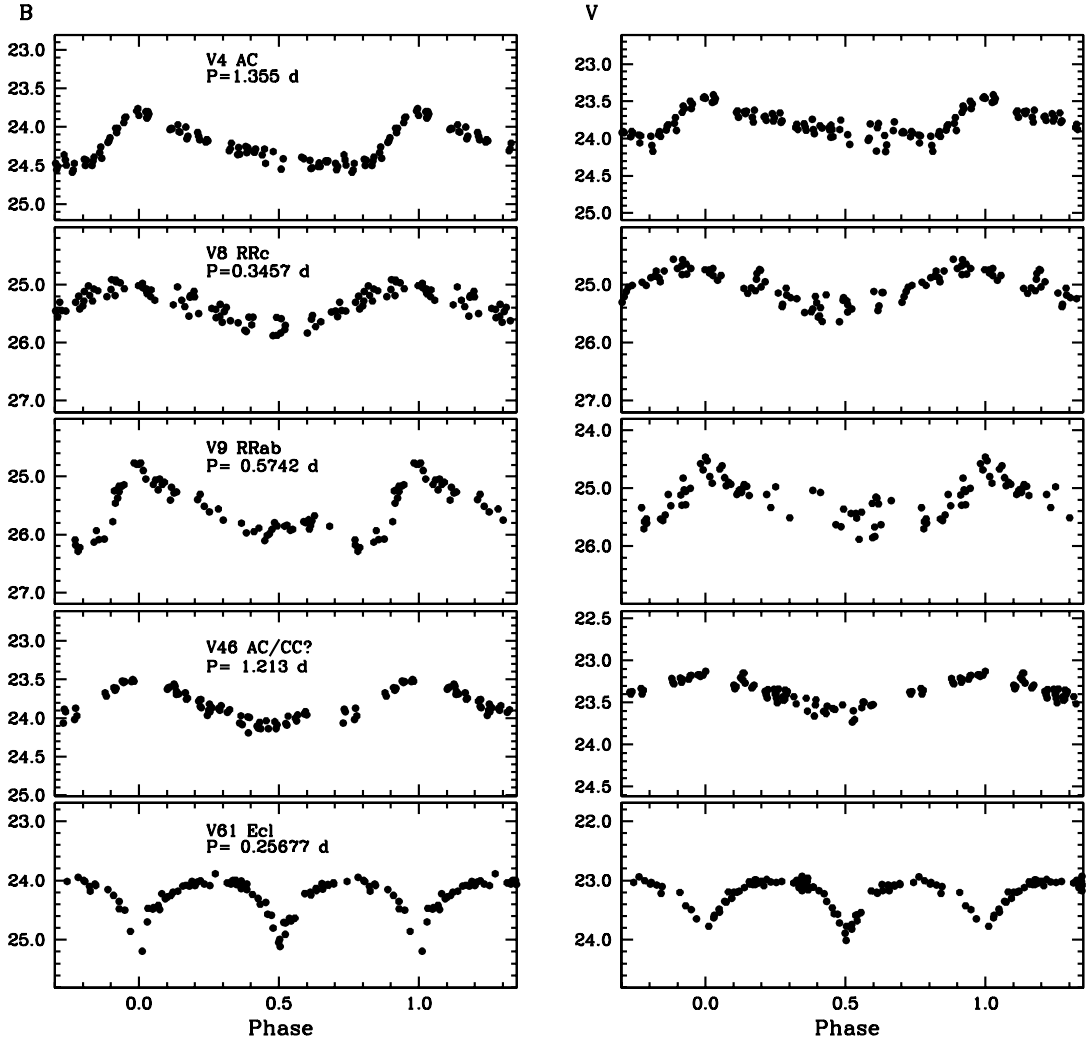

FIGURE 2.15: B-band (left panels) and V-band (right panels) light curves for a sample of variable stars [2 RRLs, 1 AC, 1 AC/CC (see Section 2.2.5) and 1 ECL] identified in And XXV. Typical internal errors of the single-epoch data range from 0.01 at $B \sim$ 21.30 mag to 0.30 mag at $B \sim$ 26.20 mag, and similarly, from 0.01 mag at $V \sim$ 19.90 mag to 0.30 mag at $V \sim$ 26.00 mag. Figure from Cusano et al. (2016).

2.2.3 RR Lyrae stars in And XXV

Among the 58 RRLs identified in the field of And XXV, 46 are RRab and 11 are RRc stars. Only one RRL, V63 (RRab), is $\sim$ 12 arcmin away from the centre of the galaxy and most likely belongs to the M31 halo, hence, we did not include this star when we derived the properties of And XXV (distance, Oosterhoff type, etc.). For all other RRLs we assume that they likely belong to And XXV.

The average period for the sample of 45 RRab stars (V63 excluded) is $\langle P_{ab} \rangle$=0.61 d (σ=0.05 d) and becomes $\langle P_{ab} \rangle$=0.60 d (σ=0.05 d) if we only consider the 15 RRab stars within an area set by the r_h of And XXV and its ellipticity, or, the 32 RRab stars within twice the galaxy's r_h. The upper panel of Figure 2.16 shows the period distribution of the And XXV RRLs that confirms the consistency in average period of the different sub-samples described above. In all cases, And XXV is classified as an Oo-Int system. An additional confirmation of the classification of And XXV as Oo Int is provided by the fraction of RRc stars over the whole number of RRLs: $f_c = N_c/N_{ab+c} = 0.19 \pm 0.07$, which is intermediate between the values expected for Oo II ($f_c \sim 0.44$) and Oo I ($f_c \sim 0.17$) systems (Catelan 2009).

The lower-left panel of Figure 2.16, shows the period-amplitude diagram of the RRLs in And XXV together with the loci defined by RRLs in the Oo I GGC M3 (lower line) and the Oo II GGC ωCen (upper line), according to Clement & Rowe (2000). The RRLs have been divided in three groups, highlighted by different colours, according to their position within the area set by the galaxy ellipticity and: once, twice the r_h or the whole LBC FoV. Almost all And XXV RRLs fall on the Oo I locus or between the two lines but remaining closer to the Oo I line. Only three RRLs are near the Oo II locus. In the lower-right panel of Figure 2.16 the period-amplitude diagram of And XXV's RRLs is compared with RRLs in And XIX, And XXI and in three halo fields at 4, 6 (Sarajedini et al. 2009) and 35 kpc (Brown et al. 2004) from the centre of M31, respectively. The RRLs in the M31 halo conform more to the Oo I type, while the dSph satellites are more Oo Int with a mild trend towards the Oo I type, which decreases with increasing the distance from the M31 centre.

Since RRLs trace the oldest stellar population in a galaxy, their projected positions on the sky may help to outline the geometry of the host system. The spatial distribution of the RRLs and other types of variables identified in And XXV is shown in Figure 2.17.

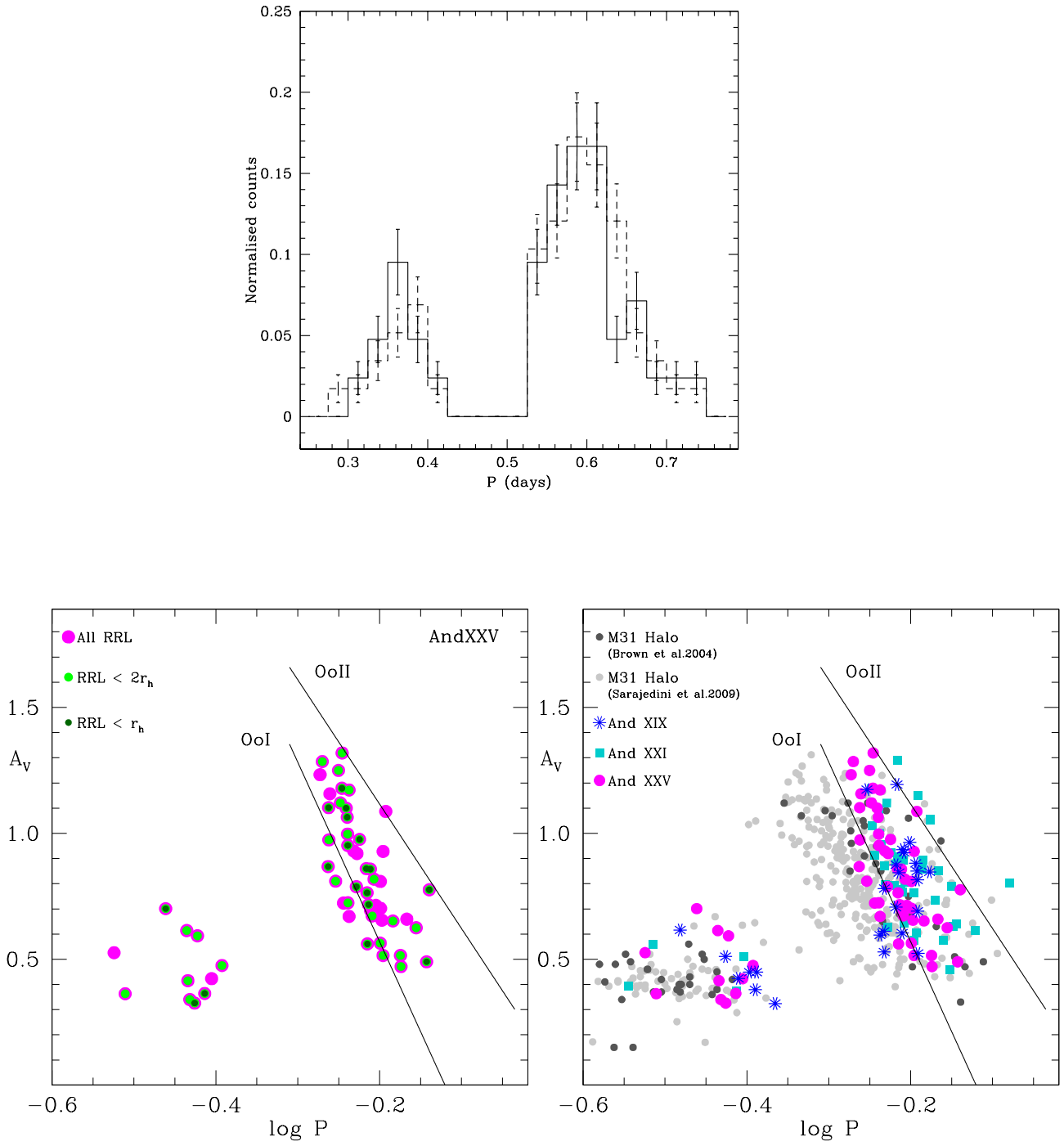

FIGURE 2.16: *Upper panel*: period distribution of the 57 RRLs identified in And XXV (dashed line) and for the 32 RRLs within twice the galaxy r_h (solid line). The bin size is 0.025 days. *Lower panels*: *Left*: Period-amplitude diagram of the RRLs identified in And XXV (magenta filled circles). The solid lines are the ridge lines of the Oo I and Oo II RRLs (Clement & Rowe 2000). Dark and light green circles are RRLs within once and twice the galaxy r_h, respectively. *Right*: Same as in the left panel but showing also RRLs in And XIX (blue asterisks), And XXI (cyan squares) and in three HST fields in the M31 halo from Sarajedini et al. (2009) (grey symbols) and Brown et al. (2004) (dark-grey symbols), respectively. Figures from Cusano et al. (2016).

Adopting the structural parameters derived by Richardson et al. (2011), many RRLs (filled red circles) appear to be placed beyond the galaxy r_h, traced by the inner black ellipse, and create a protrusion of stars that extends beyond $2r_h$. In particular, 37 out of 57 RRLs (hence, more than half of the whole sample) are located southward with respect to the galaxy centre and suggest an elongated distribution of the And XXV stars. Most of them are aligned along the direction toward M31 indicated by an arrow in Figure 2.17.

2.2.4 Distance to And XXV

The mean V magnitude of the whole sample of And XXV's RRLs, 57 stars, is $\langle V(RR)\rangle = 25.26 \pm 0.10$ mag. If we discard V31, that is about 0.4 mag brighter than the RRLs

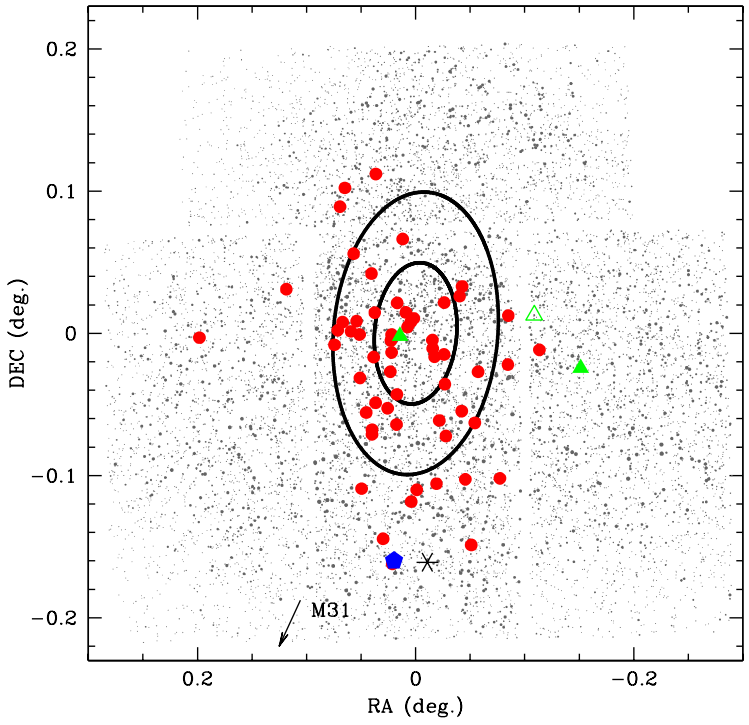

FIGURE 2.17: Spatial distribution of the variable stars discovered in the whole LBT FoV centred on And XXV. The black ellipses represent the area respectively within once and twice the r_h of And XXV as defined by Richardson et al. (2011). Red filled circles mark the RRLs, green filled triangles the ACs, an open green triangle is the uncertain AC/CC, the blue pentagon is the unclassified variable and the black asterisk is the ECL (see text for details). The arrow points to the direction of M31. Figure from Cusano et al. (2016)

average magnitude and could either be blended with a close companion or (less likely) an evolved RRL, we obtain $\langle V(RR)\rangle = 25.27 \pm 0.09$ mag. These values are almost identical. If we instead consider the sample of RRLs within an area delimited by And XXV's r_h, 18 stars, the average V magnitude is $\langle V(RR)\rangle = 25.33 \pm 0.09$ mag, and within twice the r_h it is 25.27±0.09 mag. To de-redden the V magnitudes we derived individual reddening values for the RRLs using the Piersimoni et al. (2002) method (see Section 1.1.2). The mean reddening of the sample of RRLs within the r_h is $E(B-V) = 0.08 \pm 0.04$ mag and for the whole sample of RRLs is $E(B-V) = 0.05 \pm 0.04$ mag. These values are slightly smaller than derived by Schlegel et al. (1998, $E(B-V) = 0.10 \pm 0.06$ mag), but still consistent within the errors.

The distance to And XXV was estimated using the mean V magnitude and reddening obtained from the 18 RRLs within the r_h. We adopted, for the absolute visual magnitude of RRLs with metallicity [Fe/H] = −1.5 dex the value $M_V = 0.54 \pm 0.09$ mag (Clementini et al., 2003), $\frac{\Delta M_V}{\Delta [Fe/H]} = -0.214 \pm 0.047$ mag/dex (Clementini et al., 2003; Gratton et al., 2004) for the slope of the RRL luminosity-metallicity relation and [Fe/H]=−1.9 ± 0.1 dex for the metallicity of And XXV, as derived spectroscopically by Collins et al. (2013). The distance modulus of And XXV derived from the RRLs is then $(m\text{-}M)_0$=24.63±0.17. This estimate is in very good agreement with the result of Richardson et al. (2011) from the HB level, $(m\text{-}M)_0$=24.55 ± 0.12 mag, but it is more than 1σ longer than obtained by Conn et al. (2012), $(m\text{-}M)_0 = 24.33^{+0.07}_{-0.21}$ mag, based on the TRGB. We suspect that the distance derived in Conn et al. (2012) might be hampered by the uncertain location of the TRGB which is rather scarcely populated in And XXV (see Figure 2.20).

2.2.5 Anomalous Cepheids and other variables in And XXV

Figure 2.20 shows that three variable stars in And XXV, namely, V4, V46 and V58, have luminosity exceeding the mean magnitude of the RRLs by about 1 mag and the mean colour in the range of the instability strip (see Marconi et al., 2004). Following the same procedure adopted for the classification of variable stars in Psc II (see Section 2.1.6), we combined results from the analysis of the light curves, with the comparison with PW relations for ACs and CCs, and with stellar isochrones in the CMD to classify these three stars. Specifically, to obtain the Wesenheit index of these 3 variables we subtracted the colour term multiplied by 3.1 (adopting the Cardelli et al., 1989, law

for extinction) to the absolute magnitudes derived by their intensity-averaged apparent visual magnitudes, $\langle V \rangle$, adopting the distance modulus of $(m\text{-}M)_0 = 24.63 \pm 0.17$ mag as derived from the RRLs (see Section 2.2.4). The left panel of Figure 2.18 shows the comparison of V4, V46 and V58 with the PW relations for ACs in the LMC (solid lines) derived by Ripepi et al. (2014) (converted from V, I to B and V as described in Section 2.1.6), while the right panel shows the comparison with the PW relations of the LMC CCs by Jacyszyn-Dobrzeniecka et al. (2016).

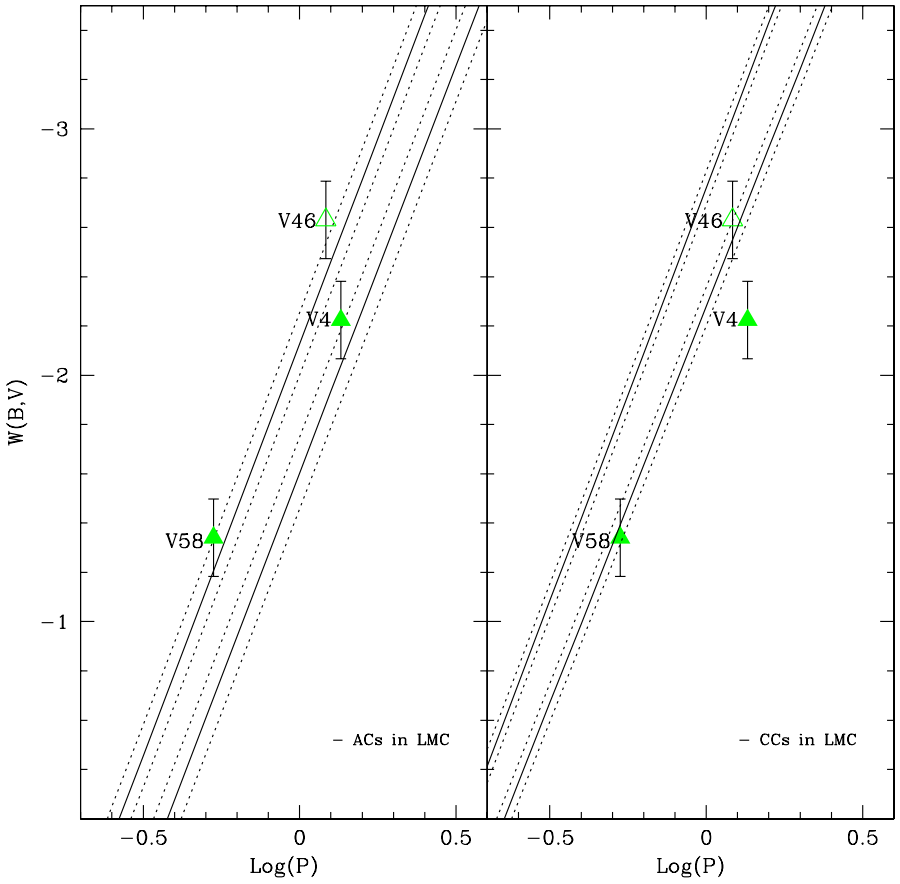

FIGURE 2.18: Position of V4, V46 and V58 with respect to the PW relations for ACs (left panel; Ripepi et al. 2014) and CCs in the LMC (right panel; Jacyszyn-Dobrzeniecka et al. 2016). The 95% confidence contours are shown as dotted lines. Figure from Cusano et al. (2016).

V4, V46 and V58 are placed within 1σ from the Ripepi et al. (2014) relations for fundamental mode and first-overtone pulsators. V46 and V58 are also within 1 σ from the fundamental mode CC PW relation while V4 does not fit the CC PW relations.

However, the light curve of V58 has the typical shape of an AC. In summary, from the analysis of the light curves, the comparison with the *PW* relations for ACs and CCs, and based on the comparison of the And XXV CMD with stellar isochrones (see Sect. 2.2.6) we classify V4 and V58 as ACs, while for V46 which could as well be a short period CC we keep an uncertain classification of AC/CC.

We note that V46 and V58 are located more than $2r_h$ from the centre of And XXV (see Figure 2.17), hence, they could either belong to a background/foreground feature in the M31 field or could have formed recently, due to a peripheral episode of star formation in And XXV triggered by tidal interaction.

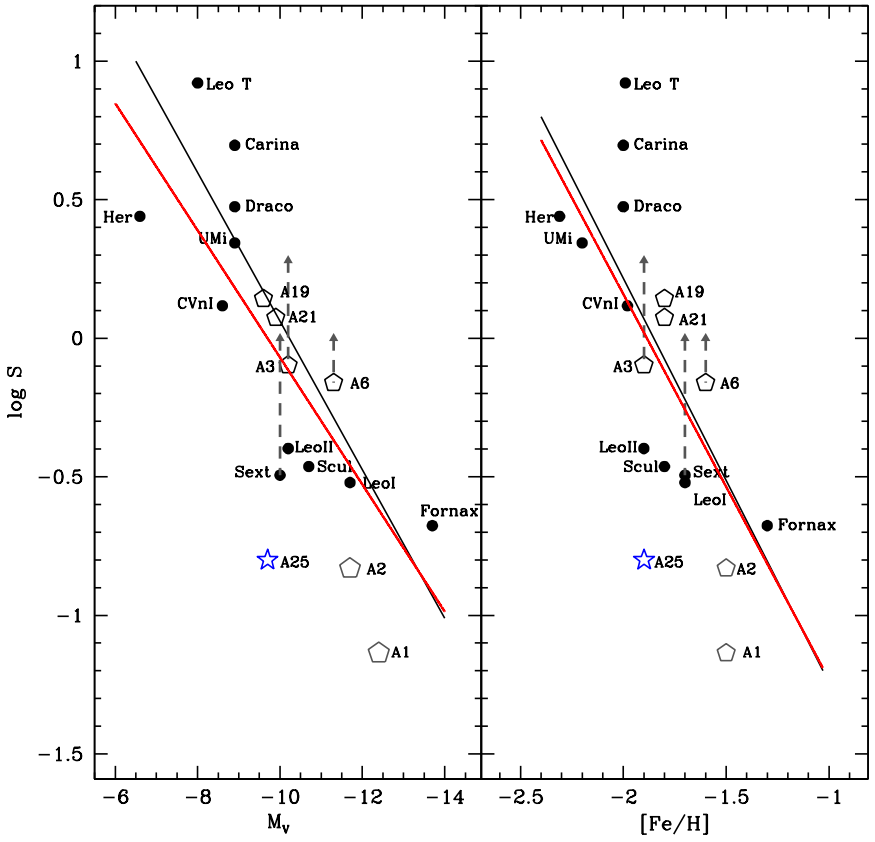

FIGURE 2.19: *Left panel*: Specific frequency of ACs in dwarf satellites of the MW (filled circles) and M31 (open pentagons) versus absolute visual magnitude. And XXV is marked by a blue star. Black lines are the least-squares fits of ACs by Pritzl et al. (2005) while the red solid lines mark the least-squares fits we have obtained using only the ACs confirmed by the comparison with the *PW* relations for ACs (see text for details). *Right panel*: Same as in the left panel, but versus metallicity of the host galaxy. Figure from Cusano et al. (2016).

Mateo et al. (1995) found that there is a trend of the specific frequency (S[8]) of ACs in the dSphs around the MW with the metallicity and luminosity of the host dSph. This correlation arises from the facts that ACs are observed only in systems more metal-poor than [Fe/H] ~ -1.4 dex and that dSphs with increasing mass, per unit of luminosity, seem to host more ACs.Pritzl et al. (2004, 2005) confirmed that the same correlation exists also among the M31 dSphs: And I, And II, And III and And VI. Given the uncertain membership of V46 and V58, we have computed the S of ACs in And XXV under the assumption that V4 is the only AC belonging to the galaxy. This is shown in Figure 2.19 together with the AC specific frequency in a number of MW and M31 dSph satellites. And XXV does not follow the relation traced by the other dSphs. To make a more consistent comparison of the AC frequency we have estimated for And XXV (this work), And XIX (Cusano et al. 2013) and And XXI (Cusano et al. 2015), and those obtained in other studies (Pritzl et al., 2005, and reference therein), we have revised the latter by considering as bona fide ACs only those falling within 1 σ of the AC *PW* relations. Following this procedure we confirmed the AC number in the following satellites: Leo I, Leo II, Draco, Ursa Minor, Carina, Sculptor, Fornax and reduced the number of ACs in And I and And II from 1 to 0, from 5 to 2 in And III, from 6 to 4 in And VI and from 4 to 2 in Sextans. The red solid lines plotted in Figure 2.19 are the least-squares fits obtained adopting the revised specific frequencies computed as discussed above. They are described by the following equations:

$$\log S = 0.23(\pm 0.57) \times M_V + 2.22(\pm 0.57) \tag{2.1}$$

$$\log S = -1.39(\pm 0.44) \times [Fe/H] - 2.62(\pm 0.83) \tag{2.2}$$

Black lines mark instead the least-squares fits originally obtained in Pritzl et al. (2005). Grey dashed arrows indicate the position the revised galaxies would occupy in these plots if we used their literature AC specific frequencies. In the right panel new and previous fits are in perfect agreement, while in the left panel the slope of the new fit is less steep showing that a smaller number of ACs is expected for fainter galaxies.

[8] $S=\frac{N_{ACs}}{L_5}$ where N_{ACs} is the number of ACs and L_5 is the luminosity of the parent dSph in units of 10^5 $L_\odot$.

Finally, in the field of And XXV we discovered two variable stars, V60 and V61, that in the CMD (Figure 2.20) are outside the classical instability strip. The shape of the light curves allowed us to classify V61 as an ECL (see lower panel of Fig. 2.15), while for V60 we cannot give a firm classification. Both the projected spatial distribution (Figure 2.17) and the position in the CMD (see Figure 2.20) suggest that they belong more likely to the M31 field or to the MW. In particular V60, with a $B-V \sim 1.5$ mag and a $V \sim 20$ mag is unquestionably a field star.

2.2.6 Colour magnitude diagram and structure of And XXV

Figure 2.20 shows the CMDs of And XXV obtained by plotting only stars within the galaxy's half-light radius convolved with the ellipticity (Richardson et al., 2011) in the left panel; stars within the region between once and twice the r_h in the central panel; and sources in the whole LBC FoV in the right panel. We minimized the contamination by background galaxies and peculiar sources by selecting only stellar objects with `DAOPHOT` quality image parameters $-0.35 \leq Sharpness \leq 0.35$ and $\chi < 1.5$. Red filled circles are the RRLs, green filled triangles are the ACs (an open green triangle is the uncertain AC/CC), a blue pentagon is the unclassified variable, while the ECL is marked by a black asterisk.

Main features of the CMD are the RGB and the HB traced by the RRLs. The majority of stars in the redder part of the CMD ($B-V \gtrsim 1.5-1.7$ mag) are foreground field objects. V60, the unclassified variable is located in this region of the CMD and is most likely a variable star belonging to the MW field. The narrow RGB and the poorly populated red HB suggest that And XXV hosts a dominant single old stellar population. In Figure 2.21 we heave compared the features of the CMD and the position of the variable stars with PARSEC stellar isochrones based on models from Bressan et al. (2012) with different age and metallicity. Isochrones for ages from 9 to 13 Gyr and metallicity Z=0.0003-0.0004 ([Fe/H]≈ -1.8,-1.7 dex) fit well the RGB and the position of the RRLs. The red HB is also well fitted by isochrones in these age and metallicity ranges.

The paucity of ACs in And XXV indicates that there is a lack of young/intermediate age stars in this galaxy, when compared, for instance, to And XIX and And XXI. The only AC discovered within twice the r_h of And XXV can either be the result of coalescence in a binary system as old as the RRLs, in which mass transfer acted in the last Gyr,

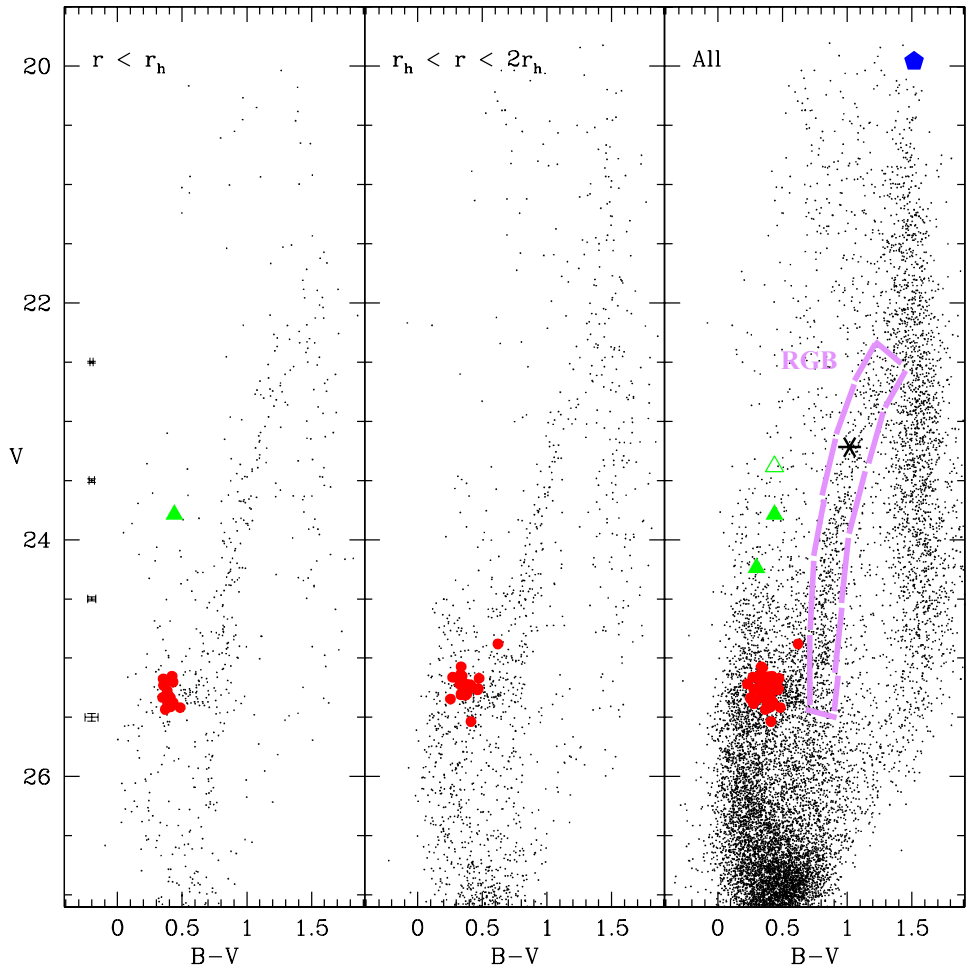

FIGURE 2.20: *Left*: CMD of sources in our photometric catalogue with $-0.35 \leq$ *Sharpness*≤ 0.35, $\chi < 1.5$ and located within the area delimited by the galaxy half-light radius and the ellipticity by Richardson et al. (2011). Red circles mark the RRLs while green triangles are the ACs. *Center*: Same as in the left panel, but for sources within the area between one and 2 r_h of the galaxy. *Right*: As in the left panel, but considering sources in the whole LBC FoV. A black asterisk is the ECL, a blue pentagon is the unclassified variable, and an open green triangle is the AC/CC. Figure from Cusano et al. (2016).

or an intermediate age (1-2 Gyr old) star with metallicity in the range Z=0.0002-0.0006 ([Fe/H]≈ from −2.0,−1.5 dex; see Cusano et al. 2013, 2015). We selected stars in the colour and magnitude ranges of ACs ($0.2 \leq B - V \leq 0.6, 23.0 \leq V \leq 24.5$) of the CMD and checked whether they are spatially segregated, but did not find any clear distribution/concentration of stars associated with this selection. The star formation in And XXV most probably was quenched by some external event such as, for instance, tidal stripping by large nearby galaxies like the NGC147/NGC185 pair (see below) or

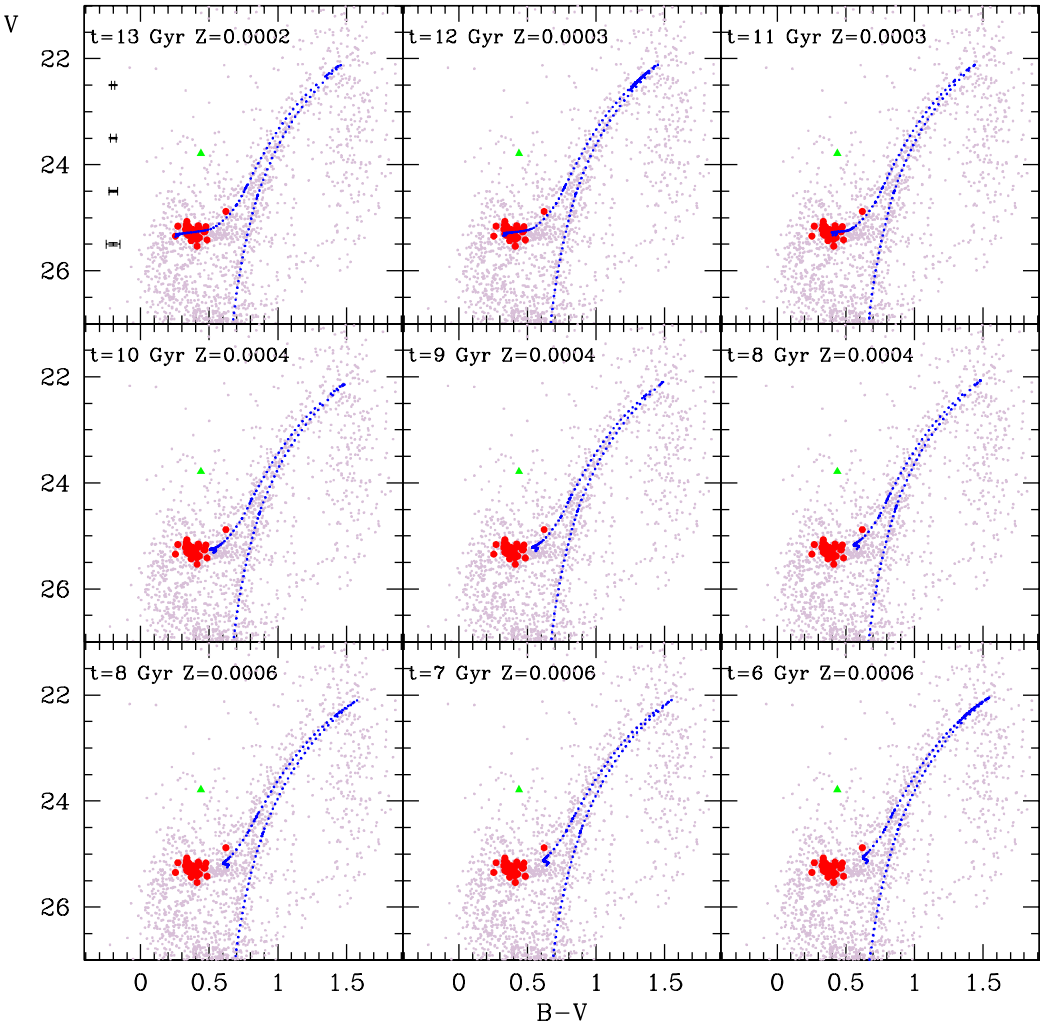

FIGURE 2.21: CMD of sources contained within twice the r_h of And XXV, overlaid by PARSEC stellar isochrones (Bressan et al. 2012) with different age (from t=13 Gyr to 6 Gyr) and metallicity (Z=0.0003, Z=0.0004 and Z=0.0006; from top to bottom). Red filled circles are the RRLs, a green filled triangle is the AC (V4). Figure from Cusano et al. (2016).

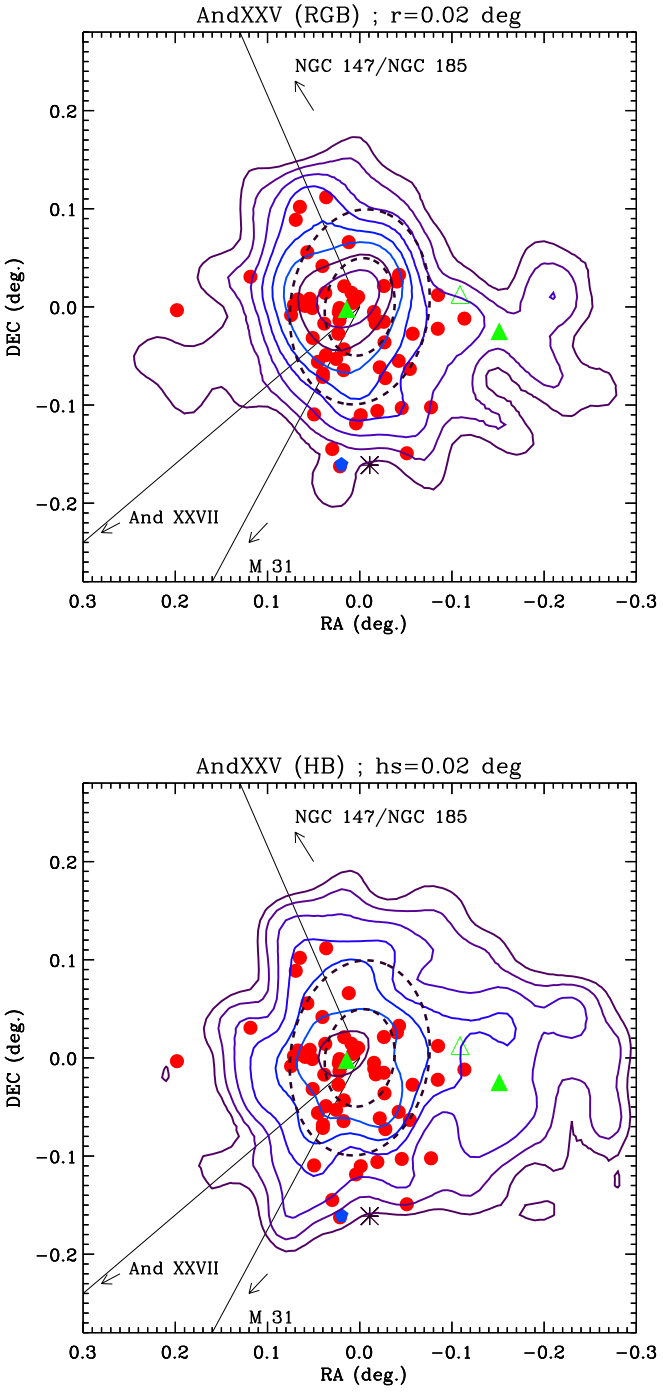

FIGURE 2.22: *Top*: Isodensity contours of RGB stars in And XXV. RA and DEC are the differential coordinates computed from the centre of the galaxy given by Richardson et al. (2011). The black dashed ellipses mark the areas within once and twice the r_h. The variable stars are shown with different colours and symbols (red filled circles for RRLs, green filled triangles for ACs, an open green triangle for the AC/CC, a black asterisk for the ECL and a blue pentagon for the unclassified variable]. *Bottom*: Same as in top panel but for And XXV HB stars. Figures from Cusano et al. (2016).

from M31 itself. In this scenario, the presence of at least one confirmed AC (V4) and one with an uncertain classification between CC and AC (V46), off-centred with respect to And XXV could indicate that a mild recent activity has been triggered from the outside.

From the CMD containing sources in the whole LBT FoV (right panel of Figure 2.20) we selected RGB stars (magenta encircled region) and built the RGB isodensity contours shown in the top panel of Figure 2.22. The variable stars are shown with different symbols and colours (red filled circles for the RRLs, green filled triangles for the ACs, an open green triangle for the AC/CC, a black asterisk for the ECL and a blue pentagon for the unclassified variable). Moving from the centre of And XXV outwards, the contours appear to be elongated towards the position of NGC147 and NGC185, the major axis of the isodensity contours changes in direction, and finally points towards the direction of these two galaxies. Since isodensity twisting is mainly due to tidal effects (di Tullio et al., 1979; Johnston et al., 2002), we suggest that And XXV is likely experiencing tidal stirring from the relatively nearby couple NGC147/NGC185 on one side and from M31 in the orthogonal direction. Perhaps, And XXV is infalling the M31 halo for the first time and feeling both the tidal force of the NGC147/NGC185 pair and of the massive host galaxy M31. The projected distances to NGC147/NGC185 and M31 are ∼95 kpc and ∼ 143 kpc, respectively, adopting the distances reported in Conn et al. (2012) for these systems. The spatial distribution of the HB stars is shown in the bottom panel of Figure 2.22. Although the HB region is heavily contaminated by background unresolved galaxies it is still possible to recognize some of the features traced by the RGB isodensities. An excess of HB stars extending in the direction of the M31 centre highlights the tidal interaction between And XXV and M31.

2.2.7 Gep I in Andromeda XXV

The visual inspection of the deep image obtained by stacking the 85 LBC images in the *B*-band of And XXV (for a total of 9.4 hour integration time), revealed a spherical assembly of stars near the photometric centre of the galaxy, that we named Gep I[9]. Figure 2.23 shows a snapshot of Gep I from our deepest LBT *B*-band image. This

[9]In the memory of a young colleague of us, Geppina Coppola, prematurely passed away.

clustering of stars is centred around coordinates R.A.=00:30:10.579 dec.=+46:51:05.58 and is of $\sim$ 12 arcsec in diameter.

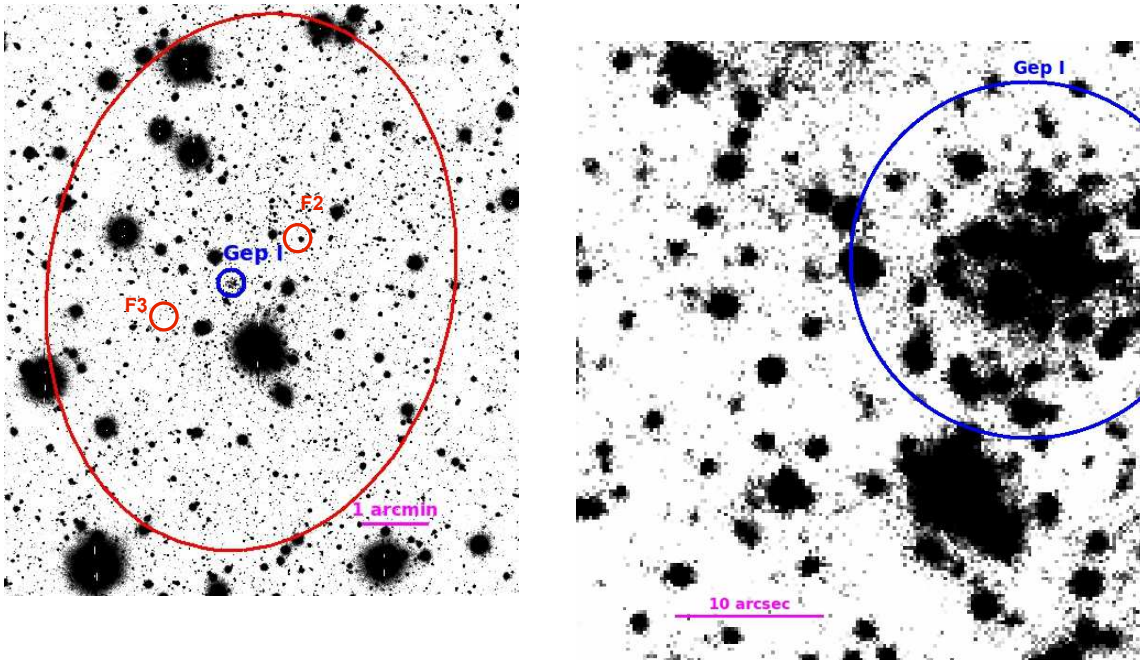

FIGURE 2.23: *Left*: Portion of the deepest image of And XXV obtained by stacking all B-band frames. The position of Gep I, the clustering of stars we have identified close to the centre of And XXV, is highlighted by a blue circle. The positions of the two comparison fields F2 and F3 are marked with red circles (see text for details). A red ellipse shows the area delimited by And XXV's r_h convolved with the galaxy ellipticity. North is up and East to the left. *Right*: a close up view of Gep I. Figures from Cusano et al. (2016).

In the discovery paper Richardson et al. (2011) published centre coordinates for And XXV with a quite large ($\sim$12 arcsec) uncertainty because in their observations the galaxy falls close to the 2 arcmin gaps among CCDs (see fig. 2 of Richardson et al. 2011). The difference between Gep I and And XXV centre coordinates is $\sim$11 arcsec, hence, Gep I is within the error box of Richardson et al. (2011) centre for the galaxy.

This stellar concentration could either be And XXV actual centre or a new star cluster belonging to And XXV or M31. Indeed, there is no known globular cluster (GC) in the Revised Bologna Catalogue of the M31 GCs (Galleti et al., 2004), nor any other known extended source, within $\sim$20 arcsec of Gep I centre coordinates. Using the (Graphical Astronomy and Image Analysis) GAIA tool we performed integrated photometry of

Gep I starting from the centre of the cluster and using circular apertures increasing from 1 to 20 arcsec in radius. We estimated the half light radius of Gep I to be $r_h \sim 6$ arcsec. The integrated magnitudes, computed within twice the r_h, are then B ∼20.6 mag and V ∼20.0 mag, respectively. Assuming that Gep I is at the same distance and reddening of And XXV, we obtained absolute magnitudes of $M_B \sim -4.2$ mag and $M_V \sim -4.9$ mag, respectively, while the r_h of Gep I at the distance of And XXV corresponds to ∼25 pc in linear extension. The r_h and M_V values we have derived place Gep I in the region of the $M_V - r_h$ plane that seems to be forbidden to ordinary GCs. Only the M31 Extended Clusters (ECs, Huxor et al. 2011) and the least luminous among the MW Palomar GCs are found to lie in this region (see Figure 10 of Huxor et al. 2011) along with the nuclei of dwarf elliptical galaxies. This leaves open the possibility that Gep I could indeed be the centre of And XXV.

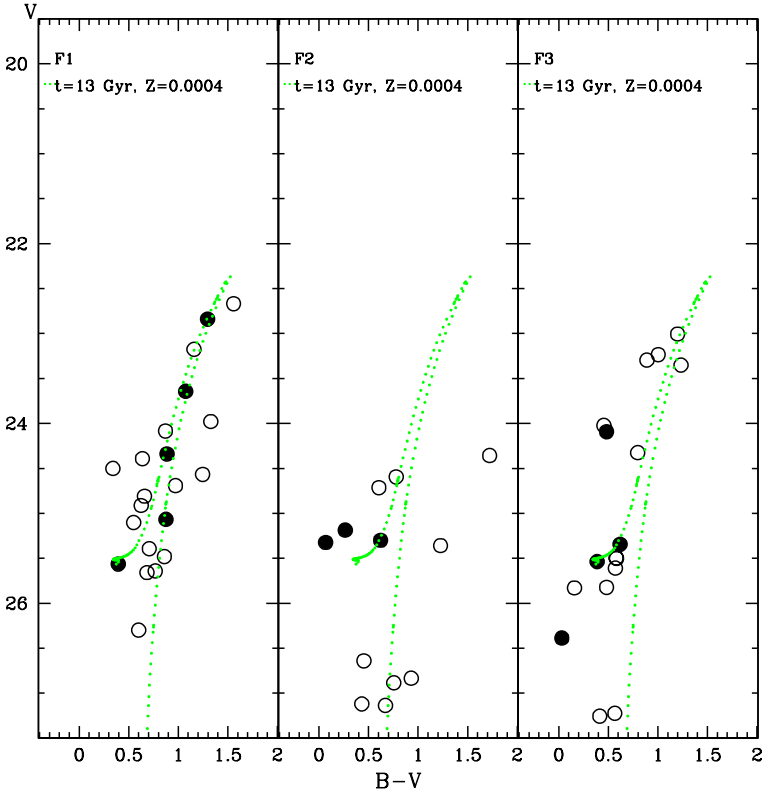

FIGURE 2.24: *Left*: CMD of sources in a circular area within a radius of 12 arcsec from the centre of Gep I (blue circle in Fig. 2.23, this area has been named F1 in Fig. 2.23). Filled circles are sources in our LBC photometric catalogue selected using the DAOPHOT χ and *Sharpness* parameters (-0.35 ≤ *Sharpness* ≤ 0.35 and $\chi < 1.5$). The green dashed line is an isochrone with t=13 Gyr and Z=0.0004 from Bressan et al. (2012). *Middle*: same as in the left panel but for sources in the F2 control field. *Right*: same as in the left panel for sources in the F3 control field. Figure from Cusano et al. (2016).

The stars that we could resolve in Gep I are just a few. Their position in the CMD is shown in the left panel of Figure 2.24. The CMD drawn taking all the objects in a circular area of 12 arcsec in radius from the centre of the stellar association (field F1), is mainly populated by RGB stars with only one or two HB stars. Their location in the CMD is compatible with an old population placed at a heliocentric distance of ∼750-800 kpc. Middle and right panels of Figure 2.24 show, for comparison, the CMDs of sources in the two circular regions F2 (middle panel) and F3 (right panel) highlighted by red circles in Fig. 2.23, which have the same radius of field F1 (twice the estimated r_h of Gep I), but are centred ∼1 arcmin to the North-West and ∼ 1 arcmin to South-East with respect to the F1 centre. The CMDs of the F2 and F3 regions show no clear evidence of a single old stellar population similar to the one observed in field F1, thus confirming that in F1 there is a real concentration of old stars. Clearly, our ground-based CMD of Gep I is severely incomplete. High resolution observations such as those achievable with HST are needed to better resolve Gep I and unveil its true nature. If the concentration of stars is proven to be a GC belonging to And XXV the galaxy would be one of the few dSphs in the Local Group known to host GCs, after Fornax and Sagittarius. The location of this candidate GC very close to the centre of And XXV (according to Richardson et al. 2011 coordinates), resembles the case of the GC M54 which is located in the core of its parent galaxy, the Sagittarius dSph (Monaco et al. 2005). Very recently, Crnojević et al. (2016) have identified a stellar cluster near the centre of the Eridanus II dwarf galaxy. The authors claim that Eridanus II is the faintest galaxy to host a stellar cluster. Following this trend, And XXV could be the faintest galaxy of the M31 complex to host a stellar cluster. Zaritsky et al. (2016) have suggested that most GCs may be hosted by undetected faint galaxies. Our discovery in And XXV along with Crnojević et al. (2016)'s discovery of the cluster in Eridanus II may lend support to Zaritsky et al. (2016)'s claim and provide hints on the connection between GCs and dwarf galaxies.

2.3 Andromeda XXVII: anatomy of a disrupting galaxy

2.3.1 Background

Andromeda XXVII (And XXVII) was discovered by Richardson et al. (2011) in the data of the PAndAS survey near a portion of Andromeda's North-West stream (NW). The authors of the discovery paper note that And XXVII seems to be in the process of being tidally disrupted by M31 and, due to the difficulty in measuring the magnitude of the galaxy HB, they reported only a lower limit of $\geq 757 \pm 45$ kpc for its heliocentric distance. Once again the distance measured by Conn et al. (2012) with the TRGB contrasts with Richardson et al. (2011)'s estimate, providing a value of 1255^{+42}_{-474} kpc that would place And XXVII well outside the M31 complex. Collins et al. (2013) measured a metal abundance [Fe/H]$= -2.1 \pm 0.5$ dex from the CaII triplet in eleven likely members, and a radial velocity of $v_r = -539.6$ km s^{-1} with $\sigma = 14.8$ km s^{-1}, however, they also warned that given the disrupting nature of the object, their estimates are very uncertain. In addition they noticed a significant kinematic substructure around ~ -500 km s^{-1}. More recently Martin et al. (2016) from a re-analysis of the PAndAS data concluded that And XXVII is, likely, a system in the final stage of tidal disruption.
In the following sections we present results, based on our LBT observations of And XXVII, that provide support to the above evidence both from the galaxy CMD and the spatial distribution of And XXVII's variable stars. This study was carried out during the second year of my PhD and its results have been published in the paper:"Variable stars and stellar populations in Andromeda XXVII: IV. An off-centred, disrupted galaxy" by F. Cusano, A. Garofalo, G. Clementini, et al. 2017, ApJ 851, 9.

2.3.2 Observations, data reduction and identification of the variable stars

LBC@LBT time series B, V observations of the field around the centre coordinates of And XXVII (R.A.=$00^h37^m27^s$, decl.=$+45°23'13''$, (J2000), Richardson et al., 2011) were acquired between October and November 2011 (see Table 2.3 for the complete log). Observations were obtained under good sky and seeing conditions (see Table 2.3).

TABLE 2.3: Log of And XXVII observations

Dates	Filter	N	Exposure time (s)	Seeing (FWHM) (arcsec)
October 20-24, 2011	*B*	87	400	0.8-1
November 27-28, 2011	*B*	5	400	0.8-1
October 20-24, 2011	*V*	86	400	0.8-1
November 27-28, 2011	*V*	4	400	0.8-1

Following the same procedures applied for Psc II and And XXV (Sections 2.1.2 and 2.2.2) we performed PSF photometry of the pre-processed images using the `DAOPHOT - ALLSTAR - ALLFRAME` packages (Stetson, 1987, 1994). As for And XXV, we used the Landolt standard fields L92 and SA113, observed during the same observing run to calibrate[10] our final photometric catalogue of And XXVII, then we proceeded to identify variable stars according to the procedure already described for Psc II and And XXV, that is, selecting candidates with the variability index computed in DAOMASTER (Stetson, 1994) and then inspecting the light curves of the candidate variables with the GRaTIS package. From this analysis 90 candidates were confirmed to vary. Of them 89 are classified as RRLs and one as AC. Coordinates, photometric and pulsation properties of the confirmed variable stars are provided in Table A.2. Examples of light curves are shown in Figure 2.25.

2.3.3 RR Lyrae stars in And XXVII

In the LBC FoV we have discovered a total of 89 RRLs, of which 58 are RRab and 31 are RRc stars. The RRLs are spread all over the LBC FoV (see Figure 2.26). The very sparse spatial distribution of the variable stars in And XXVII, in comparison with the other M31 satellites we have investigated for variability based on LBT data, confirms Richardson et al. (2011) claim that And XXVII is in the phase of tidal disruption. In Figure 2.26 the highest concentration of RRLs occurs in CCD3 (labelled C3 in the figure), where there are 32 RRLs to compare with 28 in C2, 21 in C1 and 7 in C4. However, given the proximity to M31 we cannot exclude that some of these RRLs may belong to the halo of M31.

To estimate how many RRLs belonging to the M31 halo could contaminate And XVII's RRLs we used results from a search for variable stars in six fields of M31 by Jeffery et

[10] $B - b = 27.696 - 0.113 \times (b - v)$ r.m.s.=0.03, $V - v = 27.542 - 0.060 \times (b - v)$ r.m.s.=0.03

al. (2011) using the HST data. Two of these fields are in the halo of M31, at about 35 kpc from the galaxy centre. They contain 5 and no RRLs, respectively, despite having comparable stellar densities. If we apply the M31 halo stellar density profile by Ibata et al. (2013), that in the metallicity range $-2.5 < [Fe/H] < -1.7$ dex is a power-law of $\Gamma = -2.3 \pm 0.02$, after scaling for the different area surveyed by the LBC and the HST (ACS; ~ 11 arcmin^2) we estimate a possible contamination from the M31 halo of ~ 14 RRLs in our LBC@LBT pointing of And XXVII. However, we note that the number of contaminant RRLs can be larger than this estimate as And XXVII lies in a region of the M31 halo where stars in the metallicity range $-2.5 < [Fe/H] < -1.7$ form streams all around And XXVII, as shown in figure 9 of Ibata et al. (2014). Thus decontamination of And XXVII stars from field objects is a difficult task.

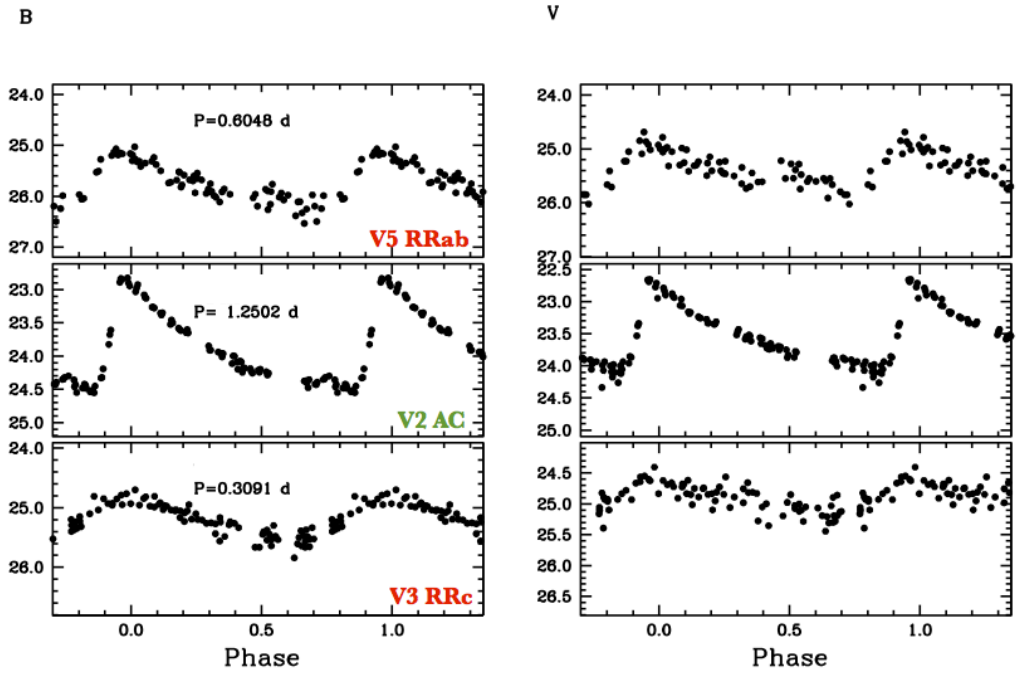

FIGURE 2.25: Examples of B-(left panels) and V-band (right panels) light curves for different types of variable stars identified in And XXVII (from top to bottom: RRab, AC and RRc stars).Typical internal errors of the single-epoch data range from 0.01 at $B \sim 22.8$ mag (corresponding to the maximum light of the AC) to 0.30 mag at $B \sim 26.8$ mag (corresponding to the minimum light of a fundamental mode RRLs), and similarly, from 0.01 mag at $V \sim 22.6$ mag to 0.30 mag at $V \sim 26.8$ mag.

The upper panel of Figure 2.27 shows the period distribution of the RRLs we have identified in the field of And XXVII:

- $\langle P_{ab} \rangle$=0.59 d (σ=0.05 d) from the 58 RRab stars;
- $\langle P_{c} \rangle$=0.35 d (σ=0.04 d) from the 31 RRc stars.

Since $\sim$ 14 RRLs in our sample could belong to the halo of M31 we performed a bootstrap re-sampling of the data, removing a total of 14 RRLs. Among the 14 RRLs we removed randomly 9 RRab and 5 RRc stars, consistently with the fraction of RRc over total number of RRLs we found in the field of And XXVII. The average period (and related σ) of the RRab and RRc stars, separately, does not change significantly, giving us confidence that the And XXVII RRLs have the same pulsation properties as those belonging to the surrounding M31 halo. The lower-left panel of Figure 2.27 shows the Bailey diagram of the RRLs in And XXVII. The majority of RRLs in And XXVII are placed near the locus of the Oo I systems and there are no differences among RRLs located in different

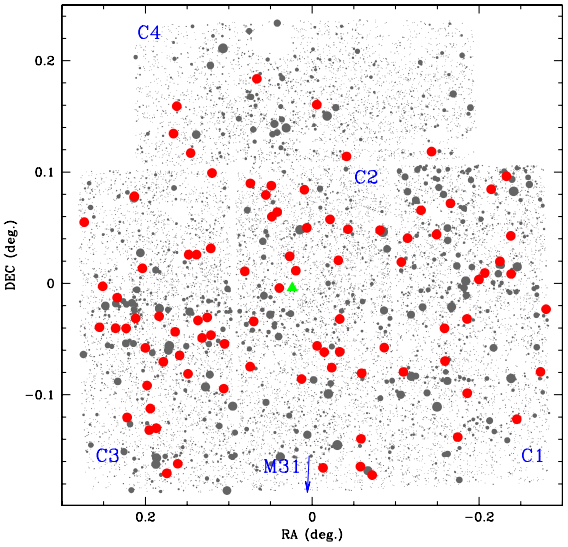

FIGURE 2.26: Spatial distribution of the variable stars discovered in the whole LBT FoV of And XXVII. The 4 CCDs of the LBC mosaic are labelled. Red filled circles mark the RRLs, a green filled triangle is the AC. Gray points are non variable sources, selected as to have `DAOPHOT` quality image parameters: $-0.35 \leq$ *Sharpness* $\leq$0.35 and χ <1.5. Their size is inversely proportional to the source B-magnitude. There are $\sim$ 4,300 constant sources and 32 RRLs displayed in C3, $\sim$ 5,000 and 28 in C2, $\sim$ 4,200 and 21 in C1 and $\sim$ 3,500 and 7 in C4. The blue arrow points to the direction of M31. North is up, east to the left. Figure from Cusano et al. (2017).

parts of the LBC FoV (see Section 2.3.6 and Table 2.4). Both the $\langle P_{ab} \rangle$ value and the RRLs distribution in the Bailey diagram suggest a classification as OoI/Int system for And XXVII. In the lower-right panel of Figure 2.27 the period-amplitude diagram of And XXVII's RRLs is compared with RRLs in And XIX, And XXI and in M31 halo fields studied by Brown et al. (2004) and Sarajedini et al. (2009).
Although And XXVII would be classified as an Oo Int/OoI system based on the $\langle P_{ab} \rangle$, we note that And XXVII has the lowest $\langle P_{ab} \rangle$ value, among the four M31 satellites we have analysed based on LBT data (see Table 2.5, column 3). Furthermore, the fraction of RRc stars to total number of RRLs in And XXVII, $f_c = N_c/N_{ab+c} = 0.35 \pm 0.07$, is much closer to the value expected for Oo II ($f_c \sim 0.44$) than for Oo I ($f_c \sim 0.17$) systems (Catelan, 2009). Hence, while the $\langle P_{ab} \rangle$ suggests a classification as Oo-Int/Oo I type, a classification more similar to Oo II type is suggested by the And XXVII f_c value.

We derived a photometric metallicity estimation for the RRLs in And XXVII using the two different methods described in Section 1.1.1 of Chapter 1, which both involve only RRab stars:

- Alcock et al. (2000) method. Figure 2.28 shows the resulting metallicity distribution using the Alcock et al. (2000) relation (Equation 1.3). Fitting a Gaussian curve to this distribution we find a peak at [Fe/H]= -1.62 dex (σ=0.23 dex) which is in good agreement with the photometric estimation of [Fe/H]=-1.7 ± 0.2 dex obtained in the discovery paper (Richardson et al., 2011) by isochrone fitting of the And XXVII CMD and is marginally consistent with the spectroscopic estimate of [Fe/H]=-2.1 ± 0.5 dex by Collins et al. (2013), which has a rather large uncertainty.

- Jurcsik & Kovacs (1996) method. As described in Section 1.1.1 of Chapter 1 this method is based on a relation linking the ϕ_{31} parameter of the Fourier decomposition of the light curves and the pulsation period of RRab stars. We performed a sine Fourier decomposition of the V-band light curves of the RRab stars in our sample deriving the ϕ_{31} values and also determining the deviation parameter D_m which measures the regularity of the light curve. We recall that, according to Jurcsik & Kovacs (1996) a reliable metallicity can be estimated from the ϕ_{31} parameter only if the light curve satisfies the condition $D_m < 3$. Among the RRab stars in our sample only V67 satisfies this condition. We applied Equation 1.2 from Jurcsik &

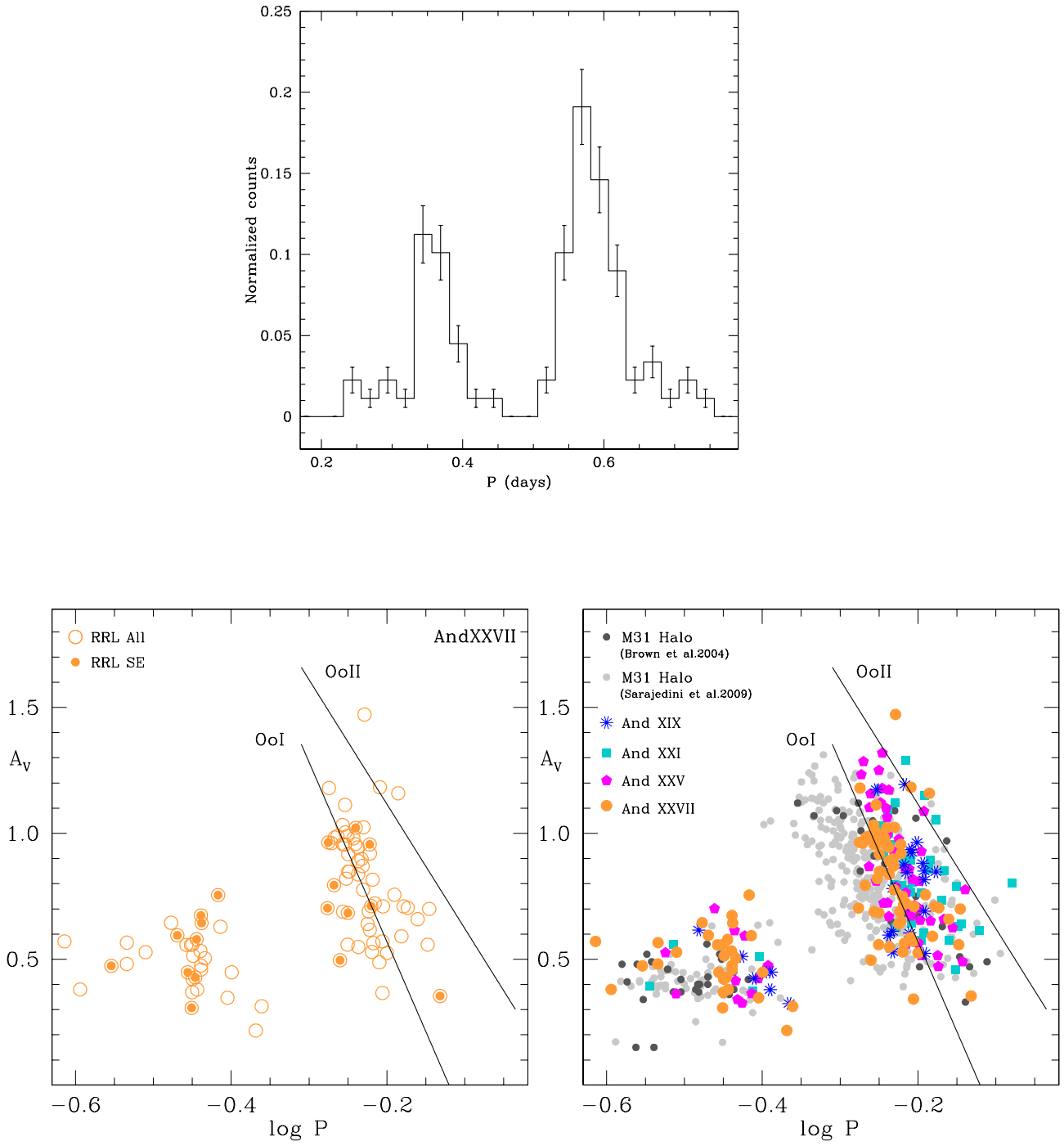

FIGURE 2.27: *Upper panel*: Period distribution of the 89 RRLs identified in the field of And XXVII. The bin size is 0.025 days. *Lower-left panel*: Period-amplitude diagram of the RRLs in And XXVII (orange open circles). RRLs highlighted with filled orange circles are those located in the SE region (see Section 2.3.6). The solid lines are the ridge lines of the Oo I and Oo II RRLs (Clement & Rowe 2000). *Lower-right panel*: Same as in the left panel but showing also the RRLs in And XIX (blue asterisks), And XXI (cyan squares), And XXV (magenta pentagons) and in three HST fields in the M31 halo from Sarajedini et al. (2009) (grey symbols) and Brown et al. (2004) (dark-grey symbols), respectively. Figures from Cusano et al. (2017).

Kovacs (1996) and derived the metallicity $[Fe/H]_{JK96} = -1.75 \pm 0.49$ dex on the Jurcsik & Kovacs metallicity scale, which becomes $[Fe/H]_{C09} = -1.86 \pm 0.50$ dex once transformed to the Carretta et al. (2009) metallicity scale using Equation 3 from Kapakos et al. (2011). All these values are consistent within their errors with the peak value of the distribution obtained applying Alcock et al. (2000)'s method.

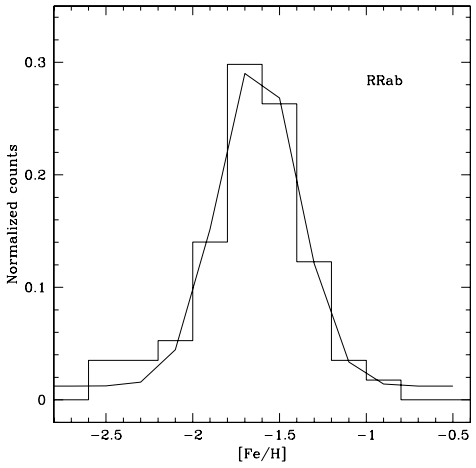

FIGURE 2.28: Metallicity distribution of And XXVII's RRab stars using the Alcock et al. (2000) method. The distribution peaks at [Fe/H]= −1.62 dex (σ=0.23 dex). Figure from Cusano et al. (2017).

2.3.4 V2, the lone AC in And XXVII

V2 is the only variable star in And XXVII that falls in the instability strip at about one magnitude brighter than the galaxy HB level (see right panel of Figure 2.30). As done for Psc II and And XXV, we have compared V2 with the *PW* relations of ACs and CCs in the LMC. These comparisons are shown in the upper-left and upper-right panels of Figure 2.29, respectively, where we adopted for And XXVII the distance inferred from the RRLs (see Section 2.3.5).

We have also plotted in both upper panels of Figure 2.29 the ACs we have identified in And XIX, And XXI, and And XXV (see Section 2.2.5). V2 well follows the *PW* relation for fundamental mode ACs, while it can be definitely ruled out that the star is a short period CC. Assuming that V2 is the only AC in the galaxy, we computed the specific frequency of ACs (S) in And XXVII and then, as done for And XXV (see Sect. 2.2.5) we compared And XXVII with other M31 and MW dSphs. This is shown in

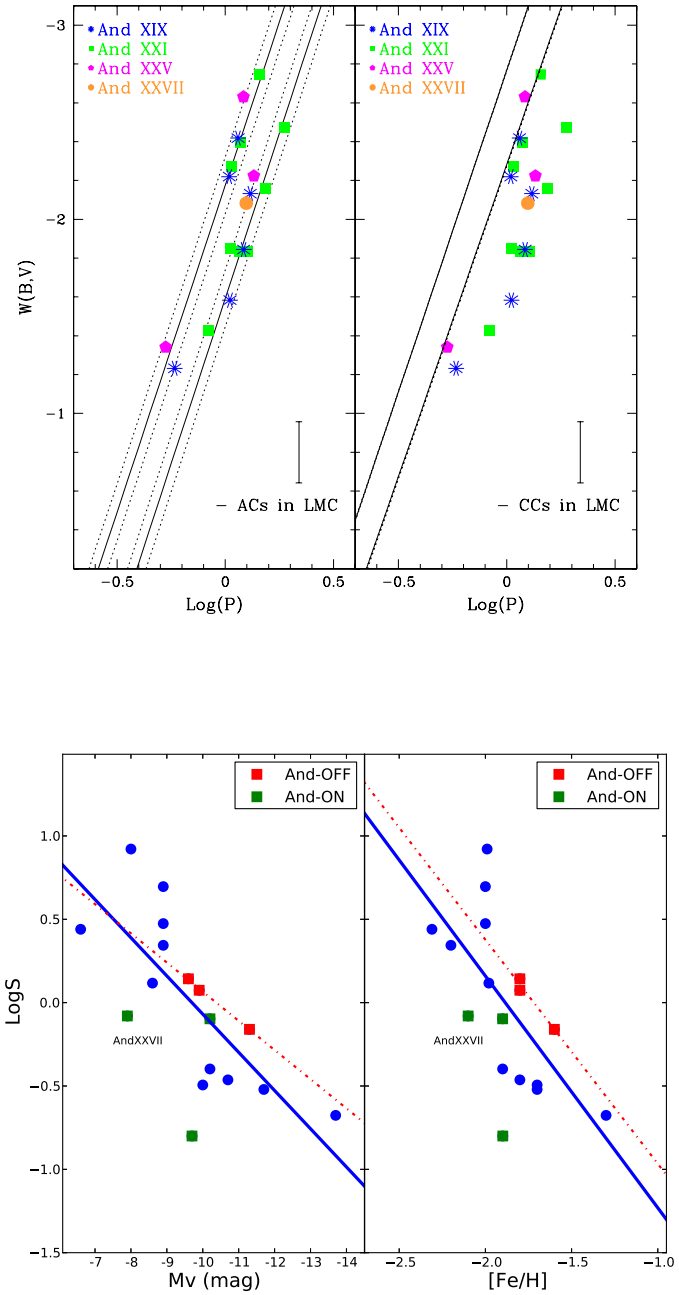

FIGURE 2.29: *Upper panels*: Position of V2 (orange symbol) with respect to the *PW* relations for ACs (left panel; Ripepi et al. 2014) and CCs in the LMC (right panel; Jacyszyn-Dobrzeniecka et al. 2016). The 95% confidence contours are shown as dotted lines. Blue, green and magenta symbols are ACs we have identified in And XIX (Cusano et al. 2013), And XXI (Cusano et al. 2015), and And XXV (Section 2.2.5). *Lower panels*: Specific frequency of ACs in dwarf satellites of M31 and the MW vs. absolute magnitude in the V-band (left panel) and metallicity (right panel) of the host systems. Blue filled circles are dSphs around the MW. Green and red filled square are M31 satellites respectively ON and OFF the GPoA (see Sect. 1.3 in Chapter 1 and Sect. 2.3.7 in this Chapter). Figures from Cusano et al. (2017).

the lower panels of Figure 2.29, where for the AC specific frequencies of the MW (blue filled circles) and M31 (green and red filled squares) dSphs we have used the revised values we derived as described in Section 2.2.5. The blue ridge line shows the relation obtained by fitting all the dSphs in the plot. The M31 satellites that are off the GPoA (see Chapter 1) Section 1.3; red squares) seem to follow a different trend that is described by the red dashed line. The sample is still statistically too poor to conclude that OFF- and ON-plane satellites obey different correlations between AC specific frequency and luminosity or metallicity, but the satellites studied so far seem to suggest that this may be the case, as further discussion in Section 2.3.7.

2.3.5 Colour Magnitude Diagram and stellar populations in And XXVII

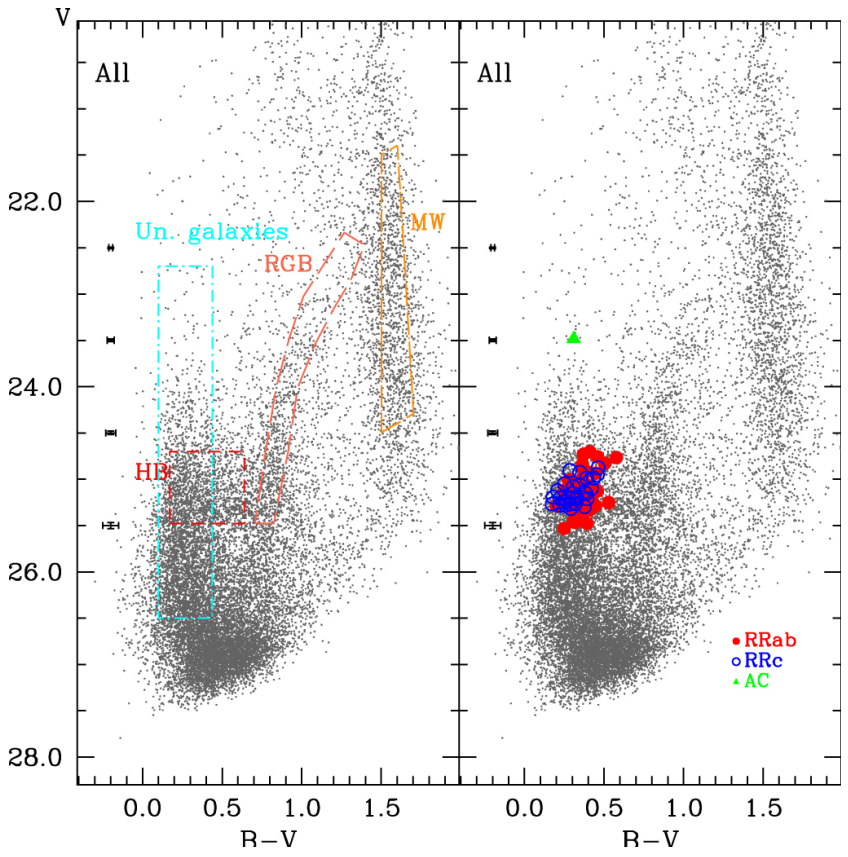

FIGURE 2.30: *Left panel*: CMD of the sources in the whole LBC FoV of And XXVII. Only objects meeting the DAOPHOT quality image parameter conditions: $-0.35 \leq$ *Sharpness* ≤ 0.35 and $\chi < 1$ are displayed. The RGB, HB and MW selections are marked by dashed contours (orange, red, yellow and cyan, respectively). *Right panel*: Same as in the left but showing the variable stars we have identified in And XXVII. Red filled circles are the RRab stars, blue open circles are the RRc stars and a green filled triangle is the AC. Figure from Cusano et al. (2017).

Figure 2.30 shows the CMD of the sources in the whole LBC FoV of And XXVII that satisfy the following DAOPHOT quality image parameter selections: $-0.35 \leq Sharpness \leq 0.35$ and $\chi < 1$. Main CMD features are highlighted in the left panel of the figure, while the right panel shows the position of the 90 variable stars (with red filled circles for the 58 RRab stars, blue open circles for the 31 RRc stars and a green filled triangle for the AC) identified in the field of And XXVII. The CMD is heavily contaminated by MW foreground stars in the red part ($1.4 \leqslant B - V \leqslant 1.9$ mag) and by background unresolved galaxies in the blue part ($-0.1 \leqslant B - V \leqslant 0.1$ mag, see section 9 in Cusano et al. 2013 and, e.g. Bellini et al. 2010; Bellazzini et al. 2011). The RRLs highlight a rather thick HB with a broad distribution in apparent V mean magnitude that ranges from 24.70 to 25.55 mag, as shown more clearly in Fig. 2.31. Two significant peaks are observed in this distribution, a main peak at $\langle V(RR) \rangle \sim 25.25$ mag and a second peak around $\langle V(RR) \rangle \sim 25.10$ mag. The four panels in Figure 2.32 show the CMDs of sources in the 4 individual CCDs of the LBC mosaic (labelled C1, C2, C3 and C4). Similarly, Figure 2.33 shows the distributions in apparent V mean magnitude of the RRLs in C1, C2, C3 and C4, separately. Although contamination by foreground MW stars/background unresolved galaxies (see left panel of Figure 2.30) and broadening of both the RGB and HB is seen in each of the four individual CMDs, C3 shows a more prominent RGB extending as bright as $V \sim 22.5$ mag, whereas the RGB in the other 3 CCDs seems to be truncated around $V \sim 23.5$ mag. Furthermore, as shown by Figure 2.33 the peak at $\langle V(RR) \rangle \sim 25.25$ mag is mainly due to the RRLs located in C3. We

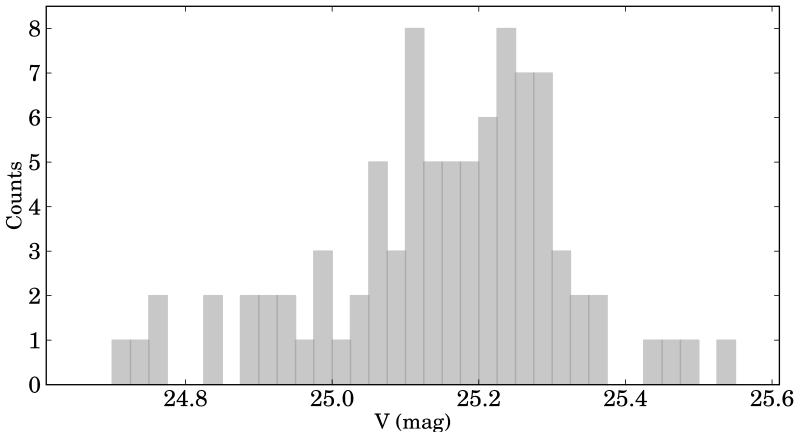

FIGURE 2.31: Distribution in apparent mean V magnitude of the 89 RRLs we have identified in the field of And XXVII. The bin size is 0.025 mag. Figure from Cusano et al. (2017).

further investigated the spatial distribution of And XXVII stars selecting objects in the RGB region of the CMD with magnitude and colour in the range of $22.5 \leq V \leq 25.3$ mag and $0.8 \leq B - V \leq 1.3$ mag, respectively. We built isodensity maps by binning these RGB stars in $1.2' \times 1.2'$ boxes and smoothing with a Gaussian kernel of $1.2'(0.02^o)$ FWHM. The upper panel of Figure 2.34 shows the RGB isodensity maps where the outermost contour levels are 3σ above the sky background. Two high-counts isodensity contours show up: one region around Richardson et al. (2011)'s centre coordinates of And XXVII, that we named C in the figure, is entirely contained into C2; the other

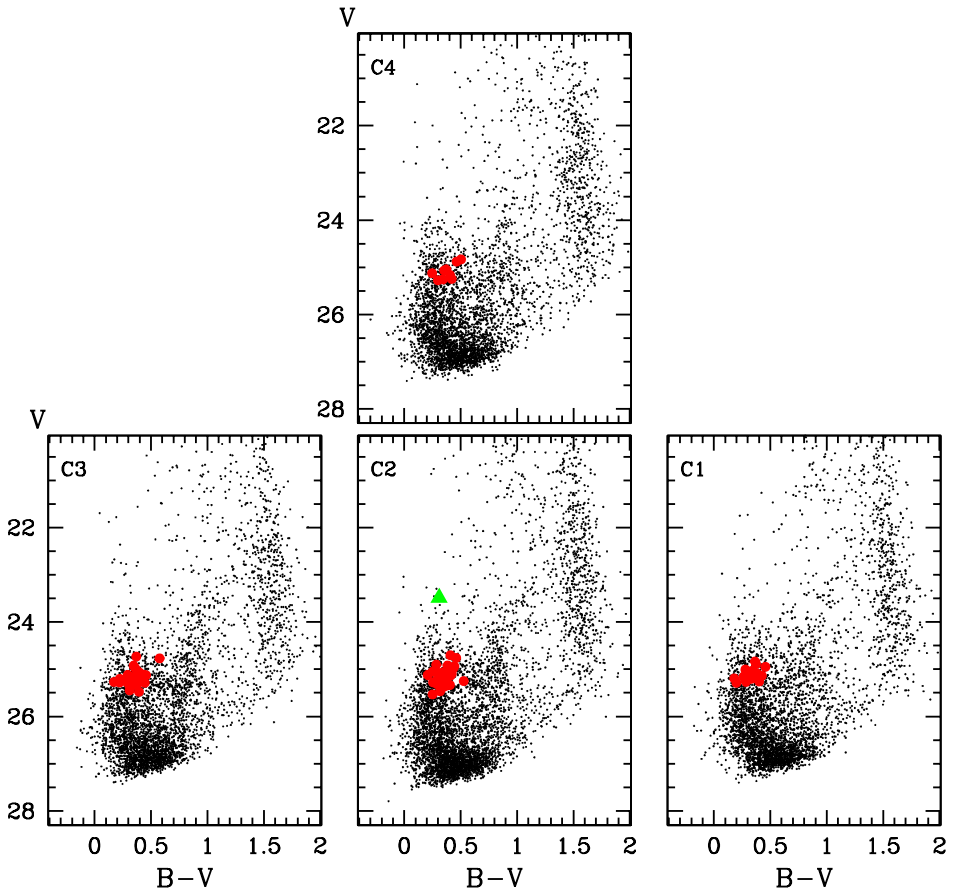

FIGURE 2.32: CMDs of sources in the 4 CCDs of the LBC mosaic. Only objects satisfying `DAOPHOT` photometric quality parameters are displayed. Red filled circles are the RRLs: 32 in C3, 29 in C2, 21 in C1 and 7 in C4. The green triangle is the AC which is in C2. Figure from Cusano et al. (2017).

isodensity, that is entirely contained into C3, has a completely elongated structure that extends in south-est direction and reaches a second high-counts isodensity displaced by about 0.2 degrees to the south-west of the centre of region C. We have named this second region SE. In both regions, SE and C, we adopted a radius of 4 arcmin (yellow solid circles in Fig. 2.34) to define areas twice the corresponding high-counts isodensity contours (assuming for the centre of the SE region the coordinates: R.A.=$00^{h}38^{m}10.4^{s}$, decl.=$+45°21'58''$). In the SE region there is a concentration of stars as high as in the C region but a higher number of RRLs (see Section 2.3.6).

The presence of two high density contours in the map shown in Figure 2.34 points out that And XXVII has a very complex physical structure. It is worth nothing that clearly the contamination by background and fore-ground sources could hamper the RGB stellar counts, however, to reduce the contamination the selection of RGB stars was done in the specific region of the CMD containing RGB stars at the distance of And XXVII (see left panel of Figure 2.30). The rather broad RGB is also a hint of the complex physical structure of And XXVII as is the large spread in mean apparent magnitude of the RRLs $\langle V(RR)\rangle \sim 25.15\pm 0.17$ mag (Figures 2.31 and 2.33) that can be caused by a distance spread. We also computed isodensity contours by selecting stars in the HB region of the And XXVII CMD: $25.6 \leqslant V \leqslant 24.6$ ma and $0.17 \leqslant B-V \leqslant 0.64$ mag. They are shown in the bottom panel of Figure 2.34. The HB region of the CMD is contaminated by unresolved background galaxies (blue box, in the left panel of Figure 2.30), still the

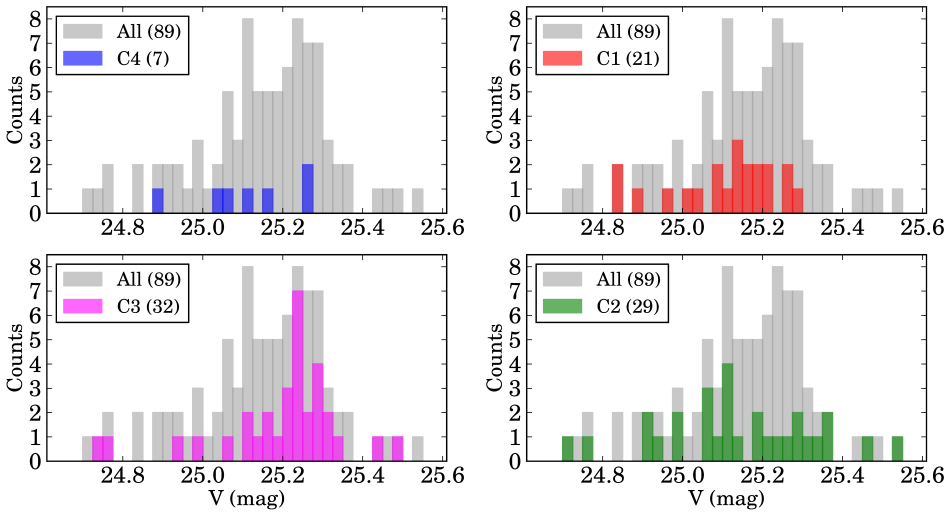

FIGURE 2.33: Distribution in apparent V mean magnitude of the RRLs in the 4 CCDs of the LBC mosaic. The bin size is 0.025 mag. Figure from Cusano et al. (2017).

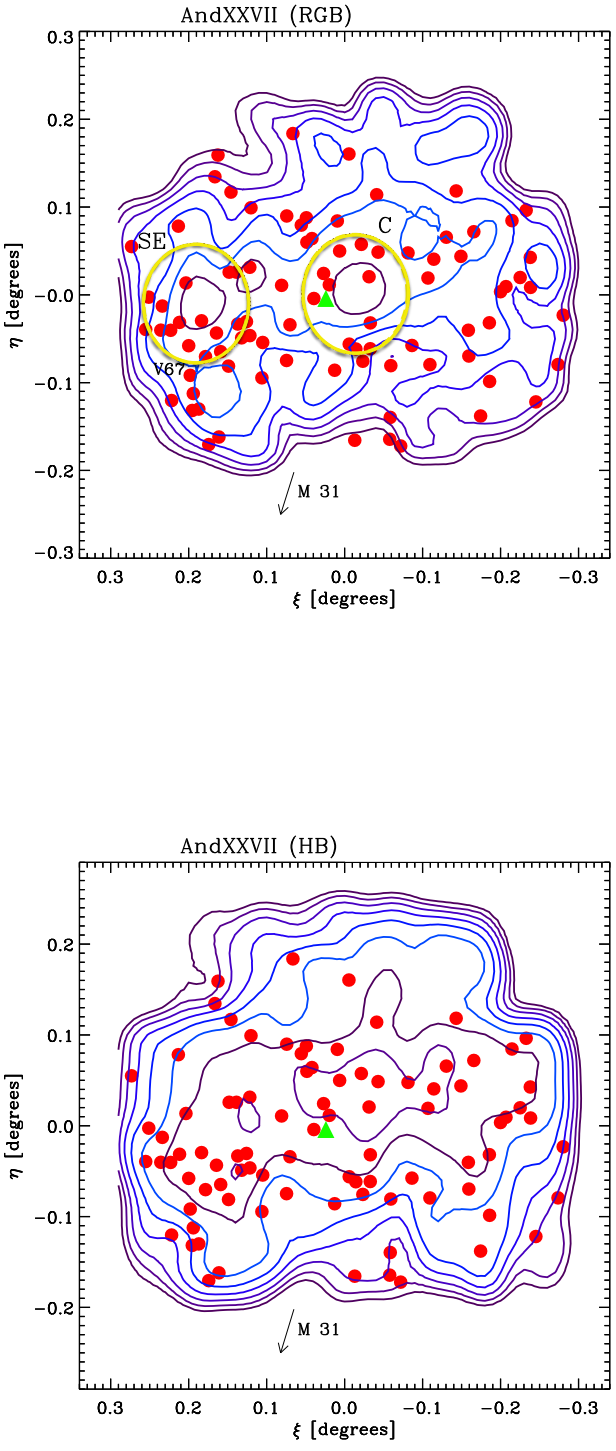

FIGURE 2.34: *Top*: Isodensity contours of RGB stars in And XXVII. RA and DEC are differential coordinates computed from the centre of the galaxy given by Richardson et al. (2011). Yellow solid circles mark areas of 4 arcmin in radius around regions C and SE, respectively. The variable stars are shown with different colours and symbols (red circles for RRLs and a green filled triangle for AC). *Bottom*: Same as in the top panel but for And XXVII HB stars. Figures from Cusano et al. (2017).

HB stars well follow the structure traced by the RGB stars. And XXVII's HB stars were selected choosing the closest objects to the CMD region defined by the RRLs, but given the presence in this region of unresolved background galaxies, we found that the shape of the HB isodensities depends significantly on how the selection is performed. Conversely, the shape of the isodensity contours does not change significantly even if we make different selections of the RGB stars, hence for the RGB the contamination is not as crucial as for HB stars.

In order to investigate in better detail the stellar populations in the C and SE regions we built separate CMDs of the sources in those regions. The result is shown in Figure 2.35:

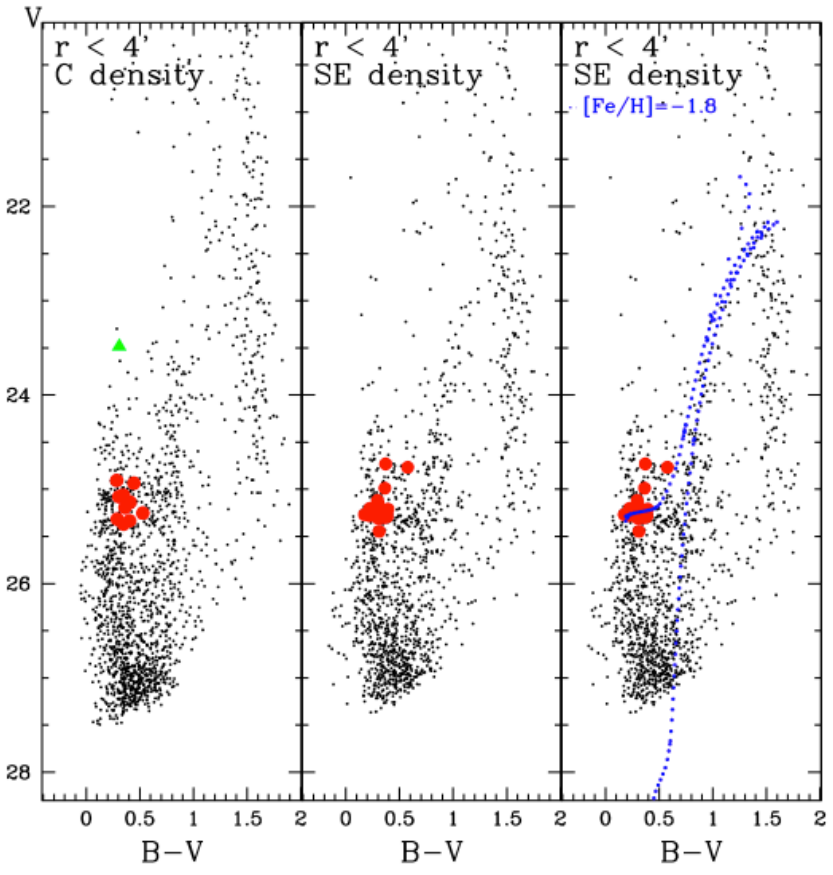

FIGURE 2.35: CMDs of the sources in the C and SE regions. Only objects satisfying the DAOPHOT quality image parameter conditions: $-0.35 \leq Sharpness \leq 0.35$ and $\chi < 1$ are displayed. Red filled circles are the RRLs, a green filled triangle is the AC. *Left panel*: CMD of the sources in the C region. *Middle panel*: CMD of the sources in the SE region. *Right panel*: Same as in the middle panel but with superimposed a stellar isochrone of 13 Gyr with [Fe/H]=−1.8 dex (blue dotted line; see text for details). Figure from Cusano et al. (2017).

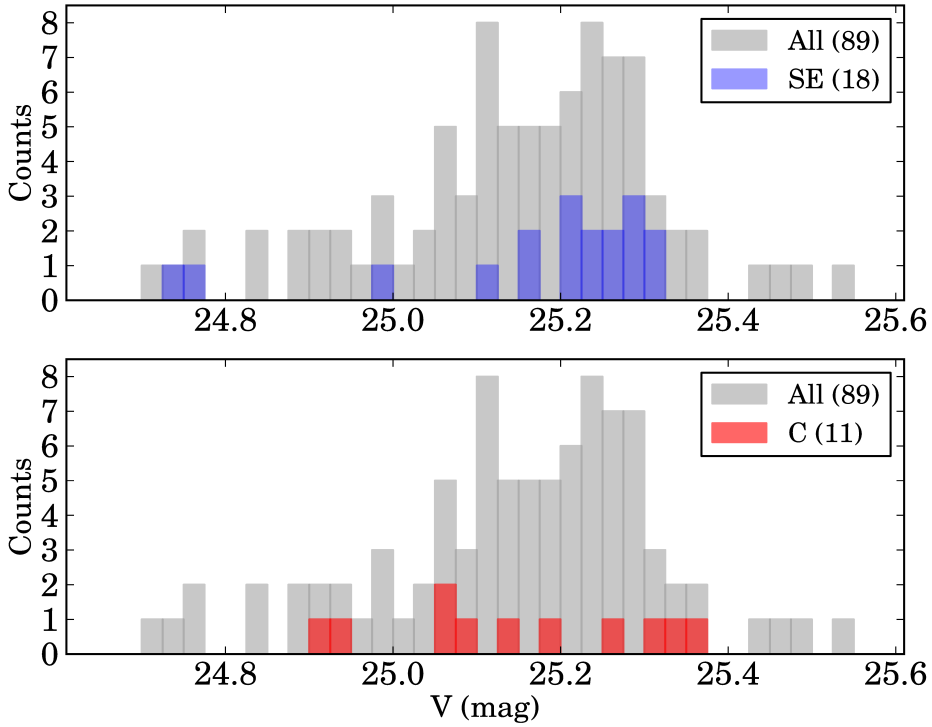

FIGURE 2.36: Distribution in apparent mean V magnitude of the RRLs in the C and SE regions. The bin size is 0.025 mag. Figure from Cusano et al. (2017).

the CMD of the SE region (centre panel of Fig. 2.35) is similar to the CMD of C3 (lower-left panel of Fig. 2.32) and shows a well extended, better defined and narrower RGB especially around the tip, than the CMD of the C region (left panel of Fig. 2.35), which is more similar to the CMD of C2 (lower-centre panel of Fig. 2.32), with an RGB truncated around $V \sim 23.5$ mag and a less defined HB. The lower panel of Figure 2.36 shows the distribution in apparent V mean magnitude of the 11 RRLs in region C, while the upper panel shows the mean magnitude distribution of the 18 RRLs in region SE. Among the 18 RRLs contained in SE, 15 trace a rather tight HB with $\langle V(RR) \rangle = 25.24$ mag and $\sigma = 0.06$ mag. Conversely, the 11 RRLs of region C are rather spread in magnitude (see left panel of Figure 2.35 and bottom panel of Figure 2.36) with $\langle V(RR) \rangle = 25.15$ mag and $\sigma = 0.15$ mag. This leads us to wonder whether the actual centre of And XXVII might be in the SE region rather than in C, which is where Richardson et al. (2011) located the centre of this dSph.

We have superimposed to the CMD of the SE region an isochrone of 13 Gyr with [Fe/H]=−1.8 (see right panel of Fig. 2.35) as derived from the web interface CMD 2.9 (Marigo et al. 2017). The isochrone was corrected for the distance and reddening derived in Section 2.3.5 for the SE region. This isochrone well fits the position of RRLs

and RGB stars. The comparison between isochrone and the CMD suggests a higher metallicity value for And XXVII than measured by Collins et al. (2013). The isochrone fit result is consistent (within the errors) with the metallicity estimated using the RRLs in Section 2.3.6. We reach a similar conclusion from the comparison with the RGB and HB ridge lines of GGCs with different metallicities. The best fit is obtained for NGC 4147 with [Fe/H]=−1.8 dex. In the following section we adopt [Fe/H]=−1.8 dex for the metallicity of And XXVII.

2.3.6 Distance and structure of And XXVII

TABLE 2.4: Properties of selected samples of RRLs in And XXVII.

id	N (RRab+RRc)	$\langle V(RR)\rangle$ mag	$\langle P_{ab}\rangle$ days	$\langle P_c\rangle$ days	E(B−V) mag	$(m-M)_0$ mag	f_c
ALL	58+31	25.15 ± 0.17	0.59 ± 0.05	0.35 ± 0.04	0.04 ± 0.05	24.61 ± 0.24	0.35
SE	9+9	25.17 ± 0.17	0.58 ± 0.05	0.35 ± 0.03	0.05 ± 0.05	24.60 ± 0.24	0.50
SE1	6+9	25.24 ± 0.06	0.55 ± 0.01	0.35 ± 0.03	0.03 ± 0.05	24.67 ± 0.20	0.60
C	6+5	25.15 ± 0.15	0.62 ± 0.03	0.33 ± 0.05	0.07 ± 0.05	24.52 ± 0.23	0.45
NORTH	29+15	25.09 ± 0.16	0.60 ± 0.04	0.36 ± 0.04	0.05 ± 0.03	24.52 ± 0.21	0.35
SOUTH	29+16	25.20 ± 0.15	0.59 ± 0.05	0.34 ± 0.04	0.03 ± 0.06	24.71 ± 0.27	0.35
EAST	39+20	25.17 ± 0.18	0.60 ± 0.05	0.35 ± 0.05	0.05 ± 0.05	24.60 ± 0.25	0.34
WEST	19+11	25.10 ± 0.13	0.59 ± 0.04	0.35 ± 0.03	0.02 ± 0.05	24.62 ± 0.22	0.37

We have used the mean luminosity of the RRLs, $\langle V(RR)\rangle$, to estimate the distance to And XXVII. Although some of the RRLs we have identified in the field of And XXVII galaxy could belong to M31 halo, in deriving the distance we used all the sample of 89 RRLs because they are indistinguishable from the M31 field. As done in And XXV, using the Piersimoni et al. (2002) method (see Section 2.2.4 and 1.1.2), from the RRab stars, we computed a reddening value $< E(B-V) > = 0.04 \pm 0.05$ mag (where the error is the standard deviation of the mean), which is slightly smaller but still in agreement with the value inferred by Schlegel et al. (1998), E(B-V)=0.08±0.06mag). For the metallicity of And XXVII we adopted [Fe/H]=−1.8 ± 0.3 dex as derived from isochrone fitting and consistently with our estimate from the RRLs. We adopted the extinction law $A_V = 3.1 \times E(B\text{-}V)$ and dereddend the mean luminosity of the RRLs in And XXVII, $\langle V(RR)\rangle$=25.15 mag (σ=0.17 mag average on 89 stars), then we adopted an absolute magnitude of $M_V = 0.54 \pm 0.09$ mag for RRLs with a metallicity of [Fe/H] = -1.5 dex (Clementini et al. 2003) and the slope of the luminosity-metallicity relation provided by Clementini et al. (2003) and Gratton et al. (2004). The resulting distance modulus

is $(m-M)_0 = 24.55 \pm 0.26$ mag. This is 0.16 mag longer but still consistent, within the large error, with Richardson et al. (2011)'s lower limit of $\geqslant 757 \pm 45$ kpc (corresponding to $(m-M)_0 = 24.39 \pm 0.13$ mag) Our estimate places And XXVII within the M31 complex and is also consistent within the errors with the lower limit of Conn et al. (2012)'s measurement. We recall here that the Conn et al. (2012) distance modulus $(m-M)_0 = 25.49^{+0.07}_{-1.03}$ mag has a very large asymmetric error likely due to the difficulty in identifying the tip of RGB which is very scarcely populated in And XXVII.

As anticipated in Section 2.3.5, And XXVII appears to be in the process of tidal disruption. This may have resulted in the RRLs being located at different distances from us, thus causing the large dispersion in $\langle V(RR) \rangle$. In order to investigate the galaxy structure we have compared the number and properties of RRLs located in different parts of the LBC FoV, including the two regions with highest stellar counts, namely, regions C and SE in Figure 2.34. As seen in Figure 2.35, 18 RRLs are in the SE region and only 11 in the C region. Average V magnitude, reddening and other properties of the RRLs in the C and SE regions, separately, are summarised in Table 2.4[11]. Differences in distance

[11]The SE region contains 18 RRLs in total, its sub-region (labelled SE1 in the table) only the 15 RRLs whose mean magnitude peaks around $\sim$ 25.24 mag.

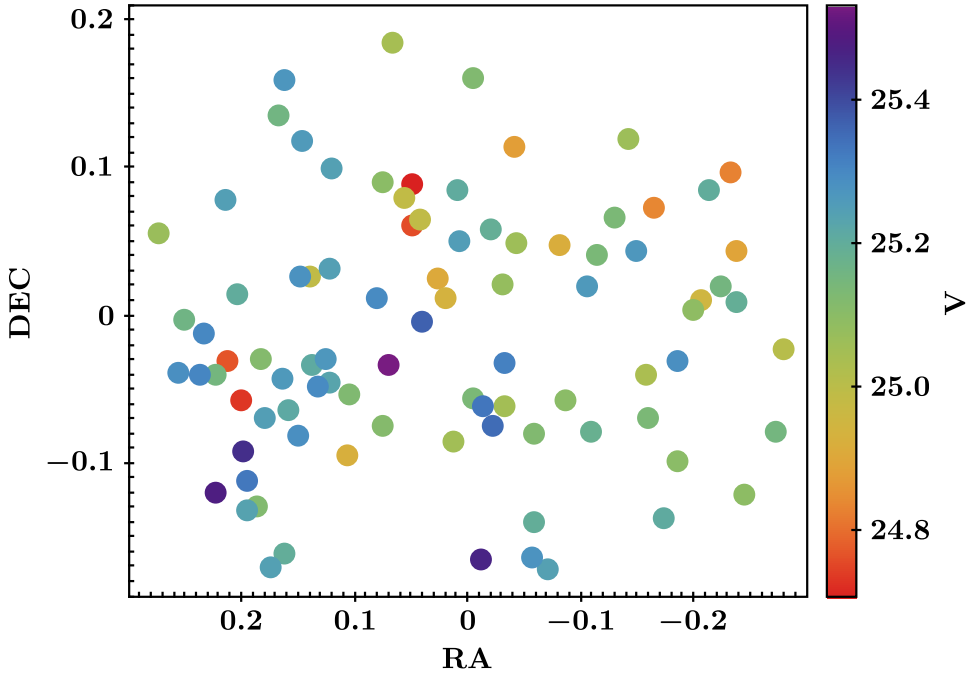

FIGURE 2.37: Spatial distribution of the 89 RRLs we have identified in the field of And XXVII. The colour bar reflects the mean apparent magnitude ($< V >$) of each RRL. Figure from Cusano et al. (2017).

moduli between the C and SE regions, or the C and SE1 regions, all are within 1σ given the still large dispersion of the estimates. Taken at face value, the difference in distance moduli between the C and SE1 regions (0.15 mag) may be due to a real radial distance effect (column 7 Table 2.4). However, considering the large errors still affecting these distance determinations, this conclusion has to be taken with caution.

The spread in magnitude can be due to a real three-dimensional (3D) effect, but not as big as 0.15 mag. The centres of the C and SE regions are $\sim$ 0.2 degree apart in the sky, that at the distance of And XXVII corresponds to a physical projected separation of $\sim$ 3 kpc. We can speculate the following two possibilities: (i) And XXVII is a disrupted system and the SE component is 3 kpc away from the galaxy centre; (ii) given that SE has the cleanest CMD and the largest concentration of RRLs most of which are located approximately at the same distance from us (SE1 has indeed the thinnest dispersion on the $\langle V(RR)\rangle$), SE could be the remaining nucleus of the now disrupted And XXVII. Driven by these two different possibilities we divided the RRLs in two samples, corresponding, respectively, to the south and north portions of And XXVII according to Richardson et al. (2011)'s centre coordinates. The RRLs properties of the north and south selections are summarised in the central part of Table 2.4. The difference in distance moduli between north and south selections is of about 0.2 mag and could indicate a 3D effect in which the north part of And XXVII is closer to us than the south part, but errors are still too large to draw any firm conclusions. We also checked whether possible zero point differences among the four CCDs of the LBC mosaic might cause the observed differences, by comparing the median apparent B and V magnitudes of objects in the blue ($-0.1 \leqslant B-V \leqslant 0.1$ mag, $24 \leqslant V \leqslant 26$ mag) and red ($1.6 \leqslant B-V \leqslant 1.9$ mag, $23 \leqslant V \leqslant 25$ mag) parts of the CMD. Differences among the 4 CCDs range from 0.001 to 0.03 mag in both the B and V passbands, hence cannot explain the difference observed between average apparent magnitudes of RRLs in the north and south RRLs subsamples. Similarly, we investigated whether differential reddening might cause the observed differences in $\langle V(RR)\rangle$, but as shown in column 6 of Table 2.4 reddening values are generally small and very similar among the various RRL subsamples. We computed also average reddenings from the RRLs contained in each of the four CCDs, separately, again obtaining very similar values: $< E(B-V) >_{C1} = 0.03\pm0.06$ mag, $< E(B-V) >_{C2} = 0.03\pm0.06$ mag, $< E(B-V) >_{C3} = 0.05\pm0.05$ mag and $< E(B-V) >_{C4} = 0.01\pm0.06$ mag. Therefore, we conclude that the magnitude differences are real and likely due to a

3D effect. We have plotted in Figure 2.37 the spatial distribution of all the 89 RRLs in the field of And XXVII. The colour bar reflects the mean apparent magnitude ($< V >$) of each RRL. Neglecting the reddening effects and assuming that differences in $< V >$ values are entirely due to a projection/distance effect, the RRLs distribution suggests that And XXVII's centre likely is in the SE overdensity and the galaxy is tilted with the north-west portion closer to us than the south-east part.

Among the three other M31 dSphs we have observed with the LBT, And XIX and And XXV do not show a large spread in the mean magnitude of the RRLs, while the larger spread of And XXI is justified by the presence in this galaxy of two populations of RRLs with different metallicity, as also suggested by the bi-modal period distribution of the RRab stars in that galaxy (see figure 2 in Cusano et al. 2015). The scatter in mean magnitude of the RRLs in the field of And XXVII is more than twice that observed in And XXI, but there is no evidence of bi-modality in the period distribution of the RRab stars (see Figure 2.27). We further tested whether different old stellar generations may be present in And XXVII by comparing the positions on the CMD of the different samples of RRLs listed in Table 2.4 with the model of Marconi et al. (2015) and the 13 Gyr isochrones of Marigo et al. (2017), adopting for reddening and distance the values obtained from the whole sample of RRLs in the field of And XXVII [$(m-M)_0$=24.55 $\pm$ 0.26 mag and $< E(B-V) >= 0.04 \pm 0.05$ mag]. This is shown in Figure 2.38, which in the left panel illustrates the comparison with two 13 Gyr isochrones with [Fe/H]=−1.5 and [Fe/H]=−1.8 dex, respectively and, in the right panel, the comparison with a 13 Gyr for [Fe/H]=−1.8 dex and two different values of the distance modulus. In this latter scenario both the RRLs and the RGB stars are well reproduced by the same 13 Gyr isochrone with [Fe/H] = −1.8 dex, shifted for distance moduli of $(m-M)_0$=24.46 mag and $(m-M)_0$=24.67 mag, that represent the extreme values reported in Table 2.4. We conclude that the case of a simple old stellar generation placed at different distances has to be preferred over the dual stellar population case, to explain the wide range in $\langle V(RR) \rangle$ as well as the large spread in spatial distribution of the RRLs in And XXVII. We thus conclude that either we are resolving the 3D structure of And XXVII in the final stage of its tidal disruption, or that we are sampling the RRLs in And XXVII along with those belonging to a background/foreground structure like, for instance, the M31 NW stream or the M31 halo.

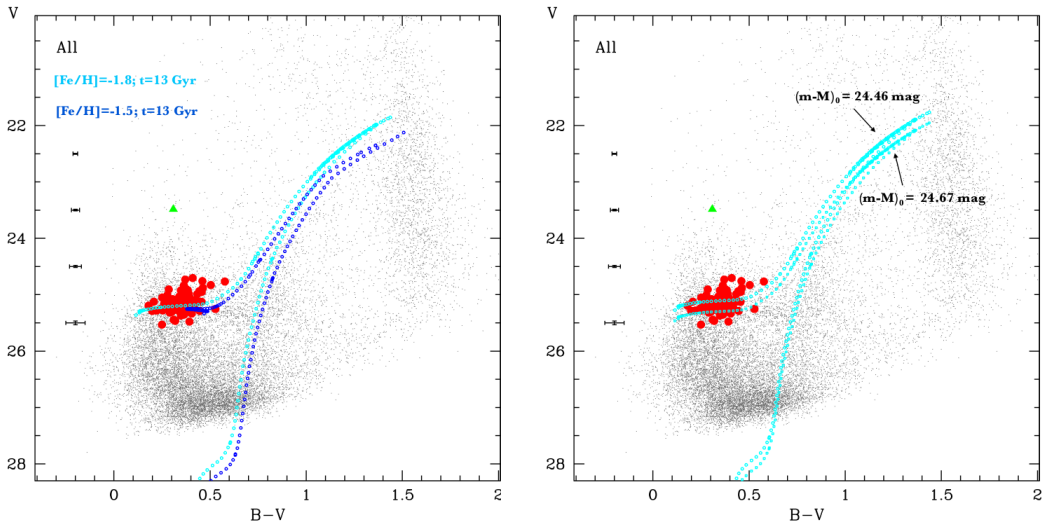

FIGURE 2.38: *Left panel*: Same as in Figure 2.30 with superimposed 13 Gyr isochrones from Marigo et al. (2017) with [Fe/H] = −1.8 dex (cyan line) and [Fe/H] =−1.5 dex (blue line), respectively. *Right panel*: Same as in the left panel, but with overplotted a 13 Gyr isochrone with [Fe/H] =−1.8 dex shifted for distance moduli of (m−M)=24.46 mag and (m−M)=24.67 mag, respectively. Figure from Cusano et al. (2017).

The M31 NW stream is a stellar debris detected by Richardson et al. (2011) in the PandAS map of metal-poor ([Fe/H]< −1.4 dex) RGB stars. It is an arc-shaped structure that extends for about 120 kpc from the centre of M31, crosses And XXVII and has seven GCs projected along its extension. Veljanoski et al. (2014) measured the radial velocity (RV) of these GCs and found for six of them a clear trend with projected distance from the M31 centre, their velocity becoming increasingly negative as the GCs approach the M31 centre. The six GCs are also physically associated to each other (with an average RV of -430 ± 30 km s^{-1}) and with the NW stellar stream. And XXVII, given its position along the stream, has a RV compatible with that found for the GCs, assuming a quasi-circular inclined orbit, where the direction of rotation goes from west to east for objects in the NW stream.

2.3.7 Comparison with other M31 satellites and conclusions

We have compared the pulsation properties of the RRL and AC populations in the 11 M31 dSphs studied for variability so far and have checked whether any correlations

exist with these M31 satellites being ON or OFF the GPoA discovered by Ibata et al. (2013) (see Sect. 1.3). The eleven M31 dSphs are listed in Table 2.5 along with their membership to the GPoA and the characteristics of their RRL and AC populations. Six of them are ON and five are OFF the GPoA.

TABLE 2.5: Properties of the variable stars in the Andromeda satellite galaxies

Name	N (RRab+RRc)	$\langle P_{ab} \rangle$ days	f_c	N (AC)	N (AC) confirmed*	ON-member	Reference
And I	72+26	0.57	0.26	1?	0	yes	(1)
And II	64+8	0.57	0.11	1	0	no	(2)
And III	39+12	0.66	0.23	5?	2	yes	(1)
And VI	91+20	0.59	0.18	6	4	no	(3)
And XI	10+5	0.62	0.33	0	0	yes	(4)
And XIII	12+5	0.66	0.30	0	0	yes	(4)
And XVI	3+6	0.64	0.33	0	0	no[1]	(5,6)
And XIX	23+8	0.62	0.26	8	8	no	(7)
And XXI	37+4	0.63	0.10	9	9	no	(8)
And XXV	46+11	0.60	0.21	2	1	yes	(9)
And XXVII	58+31	0.59	0.35	1	1	yes	(10)

* see Sections 2.2.5 and 2.3.4

[1] offset by 8 Kpc from the GPoA (Ibata et al. 2013)

(1) Pritzl et al. (2005); (2) Pritzl et al. (2004); (3) Pritzl et al. (2002);

(4) Yang & Sarajedini (2012), MNRAS, 419, 1362; (5) Mercurio et al. in preparation; (6) Monelli et al. (2016);

(7) Cusano et al. (2013); (8) Cusano et al. (2015);(9) Cusano et al. (2016); (10)Cusano et al. (2017)

Considering the number of ACs in the M31 dSphs (columns 5, 6 of Table 2.5) it seems that the ON-plane satellites host only a few or no ACs. There are 4 ACs in total in the 6 ON-plane satellites in Table 2.5 to compare with 21 ACs in the 5 OFF-plane systems. This would suggests that only OFF-plane satellites were able to retain enough gas to give rise to an intermediate-age stellar population and produce ACs. In this vein, recently, Kerp et al. (2016) detected an irregularly shaped HI cloud close to, but offset from the stellar body of And XIX and some HI emission displaced by half a degree from And XXI (Kerp, private communication). These evidence lend support to the possible presence of a 1-2 Gyr old stellar generation in And XIX and And XXI, and since both these dSphs are OFF the GPoA, maybe in the OFF-plane M31 satellites in general.

As for the RRLs, the average period of RRab stars for satellites ON and OFF the M31 GPoA is exactly the same, being $\langle P_{ab} \rangle = 0.60 \pm 0.07$ d and $\langle P_{ab} \rangle = 0.60 \pm 0.06$ d for ON and OFF dSphs, respectively. The fraction of RRc to the total number of RRLs is also similar, $f_c = 0.27$ and $f_c = 0.23$ for ON and OFF plane satellites, respectively. As shown

in the lower-right panel of Figure 2.27, both ON and OFF GPoA dSphs are compatible with an Oo-Int classification, but with a mild tendency towards the Oo-I type as the dSphs get closer to M31.

Figure 2.27 also shows similarities existing in the period-amplitude diagram between RRLs in the M31 halo and And XXVII. The fraction of RRc stars in And XXVII is unusually high, similarly to what was found by Brown et al. (2004), who in some fields of the M31 halo found a fraction of RRc stars of f_c=0.46, an average period for the RRab stars of $< P_{ab} >$=0.594 d and an average period for RRc of $< P_c >$=0.316 d, which are close to the values we derived for And XXVII (see Table 2.4). These similarities suggest 3 possible scenarios for And XXVII:

1 a fraction of the RRLs discovered in the field of And XXVII belong to the M31 halo and in particular to the NW stream. This would explain the spread in $\langle V(RR) \rangle$, hence in distance we observe among the RRLs;

2 And XXVII is not a dwarf galaxy but rather an overdensity in the NW stream (as claimed by Martin et al. 2016) that is largely composed by M31 halo stars;

3 And XXVII is the progenitor of the NW stream and part of the M31 halo. The high concentration of RRLs in the SE region of And XXVII, along with the possible connection with the GCs in the NW stream, seem to lend some support to this latter possibility.

On the other hand, as shown by Ibata et al. (2014), the M31 halo in the And XXVII neighbourhood is very complex with stellar streams running all around And XXVII. Aiming to address the nature of And XXVII and its possible connection with the NW stream, we recently obtained new B, V time series imaging (PI: F.Cusano) with the LBT, to study the variable stars and the resolved stellar populations in 5 fields along both the arc-path described by the NW stream and the M31 halo (Cusano, Garofalo et al. in prep).

Chapter 3

Gaia, the mission, the intermediate data releases and their validation using RR Lyrae stars

3.1 The *Gaia* mission

Gaia is a European Space Agency (ESA) cornerstone mission aimed at understanding how our Galaxy, the MW, formed and evolved to the present day.

Approved by the ESA's Science Programme Committee on 11-12 October 2000 and launched on 19 December 2013 from Europe's Spaceport in Kourou (French Guiana), after about a month cruise *Gaia* reached its operating orbit in the second Lagrangian point (L2[1]), where, after an initial commissioning phase formally completed on 18 July 2014, the spacecraft has been continuously scanning the sky while moving along a Lissajous orbit around L2. The *Gaia* mission is planned to operate for at least five years[2] and acquire astrometry (parallaxes, positions, proper motions) with microarcsec (μas) accuracy and multi-band optical spectrophotometry with millimag accuracy for more

[1] L2 is a point of gravitational equilibrium at about 1.5 million km from Earth away from Sun.

[2] ESA has already approved an extension of the mission for 18 months beyond the nominal five year duration and further extensions up to a total of 5 years are planned.

than one billion stars distributed over the whole sky ($\sim$ 40,000 deg^2) down to a limiting magnitude 20-21 mag. For a smaller sample (about 10^8) sources brighter than 16-17 mag *Gaia* is obtaining also spectroscopy (hence, radial velocities, rotation, chemistry) in the Calcium triplet region with the Radial Velocity Spectrometer (RVS).

Gaia builds on the heritage of its predecessor, the ESA astrometric mission *Hipparcos* (https://www.cosmos.esa.int/web/hipparcos and
http://www.esa.int/Our_Activities/Space_Science/Hipparcos_overview),
which measured parallaxes with milli-arcsecond accuracy for 117,955 objects, greatly advancing our knowledge of the MW structure and dynamics (Perryman 2009 and reference therein). *Gaia* is now superseding its predecessor by measuring each star's position and motion 200 times more accurately than *Hipparcos*, and producing 10,000 times more data than *Hipparcos*.

The main goal of *Gaia* is to chart the most complete three-dimensional spatial and the three-dimensional velocity distribution of stars and determine their astrophysical properties to understand the formation, structure, and past and future evolution of our Galaxy by near-simultaneously collecting astrometry, photometry and spectroscopy with an accuracy, sensitivity, dynamic range, and sky coverage which are practically impossible to achieve with ground-based facilities and photometric/spectroscopic surveys targeting the same scientific goal (see Gaia Collaboration et al. 2016b, for a comprehensive overview).

3.1.1 Spacecraft and payload

Gaia bases its astrometric measurements on the principles of scanning global space astrometry developed and successfully used by *Hipparcos* (see Perryman 2009). The telescopes used in both missions have a unique design of two mirrors (fields of view) separated by a large angle (of 106.5° for *Gaia*) and sharing a common focal plane, with which the sky is systematically scanned[3]. During its 5-year operational lifetime, *Gaia* spins continuously around its axis, with a constant speed of 60 arcsec s^{-1}. As a result, over a period of 6 hours, the two astrometric fields of view scan across all objects located along the great circle 'perpendicular' to the spin axis. As a result of the basic angle of 106.5° separating the astrometric fields of view on the sky, objects transit the second

[3]For details on the principles of scanning space astrometry see Lindegren & Bastian (2010).

field of view with a delay of 106.5 minutes compared to the first field. The satellite spinning slowly measures the crossing times of objects transiting its focal plane. These observation times represent the stellar positions relative to the instrument axes. The resulting astrometric catalogue is built up from a large number of such observation times, by an Astrometric Global Iterative Solution process (AGIS; e.g. Lindegren et al., 2012, 2016). *Gaia*'s spin axis does not point to a fixed direction in space (or on the sky) but is carefully controlled so as to precess slowly on the sky. As a result, the great circle that is mapped out by the two fields of view every 6 hours changes slowly with time, allowing repeated full sky coverage over the mission lifetime. Figure 3.1 shows the end-of-mission sky coverage of the *Gaia* astrometric and photometric instruments, in ecliptic (left panel) and galactic (right panel) coordinates. At the end of the 5 years nominal duration of the mission, each source will have on average 70 photometric measurements, over 200 observations for sources at |DEC|=45±10 deg and about 40 spectroscopic measurements.

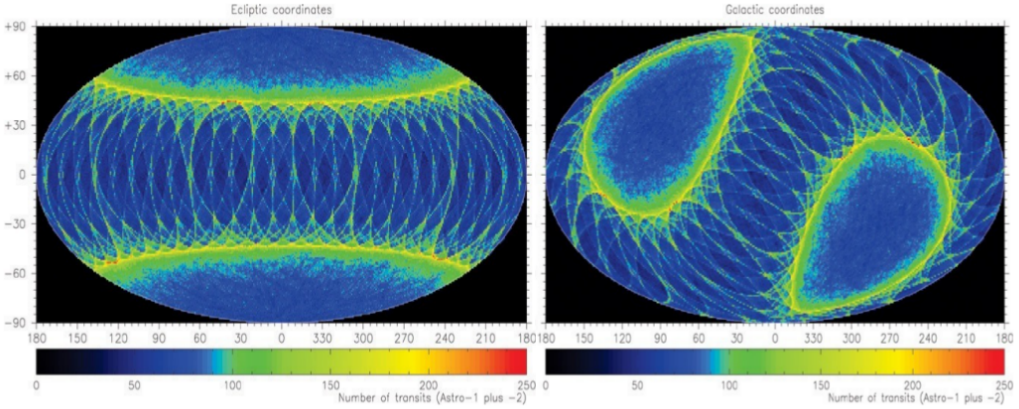

FIGURE 3.1: *Left panel* : End-of-mission sky coverage of the *Gaia* astrometric and photometric instruments, in ecliptic coordinates, in an equal-area Hammer–Aitoff projection. The colour wedge linearly spans the range from 0 (black) to 200 (red) focal-plane transits. The sky-average number of transits is 70. *Right panel* : Same as in the left panel but in galactic coordinates. Images from http://sci.esa.int/gaia.

The spacecraft itself can be basically divided into two sections: the service and the payload modules. The *service* module, generally referred to as 'the platform', contains the propulsion system and the communications units, the phased-array antenna, essential components that allow the spacecraft to function and return data to Earth as it rotates and moves on its orbit at the same time. The *payload* module consists of a single integrated instrument including two optical telescopes (aperture size $\sim 1.45 \times 0.5$ m)

with a focal length of 35 m, two fields of view, separated by a constant, large angle (the basic angle, Γ=106.5°) on the sky and merged into a common path at the exit pupil. The optical path of the two telescopes is composed of six reflectors[4] (M1-M6), the last two of which (M5-M6) are common to both telescopes. The telescope elements are built around an hexagonal optical bench with a diameter of $\sim$ 3 m, which provides the structural support. The top panel of Figure 3.2 shows a diagram of the payload optics on board of *Gaia*.

Besides the two telescopes, the payload is equipped with 3 instruments (an astrometer, a spectro-photometer and a spectrograph):

1 The astrometric instrument (ASTRO) comprises the two telescopes, and 62 CCDs in the focal plane, where the two fields of view are combined into the astrometric field (AF). In practice, stars entering the combined field of view first pass across the column of Sky Mapper (SM) CCDs (14 CCDs in total), where each object is detected. Then the information on an object's position and brightness are processed on board in real-time to define the windowed region around the object to be read out by the following CCDs. The accuracy of the measurements depends on the stellar type and relies on the stability of the basic angle between the two telescopes. This angle must be known with exquisite precision and accuracy, hence it is regularly monitored by the Basic Angle Monitoring (BAM) system, an interferometric device measuring short-term ($\lesssim$ 1 d) variations at μas precision.

2 The spectro-photometric instrument is based on two low dispersion optics (prisms) located in the common path of the two telescopes: one for the short wavelengths (BP; 320–680 nm) and one for the long wavelengths (RP; 640–1000 nm). Both photometers, BP and RP, have two dedicated CCD strips (of 7 CCDs each) that cover the full astrometric field of view ($\sim$320-1000 nm) in the across-scan direction.

3 The spectrograph, the Radial Velocity Spectrometer (RVS; shown in bottom panel of Figure 3.2) collects medium resolution (R$\sim$11,700) spectra over the wavelength range 845–872 nm (Cropper et al. 2018 and references therein). The RVS uses

[4]Since *Gaia* optics are based on mirrors only, hence are fully reflective, there are diffraction effects with residual aberrations that induce systematic chromatic shifts of the diffraction images and thus of the measured star positions. These effects are usually neglected in optical systems, but at the accuracies achieved by *Gaia* they are critical. These systematic chromatic displacements will be calibrated as part of the on-going data analysis using the colour information provided by the photometry of each observed object.

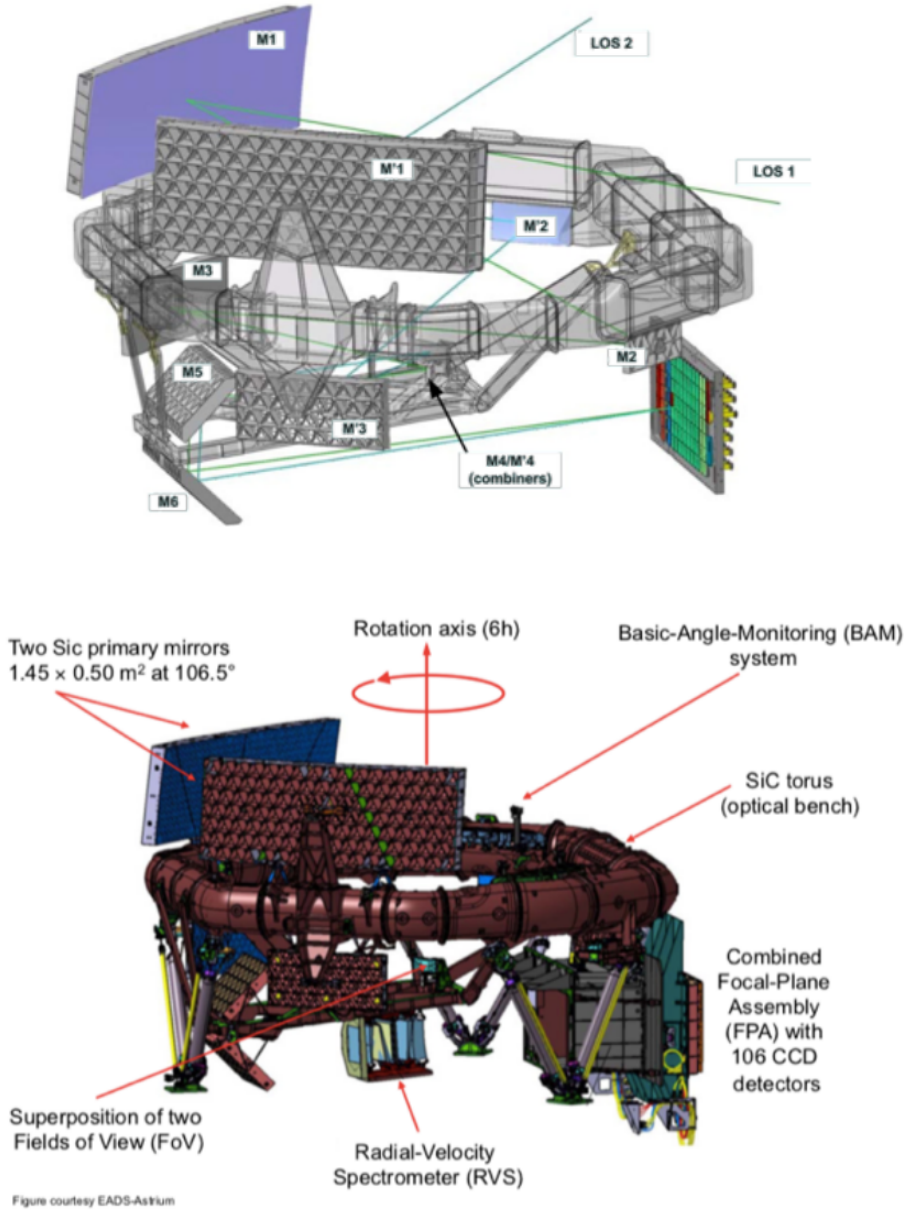

FIGURE 3.2: *Top panel:* Diagram of the telescope elements, the hexagonal optical bench with the mirror system and the focal plane. *Bottom panel:* Same as in the top panel but here all elements are covered by a Silicon Carbide (SiC) torus and are visible and labelled the RVS, the BAM system and the two fields of view. Images from http://sci.esa.int/gaia. Credit: EADS Astrium.

the SM for object detection and confirmation. Objects will be selected for RVS observation based on measurements made slightly earlier in the Red Photometer. The object's light, coming from the two viewing directions of the two telescopes, is superimposed on the 12 CCDs dedicated to the RVS.

The payload a single focal plane of 104.26 by 42.35 centimeters in size (see Figure 3.3) featuring a total of 106 CCDs that are used as detectors. Each CCD is 4500 by 1996 pixels in size with pixels that are 10 micrometers by 30 micrometers in size. The CCDs are arranged in 7 rows and 17 columns. This module is located inside a geometrical, dome-like structure called the thermal cover. Beneath the service and payload modules are the sun-shield and the solar array assembly.

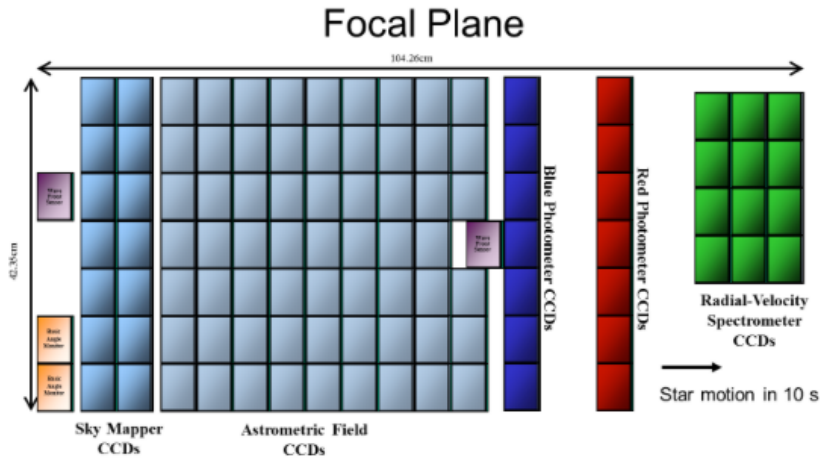

FIGURE 3.3: *Gaia* CCD array layout. Different colours indicate different functions of CCDs and sensors: purple and orange for the wave-front sensor (WFS) and BAM; CCDs of the SM and the AF, devoted to astrometric measurements are in cyan and light-cyan while the CCDs for the BP and RP are in blue and red respectively. Green for CCDs dedicated to the RVS. Image from http://sci.esa.int/gaia. Credit: ESA - A. Short.

There are three instrument functions:

- Astrometry: The astrometric instrument is dedicated to the accurate measurements of the relative positions of all objects that cross the fields of view of Gaia's two telescopes providing for each object five astrometric parameters: spatial position (α, δ), proper motion ($\mu_{\alpha*}$[5], μ_δ) and parallax (ϖ).

- Photometry: the photometer measures the spectral energy distribution (SED) of all the detected objects in the wavelength range covered by the CCDs ($\sim$ 320-1000

[5] $\mu_{\alpha*}=\mu_\alpha \times \cos\delta$

nm). From the SED measurements are derived different informations, such as an astrophysical classification (i.e., object type: star, quasar, etc.) and an astrophysical characterisation (i.e., interstellar absorption, surface gravity, metallicity, and effective temperature for stars, photometric redshift for quasars, etc.).

- Spectrometry: the primary objective of the RVS is the acquisition of radial velocities. These line-of-sight velocities complement the proper-motion measurements provided by the astrometric instrument. The RVS records 3 spectra per observation deriving one radial velocity per each observation.

A most significant distinction between *Gaia* and its precursor *Hipparcos* is, indeed, the presence of a spectrometer in the *Gaia* payload. The absence in *Hipparcos* of an instrument designed to measure stellar radial velocities was recognized as a deficiency at the time. This is the reason why the *Gaia* mission incorporated a spectrometer into its payload. The RVS allows to extend *Gaia* potential for the wide-ranging investigation of the MW structure and evolution.

The *Gaia* spacecraft is controlled from the European Space Operations Centre (ESOC, Darmstadt, Germany). Throughout the duration of the mission, *Gaia* generates a vast amount of raw data, which daily are sent, with a high data rate (up to 10 Mb/s), to one of the three ground stations (the 35 m deep-space stations): Cebreros in Spain, New Norcia in Australia and Malargüe in Argentina. The on-ground full processing of the data collected by *Gaia*, from telemetry to data releases, is the responsibility of the *Gaia* Data Processing and Analysis Consortium (DPAC), a mainly European team of more than 500 people (between scientists and software developers) from 20 European countries and ESA. DPAC members are charged with a large set of structured and interdependent data processing tasks going from the calibration of the instruments, the extraction of the astrophysical information up to the data releases. The consortium is formed by 9 coordination units (CUs): two units provide development support, CU1 for technical aspects, and CU2 through data simulations. Three units are responsible for the data processing, CU3 for the astrometric data, CU5 for the photometric data and CU6 for the spectroscopic data. Three units do basic data analysis on the processed data, CU4 for double stars, orbital binaries and solar system objects, CU7 for variable stars, and CU8 for spectral classification. Finally, CU9 takes care of the intermediate and final publication of the *Gaia* data. The activities of the CUs are coordinated through the

DPAC Executive (DPACE). *Gaia* data are made publically available worldwide without any limitations as soon as they have been fully processed and properly validated by DPAC as they are not covered by proprietary rights.

Release of the *Gaia* final catalogue of data collected over the 5 year nominal duration of the mission is foreseen after 2022. However, publication of preliminary data products is also anticipated through a number of intermediate data releases, the first of which (*Gaia* Data Release 1 - DR1) took place on 14 September 2016, the second (*Gaia* DR2) occurred on 25 April 2018 and a third one (*Gaia* DR3) is currently foreseen in the first half of 2021. Pending approvals of mission extensions further release(s) can be anticipated.

Gaia astrometric, photometric and spectroscopic performances vary according to the source magnitude and spectral type. For stars brighter than $G \leq 13$ mag parallaxes will be measured with standard errors less than 10 μas and from 30 up to 600 μas for stars from $G \sim 15$ to 20 mag respectively, while photometric standard errors are expected to remain within the milli-magnitudes. For sources with $G \sim$ 11-12 mag the standard errors of the RVS radial velocities will be of 1 kms^{-1} and 15 km^{-1} at $G \sim$ 15-16 mag, depending on the spectral type (Gaia Collaboration et al. 2016b). For the typical spectral type of RRLs (the full spectral range spanned by RRLs during the pulsation cycle varies from A8 to F7) standard errors of the integrated photometry are expected to be of 0.2 millimag (mmag) in G and 1 mmag in G_{BP} and G_{RP} at $G \sim 15$ mag, and 3.7, 56, and 48 mmag, respectively, at $G \sim 20$ mag. Astrometric standard errors are of $\sim$ 10 μas at $V \lesssim$ 12-13 mag, 24 μas at $V \sim 15$ mag and 540 μas at $V \sim 20$ mag. Radial velocity errors are below 1 kms^{-1} for $V < 12$ mag and below 15 kms^{-1} for $V <$15 mag (Clementini et al. 2018).

A summary of end-of-mission performances for sources of different magnitude and spectral type is available at: `https://www.cosmos.esa.int/web/gaia/science-performance/end-of-mission`. In the next sections we present a brief overview of the two *Gaia* intermediate data releases published so far. A complete summary of the contents of these two releases can be found in Gaia Collaboration et al. (2016a) and Gaia Collaboration et al. (2018a), respectively.

3.2 The *Gaia* first data release: DR1

The first catalogue of *Gaia* data was released on 14 September 2016 and contained positions and G-band photometry for more than one billion sources brighter than $G \sim 20.7$, astrometry (parallaxes) for about 2 million stars and G-band light curves and pulsation properties for slightly more than 3,000 Cepheids and RRLs, mainly located in the LMC (see https://www.cosmos.esa.int/web/gaia/dr1, for a detailed description of the DR1 content).

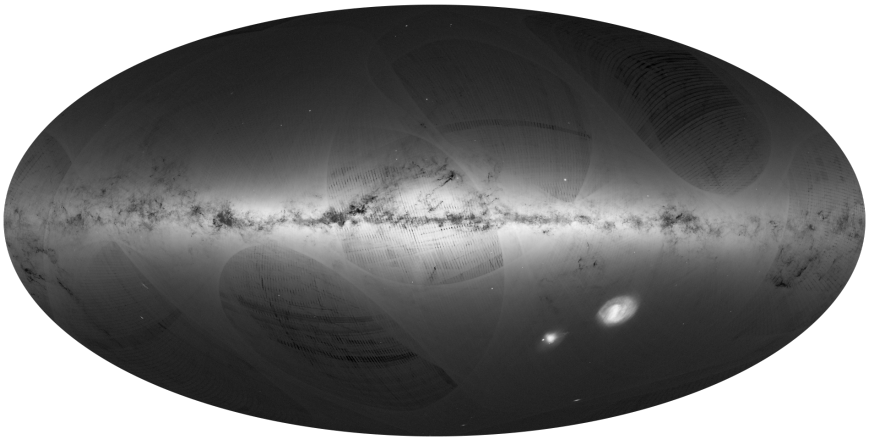

FIGURE 3.4: All-sky view of sources in the MW based on the first 14 months of *Gaia* observations, from July 2014 to September 2015. Brighter regions indicate denser concentrations of stars, while darker regions correspond to patches of the sky where few stars were observed. Copyright: ESA/Gaia/DPAC.

Gaia DR1 is based on observations collected in 14 months from 25 July 2014 and 16 September 2015. This time baseline was not sufficient to disentangle parallaxes from proper motions. In order to break this degeneracy, in *Gaia* DR1, a combined Tycho-*Gaia* Astrometric Solution (TGAS[6]) was solved for (Michalik et al. 2015), allowing to derive the 5 astrometric parameters (positions, parallax, proper motions) for 2 million stars in common with the *Hipparcos* (van Leeuwen 2007b) and Tycho-2 (Høg et al. 2000) catalogues.

The content of *Gaia* DR1 can be subdivided in the following three datasets:

[6]For a joint Tycho-Gaia Astrometric solution were adopted, as prior information, the positions of $\sim 114,000$ sources from the *Hipparcos* catalogue (van Leeuwen 2007b), and additional 2.36 million positions from the Tycho-2 catalogue (Høg et al. 2000). As explained by Lindegren et al. (2016), the parallaxes from the *Hipparcos* catalogue and the proper motions from the *Hipparcos* and Tycho-2 catalogues were not used. Therefore, the calculated parallaxes and proper motions in the primary solution are independent of the corresponding values in the earlier catalogues, which can therefore usefully be compared with the new results.

- The **astrometric** dataset, comprising primary and secondary subsets. The primary astrometric sample contains positions, parallaxes, and mean proper motions for 2,057,050 stars brighter than $V \sim 11.5$ mag, in common between the *Gaia* DR1, *Hipparcos* (93,635) and Tycho-2 (1,963,415; excluding *Hipparcos* stars) catalogues. This data set represents the realisation of the TGAS solution. The typical uncertainties for position and proper motions are ~ 0.3 mas and ~ 1 mas yr^{-1}, respectively. In this subset, for the 93,635 *Hipparcos* stars the uncertainty of the proper motions are smaller, around 0.06 mas yr^{-1} (for a statistical summary see table 1 in Lindegren et al. 2016). Lindegren et al. (2016) emphasised that these uncertainties are referred to random errors. Systematic error on the order of ± 0.3 mas (depending on position and colour of the sources) should be also added. This includes a possible global offset of the parallax zero point by ± 0.1 mas, and the colour-dependent systematics of ± 0.2 mas (see Appendix E of Lindegren et al. 2016). The secondary astrometric sample contains only positions for 1,140,622,719 sources for which the standard uncertainty of the positions is much larger (~ 10 mas)[7].

- The **photometric** data set contains mean *Gaia* G-band magnitudes for all the *Gaia* DR1 sources. These sources have magnitudes ranging from $G = 3.2$ to $G = 21$ mag (even if the nominal survey limiting magnitude is $G = 20.7$ mag). The typical uncertainty on the mean value of G ranges from 1 mmag for sources brighter than $G \leq 13$ mag, to about 0.03 mag at the survey limit. Processing and photometric validation of the *Gaia* DR1 photometry are fully described in Carrasco et al. (2016) and Evans et al. (2017).

- The **Cepheid and RRL** dataset contains G-band time series photometry and characterization by a specifically devoted CU7 pipeline (the SOS Cep&RRL pipeline, see Figure 3.5, Section 3.4 and Clementini et al. 2016) of 599 Cepheids (among which 43 newly discovered) and 2595 RRLs (343 new), mostly located within the LMC. These variable stars were observed at high cadence during the first 28 days of observation when the satellite was operated according to a special ecliptic pole scanning law.

[7]All the positions are given in a reference frame that is aligned with the International Celestial Reference Frame (ICRF) at epoch J2015.0 (being better than 0.1 mas for the primary dataset) and all proper motions are non-rotating with respect to ICRF to within 0.03 mas yr^{-1}.

One of the most impressive images of *Gaia* DR1 is the distribution on the sky of all sources released in DR1 (Figure 3.4). The high level of detail is noticeable in the dust features along the Galactic plane and the structures outlined by sources in the LMC and SMC. Also recognisable are tens of globular clusters, as well as two of the biggest MW dSphs: Fornax and Sculptor. M31 and M33 are faint, but still identifiable by *Gaia* observations of their brightest sources. However, a number of artefacts are also visible in Figure 3.4. The curved features and darker stripes have no astronomical reason but rather reflect *Gaia*'s scanning law. Since the figure is based on observations collected

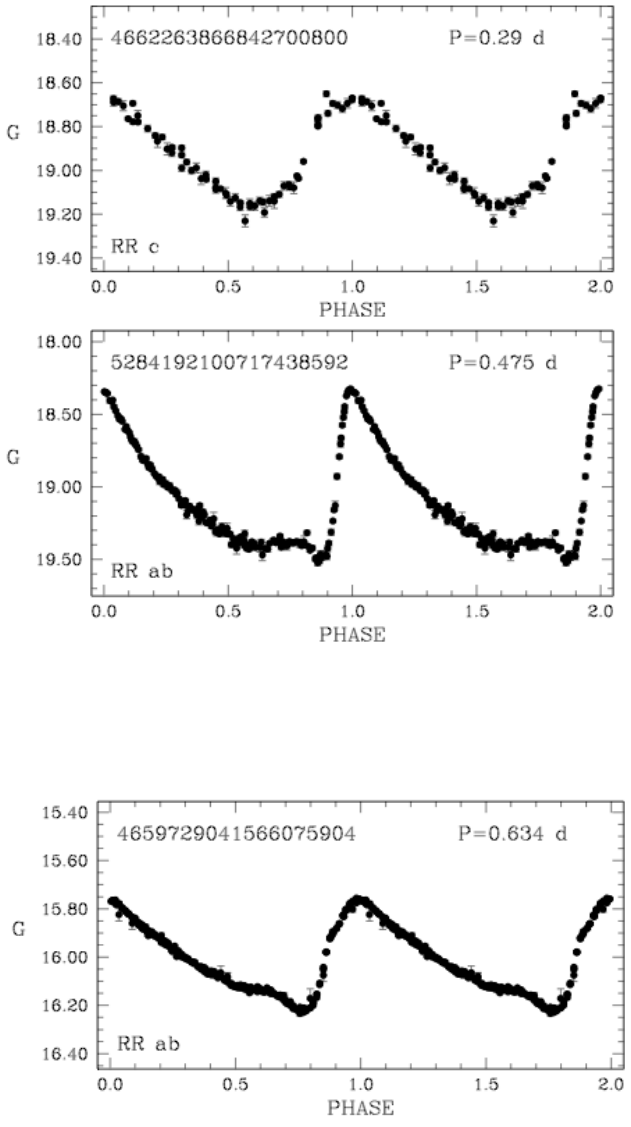

FIGURE 3.5: Examples of G-band light curves for RRLs published in *Gaia* DR1. An RRc and an RRab star in the LMC (*top and middle panels*) and an RRab star in the MW halo (*bottom panel*). The uncertainties on the individual measurements are ~ 0.02 mag at the magnitude level of the LMC RRLs. Figure from Clementini et al. (2016).

over the first 14 months of mission, the survey is not yet uniform across the sky. These artefacts will gradually disappear as more data are gathered during the five-year mission, as it is already shown by the significantly improved all-sky view of the MW published with *Gaia* DR2 (see Figure 3.6).

3.3 *Gaia* second data release: DR2

The *Gaia* second data release (hereafter DR2), on 25 April 2018, published results based on the first 22 months of mission. This baseline was long enough to separate parallax from proper motion effects, thus allowing to obtain a stand alone astrometric solution in which the 5 astrometric parameters are derived for sources down to $G \sim 20$ mag using only *Gaia* data (Lindegren et al. 2018).

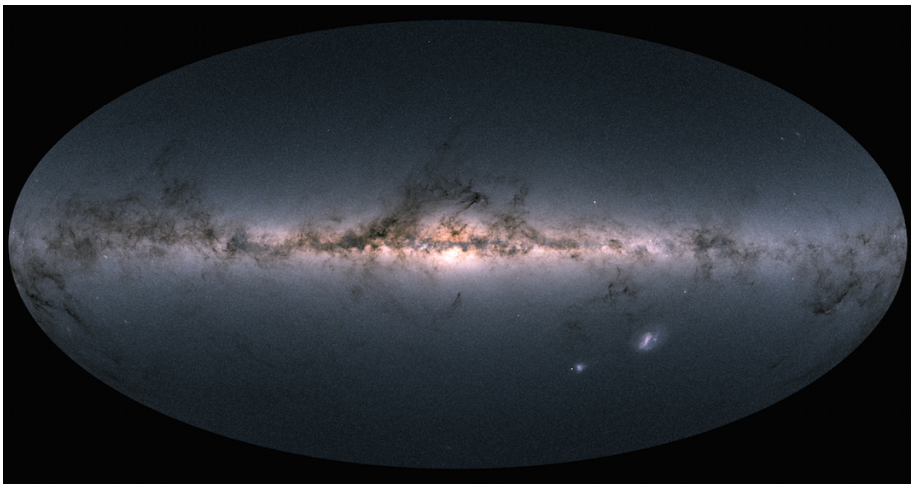

FIGURE 3.6: All-sky *Gaia* DR2 view in colour of the MW as inferred from data spanning 22 months of observations (between July 2014 to May 2016). The map combines the integrated fluxes as observed in the G_{BP}, G and G_{RP} passbands. Credits: ESA/-Gaia/DPAC.

The diversity of *Gaia* DR2 content is significantly enhanced with respect to *Gaia* DR1 by addition of data products (G, G_{BP}, G_{RP} photometry, mean radial velocities, identification and characterization of a much larger number of variable stars and first determinations of stellar parameters), improvement of the data processing and better instrumental calibrations, hence leading to reduced systematics and increased precisions for both astrometric and photometric data (Gaia Collaboration et al. 2018a). The number of stars with published G magnitudes increases from 1.1 billion of DR1 to more than 1.6 billion

in DR2 and colour information (G_{BP} and G_{RP} magnitudes) is added for 1.38 billions of them.

The *Gaia* DR2 content can be divided in six separate datasets (astrometric, photometric, radial velocity, variability, astrophysical parameter and Solar system object datasets) which are briefly described below:

- the DR2 **astrometric** dataset is split into two subsets of which the first one containing 1,331,909,727 sources for which all 5 astrometric parameters (positions, parallax, and proper motions) are released in DR2, and a second subset of 361,009,408 sources for which only positions are released. The 2 subsets are named *5-parameter* and *2-parameter* datasets, respectively, and described in detail in Gaia Collaboration et al. (2018a). The typical uncertainty of the DR2 parallaxes is of about 0.04 milliarcsecond (mas) for sources brighter than $G < 14$ mag, 0.1 mas at $G = 17$ mag, and 0.7 mas at $G = 20$ mag. In the proper motion components, uncertainties are of 0.05, 0.2, and 1.2 mas yr^{-1}, respectively[8]. The 2-parameter sources are typically fainter than the 5-parameter subset (50% of the sources with only for 2-parameter have $G \sim 20.6$ mag to compare with ~ 19.3 mag for sources in the 5-parameter subset) with very few observations, or of insufficient quality to fit the five-parameter astrometric model. All sources fainter than $G = 21$ mag have only positions (2-parameter solution) released in *Gaia* DR2. Processing and validation of the astrometric content of *Gaia* DR2 are fully described in Lindegren et al. (2018). Figure 3.7 shows the parallax uncertainties as a function of G magnitude for *Gaia* DR2 (red dots) and TGAS astrometric data set in *Gaia* DR1 (blue-yellow band) compared to the predicted 5-year *Gaia* mission parallax standard uncertainties (blue solid line). No matter the significant improvement of the DR2 parallaxes compared to DR1, the former are still based on very preliminary calibrations and only 22 months of observations which limit, in particular, the measurements of sources brighter than $G \sim 14$ mag. Indeed, in this magnitude

[8]In *Gaia* DR2 all positions and proper motions are given in the second realisation of the *Gaia* celestial reference frame (*Gaia*-CRF2) for which at the bright end ($G < 12$ mag) the alignment with the ICRF is better than 0.3 mas at epoch J2015.5 (barycentric coordinate time, TCB), while the reference frame is non-rotating to the ICRF within 0.15 mas yr^{-1}. At the faint end ($G \sim 19$ mag) alignment with the ICRF to about 0.02 mas and non-rotating with respect to the ICRF to within 0.02 mas yr^{-1}. The reference epoch, TCB=J2015.5 (TCB), chosen to minimize correlations between the position and proper motion parameters, is 0.5 yr later than the reference epoch for *Gaia* DR1, which must be taken into account when comparing the positions between the two releases (Gaia Collaboration et al. 2018a, Lindegren et al. 2018).

regime the DR2 parallaxes are still significantly more uncertain than expected at the end of the 5-year mission.

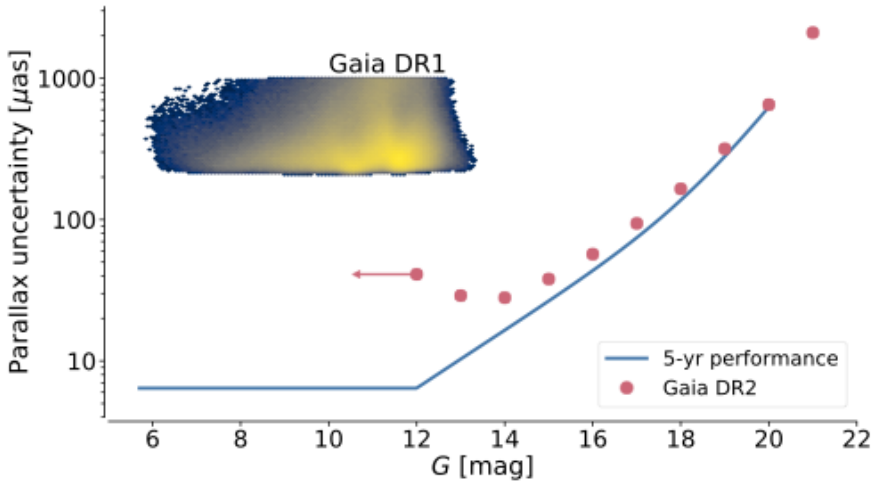

FIGURE 3.7: Parallax uncertainties as a function of G magnitude for *Gaia* DR2 (red dots) and TGAS astrometric data set in *Gaia* DR1 (blue-yellow band) compared to the predicted 5-year *Gaia* mission parallax standard uncertainties (solid blue line). The colour coding for *Gaia* DR1 parallax uncertainty distributions indicates increasing numbers of sources from blue to yellow colours. Figure from Gaia Collaboration et al. (2018a).

- the DR2 **photometric** dataset comprises *Gaia* G-band mean magnitudes for all DR2 released sources ($\sim$ 1.6 billions) and G_{BP}, G_{RP} mean values for about 1.38 billions (for 2 millions of them only the G_{RP} values are available). Processing and validation of the photometric content of *Gaia* DR2 are fully described in Riello et al. (2018) and Evans et al. (2018). For sources with G <13 mag the photometric uncertanties are of about 0.3 mmag in the G-band and 2 mmag for G_{BP} and G_{RP}, while for sources as faint as G ∼20 mag they are of 10 and 200 mmag for G and G_{BP}, G_{RP}, respectively. Each source in the data processing was classified as *Gold*, *Silver* or *Bronze*, the three different grades indicating the availability of colour information and a decreasing quality of the photometric calibration (from *Gold* to *Bronze*). In the released catalogue the numeric field labelled `phot_proc_mode` assumes values 0, 1 and 2 for *Gold*, *Silver* and *Bronze* sources, respectively. We also note that the DR2 colour information is significantly affected by systematic effects for sources towards the faint end of the survey ($G \sim 19$ mag) which are close to bright sources and in crowded regions of the sky.

- the DR2 **radial velocity** dataset consists of 7,224,631 median radial velocity measurements, averaged over the 22 months of the observations, for sources brighter than magnitude 12 in the G_{RVS} photometric band (the photometric narrow band obtained by integrating the flux over the RVS spectral range) and with effective temperatures (T_{eff}) in the range 3550-6900 K. The uncertainties of the radial velocities is of about 0.3 km s^{-1} for sources brighter than $G_{RVS} \sim 8$ mag and increases up to 1.86 km s^{-1} at $G_{RVS} = 11.75$ mag, whereas the systematics are lower than 0.1 km s^{-1} for sources with $G_{RVS} < 9$ mag and about 0.5 km s^{-1} at $G_{RVS} = 11.75$ mag.

- the **variability** dataset released in DR2 consists of 228,904 RRLs; 11,438 Cepheids; 151,761 long-period variables (LPVs); 147,535 stars with rotation modulation; 8,882 δ Scuti and SX Phoenicis stars and 3,018 short-timescale variables for a total of 550,737 sources (Holl et al. 2018), for which the G, G_{BP} and G_{RP}-band time-series photometry is also released. According to Holl et al. (2018) about 50% of the 550,737 sources are new variables identified by *Gaia*. Specific processing and analysis of the different types of variables released in DR2 is described in dedicated papers which are listed in Holl et al. (2018). The variability analysis carried out for DR2 mainly focused on large-amplitude variables and rotation modulated stars. Further classes will be added in next data releases and, specifically, MS variables will be added in *Gaia* data release 3 (DR3).

- the DR2 **astrophysical parameter** dataset consists of measurements of T_{eff}, extinction A_G, reddening E(G_{BP}-G_{RP}), radius, and luminosity for stars brighter than $G = 17$ mag. T_{eff} values are inferred from *Gaia* DR2 photometric bands for 161 millions source, A_G and E(G_{BP}-G_{RP}) values for 88 millions, luminosity and radius for 77 million sources. Details of the astrophysical parameter processing, its assumptions and limitations and the validation of the results are presented in Andrae et al. (2018).

- the DR2 **Solar system objects** (SSOs) dataset contains 14,099 among asteroids, Jupiter trojans and trans-Neptunian objects for which astrometry is provided with uncertainties ranging from 2-5 mas for the faintest asteroids ($G \sim 20.5$ mag) and up to <1 mas for objects brighter than $G \sim 17.5$ mag. G-band photometry is released only for a fraction of the observations (about 52% of the transits). Such

measurements should be considered as preliminary and will be refined in next data releases. The SSO positions measured by *Gaia* are used to determine the SSO orbits as described in Gaia Collaboration et al. (2018b).

The complete list of products (along with their related uncertainties) released in *Gaia* DR2 is summarised in table 3 of Gaia Collaboration et al. (2018a) and fully described in the *Gaia* Website[9].

Figure 3.6 shows the sky distribution of all sources published in *Gaia* DR2 and represents the most detailed all-sky map in the optical to date. When compared to Fig. 3.4 (the black and white sky map produced from the *Gaia* DR1 data), the reduction of artefacts thanks to the increased survey completeness is striking. Nonetheless, there are still sky regions not complete with clear imprints from the scanning law. The DR2 colour view of the MW is obtained by combining the integrated fluxes in the G_{RP}, G and G_{BP} bands where the fluxes in these bands are encoded in the red, green and blue channel, respectively. In 2016, during the my first year of PhD, I have become an active member of Coordination Unit 7 (CU7; variability) of the *Gaia* DPAC. Since then I have been involved in the development and validation of the SOS Cep&RRL pipeline (Clementini et al. 2016, 2018) devoted to the specific classification and full characterisation of Cepheids and RRLs observed by *Gaia*. In the following sections and in Chapter 4 I will describe my *Gaia*-related activities for the validation and exploitation of RRLs released in *Gaia* DR1 and 2.

3.4 CU7 and the SOS Cep&RRL pipeline

CU7 is the coordination unit of the *Gaia* DPAC tasked with the identification, processing and full characterisation of variable sources observed by *Gaia*. Eyer et al. (2017) describes methods, tools, and different steps of the CU7 general pipeline devoted to the identification and initial classification of variable sources. Per each main variability type identified by the CU7 general variability pipeline, validation and additional processing is carried out by a number of different pipelines, named Specific Object Study (SOS) pipelines, each specifically tailored for the analysis of a particular variability type. The pipeline that performs this task for Cepheids and RRLs is named SOS Cep&RRL. The

[9] https://www.cosmos.esa.int/web/gaia/science-performance

goal of the SOS Cep&RRL processing is twofold: firstly it validates the pre-classification as Cepheids and RRLs of the CU7 general variability pipeline and, secondly, it computes specific parameters for the confirmed Cepheids and RRLs. To this end, the SOS Cep&RRL pipeline performs a detailed analysis of all objects *pre-classified* as Cepheid and RRL candidates by previous steps of the general CU7 variability analysis chain. Specifically, it re-determines the period(s) (and period-ratios, for multi-periodic RRLs and Cepheids) of each Cepheid or RRL star candidate using the Lomb-Scargle algorithm, models its light curve using a truncated Fourier series, and refines the period using a non-linear fitting algorithm. It then identifies pulsation mode and classification in type (and sub-types) of such variables based on the period(s), light curve characteristics (as described by the parameters of the light curve Fourier decomposition) and the position with respect to PL and PW relations in the case of Cepheids, and the period-amplitude diagram in the case of RRLs. In this process, the SOS Cep&RRL pipeline can either confirm the initial classification or change it from RRL star to Cepheid (or vice-versa), or fully reject sources. Confirmed RRLs are sub-classified into RRab, RRc and RRd types, and confirmed Cepheids into CCs, ACs and T2Cs, and the latter further subdivided into W Virginis, BL Herculis and RV Tauri types.

As described in Sect. 3.2, *Gaia* DR1 published G-band time series photometry and pulsation characteristics computed by the CU7 SOS Cep&RRL pipeline for a total of 3,194 sources (599 Cepheids and 2,595 RRLs). This sample is distributed over an area which extends 38 degrees on either side from a point, offset from the centre of the LMC by about 3 degrees to the north and 4 degrees to the east. Whilst the majority of these sources are located within the LMC, 63 bright RRLs belong to the MW halo, and 24 of them are new discoveries by *Gaia*. For all the confirmed RRLs the SOS Cep&RRL pipeline provided the following pulsation quantities (along with their relative uncertainties): pulsation period, intensity-averaged mean G magnitude, epoch of maximum light, Fourier parameters ϕ_{21} and R_{21} and peak-to-peak G-band amplitude [Amp(G)]; as well as the sub-classification in RRab and RRc types for the RRLs, and in classical and Type II for the Cepheids.

For DR2, in addition to the classifier of the general variability pipeline used in DR1 (Eyer et al. 2017), a semi-supervised classification approach was devised to identify all-sky high-amplitude variables even when a few observations were available (typically less than 12 data-points), thus improving the completeness of the published variability results.

This approach is described in Rimoldini et al. (2018). The number of variable stars published in DR2 is, approximately, two orders of magnitude larger than published in DR1 (see Holl et al. 2018). In particular, *Gaia* DR2 contains a total of 150,359 RRLs and Cepheids (140,784 RRLs and 9,575 Cepheids) confirmed by the SOS Cep&RRL pipeline. These sources are distributed all over the sky. Among them 50,570 (350 Cepheids and 50,220 RRLs) likely are new discoveries by *Gaia*. In addition to position and G, G_{BP}, G_{RP} time series photometry, for all these sources *Gaia* DR2 published pulsation periods, intensity-averaged mean G, G_{BP}, G_{RP} magnitudes, epochs of maximum light in the 3 *Gaia* passbands, ϕ_{21}, R_{21}, ϕ_{31} and R_{31} Fourier parameters and peak-to-peak amplitudes [Amp(G), Amp(G_{BP}), Amp(G_{RP})] computed by the SOS Cep&RRL pipeline, along with an estimate of the interstellar absorption for 54,272 of the RRab stars, from the light and colour curves (adopting the Piersimoni et al. 2002's relation once amplitudes and colours are transformed from the Johnson to the *Gaia* passbands[10]), and photometric metallicities, from the Fourier parameters of the light curve, for 64,932 RRLs and 3,738 fundamental-mode CCs with P$<$ 6.3 d (Clementini et al. 2018).

3.5 Validation of *Gaia* DR1: testing ϖ_{TGAS} with RR Lyrae stars and Cepheids

During the first year of my PhD as part of my *Gaia* CU7-related activities, I collected literature data (mean magnitudes, metal abundances, reddening values, pulsation properties, multiplicity, etc.) for a total of more than 700 among RRLs and Classical and Type II Cepheids, for which TGAS parallaxes were published in *Gaia* DR1. These data along with the TGAS astrometry were used to construct PL, PW and optical LZ relations for Cepheids and RRLs in order to test the TGAS parallax measurements.

Results from this study are described in the following sections and have been published in the paper:

"Gaia Data Release 1, Validating the parallaxes with local Cepheids and RR Lyrae stars", by Gaia Collaboration, G. Clementini, L. Eyer, V. Ripepi, M.Marconi, T. Muraveva, A. Garofalo, et al. (+ 576 co-authors) 2017, A&A, 605, A79.

[10]See sect. 2.1.2 of Clementini et al. (2018)

3.5.1 Data sample

Gaia DR1 parallaxes were computed as part of the Tycho-Gaia Astrometric Solution (TGAS) for sources in common between *Gaia* and *Hipparcos* and Tycho-2 catalogues. In order to build the largest possible samples, since TGAS parallaxes are available for sources observed by Tycho-2 (Høg et al. 2000) only a fraction of which are also in the *Hipparcos* catalogue (ESA 1997; van Leeuwen 2007a), we used the list of RRLs and Cepheids in the Tycho-2 catalogue as reference.

For RRLs, we cross-identified the Tycho-2 catalogue with the General Catalogue of Variable Stars (GCVS database; Samus' et al. 2017) which includes information on 7,954 RRLs (labelled as RR, RR(B), RR:, RRA, RRAB, RRAB:, RRC, RRC:, where ":" means uncertain classification) and found 421 sources in common. Three sources (S Eri, V2121 Cyg, and NZ Peg) have uncertain classification according to the SIMBAD astronomical database (Wenger et al. 2000) and were removed. We then cross-matched the remaining 418 sources against sources in the `tgas_source` table of the *Gaia* Archive[11] and found a TGAS parallax for 364 of them. Their G-band apparent magnitudes are in the range $7.03 \leq G \leq 13.56$ mag and six of them have a negative TGAS parallax value.[12]

For Cepheids we considered the GCVS, which contains a total of 1,100 Cepheids, and the David Dunlap Observatory Database of Galactic CCs (DDO1; Fernie et al. 1995), which contains over 500 CCs. In particular, according to the variability types in the GCVS under the definition of CCs in these selections we included the following types: Cepheids and Classical Cepheids or Delta Cephei-type variables [CEP, CEP(B), DCEP, DCEPS, and DCEPS(B), as labelled in the GCVS]. Then we included under Type II Cepheids (T2Cs), the following types: CW, CWA, CWB, RV, RVA and RVB. Cross-matching these databases with the Tycho-2 general catalogue (2.5 billion sources) and following supplements (18 thousand sources) we found final samples of 421 (388 Classical and 33 Type II Cepheids). We then queried the `tgas_source` table in the *Gaia* Archive to retrieve TGAS parallaxes and *Gaia* G-band apparent magnitudes for these Cepheid samples. TGAS parallaxes are available for 331 CCs and 33 T2Cs. For the CCs they

[11] http://archives.esac.esa.int/gaia

[12] A simplified description about how *Gaia* parallaxes are measured is given in Luri et al. (2018). A simple demonstration of how some sources have negative parallaxes can be found in the online tutorials accompanying this paper.

span G-band apparent magnitudes in the range $4.68 \leq G \leq 12.54$ mag and, for 29 sources the TGAS parallax is negative. Among the 33 T2Cs, only 31 have G magnitudes and TGAS parallaxes available. They span G-band apparent magnitudes in the range $6.89 \leq G \leq 12.10$ mag.

To summarise, our final samples include 364 RRLs, 331 CCs and 31 T2Cs, in common between the *Gaia*, *Hipparcos* and Tycho-2 catalogues. The error distributions of the TGAS parallaxes for these 364 RRLs, 331 CCs and 31 T2Cs are shown in Fig. 3.8: upper, middle and bottom panels, respectively. Errors range from 0.2 to about 1 mas and peak around ∼0.25 mas for all 3 types[13].

Fig. 3.9 shows the distribution on the sky of the 364 RRLs, 331 CCs and 31 T2Cs considered in this work. Pink filled circles mark the CCs that, as expected, are mainly concentrated in the MW disc. Cyan filled circles and green filled triangles indicate RRLs and the T2Cs, respectively; they are distributed all over the MW halo.

3.5.2 Comparison with previous parallax measurements

In order to assess qualitatively the goodness of the TGAS parallaxes for RRLs and Cepheids we compared them with the parallaxes measured for these sources by *Hipparcos* (188 RRLs, 248 classical and 31 Type II Cepheids) and the HST (5 RRLs, 3 CCs and 1 T2C).

3.5.2.1 TGAS versus Hipparcos parallaxes

The upper panel of Figure 3.10 shows the comparison of the TGAS versus *Hipparcos* parallaxes for the RRLs. Black filled circles mark the whole sample. Red filled circles are RRLs with (σ_{ϖ}) *Hipparcos* < 0.70 mas, while cyan filled circles are the few RRLs with (σ_{ϖ}/ϖ) *Hipparcos* < 0.20. Of the 188 RRLs with both *Hipparcos* and TGAS parallax, 59 have a negative *Hipparcos* parallax (31% of the sample) compared with only 2 still having a negative parallax (1%) in TGAS. CH Aql, that we have labelled in the panel, is the source with the largest discrepancy between *Hipparcos* and TGAS among the RRLs with positive parallax values. The bottom panels of Fig. 3.10 show the same test,

[13] After publication of the *Gaia* DR1 catalogue, different authors have suggested that the standard errors of the TGAS parallaxes may be overestimated (e.g. Casertano et al. 2017; Feast 2017).

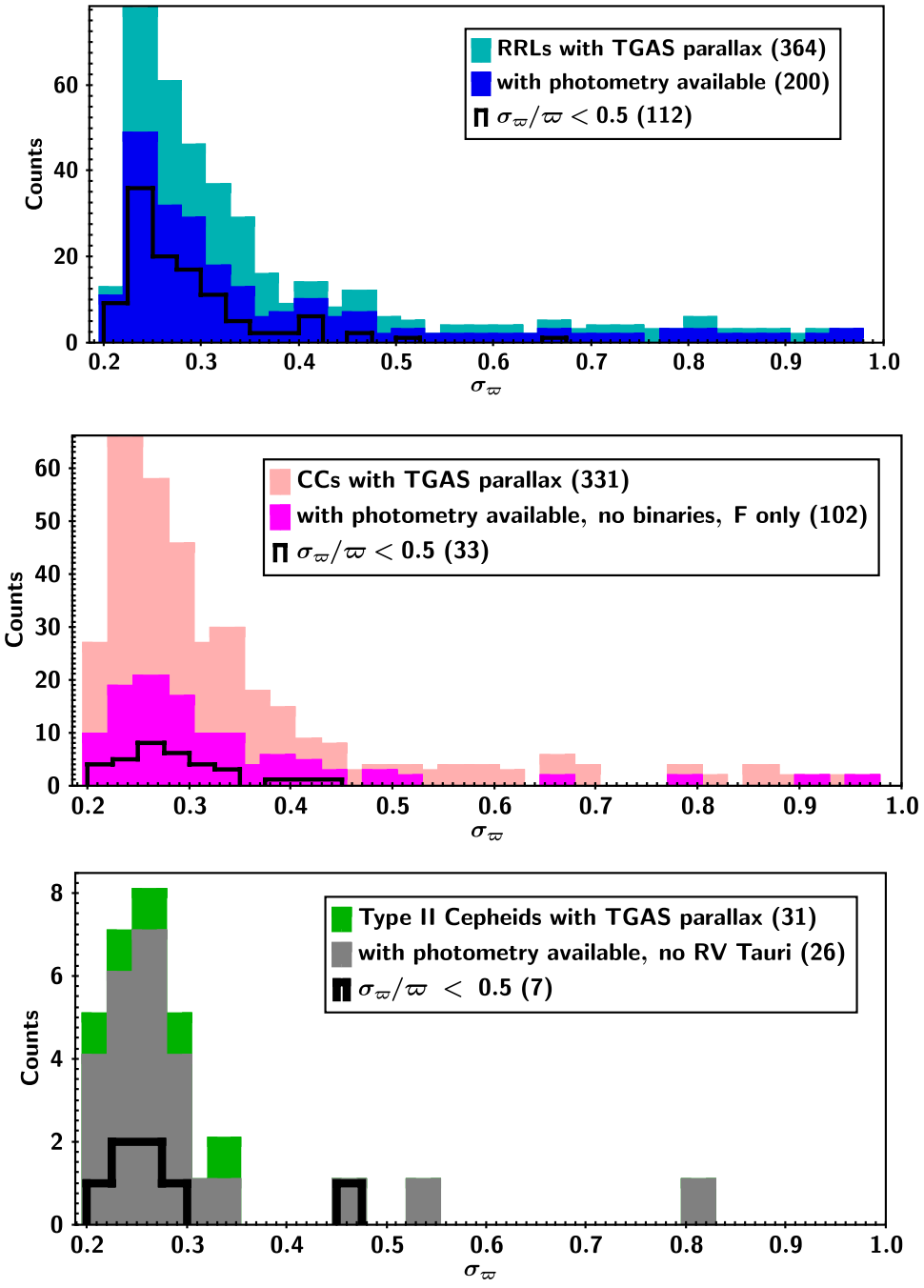

FIGURE 3.8: *Upper panel*: Error distributions of ϖ_{TGAS} for RRLs. The cyan histogram corresponds to the sample of 364 RRLs in the TGAS catalogue, the blue histogram shows a subsample of 200 stars with (V, K_S , W_1) photometry available in the literature. The black contour shows a subsample of 112 stars, among the previous 200 sources, for which $\sigma_\varpi/\varpi < 0.5$. *Middle panel*: Error distributions of ϖ_{TGAS} for CCs. The pink histogram corresponds to the sample of 331 Galactic CCs in the TGAS catalogue, the magenta histogram shows a subsample of 102 fundamental mode CCs with (V, I, J, K_S) photometry available in the literature after removing the known binaries. The black contour shows a subsample of 33 stars, among the previous sample of 102 sources, for which $\sigma_\varpi/\varpi < 0.5$. *Bottom panel*: Error distribution of ϖ_{TGAS} for T2Cs: whole sample (31 stars, green), subsample with (J and K_S) photometry and removing variables of RV Tauri type (26 stars, grey), subsample of the previous 26 sources retaining only stars with positive parallax and parallax errors $\sigma_\varpi < 0.5$ (7 stars, black contour). The bin size is 0.025 mas. Figure from Gaia Collaboration et al. (2017).

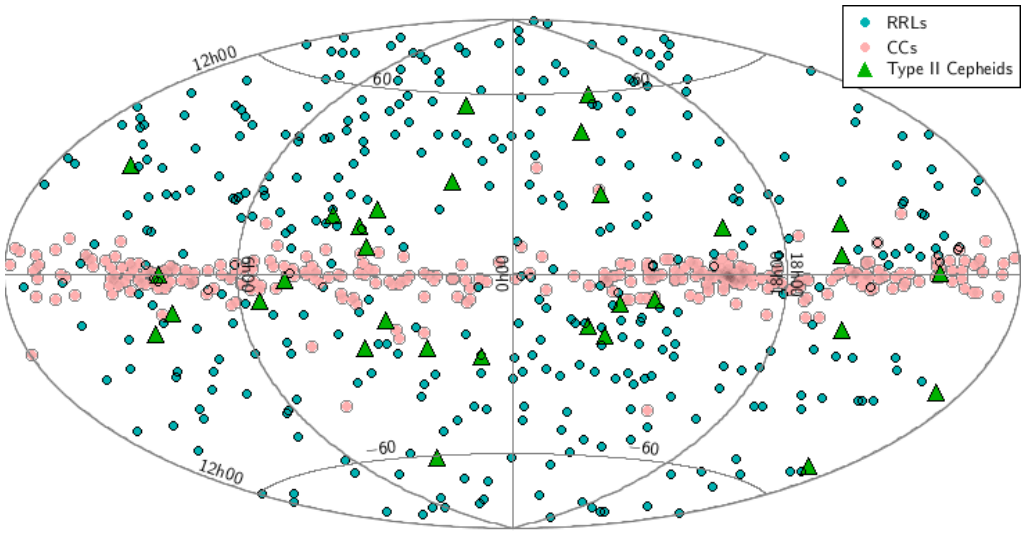

FIGURE 3.9: Sky distribution, in Galactic coordinates, of the 364 RRLs (cyan filled circles), 331 CCs (pink filled circles) and 31 T2Cs (green filled triangles) used in this study, adopting an Aitoff projection of the full sky. Adapted from Gaia Collaboration et al. (2017).

but for CCs and T2Cs, in the left and right panels, respectively. In the bottom-left panel, we have labelled the two CCs, RW Cam and SY Nor, for which a significant discrepancy exists between *Hipparcos* and TGAS parallax values. Both stars are known to have very bright close-by companions (Evans 1994; Fernie 2000). We also do not plot the three sources with the largest differences, namely V1477 Aql, UX Per, and AQ Pup. The TGAS-*Hipparcos* comparison for CCs shows comforting results; the number of negative parallaxes has reduced from 32% in *Hipparcos* to only 4% in TGAS: of the 248 CCs, 79 have a negative *Hipparcos* parallax compared with only 5 of them still having negative parallax and an additional 6 stars for a total of 11 sources in TGAS. This is not surprising, since the fraction of negative parallaxes is expected to decrease when uncertainties get smaller. We have created different subsamples based on absolute and relative errors of the *Hipparcos* parallaxes in order to highlight the samples with the most reliable parallaxes. Marked with cyan filled circles are 2 CCs with (σ_{ϖ}/ϖ) *Hipparcos* < 0.20; they are V2081 Cyg and PR Peg. Red and magenta filled circles highlight stars with (σ_{ϖ}) *Hipparcos* < 0.50 and 0.30 mas, respectively. Increasing agreement between the TGAS and *Hipparcos* results is found if we consider only sources with precise *Hipparcos* values, suggesting that more precise *Hipparcos* measures correspond to more precise TGAS measures. In the bottom-right panel, T2Cs with (σ_{ϖ}) *Hipparcos*

< 0.50 are indicated by red filled circles. Of the 31 T2Cs with both *Hipparcos* and TGAS parallaxes, 13 had a negative *Hipparcos* parallax (42% of the sample) compared with only 4 still having negative parallax and an additional 1 for a total of 5 sources (16%) in TGAS. MZ Cyg is the source with the largest discrepancy between *Hipparcos* and TGAS among the T2Cs with a positive parallax value. From these first global comparisons the improvement of *Gaia* with respect to *Hipparcos* is straighforward and is even more so for the Population II standard candles, that is for RRLs and T2Cs.

3.5.2.2 TGAS versus HST parallaxes

So far the most accurate astrometric parallaxes available in the literature are those measured with the HST. Five RRLs in our sample have an HST parallax measured by Benedict et al. (2011). The comparison between *Hipparcos*, TGAS, and Benedict et al. (2011) for these five variables is summarised in the upper portion of Table 3.1 and graphically shown in Fig. 3.11 (upper panels) for *Hipparcos* versus HST (upper sub-panel), TGAS versus *Hipparcos* (middle sub-panel) and TGAS versus HST (lower sub-panel). Errors on the *Hipparcos* parallaxes are much larger than those on the HST and TGAS measurements and, except for RR Lyrae itself, the *Hipparcos* parallaxes differ significantly from the HST values, whereas the TGAS and HST parallaxes agree within 1σ for RR Lyr, SU Dra, UV Oct, and XZ Cyg. On the other hand, the 1σ agreement of the *Hipparcos*, TGAS, and HST parallax values for RR Lyrae itself is particularly satisfactory, also in light of the much reduced error in the TGAS value: 0.23 mas compared with 0.64 mas in *Hipparcos*. For the remaining star, RZ Cep, Benedict et al. (2011) provide two different parallax values, 2.12 and 2.54 mas (Neeley et al., 2015). We show both values in Fig. 3.11. Although the Benedict et al. (2011) preferred value for this star is 2.12 mas (corresponding to the grey filled circle in the upper panel of Fig. 3.11), the alternative value of 2.54 mas is in much better agreement with the TGAS parallax of RZ Cep and nicely places the star on the bisector of the HST and TGAS parallaxes. To conclude, as also for CCs (bottom-left panel of the same figure), the best agreement is found between the TGAS and the HST parallaxes, confirming once again the higher reliability of the TGAS parallaxes and the improvement with respect to *Hipparcos*.

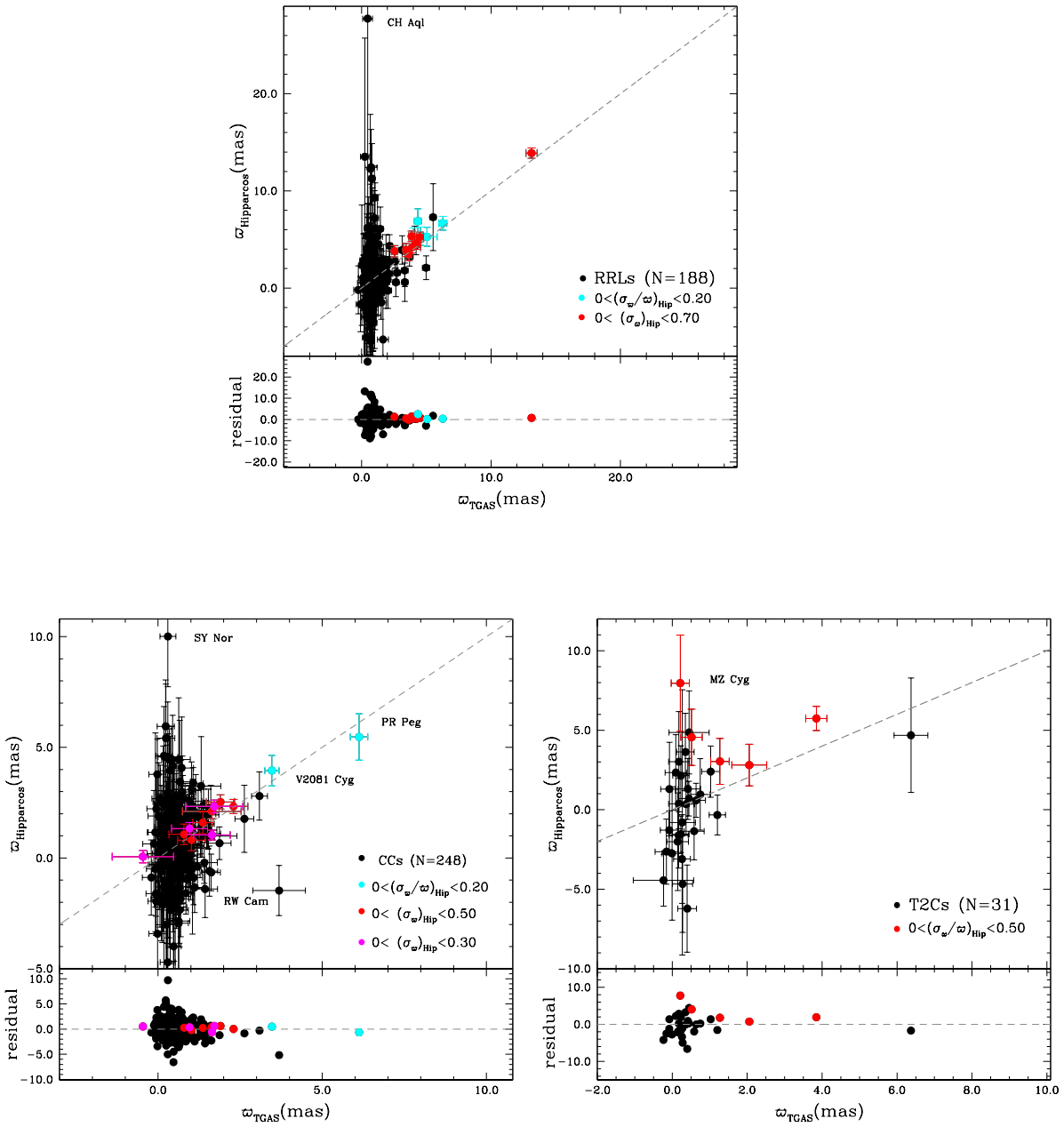

FIGURE 3.10: *Upper panel*: Comparison between *Hipparcos* and TGAS parallaxes for a sample of 188 RRLs (black filled circles) which have both measurements. Cyan filled circles mark sources with $(\sigma_\varpi/\varpi)Hipparcos < 0.20$. Red filled circles are RRLs with $(\sigma_\varpi)Hipparcos < 0.70$ mas. *Bottom-left panel*: Comparison between *Hipparcos* and TGAS parallaxes for a sample of 248 CCs which have both measurements. Red and magenta filled circles represent stars with $(\sigma_\varpi)Hipparcos < 0.50$ and 0.30 mas, respectively; cyan filled circles are two stars with $(\sigma_\varpi/\varpi)Hipparcos < 0.20$, namely V2081 Cyg and PR Peg. *Bottom-right panel*: Comparison between *Hipparcos* and TGAS parallaxes for a sample of 31 T2Cs which have both measurements. Red filled circles represent stars with $(\sigma_\varpi/\varpi)Hipparcos < 0.50$. Dashed lines show the bisector. Residuals, shown in the lower portion of each panel, are TGAS$-$*Hipparcos* parallax values. Figure from Gaia Collaboration et al. (2017).

TABLE 3.1: Comparison between *Hipparcos*, TGAS and HST parallaxes

Name	$ID_{Hipparcos}$*	$\varpi_{Hipparcos}$ (mas)	$\sigma\varpi_{Hipparcos}$ (mas)	ϖ_{TGAS} (mas)	$\sigma\varpi_{TGAS}$ (mas)	ϖ_{HST} (mas)	$\sigma\varpi_{HST}$ (mas)	HST Ref.
RRLs								
RR Lyr	95497	3.46	±0.64	3.64	±0.23	3.77	±0.13	B11
RZ Cep	111839	0.59	±1.48	2.65	±0.24	2.12 (2.54)***	±0.16	B11
SU Dra	56734	0.20	±1.13	1.43	±0.29	1.42	±0.16	B11
UV Oct	80990	2.44	±0.81	2.02	±0.22	1.71	±0.10	B11
XZ Cyg	96112	2.29	±0.84	1.56	±0.23	1.67	±0.17	B11
CCs								
FF Aql**	93124	2.110	± 0.330	1.640	±0.89	2.810	±0.180	B7
SS CMa	36088	0.400	±1.780	0.686	±0.234	0.348	±0.038	C16
SY Aur	24281	-1.840	±1.720	0.687	±0.255	0.428	±0.054	R14
T2Cs								
VY Pyx	434736	5.00	± 0.44	3.85	± 0.28	6.44	± 0.23	B7

Notes.C16=Casertano et al. (2016); R14=Riess et al. (2014); B7=Benedict et al. (2007); B11=Benedict et al. (2011)

* van Leeuwen (2007b)

**Gallenne et al. (2012) have estimated the distance to FF Aql via the interferometric Baade-Wesselink technique; the corresponding parallax is 2.755±0.554 mas.

*** Two different parallax values are provided for this star by Benedict et al. (2011); in the table we list both values.

A direct comparison of TGAS versus HST is possible for three CCs in our sample – FF Aquilae (FF Aql), SY Aurigae (SY Aur), and SS Canis Majoris (SS CMa) – their parallaxes were measured with HST by Benedict et al. (2007), Riess et al. (2014), and Casertano et al. (2016), respectively. The parallax of FF Aql was determined with the HST Fine Guidance Sensor, reaching a precision of $\sigma_{\varpi}/\varpi \sim 6\%$. The astrometric measurements of SY Aur and SS CMa were obtained with the Wide Field Camera 3 (WFC3) by spatial scanning that improved the precision of the source position determination allowing parallaxes with uncertainties in the range of $\sim$ 0.3-0.5 mas ($\sigma_{\varpi}/\varpi \sim$11–12%) to be derived. Parallax measurements available for these three stars are summarised in the central portion of Table 3.1. Taking into account the rather small sample and the much larger errors, as expected for these first *Gaia* parallaxes, agreement between TGAS and HST is within 2σ for FF Aql and SS CMa, and within 1σ for SY Aur. We also note that FF Aql is known to be in a binary system and this may have affected the measurement of its parallax (see Sect. 3.5.3.2).

Figure 3.11, bottom-left panels, shows for these three CCs the comparison between the TGAS and HST parallax values (lower sub-panel), between TGAS and *Hipparcos* (middle sub-panel), and between *Hipparcos* and the HST (upper sub-panel). In each panel going from top to bottom the agreement between the different parallax values increases, the best agreement existing between the TGAS and HST values, thus confirming that

TGAS, although less precise than HST, provides more reliable parallax measurements and an improvement with respect to *Hipparcos*.

The HST parallax has been measured for only one of the T2Cs in our sample, VY Pyx (Benedict et al. 2011). Results of the comparison between the TGAS, *Hipparcos*, and HST parallaxes for this star are summarised in the lower portion of Table 3.1 and are shown in the bottom-right panels of Fig. 3.11. While HST and *Hipparcos* parallaxes seem to be in reasonable agreement with each other, the TGAS value for VY Pyx differs significantly from the HST one[14].

Although globally possible systematic errors in the TGAS parallaxes are well below their released errors, Lindegren et al. (2016) warn that systematic effects at a typical level of ± 0.3 mas depending on the sky position and the colour of the source (see Sect. 3.2) may affect the TGAS parallaxes. We have not found information in the literature about systematic effects on the HST parallaxes. Nevertheless, the direct star-by-star comparison of the parallaxes in Table 3.1 and Figure 3.11 bottom sub-panels does not seem to show evidence of the presence of a systematic difference between the TGAS and HST parallaxes, for the small samples for which a direct comparison with the HST is possible.

3.5.3 Luminosity calibrations based on different fitting approaches

3.5.3.1 Methods

Different fitting approaches can be applied to obtain a luminosity calibration, that is, a PL, PW, PLZ, or M_V – [Fe/H] relation. The most widely applied procedure is the direct transformation to distance (hence absolute magnitude) by parallax inversion and then the least-squares fit (LSQ) of the derived parameters. This method should be avoided if parallax errors are larger than 10% as it may lead to significantly biased results.

The absolute magnitude (M) of a star is calculated from its parallax (ϖ, in mas) through the relation

[14] For a wide discussion, see sect. 2.2 of Gaia Collaboration et al. (2017).

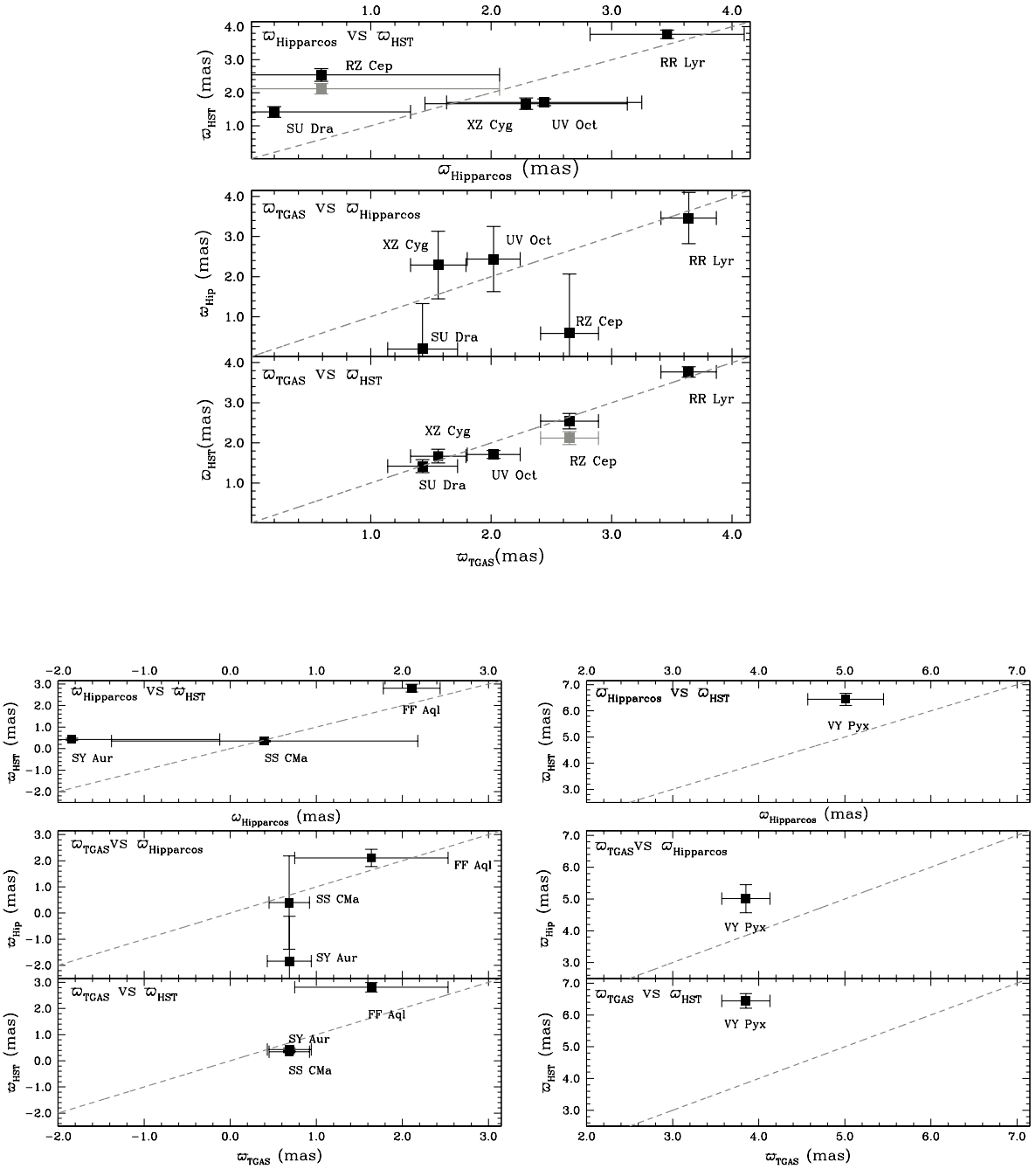

FIGURE 3.11: *Upper panel*: Comparison between *Hipparcos* and HST parallaxes (upper panel), TGAS and *Hipparcos* (middle panel), TGAS and HST (lower panel) for the RRLs: RR Lyr, RZ Cep, SU Dra, XZ Cyg, and UV Oct. Two values from Benedict et al. (2011) are shown for RZ Cep: 2.12 mas (grey filled square) and 2.54 mas (black filled square). TGAS parallax for RZ Cep is in good agreement with the larger, less favoured value in Benedict et al. (2011). *Bottom-left panel*: Comparison between *Hipparcos* and HST parallax (upper panel), TGAS and *Hipparcos* parallax (middle panel), and TGAS and HST parallax (lower panel) for the CCs FF Aql, SY Aur, and SS CMa. FF Aql is the brightest star in our sample of 331CCs and is known to be a component of a binary system. *Bottom-right panel*: Comparison between *Hipparcos* and HST parallax (upper panel), TGAS and *Hipparcos* parallax (middle panel), and TGAS and HST parallax (lower panel) for the T2C VY Pyx. Dashed lines show the bisectors. Figures from Gaia Collaboration et al. (2017).

$$M = m_0 + 5\log(\varpi) - 10, \tag{3.1}$$

where m_0 is the apparent de-reddened magnitude of the star. While errors in the parallaxes are approximately Gaussian, and thus symmetrical due to the logarithm term in Eq. 3.1, the derived error in M becomes asymmetrical and can thus lead to biases. In particular, the LSQ of values (absolute magnitudes) obtained through Eq. 3.1 is not advisable since LSQ relies on the errors of the fitted quantities being Gaussian or at least symmetrical. Besides, negative parallaxes cannot be used in an LSQ fitting procedure. Approaches that allow to both use stars with negative parallaxes and avoid non-linear transformations when fitting the PL, PW, PLZ, or $M_V - [\mathrm{Fe/H}]$ relations, are those operating directly in parallax space, such as, for instance, that using the Astrometry-Based Luminosity (ABL), defined by Arenou & Luri (1999) as

$$ABL = 10^{0.2M} = \varpi 10^{0.2m_0 - 2}, \tag{3.2}$$

where M is the absolute magnitude, ϖ the parallax in mas, and m_0 the extinction corrected apparent magnitude. The ABL avoids the absolute magnitude transformation, using parallaxes directly, hence maintaining symmetrical errors and also allowing negative parallaxes to be used. Assuming that stars follow a relation between period and absolute magnitude M (such as a PL or a PW relation) of the form

$$M = \alpha \mathrm{logP} + \rho, \tag{3.3}$$

where P is the period and α and ρ are the slope and zero point, using the ABL Eq. 3.2 becomes:

$$10^{0.2(\alpha \log P + \rho)} = \varpi 10^{0.2m_0 - 2} \tag{3.4}$$

and can be fitted using a weighted non-linear least squares. The same approach can be used to fit the PLZ and $M_V - [\mathrm{Fe/H}]$ relations of RRLs that, adopting the ABL formalism, become:

$$10^{0.2(\alpha \mathrm{logP} + \beta [\mathrm{Fe/H}] + \rho)} = \varpi 10^{0.2m_0 - 2} \tag{3.5}$$

and

$$10^{0.2(\alpha [\mathrm{Fe/H}] + \rho)} = \varpi 10^{0.2m_0 - 2}, \tag{3.6}$$

which can both be fitted by non-linear least-squares fit.

Finally, in our analysis to fit the PL, PW, PLZ, or M_V − [Fe/H] relations we applied also a Bayesian estimation approach (hereinafter, BA). The Bayesian estimate was performed by means of a hierarchical model which is described in detail in Sect. 3.2 of Gaia Collaboration et al. (2017) and Delgado et al. (2018).

Although the ABL and Bayesian methods are to be preferred as they do not introduce additional biases, in our study we applied also the LSQ fitting, to be able to make comparisons with literature results obtained with this method.

3.5.3.2 Selection biases

In the determination of a luminosity calibration based on astrometric data, (e.g. a PL, or PW, or PLZ or M_V − [Fe/H] relations in our case), we have to be very careful in taking into account possible sources of bias that if are not properly taken into account, may significantly affect the results. A main source of bias is the way by which the sample has been obtained, due to either censorship (missing data) or truncation (some selection process done on purpose for the study). Selection criteria that directly or indirectly favour brighter or fainter stars can also affect the PL, PW, PLZ, or M_V − [Fe/H] relations derived from the sample. Our samples are the result of several processing stages each with a different impact on the resulting sample. Overall, the complexity of the censorships of the samples available for our analysis is not easy to interpret and makes it difficult to produce a reliable estimation of all possible biases introduced by them. Nevertheless, we have identified at least three clear sources of biases; two are directly related to truncations and censorships operated in the generation of the TGAS catalogue of parallaxes (see Sect. 3.1.1 of Gaia Collaboration et al. 2017 for details) and a third one introduced by our space/ground-based collection of external data (photometry, spectroscopy, etc.; Sect. 3.1.2 of Gaia Collaboration et al. 2017).

3.5.4 RR Lyrae stars

TGAS parallaxes are available for 364 MW RRLs. Photometry and metallicity for most of these stars is available in the literature, although fragmented in many different

catalogues and works. Dambis et al. (2013) have collected and homogenised the literature data of 403 MW RRLs for which they publish:

- period and pulsation mode;
- visual absorption (A_V);
- iron abundance ([Fe/H]) on the Zinn & West (1984) metallicity scale[15] (for 402 stars);
- intensity-averaged mean magnitudes in the V, K_s (2MASS), and Wide-field Infrared Survey Explorer (*WISE*) W_1 (3.4 μm) passbands for 384, 403, and 398 stars, respectively.

The pulsation periods are taken from the ASAS3 (Pojmanski 2002, Maintz 2005) and the GCVS (Samus' et al., 2017) catalogues. The absorption values are estimated from the 3D model by Drimmel et al. (2003). These authors do not provide individual errors for such values, but they compared their estimations with those derived from NIR colour-magnitude diagrams of different MW fields based on 2MASS data, finding differences smaller than 0.05 mag. We adopt this value as the mean uncertainty of the absorption. The mean V magnitudes were calculated from nine overlapping sets of observations (see details in Dambis et al. 2013 and references therein); the K_s-band mean magnitudes were calculated from the 2MASS single-epoch observations of Cutri et al. (2003) and by applying the phase-correction procedure described in Feast et al. (2008)[16]. Mean magnitudes in the mid-infrared (MIR) $W1$ passband were calculated from the *WISE* single-exposure database. We cross-matched our sample of 364 RRLs with TGAS parallaxes against the catalogue of Dambis et al. (2013) and found 200 sources in common. They span the period range from 0.27 to 0.80 d. The error distribution of the TGAS parallaxes for these 200 RRLs is shown by the blue histogram in Fig. 3.8 (upper panel). The complete dataset (*Gaia*/Hipparcos/Tycho-2 IDs; period; pulsation mode; G, $\langle V \rangle$,

[15]This scale is widely used in the literature and is based on the average of integrated-light and spectroscopic indices calibrated on a small number of photographic high resolution spectra. However, different metallicity scales were later developed based on abundance analysis of high resolution spectra of red giant branch stars in MW globular clusters. A widely used one is the Carretta & Gratton (1997) scale, that is now superseded by the Carretta et al. (2009) metallicity scale. On average ZW and Carretta et al. (2009) scales differ by only 0.01 dex. Detailed transformation relations between the two scales are provided by Carretta et al. (2009).

[16]For 32 RRLs in the Dambis et al. (2013) sample, the 2MASS magnitudes do not have phase correction; however, only one of them falls in our sample of 364 stars.

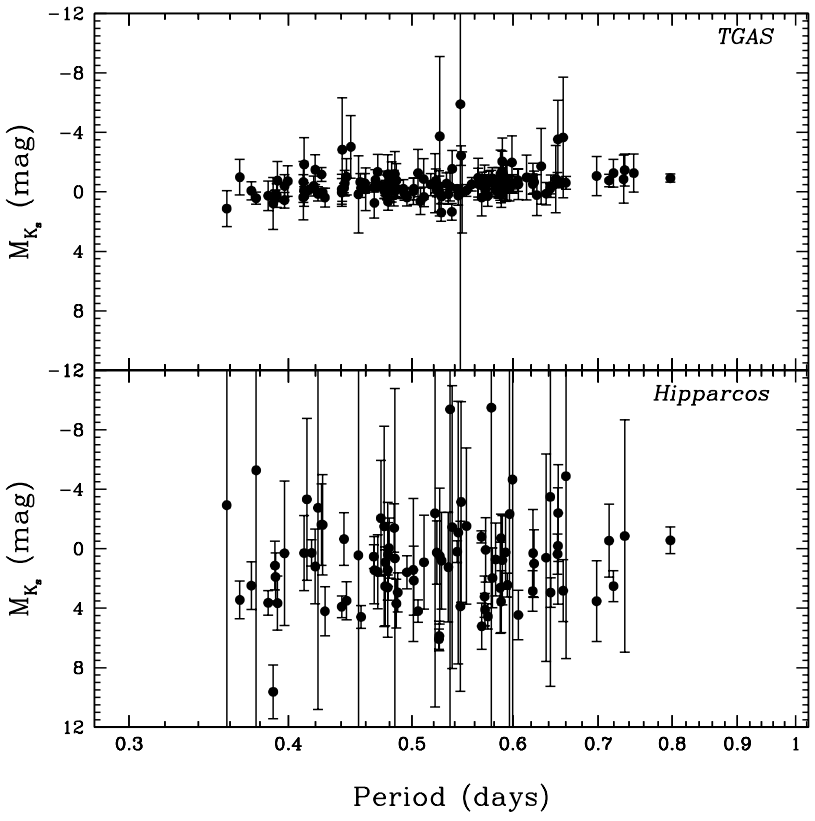

FIGURE 3.12: RRL PL relation in the K_S-band using $\varpi_{Hipparcos}$ (bottom panel) and ϖ_{TGAS} (upper panel). Figure from Gaia Collaboration et al. (2017).

$\langle K_s \rangle$, $\langle W_1 \rangle$ magnitudes; A_V and [Fe/H] values) along with TGAS parallaxes and errors for the total sample of 364 RRLs are presented in Table A.3 of Appendix A. For the first 200 entries in the table, the literature values are from Dambis et al. (2013), for the remaining 164 sources the literature information is mainly taken from the GCVS catalogue. Both *Hipparcos* and TGAS parallaxes are available for 145 out of these 200 RRLs. We applied Eq. 3.1 to transform the TGAS and *Hipparcos* parallaxes to absolute M_{K_s} magnitudes. This transformation was possible only for stars with positive parallax values, 143 out of 145 stars with TGAS parallax and only 91 out of 145 for *Hipparcos*. We "fundamentalised"[17] the periods of the RRc stars and then fit them together using a single PL relation. The corresponding PM_{K_s} relations for ϖ_{TGAS} and $\varpi_{Hipparcos}$ are

[17] The first overtone pulsators were transformed into fundamental pulsators modifying their periods according to the equation:

$$\log P_f = \log P_{RRc} + 0.127 \tag{3.7}$$

(Iben, 1974).

shown in Fig. 3.12, upper and lower panels, respectively. The figure shows an impressive improvement of the TGAS parallaxes for RRLs with respect to *Hipparcos*, revealing a PM_{K_s} relation which becomes markedly visible.

We have used the sample of 200 RRLs with TGAS parallaxes along with magnitudes, period, and metallicity values from Dambis et al. (2013) to fit the PL relations in the K_s and $W1$-bands, the PLZ relation in the K_s-band, and the optical $M_V - [Fe/H]$ relation adopting the three different fitting approaches described in Sect. 3.5.3.1[18]. Firstly we de-reddened the K_s magnitudes using the A_V values from Dambis et al. (2013), and the

[18]The presence of RRLs in binary systems is a rather rare event. Only one RRL, TU UMa, has been confirmed to reside in a binary system (Wade et al. 1999 and references therein for a detailed analyses of this star). Hence, we do not expect extra-scatter in the RRL relations due to this effect. Indeed, TU UMa is in our cleanest sample of 200 RRLs that we use to derive the relations for the RRLs and we found that it is very well placed on the best fit line of the various relations.

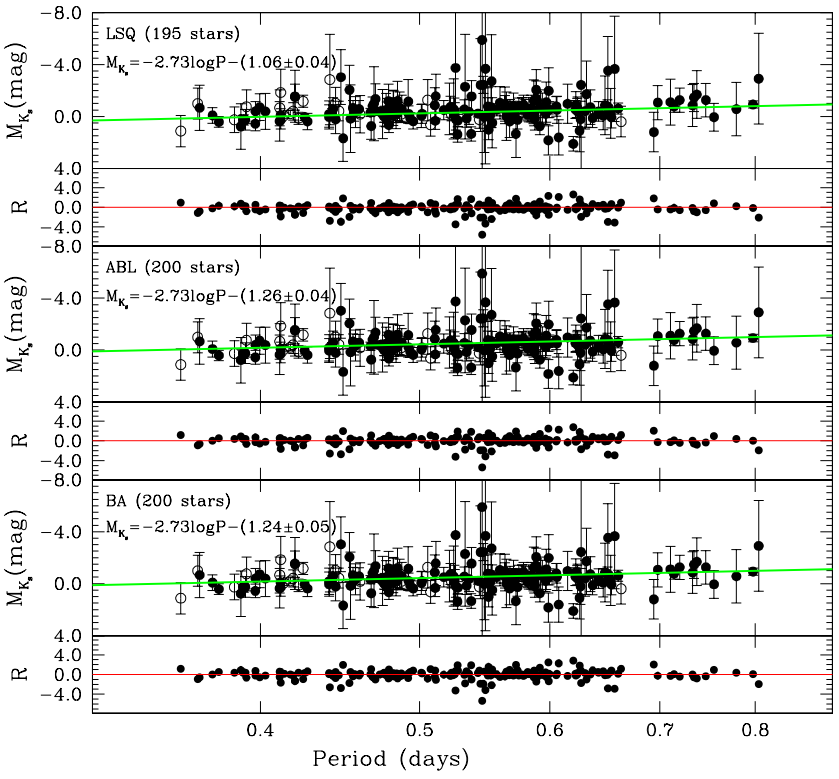

FIGURE 3.13: RRL PL relation in the K_s band obtained: via linear least-squares fit of the stars' absolute magnitudes inferred from direct transformation of the TGAS parallaxes (upper panel); via non-linear least-squares fit and the ABL method (middle panel) and using the Bayesian approach (bottom panel). The slope of the fit is taken from Muraveva et al. (2015). Filled and empty circles represent fundamental-mode (RRab) and first overtone (RRc) stars, respectively. The bottom part of each panel shows the residuals from the best fit line. Figure from Gaia Collaboration et al. (2017).

$A_K/A_V = 0.114$ extinction law for the K band from Cardelli et al. (1989) (Cardelli's law). The periods of the first overtone RRLs (RRc) were *fundamentalised*. Since errors on the TGAS parallaxes are large we did not attempt to derive both slope and zero point, but we used the TGAS parallaxes only to estimate the zero point and adopted the slope from published works.

The RRLs NIR PM_KZ relation has been studied by many authors with different dataset and instruments and, as described in Section 1.2.2 of Chapter 1, the literature coefficients and zero points of the relation differ significantly from one study to the other.

We adopted the slope of the PM_{K_s} relation from Muraveva et al. (2015), which derived this slope from a study of RRLs in the LMC.

Figure 3.13 shows the PL relation in the K_s band obtained: (i) via linear least-squares fits of the stars' absolute magnitudes inferred from direct transformation of the TGAS parallaxes (upper panel). The LSQ has been applied only to 195 RRLs, as five RRLs in the sample have a negative parallax value; (ii) via non-linear least-squares fits and the ABL method (middle panel); and (iii) using the Bayesian approach (bottom panel). The whole sample of 200 RRLs could be used with these latter two methods. The PM_{K_s} and other (PL, PLZ and M_V-[Fe/H]) relations obtained with the three different approaches are summarised in Table 3.2.

TABLE 3.2: PL, PLZ and M_V – [Fe/H] relations for RRLs based on ϖ_{TGAS}.

RRLs	Relation	r.m.s. (mag)
PM_{K_s} 195 stars (LSQ)	$-2.73\log P-(1.06\pm0.04)$	0.84
PM_{K_s} 200 stars (ABL)	$-2.73\log P-(1.26\pm0.04)$	0.90
PM_{K_s} 200 stars (BA)	$-2.73\log P-(1.24\pm0.05)$	1.02
$PM_{K_s}Z$ 195 stars (LSQ)	$-2.73\log P-(0.01\pm0.07)$[Fe/H] $-(1.08\pm0.09)$	0.84
$PM_{K_s}Z$ 200 stars (ABL)	$-2.73\log P+(0.07\pm0.07)$[Fe/H] $-(1.17\pm0.10)$	0.89
$PM_{K_s}Z$ 200 stars (BA)	$-2.73\log P-(0.01^{+0.11}_{-0.07})$[Fe/H] $-(1.22^{+0.40}_{-0.09})$	1.02
PM_{W_1} 193 stars (LSQ)	$-2.44\log P-(1.02\pm0.04)$	0.82
PM_{W_1} 198 stars (ABL)	$-2.44\log P-(1.21\pm0.04)$	0.87
PM_{W_1} 198 stars (BA)	$-2.44\log P-(1.20\pm0.05)$	1.02
M_V – [Fe/H] 195 stars (LSQ)	0.214[Fe/H] $+(1.01\pm0.04)$	0.82
M_V – [Fe/H] 200 stars (ABL)	0.214[Fe/H] $+(0.82\pm0.04)$	0.87
M_V – [Fe/H] 200 stars (BA)	0.214[Fe/H] $+(0.88^{+0.04}_{-0.06})$	1.21

We note that the zero points obtained via ABL and BA are in perfect agreement with the zero point of the $PM_{K_s}Z$ relation obtained in Muraveva et al. (2015) using the HST parallaxes of four RRLs from Benedict et al. (2011) (Eq. 6 in Muraveva et al. 2015). The zero points obtained for the various RRL relations with the ABL and Bayesian approaches are in good agreement with each other and are, on average, about 0.2 mag brighter than the values found with the LSQ fitting method.

3.5.5 Classical and Type II Cepheids

3.5.5.1 Classical Cepheids

TGAS parallaxes are available for 331 Galactic CCs. For this sample, we assembled a catalogue as uniform and homogeneous as possible collecting from the literature:

- V, I and K_S (from 2MASS) photometry
- reddening values E(B-V) and metal abundances
- period (P) and pulsation mode classification

P and V, I, K_S photometry values were taken from different catalogues, primarily Groenewegen (1999), Berdnikov et al. (2000), Fernie et al. (1995, DDO Database of Galactic Classical Cepheids), Ngeow (2012), the GCVS (Samus' et al. 2017), and the ASAS3 catalogue (Pojmanski 2002), among others. For the mean magnitudes, we collected intensity-averaged mean V, I, K_S magnitudes based on a complete sampling of the light curves whenever available. In several cases, when it was not available, we computed the intensity-averaged mean values ourselves from the light curves published in the literature. The $E(B-V)$ reddening values and related errors were taken from Fernie et al. (1995), Groenewegen (1999), Turner et al. (2001), Fouqué et al. (2007), and Pejcha & Kochanek (2012). In a few cases we specifically estimated the reddening for this study from the available photometry. Metal abundances were mainly taken from Genovali et al. (2014), and for a few stars from Ngeow (2012). Information about duplicity is from Klagyivik & Szabados (2009) and Anderson et al. (2016). Once completed the collection of data from the literature we had period values for 312 CCs in our sample (94%); $E(B-V)$ reddening values for 276 stars (83%); and photometry in the V, I, and K_s

bands for 297 (90%), 250 (76%), and 292 (88%) CCs, respectively.

Among the CCs with TGAS parallaxes, 248 have parallax values measured also by

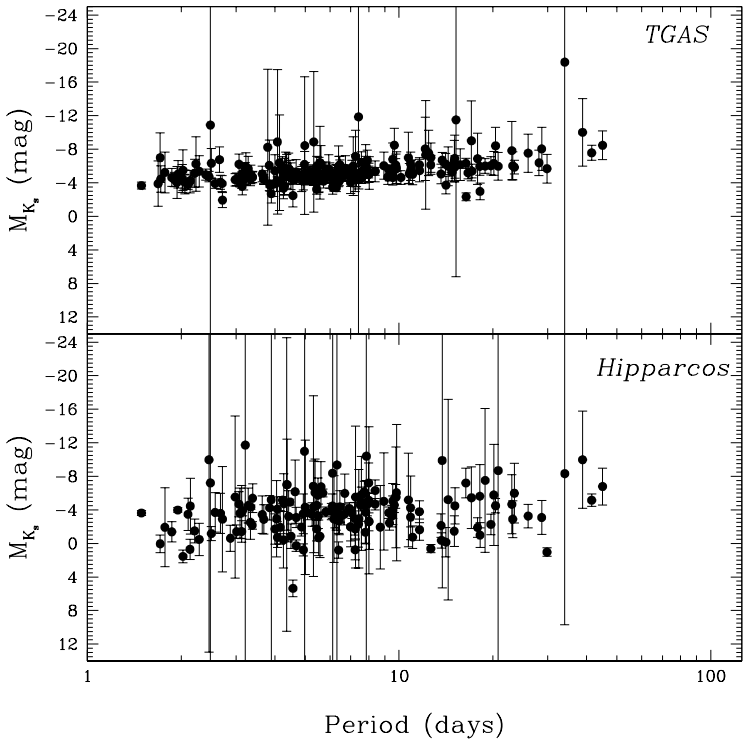

FIGURE 3.14: CC *PL* relations in the K_S-band using TGAS and *Hipparcos* parallaxes (upper and lower panels, respectively. The upper panel shows the absolute magnitudes, M_{K_S} for 221 CCs with positive parallaxes from TGAS. The lower panel shows 156 CCs with positive *Hipparcos* parallaxes. Figure from Gaia Collaboration et al. (2017).

Hipparcos, and for 228 of them K_s magnitudes, reddening values, and periods are available in the literature. We corrected for extinction the K_s magnitudes using Cardelli's law and adopting for the ratio of total to selective extinction the value $R_V = 3.1$, we then derived de-reddened magnitudes through the relation: $K_{s,0} = K_s - 0.35E(B-V)$. As done for RRLs, we transformed the TGAS and *Hipparcos* parallaxes to absolute M_{K_s} magnitudes applying Eq. 3.1. This transformation was possible only for stars with positive parallax values, namely 221 out of 228 stars with TGAS parallax and only 156 out of 228 for *Hipparcos*. The resulting PM_{K_s} relations are shown in Fig. 3.14 for the TGAS (upper panel) and *Hipparcos* parallaxes (lower panel), respectively. The improvement of the TGAS parallaxes is remarkable, even if less impressive than in the case of RRLs. The scatter of the PM_{K_s} relation is very much reduced, the sample of CCs is

about 30% larger, and although errors are still very large a clear PM_{K_s} relation can now be seen in the data. CCs are Population I stars, therefore occurrence of binaries among them is a common phenomenon. However, it is not easy to detect the presence of a companion because it is the supergiant Cepheid that dominates the system. For the brightest Cepheids, the frequency of binaries (including systems consisting of more than two stars) exceeds 50% (Szabados 2003). For Galactic CCs, there is an online database developed and maintained at the Konkoly Observatory[19] which contains the actual list of known Cepheids having physical companion(s). Combining information from the online database of the Konkoly Observatory (Klagyivik & Szabados 2009) and Anderson et al. (2016) on a few new binary Cepheids recently detected, we found that 198 (60%) of the 331 CCs in our sample are binaries. We decided to eliminate binary Cepheids from the final sample in order to compute the PL relations with the cleanest possible dataset thus reducing the dispersion and avoiding additional factors that could lead to erroneous PL zero-point determinations. Once known binaries are discarded our sample reduces to 133 non-binary CCs. Furthermore, we discarded three additional sources: BB Her, EV Aql, and V733 Aql, because in the McMaster Cepheid Photometry and Radial Velocity Data Archive[20] they are classified as T2Cs; however, since their classification remains uncertain, we did not include them in the list of T2Cs. After this additional cleaning and taking into account that we found external information (P, V, I_c and K_s photometry and reddening) only for 125 CCs in the end we were left with a sample of 122 bona-fide CCs divided in fundamental mode (F) and first-overtone (FO) pulsators. Combining pulsation information from the studies of Udalski et al. (1999), Sziládi et al. (2007), Klagyivik & Szabados (2009), Molnár & Szabados (2014), and Inno et al. (2015), we found that our sample contains 102 fundamental mode CCs with periods ranging from 1.68 to 51.66 d. fundamental and first overtone CCs follow different PL relations. To remove any scatter caused by mixing multiple PL relations in the following analysis we only considered F CCs. The central panel of Fig. 3.8 shows the error distribution of the TGAS parallaxes for these 102 F CCs (magenta histogram).

We computed PL relations in the V, I, and K_s bands (hereafter PM_V, PM_I, PM_{K_s}), as well as $(V, V-I)$, $(K_s, V-K_s)$ PW relations [hereafter $PW(V, V-I)$, $PW(K_s, V-K_s)$] from the 102 F CCs in our sample (see Section C.1 of Appendix C for a brief description of CCs and the relations they conform to). Firstly, we corrected for extinction the V,

[19] http://www.konkoly.hu/CEP/intro.htm
[20] http://crocus.physics.mcmaster.ca/Cepheid/

I, and K_s magnitudes using $V_0 = V - 3.1E(B-V)$, $I_0 = I - 1.48E(B-V)$, and $K_{s,0} = K_s - 0.35E(B-V)$ obtained adopting the extinction relations from Cardelli et al. (1989) and $R_V = 3.1$. For the PW relations, we transformed magnitudes into Wesenheit indices according to the following definitions: $W(V,I) = V - 2.55(V-I)$ (Fouqué et al., 2007) and $W(V,K_s)$=$K_s - 0.13\,(V-K_s)$ (Ripepi et al., 2012).

As for RRLs, we fixed the slope of the PL and PW relations and used the TGAS parallaxes just to estimate the zero points. We adopted the slopes from Fouqué et al. (2007) for the PM_V, PM_I, PM_{K_s}, and $PW(V,V-I)$ relations and from Ripepi et al. (2012) for the $PW(K_s,V-K_s)$ relation. The PL and PW relations obtained by applying the three different approaches described in Sect. 3.5.3.1 (LSQ, ABL and BA) to the various passbands considered in our study (V, I and K_s) are summarised in the upper portion of Table 3.3. The LSQ fit was possible only for 95 CCs in the sample for which TGAS parallaxes have positive values. The PM_V, PM_I, PM_{K_s}, $PW(V,V-I)$, and $PW(K_s,V-K_s)$ relations were then computed using the ABL method along with a weighted non-linear least-squares fit in the form of Eq. 3.4 and, finally, using the Bayesian approach. With the ABL and the BA methods, it was possible to use the whole sample of 102 CCs without discarding stars with negative parallax. Results in Table 3.3 show that the ABL and the Bayesian approaches are generally in good agreement with each other and provide brighter absolute magnitudes (hence longer distances) than the direct transformation of parallaxes and the LSQ fit, whose absolute magnitudes are about ~ 0.5 mag systematically fainter. However, we also note that the r.m.s. scatter of all relations is very large, due to the large parallax uncertainties. The r.m.s. of the Bayesian solution is particularly large as it represents the un-weighted residuals with respect to the maximum a posteriori solution.

3.5.5.2 Type II Cepheids

The sample of 31 T2Cs that have TGAS parallaxes includes 12 BL Herculis (BL Her), 14 W Virginis (W Vir), and 5 RV Tauri (RV Tau) stars. We excluded the RV Tau variables because they follow different and more dispersed relationships than BL Her and W Vir stars (Ripepi et al. 2015; see Appendix C for details). The sample, cleaned from RV Tau stars, contains 26 T2Cs spanning the period range from 1.16 to 30.0 d. The error distribution of the TGAS parallaxes for these 26 T2Cs is shown by the grey histogram in

TABLE 3.3: *PL* and *PW* relations for CCs and T2Cs with zero points based on TGAS parallaxes

CCs	Relation	r.m.s. (mag)
PM_V 95 objects (LSQ)	$-2.678\log P-(1.00\pm0.08)$	0.74
PM_V 102 objects (ABL)	$-2.678\log P-(1.54\pm0.10)$	0.85
PM_V 102 objects (BA)	$-2.678\log P-(1.49^{+0.12}_{-0.11})$	1.31
PM_I 95 objects (LSQ)	$-2.98\log P-(1.28\pm0.08)$	0.78
PM_I 102 objects (ABL)	$-2.98\log P-(1.84\pm0.10)$	0.87
PM_I 102 stars (BA)	$-2.98\log P-(1.80^{+0.13}_{-0.12})$	1.33
$PM_{\rm K_s}$ 95 objects (LSQ)	$-3.365\log P-(2.06\pm0.08)$	0.74
$PM_{\rm K_s}$ 102 objects (ABL)	$-3.365\log P-(2.63\pm0.10)$	0.88
PM_{K_S} 102 stars (BA)	$-3.365\log P-(2.60^{+0.11}_{-0.15})$	1.33
$PW(V,V-I)$ 95 objects (LSQ)	$-3.477\log P-(2.21\pm0.08)$	0.77
$PW(V,V-I)$ 102 objects (ABL)	$-3.477\log P-(2.82\pm0.11)$	0.90
$PW(V,V-I)$ 102 stars (BA)	$-3.477\log P-(2.63\pm0.13)$	1.36
$PW(K_{\rm s},V-K_{\rm s})$ 95 objects (LSQ)	$-3.32\log P-(2.32\pm0.08)$	0.73
$PW(K_{\rm s},V-K_{\rm s})$ 102 objects (ABL)	$-3.32\log P-(2.87\pm0.10)$	0.87
$PW(K_{\rm s},V-K_{\rm s})$ 102 stars (BA)	$-3.32\log P-(2.81^{+0.14}_{-0.12})$	1.33
T2Cs	**Relation**	**r.m.s. (mag)**
PM_J 22 objects (LSQ)	$-2.19\log P-(0.97\pm0.13)$	0.88
PM_J 26 objects (ABL)	$-2.19\log P-(1.50\pm0.20)$	1.25
PM_J 26 objects (BA)	$-2.19\log P-(1.36^{+0.26}_{-0.25})$	1.15
$PM_{K_{\rm s}}$ 22 objects (LSQ)	$-2.385\log P-(1.18\pm0.12)$	0.81
$PM_{K_{\rm s}}$ 26 objects (ABL)	$-2.385\log P-(1.58\pm0.17)$	1.10
$PM_{K_{\rm s}}$ 26 objects (BA)	$-2.385\log P-(1.51^{+0.23}_{-0.22})$	1.14
$PW(K_{\rm s},J-K_{\rm s})$ 22 objects (LSQ)	$-2.52\log P-(1.34\pm0.10)$	0.80
$PW(K_{\rm s},J-K_{\rm s})$ 26 objects (ABL)	$-2.52\log P-(1.59\pm0.13)$	1.04
$PW(K_{\rm s},J-K_{\rm s})$ 26 objects (BA)	$-2.52\log P-(1.66^{+0.21}_{-0.22})$	1.13

Fig 3.8 (lower panel). J and $K_{\rm s}$ photometry for these stars was taken from the 2MASS catalogue (Cutri et al. 2003); the pulsation periods were taken from the GCVS (Samus' et al., 2017); and the $E(B-V)$ reddening values and related errors were taken from the NASA/IPAC Infrared Science Archive[21], which is based on the reddening maps of Schlafly & Finkbeiner (2011). For the T2Cs we only have single-phase 2MASS J and $K_{\rm s}$ magnitudes instead of magnitudes averaged over the whole pulsation cycle, which introduced additional uncertainty. The typical amplitude of the T2Cs in these bands

[21] http://irsa.ipac.caltech.edu/applications/DUST/

is ~ 0.3 mag, and so we adopted mean errors of the apparent J and K_s magnitudes of 0.15 mag. K_s and J magnitudes were de-reddened applying the Cardelli's laws $A_J = 0.87E(B-V)$ and $A_K = 0.35E(B-V)$ (adopting $R_V = 3.1$) as done for CCs. We converted the NIR-magnitudes in Wesenheit indices with $W(K_s, J) = K_s - 0.69(J-K_s)$ and fitted the PM_{K_s}, PM_J, and $PW(K_s, J-K_s)$ relations, using as reference slopes the ones derived by Ripepi et al. (2015) for BL Her and W Vir stars in the LMC. The sample of 26 T2Cs contains four stars with negative parallaxes, hence we performed the linear least-squares fitting of the absolute magnitudes only for the 22 T2Cs with a positive parallax, while we applied the ABL and Bayesian methods to the whole sample of 26 T2Cs. In the lower portion of Table 3.3 are listed the T2Cs PL and PW relations obtained in the various bands considered in this study. As found for CCs, the ABL and BA methods are generally in good agreement with each other and are, on average, about 0.4 mag brighter than found with the LSQ fit. However, the r.m.s. of all relations remains fairly large.

3.5.6 Sanity check and Conclusions

As a test we used the TGAS-based PL, PW, PLZ, and M_V – [Fe/H] relations of CCs, T2Cs, and RRLs derived with the three alternative fitting approaches presented in Section 3.5.3.1 to infer the distance to the LMC. Of the various relations obtained in this work, we considered only the PM_{K_s}, $PW(V,I)$, and $PW(V,K_s)$ relations for the Cepheids and the PM_{K_s}, $PM_{K_s}Z$, and M_V – [Fe/H] relations for the RRLs because they are the most relevant in distance scale studies. This comparison provides both potential and expected levels of systematics of the TGAS parallaxes for RRLs and Cepheids. It also gives some perspective on the effects of the treatment of parallaxes in parallax or distance (absolute magnitude) space.

The LMC is a fundamental anchor of the extragalactic distance ladder and is its first step. Over the last two decades the distance modulus of the LMC has been measured countless times using different Population I and II distance indicators and many independent techniques (see e.g. Gibson 2000, Benedict et al. 2002, Clementini et al. 2003, Schaefer 2008, and a recent compilation of literature values by de Grijs et al. 2014), most of which are now converging on a median value of $\mu_{\rm LMC} = 18.49 \pm 0.09$ mag, which is in close agreement with the value $(m-M)_0 = 18.493 \pm 0.008$ (stat) $\pm$ 0.047 (syst) mag derived by Pietrzynski et al. (2013) using eclipsing binaries in the LMC bar.

The LMC distance moduli inferred from some of the relations obtained in this work are listed in Table 3.4, where results from RRLs, CCs and T2Cs are collected in the upper, middle and lower portions of the table, respectively. These distance moduli were calculated according to the following procedure:

- For the RRLs we applied the PM_{K_s} and $PM_{K_s}Z$ relations from Muraveva et al. (2015) and the $M_V - [Fe/H]$ relation from Clementini et al. (2003).
- For the CCs we adopted the PM_{K_s} and $PW(V, I)$ relations derived for the LMC variables by Fouqué et al. (2007) (rows 4 and 2 from the bottom of their table 8) and the $PW(V, K_s)$ relation by Ripepi et al. (2012) (their table 4).
- For the T2Cs we used the PM_{K_s}, PM_J and $PW(J, K_s)$ relations for the LMC in table 5 of Ripepi et al. (2015).
- Our corresponding TGAS-based zero points have been subtracted from the zero points of these relations, which are in apparent magnitude.

Errors on the distance moduli were calculated as the r.m.s. of our relations divided by the square root of the number of sources used in the fit. Different values are graphically compared in Fig. 3.15, where we adopt as a reference value the LMC distance modulus from Pietrzynski et al. (2013) (solid, vertical line) $\pm 2\sigma_{syst}$ (dashed, vertical lines).

We find that there is good consistency, within the errors, between results obtained with the ABL and Bayesian approaches for all three types of variables. On the other hand, the LSQ fit provides systematically shorter moduli. This discrepancy is larger (about 0.5-0.6 mag, on average) for the CCs, reduces to 0.4-0.5 mag for the T2Cs, and is the smallest one, 0.2 mag, for the RRLs. When compared with the LMC distance modulus of Pietrzynski et al. (2013), results from the Bayesian approach applied to CCs are always well consistent within the errors with the canonical value, the ABL results infer slightly longer distances than Pietrzynski et al. (2013), whereas results from the LSQ fit are 0.2-0.4 mag shorter than currently accepted in the literature. For the T2Cs, all three methods provide longer moduli than the canonical value, by 0.3-0.5 mag the ABL and Bayesian approaches and by 0.2 mag the LSQ fit, hence for the latter being still consistent, within the errors, with the Pietrzynski et al. (2013) estimate.

TABLE 3.4: Distance moduli of the LMC obtained from some of the TGAS-based PL, PW, PLZ, and $M_V - [Fe/H]$ relations derived in this study.

Relation	μ (LSQ) (mag)	μ (ABL) (mag)	μ (BA) (mag)
RRLs			
PM_{K_s} for 195 (200) objects	18.49 ± 0.06	18.69 ± 0.06	18.67 ± 0.07
$PM_{K_s}Z$ for 195 (200) objects	18.51 ± 0.06	18.61 ± 0.06	18.65 ± 0.07
$M_V - [Fe/H]$ for 195 (200) objects	18.37 ± 0.06	18.56 ± 0.06	18.50 ± 0.09
CCs			
PM_{K_s} for 95 (102) objects	18.05 ± 0.08	18.62 ± 0.09	18.59 ± 0.13
$PW(V, V-I)$ for 95 (102) objects	18.09 ± 0.08	18.70 ± 0.09	18.51 ± 0.13
$PW(K_s, V-K_s)$ for 95 (102) objects	18.19 ± 0.07	18.74 ± 0.09	18.68 ± 0.13
T2Cs			
PM_J for 22 (26) objects	18.67 ± 0.19	19.20 ± 0.24	19.06 ± 0.22
PM_{K_s} for 22 (26) objects	18.65 ± 0.17	19.05 ± 0.22	18.98 ± 0.22
$PW(K_s, J-K_s)$ for 22 (26) objects	18.65 ± 0.16	19.10 ± 0.19	18.98 ± 0.22

Bearing in mind that the RRLs used in this analysis are twice in number the CCs and more than 7 times the T2Cs, the results obtained for the RRLs show a much better agreement among the three methods and also a reasonably good agreement with the literature, once again confirming the impressive improvement in quality and statistics of the TGAS parallaxes for RRLs compared to *Hipparcos*.

In a similar approach as applied here, Luri et al. (1998) used the $M_V - [Fe/H]$ relation defined by 144 RRLs and the PM_V relation defined by 219 CCs, both calibrated on *Hipparcos* end-mission parallaxes, to estimate the distance modulus of the LMC, obtaining values of $(m-M)_0 = 18.37 \pm 0.23$ mag and $(m-M)_0 = 18.32 \pm 0.17$ mag from RRLs and CCs, respectively. In Figure 3.16 we compare those *Hipparcos*-based estimates (blue and red boxy-shadowed regions) with our present determinations (as summarised in Fig. 3.15) and with Pietrzynski et al. (2013)'s fiducial value.

Luri et al. (1998)'s distance moduli for the LMC are in agreement with each other, but shorter than Pietrzynski et al. (2013)'s value, although still consistent with it given their very large uncertainties. The comparison with our DR1-based distance moduli for the LMC, inferred from the corresponding samples, reveals the significant improvement and the high potential of these *Gaia* preliminary results. However, taken at face value the results summarised in Table 3.4 and Fig. 3.15 span an uncomfortable, large range of

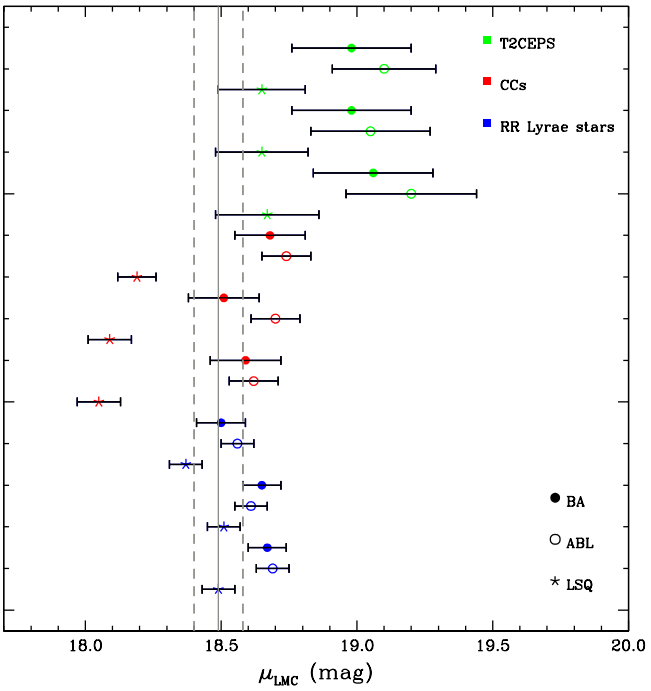

FIGURE 3.15: LMC distance moduli obtained by fitting the TGAS-based PL_{Ks} , $PL_{Ks}Z$ and $M_V - [Fe/H]$ relations for RRLs (blue symbols); PM_{K_s}, $PW(V,I)$, and $PW(V,K_s)$ relations for the CCs and T2Cs (red and green symbols respectively) with the LSQ (asterisks), the ABL (open circles) and the Bayesian approaches (filled circles), respectively. From bottom to top, RRLs: PM_{K_s} relations for 195, 200 and 200 stars (LSQ, ABL, BA methods, respectively) and slope from Muraveva et al. (2015); $PM_{K_s}Z$ relations for 195, 200 and 200 stars and slope from Muraveva et al. (2015); $M_V - [Fe/H]$ relations for 195, 200 and 200 stars with slope from Clementini et al. (2003). For CCs: PM_{K_s} and $PW(V,V-I)$ relations for 95, 102 and 102 stars with slopes from Fouqué et al. (2007); and $PW(K_s,V-K_s)$ relation for 95, 102, and 102 stars with slope from Ripepi et al. (2012). For T2Cs: PM_J, PM_{K_s} and $PW(K_s,J-K_s)$ relations for 22, 26 and 26 stars with slopes from Ripepi et al. (2015). Figure from Gaia Collaboration et al. (2017).

over one magnitude around the commonly accepted value of 18.5 mag for the distance modulus of the LMC. Because errors in this first data release are still fairly large, it is not clear, at this stage, whether this hints to some systematics in the parallax derivation that may affect in different way the different types of variables used in this paper. For instance, since no chromatic corrections were applied to derive the TGAS parallaxes, a colour effect could affect more CCs, which are both intrinsically redder and more reddened, than RRLs or T2Cs. Nevertheless, it is not easy to interpret these results unless in light of the still very large uncertainties affecting the TGAS parallaxes and, perhaps, the relatively small sample of variable stars that could be used, for instance, in the analysis of the T2Cs. We also remind the reader that the complexity in the censorships of the available samples prevented us from producing a more reliable estimation of the

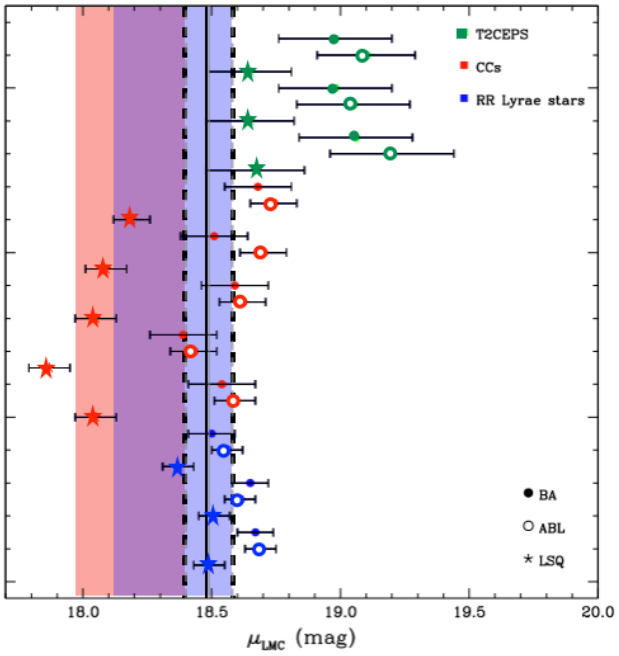

FIGURE 3.16: Same as in Fig 3.15 but including LMC distance moduli $\pm 1\sigma$ from the $M_V - [\mathrm{Fe/H}]$ relation of RRLs (blue shadow) and the PM_V relation of CCs (red shadow) both calibrated on end-mission *Hipparcos* parallaxes (Luri et al. 1998).

possible biases introduced by them. As such the results presented in these sections have to be considered as preliminary, and are superseded by results from further releases of *Gaia* data, starting with the first *Gaia*-only parallaxes published in DR2 (see next sections), allowing the use of samples with more accurate parallaxes and less affected by uncontrolled censorship effects.

3.6 Validation of *Gaia* DR2: testing SOS-confirmed RR Lyrae stars in Galactic Globular Clusters and MW dwarf spheroidal galaxies

Activities for the validation of *Gaia* DR2 products were mainly carried out in the second and third years of the PhD and include: (i) validation of the results produced by the SOS Cep&RRL pipeline for RRLs (and Cepheids) observed by *Gaia* full-sky in 22 months of science operations; and (ii) test and validation of *Gaia* DR2 parallaxes (ϖ_{DR2}) with PL, PLZ and $M_V - [\mathrm{Fe/H}]$ relations for RRLs based on ϖ_{DR2}, in a similar approach as done with ϖ_{TGAS} in DR1 (see Sect. 3.5.4).

In particular, in order to establish the performance of the SOS Cep&RRL pipeline we used catalogues of known RRLs belonging to 150 GGCs and 54 (classic and ultra-faint) dwarf MW satellites. These catalogues contain information for more than 4,000 known RRLs, that I have collected and constantly updated through literature search and data archive query tools. Results from this validation are summarised in the following sections and fully presented in the paper:

"Gaia Data Release 2: Specific characterisation and validation of all-sky Cepheids and RR Lyrae stars", by G. Clementini, V. Ripepi, R. Molinaro, A. Garofalo, T. Muraveva et al. 2018, A&A, in press, arXiv:1805.02079.

Results from the test and validation of *Gaia* DR2 parallaxes for RRLs are summarised in Section 3.7 and fully described in the paper:

"RR Lyrae stars as standard candles in the *Gaia* Data Release 2 Era" by T. Muraveva, H.E. Delgado, G. Clementini, L.M. Sarro & A. Garofalo 2018, MNRAS, 481, 1195.

3.6.1 Data sample

To build a catalogue as large as possible of stellar systems (GCs and dSphs) potentially hosting RRLs within the reach of *Gaia* (limiting magnitude $G \lesssim 20.7$ mag) we considered all the 150 GCs and 54 dwarfs (divided in "classical dSphs" and UFDs) known, at present, in our Galaxy, with no distinction between systems with or without known RRLs. Figure 3.17 shows their distribution on the sky in Galactic coordinates. GCs are marked with blue circles and dSphs with magenta squares. Thirty out of 150 GCs and 29 out of 54 dSphs are not known to contain RRLs (grey symbols). Among the remaining 25 dwarfs three classical dSphs (Fornax, Leo I and Leo II) and seven UFDs are placed too far (d $\geqslant$ 110 kpc) in the MW halo to host RRLs brighter than the *Gaia* detection limit. Our starting catalogue includes more than 4,000 known RRLs located in 120 GCs and 15 (25-10) dwarfs. This catalogue was cross-matched against the SOS-confirmed RRLs (140,784; see Sec 3.4) and we found that 1,986 of them reside in GCs and dwarf galaxies: 1,569 are distributed over 87 GCs and 417 over 12 dSphs, with the largest numbers being in M3 (159 out of 222 known in the literature), NGC 3201 (83 out of 86), Sculptor (176 out of 226) and Draco (176 out of 270). Figure 3.18 shows the distribution on the sky, in galactic (top) and equatorial coordinates (bottom), of the SOS-confirmed

RRLs (orange points). Blue dots and magenta squares indicate 87 GCs and 12 dSphs (classical and ultra faint) dSphs containing 1,986 of the SOS-confirmed RRLs that are published in DR2. Figure 3.19 shows instead the CMDs defined by the confirmed RRLs in GCs (blue) and dSphs (magenta) for which G_{BP} and G_{RP} photometry is available (1,167 sources in total). Each concentration of blue points corresponds to a different GC. Although not used for the DR2 processing, CMDs like this will be largely used by the SOS Cep&RRL pipeline for the classification of RRLs for the processing of sources to be published in the next *Gaia* release (DR3), which is currently foreseen for the first half of 2021.

3.6.2 SOS-confirmed RR Lyrae stars in M3, M62 and Sculptor

We specifically tested the SOS Cep&RRL pipeline on the RRLs in GCs, in order to establish its performance in crowded fields and to verify the reliability of the derived pulsation characteristics (e.g. periods, amplitudes, intensity-averaged mean G, G_{BP} and G_{RP} magnitudes) and stellar parameters (metallicity and G-band interstellar absorption) in systems, like the GCs, for which metallicity and reddening are generally

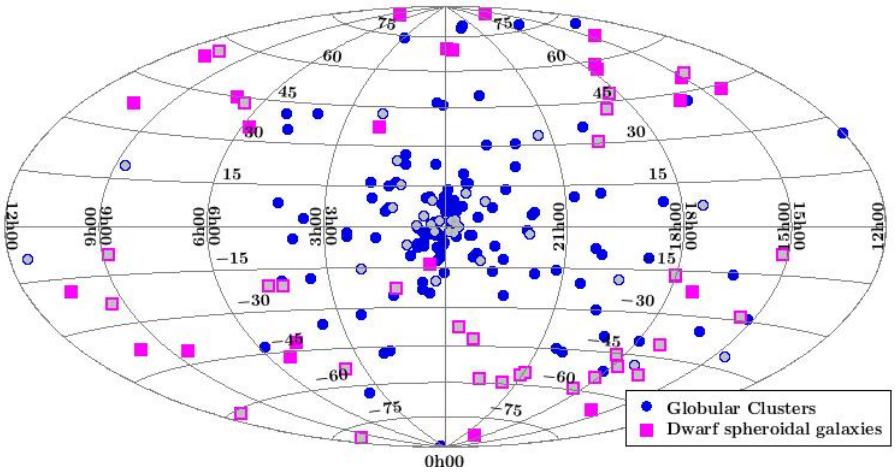

FIGURE 3.17: Distribution on sky of 150 globular clusters (blue circles) and 54 dwarf spheroidal galaxies (magenta squares) in Galactic coordinates. Grey symbols mark stellar systems without RRLs.

well known from the literature. Here we present tests on two GCs, M3 (NGC5272) and M62 (NGC6266), and the classical dSph Sculptor, which have the largest samples of SOS-confirmed RRLs.

In M3, a relatively low central concentration cluster (c=1.89, Harris 1996), *Gaia* recovered 159 of the 222 known RRLs (Benkő et al. 2006[22]). *Gaia* has been capable to identify RRLs even within the core radius of M3 ($r_c = 0.37$ arcmin, Harris 1996). The M3 RRLs

[22] Actually, in his work, Benkő et al. (2006) identified 224 RRLs in the field of M3, but coordinates for two of them were not published.

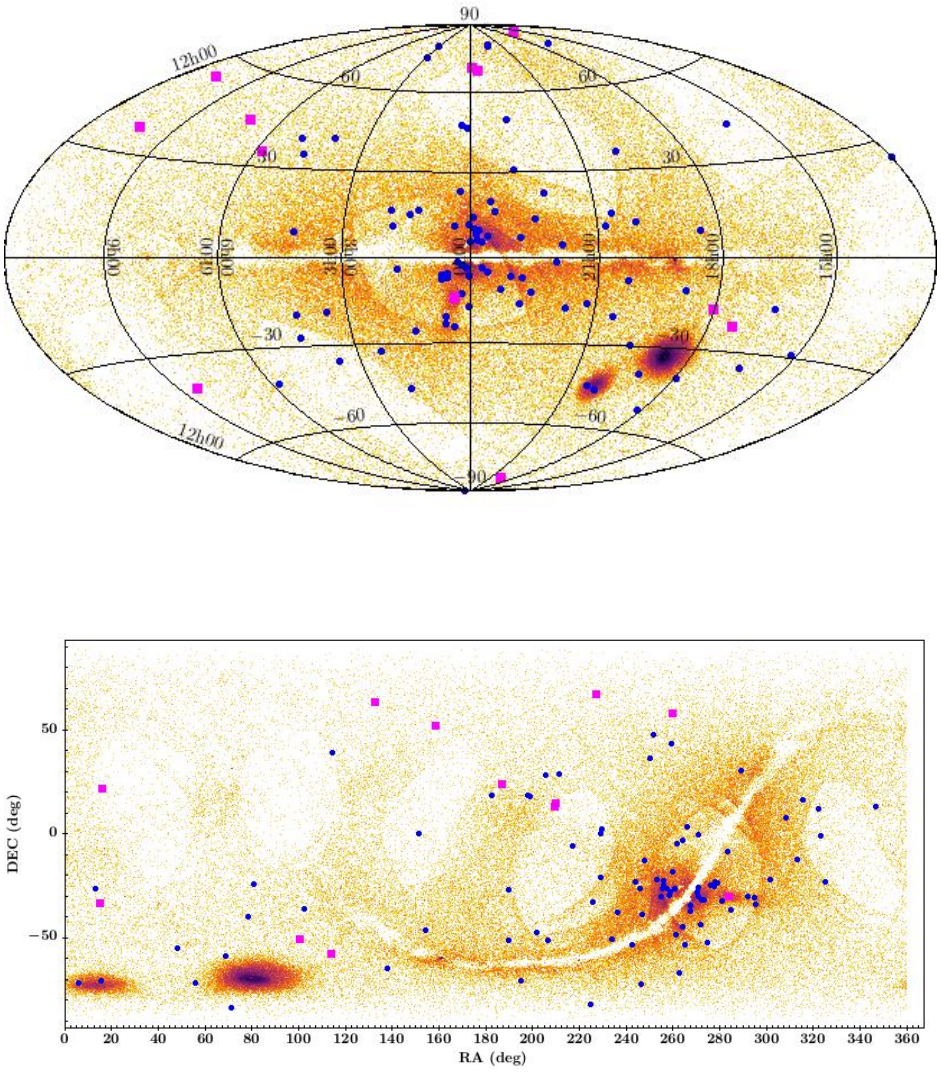

FIGURE 3.18: *Top:* Distribution on the sky of 140,784 SOS-confirmed (known and new) RRLs in Galactic coordinates. Blue and magenta symbols mark 87 globular clusters and 12 (classical and ultra-faint) dwarf spheroidal galaxies in which *Gaia* has observed RRLs that are confirmed by the SOS Cep&RRL pipeline. *Bottom:* Same as in the top panel but in equatorial coordinates. Figure from Clementini et al. (2018).

observed by *Gaia* are plotted as large black filled circles in the map in Figure 3.20, where different colours are used for stars at different distance from the M3 centre ($< r_c$, red; $< 2r_c$, grey; $< r_h$, yellow; $< 2r_h$; cyan and $> 2r_h$, magenta). Centre and right panels of Figure 3.20 show the *Gaia* CMD of M3 using the same colour-coding as in the left panel. The RRLs brighter than the cluster HB level in the right panel of Fig. 3.20 are located closer to the cluster centre where their G_{BP} photometry is more likely to be contaminated by companions. The effect of contamination by companions in the M3 central regions is better seen in the two panels of Figure 3.21 which show an enlargement of the HB region in the *Gaia* CMD of the cluster. Although the *Gaia* photometry may suffer from blending in crowded regions like the centre of a globular cluster, the periods measured by the SOS Cep&RRL pipeline and the literature periods for the 159 RRLs observed in M3 by *Gaia* are in excellent agreement, as shown by Figure 3.22. The three *outliers* in the figure are RRLs known to be affected by Blažko effect (Blazhko 1907), a modulation of shape and amplitude of the light variation that may occur on

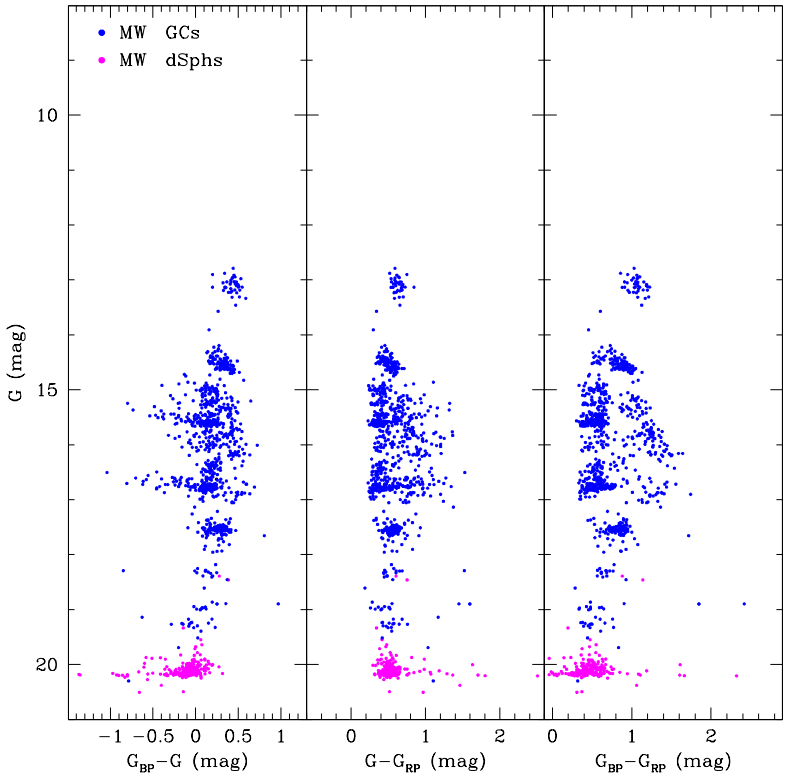

FIGURE 3.19: G, $G_{BP}-G$; G, $G-G_{RP}$; and G, $G_{BP}-G_{RP}$ CMDs of RRLs confirmed by the SOS Cep&RRL pipeline for which the colour information is available (1,167 sources out of 1,986) that are in GCs (blue points) and dSphs (magenta points). Each concentration of blue points corresponds to a different GC. The magenta overdensity below $G \sim 20$ mag is due to RRLs in the Draco and Sculptor dSphs. Adapted from Clementini et al. (2018).

time span ranging from a few tens to hundreds of day[23]. The SOS Cep&RRL pipeline computed also stellar parameters (e.g., the G-band absorption for 54,272 RRab stars, and metallicity,[Fe/H], for 64,932 RRLs from the ϕ_{31} Fourier parameter of the G-band light curves). Metal abundances were measured for 111 RRLs in M3. The corresponding metallicity distribution is shown in Figure 3.23.

We made similar comparisons also for M62, a likely core-collapsed GC with c=1.71, r_c = 0.22 arcmin and r_h=0.92 arcmin (Harris 1996). Due to higher concentration, only 91 out of 214 ($\sim$ 42.5%) RRLs known in M62 were recovered, to compare with 71.6% in M3 that hosts the same RRL population. Their metallicity distribution is shown in the histogram plotted in Fig. 3.24.

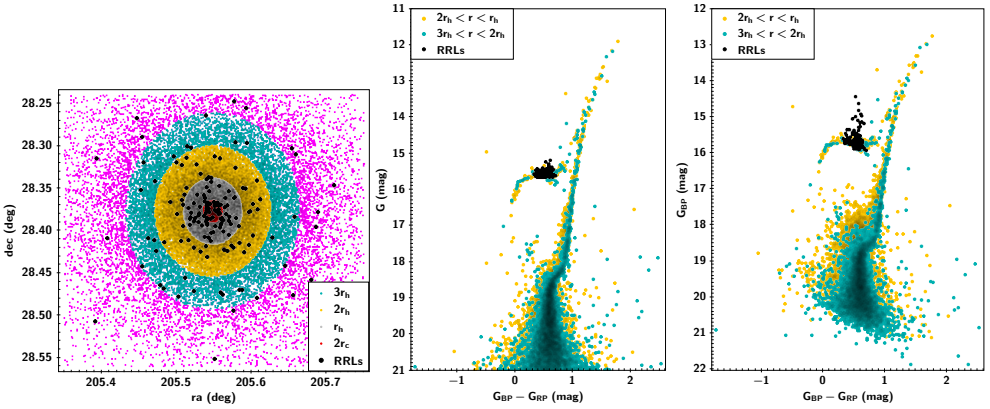

FIGURE 3.20: *Left panel*: Map of *Gaia* DR2 stars in a 0.31 × 0.30 degree^2 area centred on the Galactic globular cluster M3. Different colours highlight stars within twice the cluster r_c (red filled circles), once (grey filled circles), twice (yellow filled cicles), three times (cyan filled circles) the cluster half-light radius (r_h=2.31 arcmin) and beyond $3 \times r_h$ (magenta filled circles). The RRLs observed by *Gaia* in the cluster (159 over the 222 RRLs known in M3) are marked as large black filled circles. The M3 centre coordinates and r_c, r_h values are from Harris (1996). *Centre panel*: G vs (G_{BP} - G_{RP}) CMD for stars within twice the M3 r_h, colour-coding is as in the left panel. *Right panel*: Same as in the centre panel but for the cluster G_{BP} vs (G_{BP} - G_{RP}) CMD. Figure from Clementini et al. (2018).

More than 200 RRLs are known in the Sculptor dSph from the study of Kaluzny et al. (1995). We recovered 176 of them by cross-matching the SOS confirmed RRLs against Kaluzny et al. (1995)'s catalogue, that remains so far the only study where identification and coordinates for the Sculptor variable stars have been published. As done for M3,

[23]Star by star comparison: V79, Clement et al. (2001) first revealed that this star switched from single-mode first overtone to double-mode pulsation. Benkő et al. (2006) confirm the classification of V79 as a double-mode RRL (RRd). Even if the SOS pipeline gives for V79 a classification as RRab star, the published SOS period, P_{SOS} = 0.48323 d, is in agreement with the P0 provided by Benkő et al. (2006), that is 0.47881 d. V170, the SOS pipeline provides for V170 a classification as RRab star. Looking at the light curve Benkő et al. (2006) noticed that has an asymmetric shape with amplitude between RRab and RRc stars. They suggest that it may be an evolved RRL, in addition this star is blended with another M3 RRL, V136. V180, is affected by Blažko modulation (Benkő et al. 2006).

Figure 3.25 shows the comparison between the periods measured by the SOS Cep&RRL pipeline and the literature periods for more then 100 RRLs observed in Sculptor. Also in this case results are impressive, considering that Sculptor's RRLs are $\sim$ 4 mag fainter than the M3 HB level and only 0.8-1 mag brighter than the *Gaia* limiting magnitude.

In Sculptor after cross-matching with the Kaluzny et al. (1995) catalogue of 226 RRLs, we found a large number of new RRLs, placed in the same area of the known RRLs around the Sculptor centre and beyond the galaxy's half-light radius (r_h=11.30 arcmin, McConnachie 2012), which potentially are Sculptor members.

Figure 3.26 shows the *G*-band Period-Amplitude diagram defined by the Sculptor RRLs,

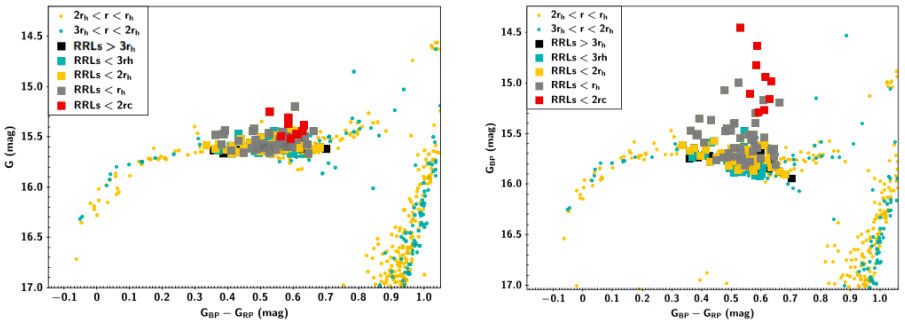

FIGURE 3.21: *Right panel:* Zoom of the HB region in the G vs (G_{BP} - G_{RP}) CMD of M3. RRLs are plotted as filled squares and different colours according to their position with respect to the cluster centre, adopting the same colour-coding as in the left panel of Fig. 3.20 and using black filled squares for the variables beyond $3 \times r_h$. *Left panel:* Same as in the left panel but for the G_{BP} vs (G_{BP} - G_{RP}) CMD. Figure from Clementini et al. (2018).

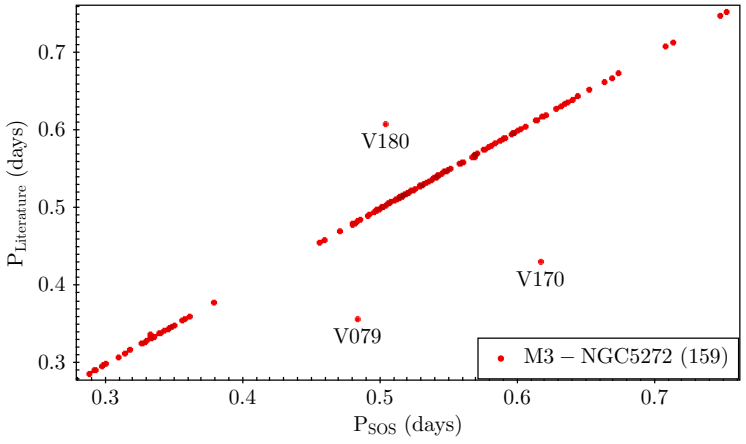

FIGURE 3.22: Comparison between periods measured by the SOS Cep&RRL pipeline and literature periods for 159 RRLs observed in M3 by *Gaia*. The three deviating objects are variable stars affected by the Blažko effect (Blazhko 1907). Figure from Clementini et al. (2018).

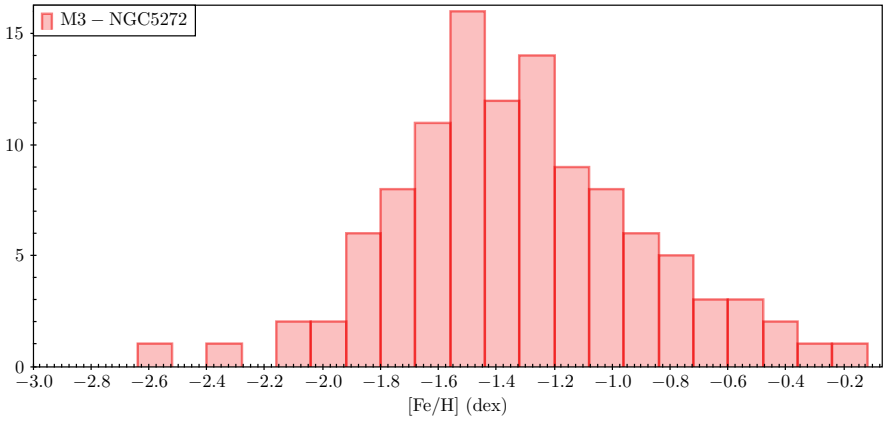

FIGURE 3.23: Metallicity distribution of the RRLs observed by *Gaia* in M3, based on individual estimates from the SOS Cep&RRL pipeline. Figure from Clementini et al. (2018).

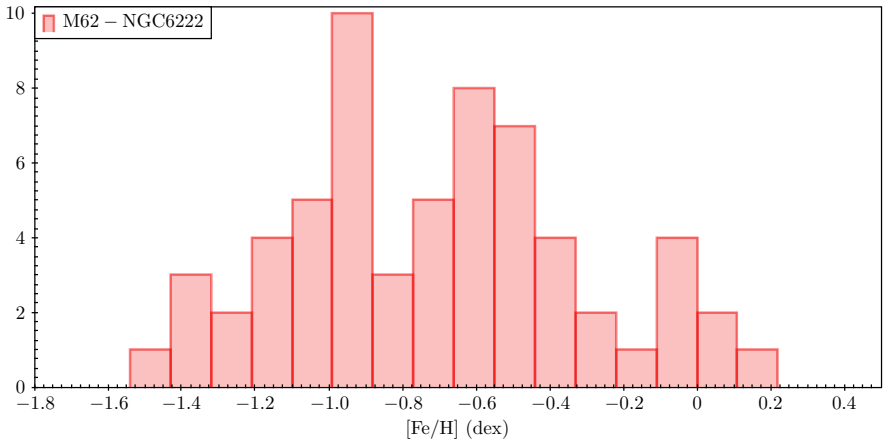

FIGURE 3.24: Metallicity distribution of the RRLs observed by *Gaia* in M62, based on individual estimates from the SOS Cep&RRL pipeline.

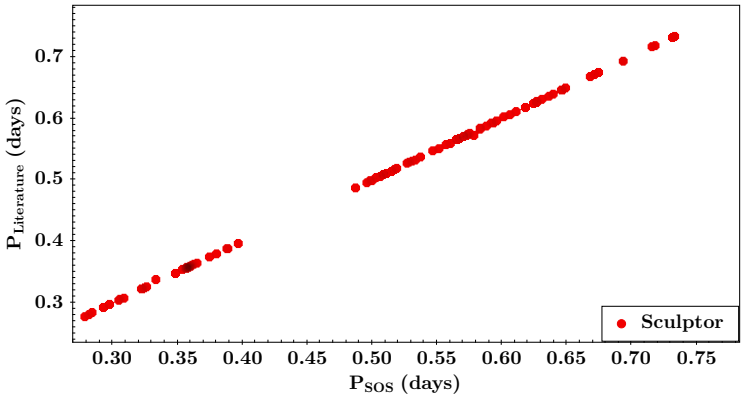

FIGURE 3.25: Comparison between periods measured by the SOS Cep&RRL pipeline and literature periods for RRLs observed by *Gaia* in the Sculptor dSph.

where filled symbols are known variables that cross-match with Kaluzny et al. (1995) catalogue, while open symbols are new RRLs observed by *Gaia*. Blue, red and grey symbols are RRc, RRd and RRab stars, respectively. The new RRLs populate the same loci occupied by the known RRLs, thus confirming their membership to the Sculptor dSph.

Finally, metal abundances were measured from the ϕ_{31} Fourier parameter for 102 RRLs in Sculptor. Figure 3.27 shows that a good agreement is found between the individual metallicities estimated by the SOS Cep&RRL pipeline (blue histogram) and the corresponding spectroscopic metallicities from Clementini et al. (2005) (red histogram). For a more direct comparison in Table 3.5, we list for a few GCs and dSphs the mean

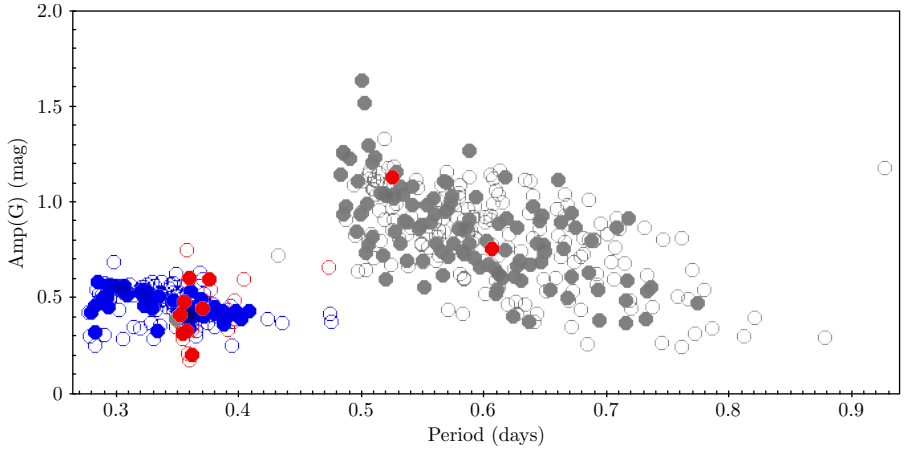

FIGURE 3.26: Period-Amplitude diagram in the G band of known (filled circles; Kaluzny et al. 1995) and new (empty circles) RRLs observed by *Gaia* in the Sculptor dSph. Blue, red and grey symbols are RRc, RRd and RRab stars, respectively. Figure from Clementini et al. (2018).

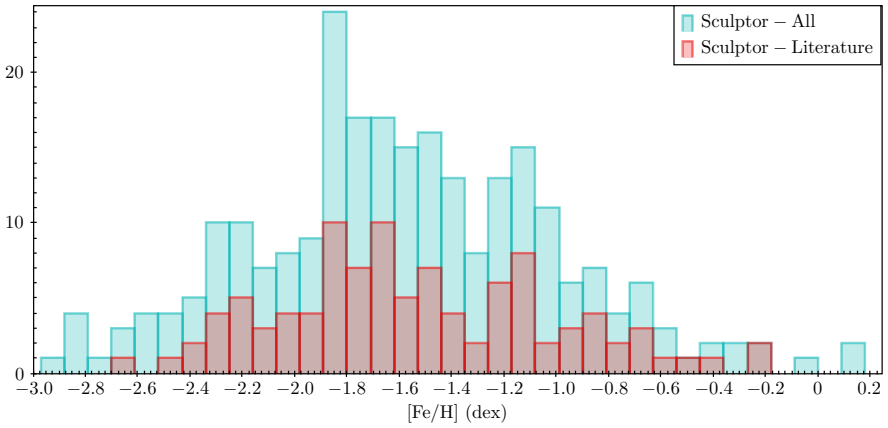

FIGURE 3.27: Metallicity distribution of RRLs in Sculptor. The blue histogram is obtained from metallicities estimated by the SOS Cep&RRL pipeline. The red histogram shows the metallicity distribution of the RRLs studied spectroscopically by Clementini et al. (2005). Figure from Clementini et al. (2018).

metallicity and G-band absorption (with the related standard deviations) as derived averaging individual [Fe/H] and A(G) values inferred from the RRLs by the SOS Cep&RRL pipeline (columns 3, 4 and 6, 7, respectively) and the corresponding literature reference values (Carretta et al. 2009 for GCs, Clementini et al. 2005 and Kirby et al. 2011, for RRLs in Sculptor, Draco, UMa I, UMa II, respectively) while column 10 reports the literature reference corresponding to the RRL catalogue adopted for each GC or dSph. In the table, N1 and N2 are the number of variable stars on which the mean quantities were computed. Overall, the agreement is quite satisfactory. On the other hand, the rather high value of A(G) derived for Sculptor is likely due to the poor S/N of the G_{BP}, G_{RP} photometry at the faint magnitudes of the RRLs in this dSph.

Examples of RRL light curves in the GGCs M3 and M62 and in the Sculptor dSph are shown in Figure 3.28. In all plots the light curves are folded according to the period and epoch of maximum light in the G, G_{BP} and G_{RP} bands, respectively, computed by the SOS Cep&RRL pipeline.

TABLE 3.5: Mean metallicity and absorption in the G-band for 10 GCs and 4 dSphs, obtained by averaging individual values for RRLs derived by the SOS Cep&RRL pipeline.

Name	$[Fe/H]_{C09}$ dex	$[Fe/H]_{Gaia}$ dex	stdev($[Fe/H]_{Gaia}$) dex	N_1	$A(G)$ mag	stdev[$A(G)$] mag	$A(V)$ mag	N_2	Ref.
NGC1261	-1.27	-1.33	± 0.55	14	1.07	± 1.33	0.03	10	(1)
NGC1851	-1.18	-1.17	± 0.48	9	0.46	± 0.34	0.06	8	(2)
NGC288	-1.32	-1.33	± 0.22	1	0.17		0.09	1	(3)
NGC3201	-1.59	-1.30	± 0.04	82	0.67	± 0.21	0.74	73	(4)
NGC5024	-2.10	-1.62	± 0.48	8	0.73	± 0.75	0.06	20	(5)
NGC5139- ω Cen	-1.53	-1.17	± 0.79	8	0.32	± 0.14	0.37	9	(6)
NGC5272-M3	-1.50	-1.32	± 0.43	111	0.49	± 0.87	0.03	92	(7)
NGC6266-M62	-1.18	-0.71	± 0.39	81	2.18	± 0.78	1.46	52	(8)
IC4499	-1.53	-1.47	± 0.53	56	0.81	± 0.35	0.71	54	(9)
NGC7078-M15	-2.37	-1.26	± 0.87	5	0.22		0.31	1	(10)
Sculptor	-1.68	-1.52	± 0.53	102	0.68	± 0.43	0.06	105	(11)
Draco	-1.93	-1.70	± 0.74	30	0.54	± 0.32	0.09	13	(12)
Ursa Major I	-2.18	-1.92	± 0.18	2	0.53	± 0.05	0.02	2	(13)
Ursa Major II	-2.47	-2.28	± 0.23	1	0.33		0.30	1	(14)

N_1 and N_2 are, respectively, the number of RRLs on which the mean [Fe/H] and $A(G)$ values were computed. **References:** (1)Salinas et al. (2016); (2)Walker (1998); (3)Kaluzny et al. (1995), Arellano Ferro et al. (2013); (4)Layden & Sarajedini (2003), Arellano Ferro et al. (2014); (5)Cuffey (1966), Goranskij (1976), Arellano Ferro et al. (2011); (6)Braga et al. (2016); (7)Benkő et al. (2006); (8)Contreras et al. (2010); (9)Walker & Nemec (1996); (10)Corwin et al. (2008); (11)Kaluzny et al. (1995), Clementini et al. (2005); (12)Kinemuchi et al. (2008); (13)Garofalo et al. (2013); (14)Dall'Ora et al. (2012).

3.7 Validation of Gaia DR2 parallaxes: testing ϖ_{Gaia} with RR Lyrae stars

3.7.1 RRL sample

Use of an RRL catalogue as much as possible homogeneous and extended is the first step to properly test ϖ_{Gaia} and minimize bias factors. That is why, as in Gaia Collaboration

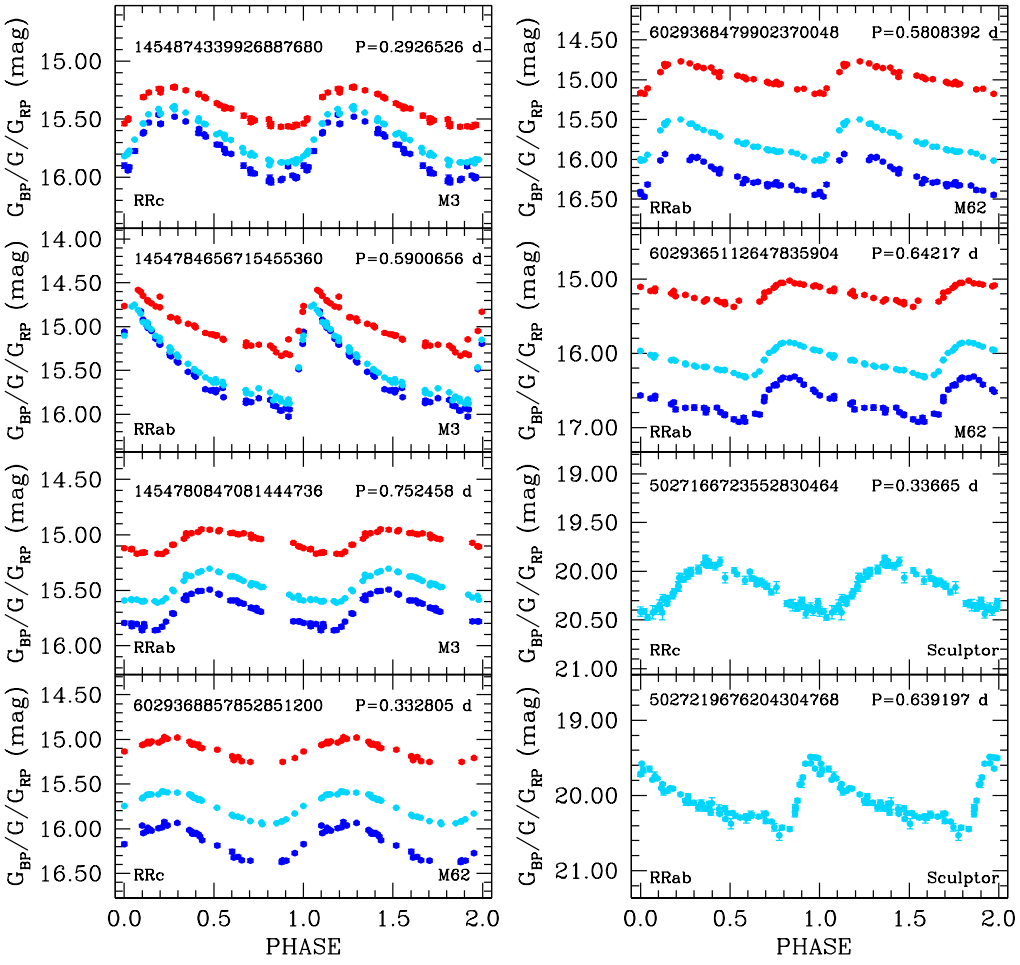

FIGURE 3.28: G (cyan), G_{BP} (blue) and G_{RP} (red) light curves of RRLs of different pulsation mode in the Galactic globular clusters M3 and M62 and in the Sculptor dSph galaxy (G-band only), released in DR2. Gaia DR2 1457784656715455360 is located within the M3 half-light radius (r_h =2.31 arcmin, Harris 1996), star # 6029368479902370048 is within twice the r_h of M62 (r_h =0.92 arcmin, Harris 1996). *Gaia* DR2 5027166723552830464 in Sculptor is a new discovery by *Gaia*. Only the G-band light curves are shown for Sculptor, because of the low S/N of the G_{BP} and G_{RP} time-series data at the faint magnitudes of the RRLs in this galaxy. The multi-band time series data are folded according to the period and epoch of maximum light derived by the SOS Cep&RRL pipeline. Error bars are comparable to or smaller than symbol size. Figure from Clementini et al. (2018).

et al. (2017), we adopted the Dambis et al. (2013) catalogue having period, pulsation mode, multi-band intensity-averaged magnitudes (V, K_S from 2MASS and W_1 from WISE) absorption in the V-band A(V) and metal abundance [Fe/H] for 403 MW field RRLs. Here we recall that 32 RRLs in the Dambis et al. (2013) sample do not have phase corrections of the 2MASS magnitudes (see Sec. 3.5.4), hence we adopted for these stars the single-epoch K_S magnitudes. Given that the largest amplitude of RRLs in the K_S band is ~ 0.35 mag (Feast et al. 2008) for these 32 RRLs we assume an uncertainty for the mean K_S magnitude of 0.175 mag, that is half the maximum amplitude. Since Dambis et al. (2013) do not provide individual uncertainties for periods, absorption values and metallicities, in our analysis we assumed the following uncertainties relative to these quantities:

- period uncertainties of 1% in the decadic logarithm;
- reddening uncertainties in V-band computed as 0.16 $\times$ E(B-V) from Schlegel et al. (1998)
- Dambis et al. (2013)'s metallicities are provided on Zinn & West (1984) metallicity scale. They are a combination of spectroscopic and photometric measurements. We adopted 0.1 dex, 0.2 dex and 0.3 dex as the uncertainty in metallicity of stars that have metal abundance from high-resolution spectroscopy, from mid-low resolution spectroscopy (or for which we have not found the source of metallicity estimate), from photometry or from other non-spectroscopic methods, respectively.

In addition, since the intensity-averaged W_1 magnitudes in the Dambis et al. (2013) catalogue were inferred from WISE single-exposure data, we put an additional uncertainty of 0.02 mag to the uncertainties of the mean W_1 magnitudes (to a specific request by the referee). Furthermore between *Gaia* first and second data releases we became aware of updated parameter values for some RRLs included in the Dambis et al. (2013) sample (J. Lub, private communication). Following these updates, we adopted a different period value for six RRLs (namely, DH Peg, ER Aps, DN Aqr, DM Cyg, DD Hya, DH Hya), and the pulsation mode of DH Peg was changed to RRc accordingly. The extinction values of CG Lib and RZ Cep were also revised. Finally, BB Vir turned out to be a blend of two stars, hence was discarded. On the other hand, the rather long period of BI Tel (P=1.17 days) would place the star in the anomalous Cepheid domain.

Hence, we decided to discard this RRL as well. The final Dambis et al. (2013)'s sample that we thereby cross-matched with the *Gaia* DR2 catalogue consists of 401 RRLs. We re-covered the DR2 parallaxes for all of them. They span the range from −2.61 to 2.68 mas, with seven RRLs having a negative parallax value, among which, RR Lyr itself, the RRL that gives its name to the whole class (see Section 3.7.2). The distribution in uncertainty of the *Gaia* DR2 parallaxes (ϖ_{DR2}) for our sample of 401 RRLs is shown by the red histogram in Figure 3.29. Values range from 0.01 to 0.61 mas. The comparison with the distribution of the TGAS parallax uncertainties for the subsample of 199 RRLs for which TGAS parallaxes were released in DR1 (blue histogram) clearly shows the improved of DR2 parallax values compared to DR1.

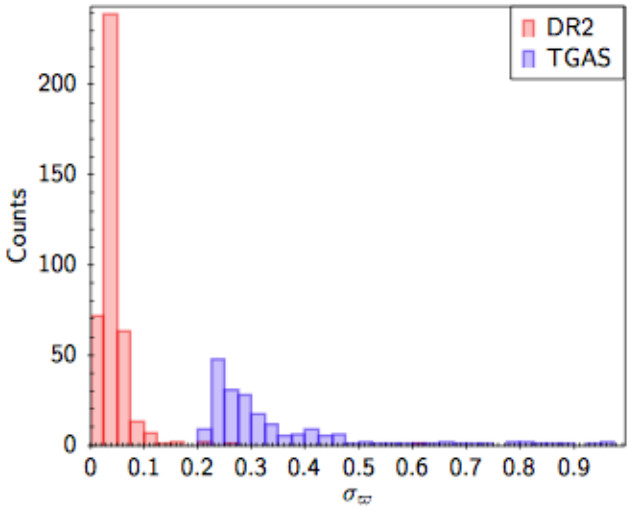

FIGURE 3.29: Distributions of the ϖ_{DR2} uncertainties for the sample of 401 RRLs (red histogram) and of the ϖ_{TGAS} uncertainties for the subsample of 199 RRLs for which TGAS parallaxes were published in *Gaia* DR1 (blue histogram). The bin size is 0.025 mas. Figure from Muraveva et al. (2018b).

Possible selection biases can mainly be resulting from sample selection applied by Dambis et al. (2013). Figure 3.30 shows the mean magnitude $< V >$, period and metallicity of our sample of 401 RRLs in the upper, middle and lower panels, respectively. Periods range from 0.25 to 0.96 d. [Fe/H] range from −2.84 to +0.07 dex. The distribution in $< V >$ magnitude transformed into a distribution in distance moduli (using the mean V absolute magnitude value M_V =0.59 mag at [Fe/H]=-1.5 dex from Clementini et al. 2003) returns a distribution in distances ranging from about 250 to about 16,000 pc. Such wide ranges in period, metallicity and distance along with the all sky average of our sample (see Figure 3.9, Sec. 3.5) make our dataset free from selection effects and

hence a valid sample to calibrate both slope and zero-point of the $M_V - [\mathrm{Fe/H}]$, PM_KZ and PMW_1Z relations of RRLs, and derive for the first time the LZ relation in the *Gaia* G-band: $M_G - [\mathrm{Fe/H}]$.

3.7.2 DR2 parallaxes versus Hipparcos, TGAS and HST

TABLE 3.6: *Hipparcos*, HST, TGAS and DR2 parallaxes for RRLs

Name	$\varpi_{\mathrm{Hipparcos}}$ (mas)	$\sigma\varpi_{\mathrm{Hipparcos}}$ (mas)	ϖ_{TGAS} (mas)	$\sigma\varpi_{\mathrm{TGAS}}$ (mas)	ϖ_{HST} (mas)	$\sigma\varpi_{\mathrm{HST}}$ (mas)	ϖ_{DR2} (mas)	$\sigma\varpi_{\mathrm{DR2}}$ (mas)
RR Lyr	3.46	±0.64	3.64	±0.23	3.77	±0.13	-2.61	±0.61
RZ Cep	0.59	±1.48	2.65	±0.24	2.12 (2.54)*	±0.16	2.36	±0.03
SU Dra	0.20	±1.13	1.43	±0.29	1.42	±0.16	1.40	±0.03
UV Oct	2.44	±0.81	2.02	±0.22	1.71	±0.10	1.89	±0.03
XZ Cyg	2.29	±0.84	1.56	±0.23	1.67	±0.17	1.57	±0.03

* Two different parallax values are provided for this star by Benedict et al. (2011); in the table we list both values.

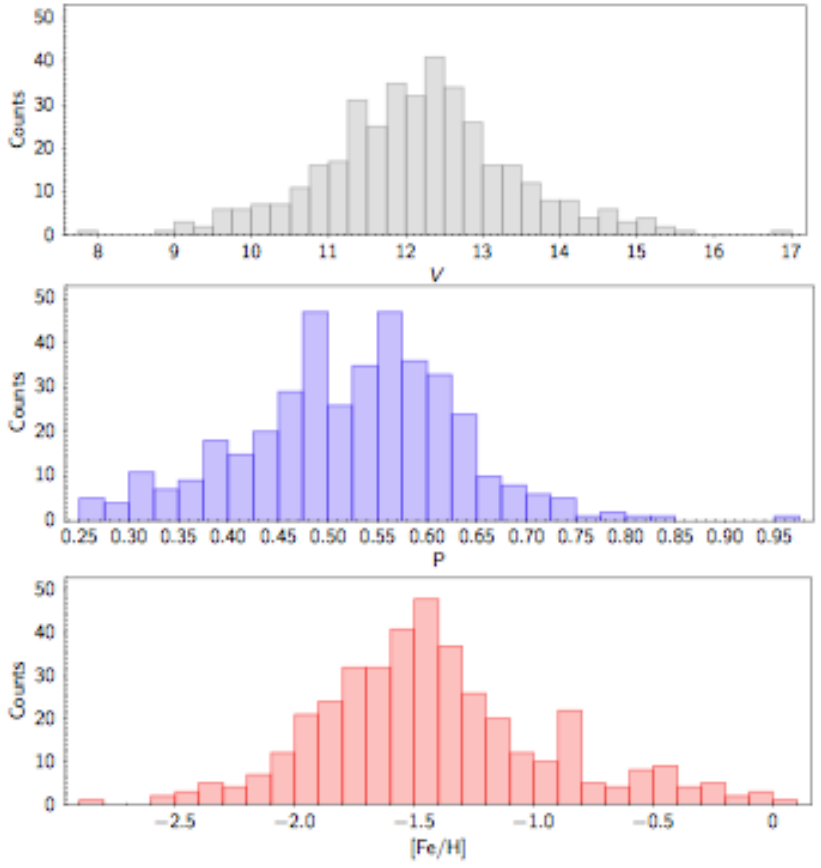

FIGURE 3.30: Distribution of $< V >$ (upper panel), period (middle panel) and metallicity values (lower panel) for the RRLs in our sample. $< V >$ magnitudes are available for 382 RRLs out of 401 RRLs, metallicities for 400 RRLs and pulsation periods for the whole sample. Figure from Muraveva et al. (2018b).

As we have done for DR1 (see Section 3.5.2.2) in Table 3.6 we have compared the *Gaia* DR2 parallaxes with the *Hipparcos*, HST, TGAS values for five RRLs for which all these measurements are available. There is a general agreement between the HST, TGAS and DR2 parallaxes except for RR Lyr itself.

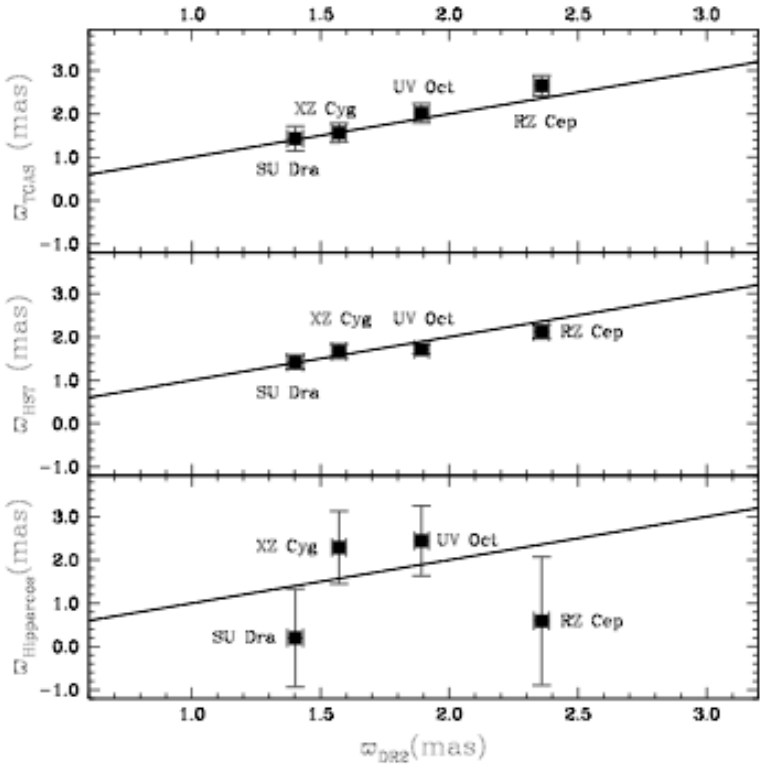

FIGURE 3.31: Comparison between the DR2 and TGAS (upper panel), DR2 and HST (middle panel), and DR2 and *Hipparcos* (lower panel) parallaxes for RRLs. The HST values are from Benedict et al. (2011). RR Lyr was omitted (see text for the details). The solid lines represent the bisectors. Figure from Muraveva et al. (2018b).

The DR2 parallax of RR Lyr has a large negative value (-2.61 ± 0.61 mas) that it is clearly wrong and deviates significantly from the TGAS parallax estimate (3.64 ± 0.23 mas). The wrong DR2 parallax of RR Lyr was caused by an incorrect estimation of the star's mean G magnitude (17.04 mag, which is $\sim$ 10 mag fainter than the star's true magnitude), which induced an incorrect estimation of the magnitude-dependent term applied in the astrometric instrument calibration (Arenou et al. 2018, Gaia Collaboration et al. 2018a).Fig. 3.31 shows, from top to bottom panels, the TGAS, HST and *Hipparcos* parallaxes plotted versus *Gaia* DR2 values for 4 of the RRLs (that is excluding RR Lyr). While agreement between the *Gaia* DR2 and *Hipparcos* parallaxes (lower panel) exists only for two RRLs, a good agreement is found between both TGAS and DR2 parallaxes (upper panel) and the DR2 and HST parallaxes (middle panel). However, the sample

of RRLs with both DR2 and HST parallax estimates is too small to measure possible zero-point offsets of the *Gaia* parallaxes with respect to HST[24].

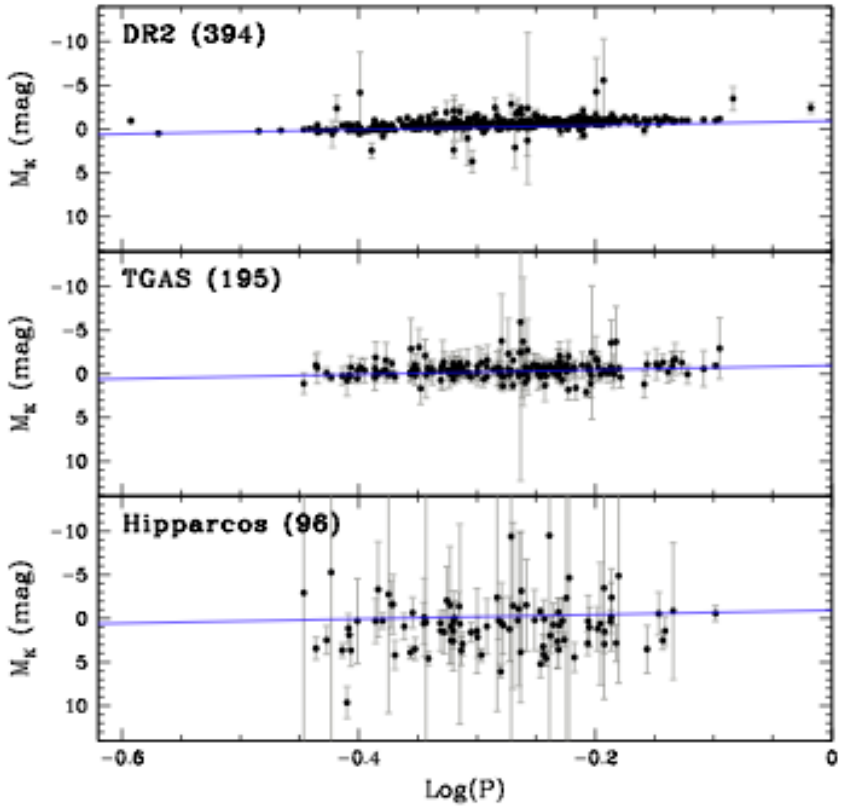

FIGURE 3.32: RRL PM_K distributions obtained inferring the absolute magnitudes in the K_S-band (M_K) by direct transformation of the *Gaia* DR2 (upper panel), TGAS (middle panel) and *Hipparcos* (lower panel) parallaxes using Eq. 3.1. Blue lines represent the PM_K relation as described by eq. 14 from Muraveva et al. (2015). Figure from Muraveva et al. (2018b), adapted from Gaia Collaboration et al. (2017).

Figure 3.12 in Section 3.5.4 shows the remarkable improvement of the RRL PM_{Ks} relation going from the *Hipparcos* to the TGAS parallaxes. In Figure 3.32 we extend this comparison including also the DR2 parallaxes. Once again we transformed the trigonometric parallaxes to the corresponding absolute M_{Ks} magnitudes using the canonical relation in Eq. 3.1. This transformation is possible only for 394, 195 and 96 RRLs in our sample, for which positive parallaxes are available in the DR2, TGAS and *Hipparcos* catalogues, respectively. We corrected the apparent K_S mean magnitudes for absorption and *fundamentalized* the RRc stars by adding +0.127 to the logarithm of the period. Results from this comparison are presented in Figure 3.32: the PM_{Ks} relation in the

[24]For the sake of completeness, Arenou et al. (2018) found a negligible (-0.01 ± 0.02 mas) offset between the HST and DR2 parallaxes using a sample of stars significantly larger than the 4 RRLs we considered here.

upper panel shows the significant improvement of the DR2 parallaxes with respect to the TGAS (middle panel) and *Hipparcos* (lower panel) measurements. Blue lines are the PM_{Ks} relations provided by eq. 14 in Muraveva et al. (2015)[25].

3.7.3 RRL M_V − [Fe/H], M_G − [Fe/H], PM_KZ and PMW_1Z relations

3.7.3.1 M_V − [Fe/H] relation

We computed slope (α) and zero point (β) of the M_V − [Fe/H] relation using 381 RRLs, out of our sample of 401 with DR2 parallaxes, applying the Bayesian approach described in Muraveva et al. (2018b) and, more in details in Delgado et al. (2018). These 381 RRLs have all relevant information: ($< V >$, A_V, [Fe/H] and ϖ_{DR2} values). We obtain a metallicity slope $\alpha = 0.40 \pm 0.03$ mag/dex, that implies a much stronger dependence of the RRLs absolute V magnitude on metallicity than ever reported previously in the literature. We explored two possible causes of the rather large value of α: (i) a flaw in the Bayesian procedure we have adopted, or (ii) an offset affecting the DR2 parallaxes. To check case (i) the Bayesian procedure was applied to semi-synthetic data[26] and showed that Bayesian model is not the cause for the slope being higher than expected (according to the previous studies), but rather reflects the real nature of data.

An important limitation of the Dambis et al. (2013) sample is that metallicities are from a collection of rather inhomogeneous literature measurements either derived from photometry, or from low and high resolution spectroscopy. To check whether this might affect our dataset, hence bias our results, we extracted a sub-sample of 23 MW RRLs from our dataset of 401 variables for which homogeneous metallicities (and related uncertainties) based on abundance analysis of high-resolution spectroscopy are available from the studies of Clementini et al. (1995) and Lambert et al. (1996). Figure 3.33 shows their distribution on the sky (top panel) whereas the bottom panels show their $< V >$, period and metallicity distributions. The ranges covered by the $< V >$ magnitude and period (from 9.55 to 12.04 mag in V and from 0.31 to 0.71 d in P, respectively) are narrower than for our full sample (see upper and middle panels of Figure 3.30); instead, metallicities for these 23 RRLs range from −2.5 to +0.17 dex, which is comparable with

[25] $M_K = -2.53\log(\mathrm{P}) - 0.95$

[26] The aim with this semi-synthetic data is to evaluate the capability of our methodology to recover unbiased estimates of the true parameters, in particular of the relationship slope. Details on criteria to the semi-synthetic data creation and results are described in sec. 5.1 of Muraveva et al. (2018b).

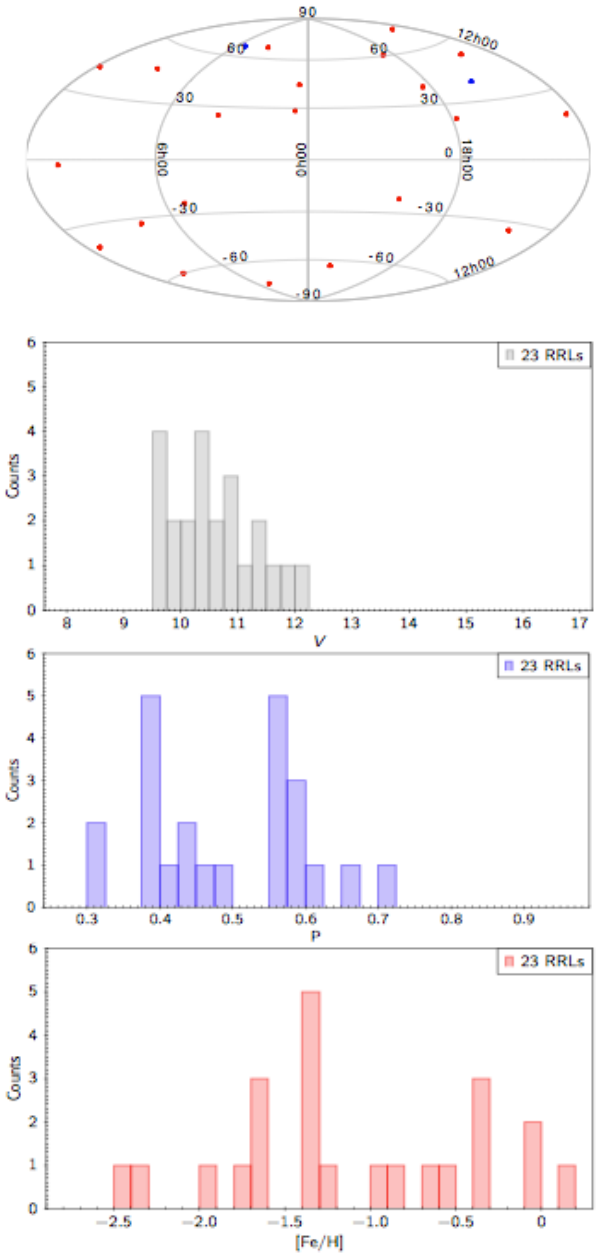

FIGURE 3.33: *Top panel*: Sky distribution in Galactic coordinates of 23 RRLs with metallicities measured from high resolution spectra. Red and blue filled circles show RRab and RRc stars, respectively. *Bottom panels*: $< V >$, period and metallicity distributions of the 23 RRLs. The abscissa axes are in the same scales as in Fig. 3.30. Figures from Muraveva et al. (2018b).

the range of metallicities spanned by the full sample (see bottom panel of Fig. 3.30). Applying our Bayesian approach to the sample of 23 RRLs we obtained $\alpha = 0.27 \pm 0.06$ that is shallower than obtained from the whole sample of 381 RRLs. This likely thanks to the use of those more accurate and homogeneous spectroscopic metallicities, but even in almost perfect agreement with the value obtained by Catelan et al. (2004, see eq.(7)) still steeper than found in many studies of the recent literature (although in marginal agreement within the uncertainties).

The other possible cause of the high slope we find for the RRL $M_V - [\mathrm{Fe/H}]$ relation may be an offset in the *Gaia* DR2 parallaxes. We examined whether the zero-point offset in the *Gaia* DR2 parallaxes can affect not only the slope but also the zero-point of the $M_V - [\mathrm{Fe/H}]$ relation. Arenou et al. (2018) in their paper describing the final validation of all data products published in *Gaia* DR2 estimate an offset $\delta\varpi_0 = -0.056 \pm 0.005$ mas to affect the RRL parallaxes in the *Gaia* DR2 catalogue and an offset of -0.033 ± 0.009 mas for a sub-sample of RRLs in the GCVS catalogue. Keeping in mind that due to the logarithmic term in Eq. 3.1, a given parallax offset does not affect equally the absolute magnitudes; our RRLs are in a relatively metal-rich area of the MW, while farther RRLs in our sample belong to the halo and likely are more metal-poor. Hence, a negative zero-point offset, as the one found by Arenou et al. (2018) will make farther/metal-poor RRLs appear intrinsically brighter, hence causing an overestimation of α in the $M_V - [\mathrm{Fe/H}]$ relation. Therefore, the effect of a potential parallax offset must be included in the analysis. We found that for the whole sample of RRLs the slope of the relation decreases from $\alpha = 0.40$ (no offset), to $\alpha = 0.37$ for an offset of -0.03 mas. Applying the same Bayesian model to the sub-sample of 23 RRLs (with homogeneous metallicity estimations), assuming either no parallax offset or an offset of -0.03 mas, the slope of the $M_V - [\mathrm{Fe/H}]$ relation varies from 0.27 (no offset) to 0.26 (offset of -0.03 mas), showing that for the sample of 23 RRLs, covering a much smaller range of distances than the full sample, the impact of a potential parallax offset on the slope of the $M_V - [\mathrm{Fe/H}]$ relation is reduced. In the BA model the parallax offset can be included and treated as a parameter to be determined by the model or, conversely, fixed to a predefined value. From our sample of 381 RRLs we obtained a mean posterior metallicity slope of 0.34 for an inferred mean offset of -0.062 mas (first row in Table A.4 in Appendix A). The resulting $M_V - [\mathrm{Fe/H}]$ fit is shown in Figure 3.34, where colours encode the (natural)

logarithm of the inferred distance. We applied the same BA model to the sample of 23 MW RRLs.

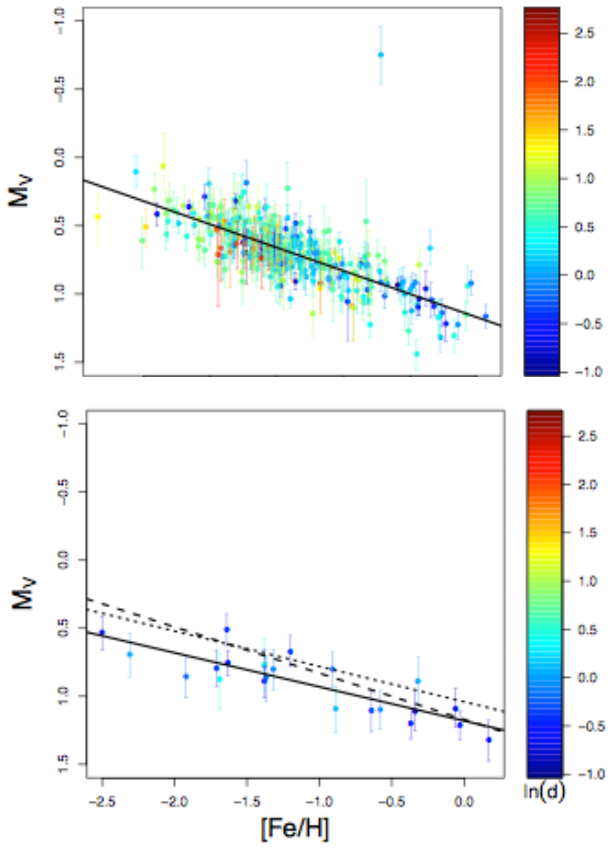

FIGURE 3.34: *Top panel*: M_V − [Fe/H] relation defined by the 381 RRLs in our sample. The absolute magnitudes M_V were inferred from the BA model. The solid line represents the linear fit. Its slope and zero-point are summarised in Table A.4 (first row). The colour scale encodes the (natural) logarithm of the inferred distance measured in units of kpc. *Bottom panel*: Same as in the top panel but for a sample of 23 RRLs with metallicity from high resolution spectroscopy. Figures from Muraveva et al. (2018b).

In this case the reduced number of sources and the smaller range in distance do not constrain the value of the offset, giving an unrealistic mean offset of −0.142±0.06 (first row in the mid portion of Table A.4) and a metallicity slope of 0.25±0.05 mag/dex.

The first row in the lower portion of Table A.4 summarises the M_V − [Fe/H] relations obtained adopting for the parallax offset a constant value =−0.057 mas, which corresponds to the mean of the offsets obtained from the full sample of RRLs fitting the linear M_V − [Fe/H] relation (−0.062 mas; this Section) and the PM_KZ, $PM_{W1}Z$ relations (−0.054 and −0.056 mas, respectively; next Sections). To conclude even though using the reduced sample of 23 RRLs has the advantage of (i) a smaller effect of the

parallax offset as the 23 RRLs are nearby stars; and (ii) a more accurate estimation of metallicity based on high-resolution spectroscopy, we must stress that selection effects can potentially be much stronger, as only nearby bright RRLs are characterised by high enough signal-to-noise ratios to be analysed with high-resolution spectroscopy, hence, biasing the results.

We used the relations summarised in Table A.4 to calculate the mean absolute magnitude of RRLs with metallicity [Fe/H]=−1.5 dex and found values of $M_V = 0.66 \pm 0.06$ and $M_V = 0.65 \pm 0.10$ based on the linear M_V − [Fe/H] relations inferred from the full RRL sample and the reduced sample of 23 RRLs with an adopted value of the parallax offset, respectively (column 6 of Table A.4). These values are in a very good agreement with each other and with the absolute magnitude found by Catelan & Cortés (2008) for RR Lyr ([Fe/H]=−1.48 dex), $M_V = 0.66 \pm 0.14$ mag.

Since a number of theoretical studies suggest a non-linear M_V − [Fe/H] relation, Table A.4 includes a summary of the posterior distributions of selected model parameters to infer a quadratic relationships between M_V and [Fe/H]. In the two datasets (381 and 23 RRL samples), the effect of including a second order term is to increase the mean value of the first order term posterior distribution from 0.34 to 0.39 (sample of 381 stars; row 2 in the upper portion of Table A.4) and from 0.25 to 0.41 (sample of 23 stars; row 2 in the mid portion of Table A.4). The comparison of the values (LMC distance moduli) obtained for the two models is inconclusive: the mean value of the paired differences is -4.4 ± 8.8 favouring the more complex (quadratic) model but with no statistical significance.

3.7.3.2 M_G − [Fe/H] relation

Only 306 sources in our sample are SOS-confirmed RRLs, hence their intensity-averaged mean G, G_{BP} and G_{RP} magnitudes are published in DR2. For a sub-sample of 160 RRLs among them G-band absorption values are also available. We used this sample of 160 RRLs along with their metallicities from Dambis et al. (2013) to infer the RRL M_G − [Fe/H] relation from the BA adopting a parallax offset of −0.057 mas. The resulting relation is presented in the last row portion of Table A.4 and graphically shown in Figure 3.35. The corresponding RRL G-band absolute magnitude at [Fe/H]=−1.5 dex is $M_G = 0.63 \pm 0.08$ mag, which is consistent with the V-band absolute magnitudes

derived in Sec. 3.7.3.1 and can be used to infer an approximate estimation of distance to RRLs whose apparent mean magnitude and extinction in the G-band are available in the *Gaia* DR2 catalogue.

3.7.3.3 $PM_{Ks}Z$ and PMW_1Z relations

PM_KZ and PMW_1Z relations were derived for the whole sample of RRLs (400 RRLs for the PMK_sZ relation and 397 RRLs for the PMW_1Z relation) and the subset of RRLs with metallicities from high resolution spectroscopy using the Bayesian approach and inferring the parallax zero-point offset from the BA model using the K_S and W_1 magnitudes (and related uncertainties) from Dambis et al. (2013).Rows 3 and 4 in the upper portion of Table A.4 list the slopes and zero-points of the resulting relations:

- for the PM_KZ relation, we derive a slope in period of -2.58 ± 0.20, which is very well consistent with the literature values that range from -2.101 (Bono et al. 2003) to -2.73 ± 0.25 (Muraveva et al. 2015), while the metallicity slope 0.17 ± 0.03 is higher than found in previous empirical studies but in excellent agreement with the theoretical findings (e.g. Bono et al. 2003, Catelan et al. 2004). The inferred parallax offset is -0.054 ± 0.006 mas.

- for the $PM_{W1}Z$ relation we derive a slope in period of -2.56 ± 0.19 which is slightly steeper than the literature values. We also find a non-negligible metallicity dependence of 0.17 ± 0.03, which is consistent with results from Neeley et al. (2017,

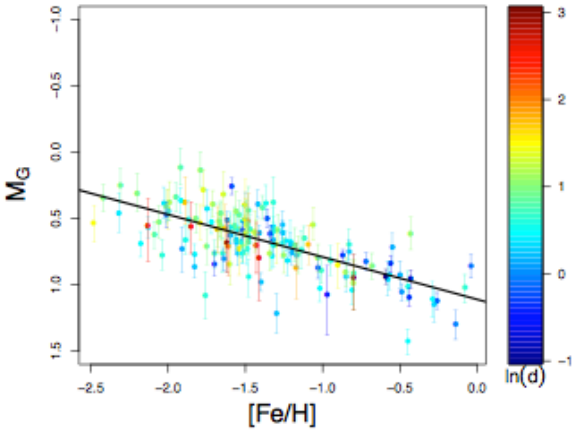

FIGURE 3.35: M_G – [Fe/H] relation defined by 160 RRLs in our sample. Figure from Muraveva et al. (2018b).

0.180±0.003 mag/dex) and Sesar et al. (2017, $0.15^{+0.09}_{-0.08}$ mag/dex). The inferred parallax offset is -0.056 ± 0.006 mas.

The top panel of Figure 3.36 show the RRL $PM_{Ks}Z$ relation where the colours encode the RRL metallicities on the Zinn & West (1984) metallicity scale.

Likewise we proceeded with the sub-sample of 23 RRLs both inferring the parallax offset as a parameter of the model, and assuming a constant offset value (-0.057 mas). The resulting relations are presented, respectively, in rows 3 and 4 of the mid and lower portions of Table A.4.

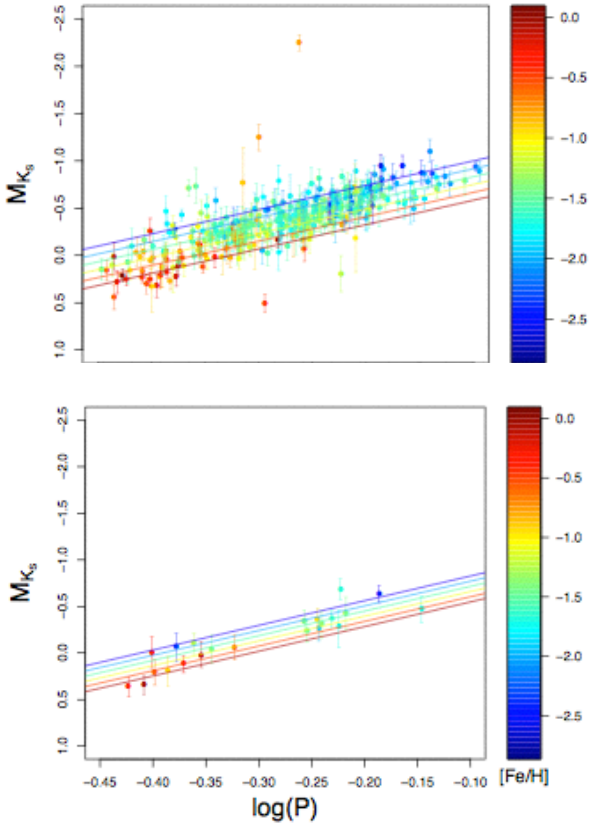

FIGURE 3.36: *Top panel*: PM_{Ks} relation defined by 400 RRLs in our sample, for which absolute M_{Ks} magnitudes were inferred from the BA. The lines are projections of the fit in the first portion of Table A.4 onto the Magnitude-Period plane. The colour scale encodes metallicity values measured on the Zinn & West (1984) metallicity scale. *Bottom panel*: Same as in the top panel for the sub-sample of 23 RRLs having metallicity from high-resolution spectroscopy. Figures from Muraveva et al. (2018b).

The bottom panel of Figure 3.36 shows the PM_KZ relation obtained from this sub-sample of 23 RRLs inferring the parallax offset as a parameter of the model. The mean M_{Ks} and M_{W1} absolute magnitudes of an RRL with metallicity [Fe/H]=−1.5 dex and period P=0.5238 d derived from the PM_KZ and $PM_{W1}Z$ relations are found in column 6 of Table A.4. The parallax offset derived by averaging the offsets inferred from the BA models of the M_V − [Fe/H], PM_KZ and $PM_{W1}Z$ relations, −0.057 mas, is in excellent agreement with the offset derived by Arenou et al. (2018).

3.7.4 Sanity check and conclusions

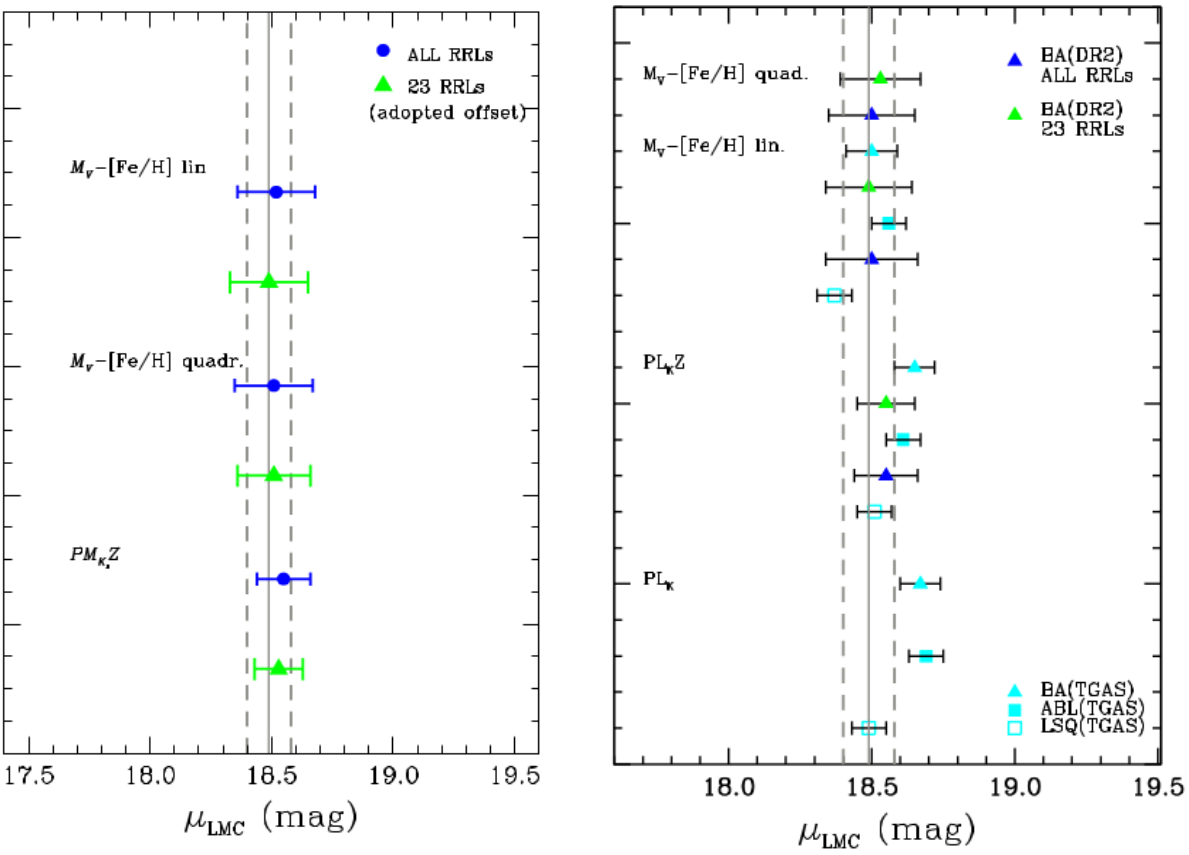

FIGURE 3.37: *Left panel*: LMC distance moduli obtained by fitting the DR2-based $PL_{Ks}Z$ and M_V − [Fe/H] relations using the Bayesian approach for the whole sample of RRLs (blue filled circles) and the subset of 23 RRLs (green triangles) with an assumed constant value of the parallax offset of −0.057 mas. *Right panel:* As in the left panel but including LMC distance moduli derived from the TGAS-based PM_K, PM_{Ks}Z and M_V − [Fe/H] relations of RRL stars and the LSQ (cyan empty squares), ABL (cyan filled squares) and Bayesian (cyan triangles) approaches, respectively (see Sec. 3.5.6).

As done in section 3.5.6 for the TGAS-based PL, PW, PLZ, and $M_V - [Fe/H]$ relations, we tested our DR2-based PLZ and $M_V - [Fe/H]$ relations of RRLs, derived with the BA, applying them to infer the distance to the LMC, the sanity check traditionally done in this type of studies. Similarly to what done for TGAS-based relations, we used 70 RR RRLs located close to the LMC bar, for which spectroscopically measured metallicities (Gratton et al. 2004), extinction, periods and mean magnitudes in the V-band from Clementini et al. (2003) and K_s bands from Muraveva et al. (2015) are available. No W_1- band photometry is available for these 70 stars, intensity-averaged G mean magnitudes are available only for 44 of them, and the G-band absorption values only for two of the stars in the sample. Therefore we inferred the LMC distance moduli using only the $M_V - [Fe/H]$ relation (in linear and quadratic forms), and the $PM_{Ks}Z$ relation derived from both our whole sample and the sub-sample of 23 RRLs. Moreover the metallicity scale adopted from Gratton et al. (2004) for the 70 LMC RRLs is 0.06 dex more metal-rich than the Zinn & West (1984) metallicity scale with which are reported the metallicities in our full sample. Furthermore, we subtracted 0.06 dex from the Gratton et al. (2004) metallicities of the LMC RRLs to convert them to the Zinn & West (1984) metallicity scale (0.06 dex is indeed the difference in metallicities between the two scales, where Gratton et al. (2004) is the most metal-rich) while no correction was applied using the relations based on the 23 MW RRLs (with metal abundances obtained from high-resolution spectroscopy). The left panel of Figure 3.37 shows the LMC distance moduli obtained by fitting the DR2-based $PM_{Ks}Z$, and $M_V - [Fe/H]$ relations (with the latter both in linear and quadratic forms), using the whole sample (blue symbols) and the 23 RRLs subsample (green symbols), respectively, and adopting in the latter case a fixed parallax offset of -0.057 mas. The corresponding moduli are summarised in the last column of Table A.4. They are all in excellent agreement with the very precise LMC modulus inferred by Pietrzynski et al. (2013): $\mu = 18.493 \pm 0.008$(stat.) ± 0.047(syst.) mag (grey solid line). The grey dashed lines mark the $2\sigma_{syst}$ uncertainty. We can conclude that the LMC distance moduli obtained in this study using RRLs relations based on *Gaia* DR2 parallaxes are in good agreement with the canonical value, once the *Gaia* DR2 parallax offset is properly accounted for. If for the 23 sample instead we use the large offset inferred by the BA model (-0.142 mas, Sec. 3.7.3.1), the derived LMC distance moduli could be much shorter than the Pietrzynski et al. (2013) value (see last column of Tab A.4). Finally the right panel of Figure 3.37 shows the comparison of the LMC distance moduli obtained from the

DR2-based and TGAS-based PM_K, PM_{Ks}Z and $M_V - [Fe/H]$ relations, where for the latter we also show results from the LSQ (cyan empty squares).

Chapter 4

Gaia exploitation: CRRP and SMHASH projects

4.1 Exploitation of *Gaia* DR1 and DR2 RRL parallaxes

With *Gaia* DR1 and DR2, the number of known RRLs in our Galaxy and beyond, along with their distances (through parallax measurements), has steadily increased. This number is likely to grow, in coming *Gaia* data releases, beyond the current value of more than a couple hundred thousands of known RRLs.

With hundreds of thousands RRLs known in the MW, Magellanic Clouds and close by dSphs and UFDs, and fresher calibrations of their fundamental relations, based on the unprecedented accuracy of *Gaia* end-of-mission astrometric measurements, it will become possible to study in detail the systematics affecting those relations and test their universality across different stellar systems.

In addition, the precise RRL distances measured by *Gaia* or inferred from RRL relations calibrated on *Gaia*, will allow us to trace the distribution of the oldest stars and will reveal the 3-dimensional structure of the MW halo, disk and bulge, in order to understand, from the comparison with existing theoretical models, how our Galaxy formed and evolved.

Soon after its first two releases *Gaia* has become the crucial reference point for this type of studies. I am involved in a number of different projects aiming at fully exploiting

Gaia's potential in these fields. They include: (i) the Carnegie RR Lyrae Program (CRRP, PI: W. Freedman) and the Carnegie-Chicago Hubble Program (CCHP; Beaton et al. 2016) that, based on *Spitzer* and HST data, along with *Gaia*'s recalibration of RRLs as standard candles, aims at providing a new and independent pathway to measure H_0 with an accuracy better than 3% , by adopting a distance ladder comprised of RRLs, Tip of the Red Giant Branch (TRGB) stars and Type Ia Supernovae; (ii) *Spitzer* Merger History and Shape of the Halo (SMHASH, PI: Johnston), a program that uses high-precision MIR distances from RRLs, calibrated on *Gaia*'s parallaxes, to build an accurate 3-dimensional map of our Galaxy and reconstruct the orbits of its satellite galaxies; and (iii) a project that, based on data of the Vista Variables in the Via Lactea (VVV, PI: D. Minniti) and the deep DECam PLane (DECaPS) Surveys, is looking for new GCs in the Galactic bulge using RRLs and multi-band CMDs as probes. Most recent publication of the CCHP and VVV+DECaPS projects are the papers: "The CCH-PROGRAM: Calibration of the near-infrared RR Lyrae Period-Luminosity relation with HST", by J.Rich, [...], A. Garofalo et al. 2018, ApJ, in press;

"Confirmation of a new metal-poor Globular Cluster in the Galactic Bulge" by D.Minniti, [...], A. Garofalo et al. 2018, ApJ, 866, 12.

In the following sections we describe more in detail the CRRP and the SMHASH projects, to which was devoted part of the work done in the third year of my PhD. The key feature of both projects is the acquisition of infrared observations of RRLs with the *Spitzer* space telescope. *Spitzer* operates at wavelengths with low sensitivity to extinction, and it has proven to be a perfect tool for undertaking variable star studies (Freedman et al. 2011, and references therein) as it provides a uniform light curves coverage of variable stars with a high-precision stellar photometry since it is very stable in its calibrated zero point. In addition to that, both the CRRP and SMHASH projects share the common set of benefits which characterise RRLs at mid-infrared wavelengths: (i) the intrinsic dispersion of the RRL PL relation becomes narrower compared to the PL at shorter wavelengths; (ii) RRL MIR light curves have more symmetrical shapes and smaller amplitudes, providing more precise mean magnitudes; (iii) the effects of extinction/reddening are dramatically reduced; and (iv) the metallicity effect on the MIR PLs is small, if any.

4.1.1 The CRRP and SMHASH projects

The Carnegie RR Lyrae Program (CRRP, PI: W. Freedman) is a Warm *Spitzer* program which uses the Infrared Array Camera (IRAC) to observe RRLs in 31 globular clusters of the MW and LMC and in the fields (Monson et al. 2017), and bulge of the MW.

The project aims to pin down the slope and the zero point of the RRL MIR PL relation as to establish a self-consistent pure Population II distance scale and provide a totally independent determination of the Hubble constant (Freedman et al. 2012). As part of the CRRP project I contributed to the analysis of a sample of RRLs in the LMC cluster Reticulum. We derived new MIR PL relations calibrated using trigonometric parallaxes from the HST and from *Gaia* measurements (both TGAS from *Gaia* DR1 and *Gaia* DR2). Results obtained from this study are presented in Section 4.1.2 and were published in the paper: "The Carnegie RR Lyrae Program: Mid-infrared Period-Luminosity relations of RR Lyrae stars in Reticulum" Muraveva T., Garofalo A., Scowcroft V., Clementini G., Freedman W. L., Madore B. F. & Monson, A. J. 2018; MNRAS 480, 4138M.

A complementary program to CRRP is the *Spitzer* Merger History and Shape of the Halo Program (SMHASH, PI: Johnston). This project aims at using high-precision MIR distances from RRLs in the MW halo, its debris streams (e.g., the Sagittarius and Orphan streams; Hendel, D. [...], Garofalo, A. [...], 2018 MNRAS, 479, 570), and dSph satellites, to build an accurate 3-dimensional map of our Galaxy and recover the orbits of its satellite galaxies. In particular, SMHASH targeted four Classical dSphs: Ursa Minor, Bootes, Sculptor and Carina whose variable star populations have revealed a diversity in morphological properties. These dSphs, along with the Sagittarius and Orphan streams are the residuals of the disruption events that formed the MW halo. They can be considered 'fossils' of the halo formation. The combination of the SMHASH results with proper motions from *Gaia*, will be used to create full 6D phase-space maps of our Galaxy that provide constraints on the mass, shape and orientation of the MW dark matter halo and on the evolutionary history of its 'fossils'. As part of the SMHASH project, I completed the study of the dwarf spheroidal galaxy Sculptor. I determined a new distance modulus for Sculptor using multi-epoch MIR photometry of the RRLs located in the inner region of the galaxy and adopting as fiducials the empirical MIR PL and PLZ relations derived by Muraveva et al. (2018a) and Muraveva et al. (2018b).

Results from this study are described in Section 4.1.3 and were published in the paper: "SMHASH: a new mid-infrared RR Lyrae distance determination for the Local Group dwarf spheroidal galaxy Sculptor" by Garofalo et al. (2018, MNRAS, 481, 578)

4.1.2 CRRP: Mid-infrared Period-Luminosity relations of RR Lyrae stars in Reticulum

4.1.2.1 RRL variables in Reticulum

The first 22 RRLs in the Reticulum cluster were discovered by Demers & Kunkel (1976). Their number is increased as well as their classification through a number of different studies going from the optical (Walker 1992, Ripepi et al. 2004) to the near-IR passbands (Jones et al. 1996, Dall'Ora et al. 2004) up to the most recent optical studies by Kuehn et al. (2013). Therefore, the RRLs in Reticulum now include a total of 32 variables: 22 RRab, 4 RRc and 6 RRd stars. Kuehn et al. (2013) estimated an accuracy of ± 0.00001 and ± 0.00002 d for the period of the RRab and RRc variables, respectively, and an uncertainty approximately one order of magnitude larger for the period of the RRd stars. All RRLs in the cluster share the same reddening, distance and metallicity (Kuehn et al. 2013). Additionally, the majority of the RRLs in the cluster are located in uncrowded fields, which allows us to accurately determine their mean magnitudes at 3.6 and 4.5 μm passbands.

4.1.2.2 Observations and PSF photometry

Reticulum was observed during Cycle 9 of the Warm *Spitzer* mission. The observations were executed on 2012 November 27 and consist of 12 epochs (each with individual exposures of ~ 31 s), simultaneously in the 3.6 ([3.6]) and 4.5 μm ([4.5]) passbands distributed over a time interval of approximately 14 hours. The spacing and time coverage were chosen to optimise the phase coverage of the RRLs that were known to exist in the field. Figure 4.1 shows the total area mapped by the *Spitzer* observations of Reticulum; the cluster is located at the intersection of the *Spitzer* [3.6] and [4.5] fields of view. Observations were taken simultaneously in the two passbands. The elongated shape of the field is due to the dither pattern of the observations. Colour information is available for the central region, highlighted by dashed colours in Figure 4.1 and single band data are

available for the two side regions. We outlined the cluster with a black circle of radius equal to twice the half-light radius of Reticulum (2.35 arcmin, Bica et al. 1999). Individual Basic Calibrated Data (BCDs) were downloaded from the *Spitzer* Science Center (SSC) and mosaics were created with the SSC-provided software `MOPEX` (Makovoz & Khan 2005) to obtain 12 single epoch mosaic images in the two passbands. Point spread function (PSF) photometry was performed using the `DAOPHOT/ALLSTAR/ALLFRAME` program suite (Stetson 1987, 1994); further details on the reduction of the *Spitzer*-IRAC images are provided in section 4.1.3.2.

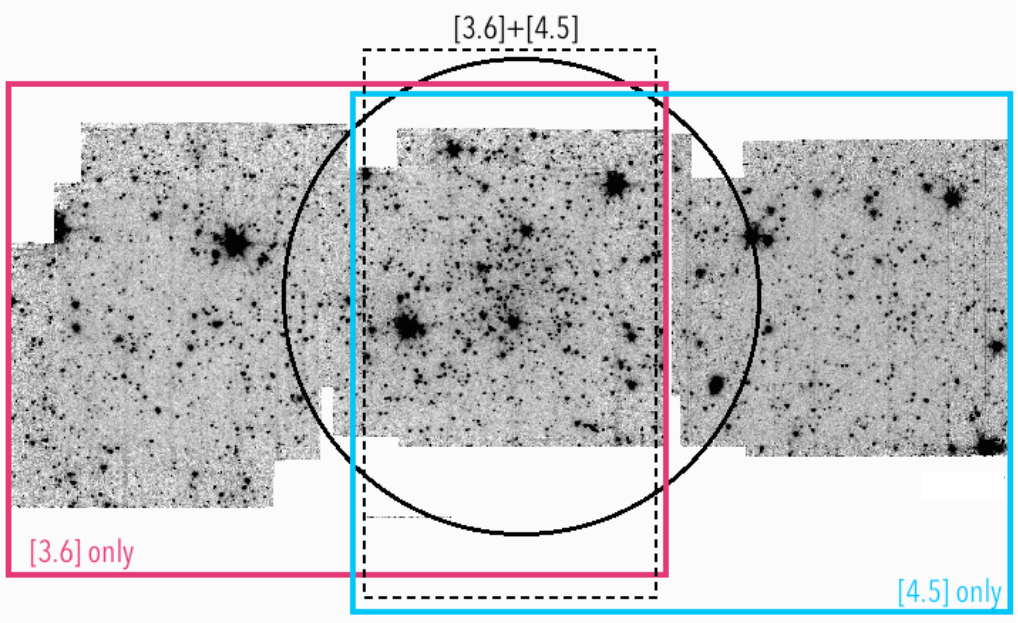

FIGURE 4.1: Total area mapped by the *Spitzer*-IRAC observations of the Reticulum GC in the LMC. The cyan and magenta boxes indicate the coverage of the IRAC 3.6 and 4.5 μm data, respectively. A black circle with a radius equal to twice the half-light radius of Reticulum (2.35 arcmin, Bica et al. 1999) shows the location of the cluster. Figure from Muraveva et al. (2018a).

The final photometric catalogues contain 4,068 and 3,379 sources at 3.6 and 4.5 μm, respectively, instead photometry is available in both passbands for 1,284 sources. The 3.6 μm photometry spans the range from 21.57 to 9.23 mag, while the 4.5 μm photometry ranges from 21.11 to 10.36 mag, where the upper limits are due to saturation. Uncertainties in the 3.6 μm magnitudes range from 0.003 to 0.100 mag, while uncertainties in the 4.5 μm magnitudes span the range from 0.005 to 0.100 mag. The typical internal uncertainties[1] at the level of the Reticulum HB ([3.6]$\sim$ 18 mag) are of 0.017 mag and

[1]We note that the magnitudes uncertainties as provided by the `ALLFRAME` software can be significantly underestimated as they only include the internal errors of the PSF fitting.

0.022 mag in the 3.6 μm and 4.5 μm bands, respectively. Jeon et al. (2014) publish B, V photometry for 766 sources in Reticulum. We cross-matched the Jeon et al. (2014) catalogue with our MIR catalogue of 1,284 sources and found 364 objects in common. The [3.6], (V-[3.6]) and [3.6], (B-[3.6]) CMDs of these 364 sources are shown in the left panels of Figure 4.2. The cluster RGB and the HB are well defined, demonstrating the quality of our photometry and the precision of the calibration procedure.

4.1.2.3 RRLs in Reticulum: first MIR light curves

To identify the RRLs we cross-matched the positions of the 32 RRLs in Kuehn et al. (2013)'s catalogue with our catalogue of 1,284 sources with 3.6 and 4.5 μm photometry. Only for two variables (V20 and V31) we did not find a counterpart in our catalogue

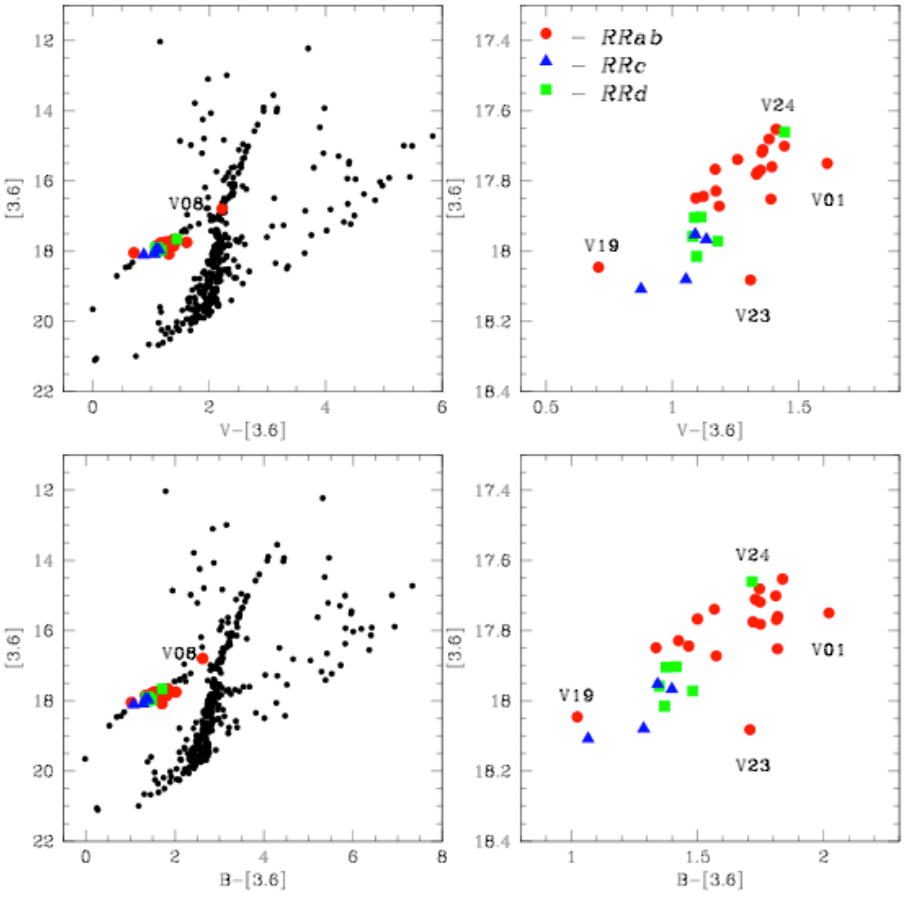

FIGURE 4.2: *Left panels*: [3.6] vs V-[3.6] and [3.6] vs B-[3.6] CMDs (upper- and bottom-left panels, respectively) of 364 sources in Reticulum observed with *Spitzer* in common with Jeon et al. (2014)'s photometry in the B and V bands. Red circles, blue triangles and green squares represent RRab, RRc and RRd stars, respectively. *Right panels*: Zoom-in of the region populated by RRLs in the CMDs shown in the left panels. Figure from Muraveva et al. (2018a).

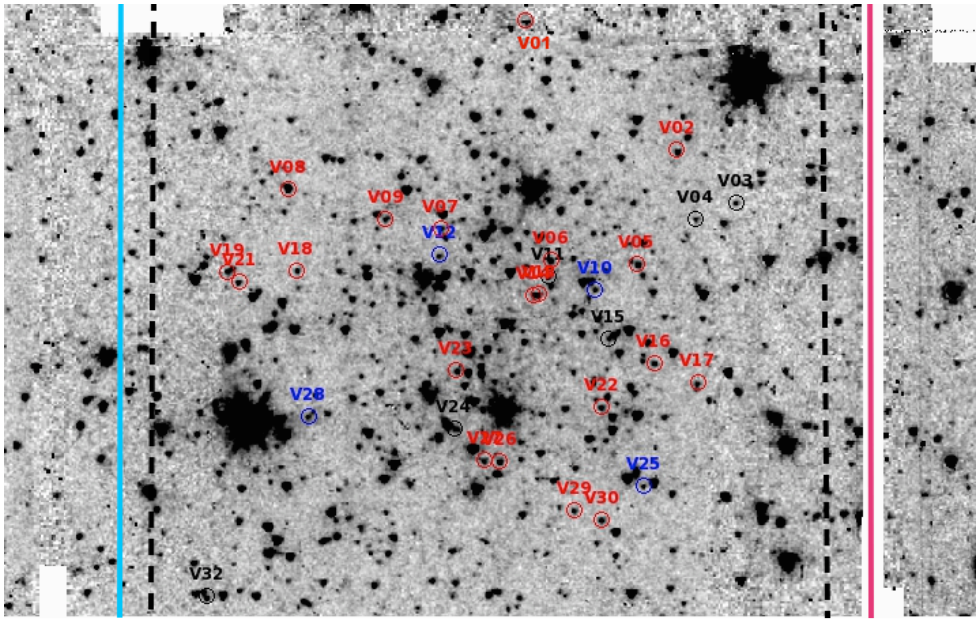

FIGURE 4.3: Zoom-in of Fig. 4.1 showing the region of the Reticulum cluster. Open red, blue and black circles display RRab, RRc and RRd stars, respectively. Figure from Muraveva et al. (2018a).

since these two stars are embedded into non-resolved elongated groups of sources in our *Spitzer* data. The 30 RRLs (20 RRab, 4 RRc and 6 RRd stars) we were able to counter identify are listed in Table 4.1 (name, coordinates, period, and classification in type from Kuehn et al. 2013). Periods range from 0.29627 to 0.65696 d. For the 6 RRd stars we list only the first-overtone periodicity. The position of the 30 RRLs in the *Spitzer*-IRAC images is shown in Figure 4.3. The RRab, RRc and RRd stars are marked by red, blue and black open circles, respectively, and labelled according to the identification number in Kuehn et al. (2013). The 3.6 and 4.5 μm light curves are presented in Figure 4.4. The epoch of maximum light (Column 6 in Table 4.1) is the same for 3.6 and 4.5 μm passbands for all sources except for V10. The 4.5 μm data of this star had to be shifted by $\sim$0.4 in phase when folded according to the epoch in the 3.6 μm passband. By Fourier fitting of RRLs light curves with the GRaphical Analyzer of TImes Series package (GRATIS, Clementini et al. 2000) we derived intensity-averaged mean 3.6 and 4.5 μm magnitudes (and related uncertainties) and measured also amplitudes from the modelled light curves. They are listed in Columns from 7 to 10 of Table 4.1. Since the model fitting performed with GRATIS needs a minimum number of 11 data points, we

discarded obvious outliers very carefully. The standard deviation of the phase points from the fit was calculated considering only data points retained after removing outliers. The final uncertainty in the mean magnitude was calculated as the sum in quadrature of the fit uncertainty provided by GRATIS and the photometric uncertainty ($\Sigma\sigma_i^2$/N), where σ_i is the photometric uncertainty of the individual observations and N is the number of observations. For very noisy light curves such as those of V04 and V12 in both the 3.6 and 4.5 μm passbands and V08, V24, V28, V32 in the 4.5 μm passband, GRATIS failed to fit a reliable model to the data. For these stars the mean magnitudes were calculated as the weighted mean of the intensity values of each data point then transformed back to magnitudes, while the uncertainty of the mean values was estimated as the standard deviation of the weighted mean. No amplitudes were calculated for these stars. In Figure 4.4 we show only the data points retained in the analysis; the blue lines show the best fit models obtained with GRATIS.

TABLE 4.1: Properties of RRLs in the Reticulum cluster observed at 3.6 and 4.5 μm.

Name	α (J2000)	δ (J2000)	Type	P[a] (days)	Epoch[a] (max) JD (−2440000)	$\langle[3.6]\rangle$[b] (mag)	$Amp_{[3.6]}$ (mag)	$\langle[4.5]\rangle$[b] (mag)	$Amp_{[3.6]}$ (mag)	ϖ_{DR2} (mas)	Flag[c]
V01	04:35:51.5	−58:51:03.4	RRab	0.50993	56258.032	17.750±0.109	0.410	17.825±0.185	0.217	−0.18±0.19	1
V02	04:35:56.6	−58:52:32.1	RRab	0.61869	56257.239	17.719±0.047	0.153	17.603±0.108	0.238	−0.13±0.18	0
V03	04:35:58.6	−58:53:06.7	RRd	0.35350	56257.592	18.015±0.068	0.204	17.918 ± 0.077	0.244	−0.02±0.18	0
V04	04:36:00.3	−58:52:50.0	RRd	0.35320	56268.034	17.958±0.056	-	17.908±0.103	–	0.20±0.18	0
V05	04:36:04.1	−58:52:29.3	RRab	0.57185	56257.444	17.711±0.042	0.249	17.617±0.063	0.322	0.14±0.21	0
V06-BL	04:36:05.4	−58:51:47.8	RRab	0.59526	56257.439	17.775±0.041	0.276	17.862±0.094	0.363	−0.01±0.18	0
V07	04:36:05.5	−58:50:51.8	RRab	0.51044	56257.550	17.849±0.052	0.280	18.010± 0.097	0.255	0.43±0.23	0
V08	04:36:05.7	−58:49:34.3	RRab	0.64496	56257.608	16.796±0.055	0.144	16.558±0.097	-	0.19±0.20	1
V09	04:36:05.9	-58:50:24.5	RRab	0.54496	56257.824	17.739±0.047	0.166	17.732±0.069	0.261	−0.09±0.17	0
V10	04:36:06.4	−58:52:12.6	RRc	0.35256	56257.813	17.967±0.044	0.185	17.964±0.077	0.160	0.02±0.21	0
V11	04:36:06.4	−58:51:48.7	RRd	0.35540	56257.987	17.904±0.045	0.160	18.000±0.103	0.160	0.02±0.21	0
V12	04:36:07.1	−58:50:54.9	RRc	0.29627	56258.029	18.108±0.056	-	18.184±0.104	-	0.11±0.19	0
V13	04:36:07.8	−58:51:46.8	RRab	0.60958	56257.456	17.782±0.039	0.175	17.716±0.055	0.209	-0.05±0.18	0
V14-BL	04:36:07.8	−58:51:44.4	RRab	0.58661	56257.679	17.681±0.044	0.288	17.728±0.052	0.289	0.10±0.19	0
V15	04:36:09.1	−58:52:25.8	RRd	0.35430	56257.790	17.972±0.053	0.138	18.040±0.115	0.200	−0.04±0.20	0
V16	04:36:09.8	−58:52:50.7	RRab	0.52290	56257.913	17.829±0.056	0.246	17.827±0.073	0.210	0.10±0.19	0
V17	04:36:10.3	−58:53:13.6	RRab	0.51241	56257.599	17.767±0.045	0.302	17.757 ±0.076	0.340	0.39 ±0.20	0
V18	04:36:10.6	−58:49:50.2	RRab	0.56005	56257.751	17.701 ±0.050	0.291	17.722±0.066	0.247	−0.50±0.19	0
V19	04:36:11.9	−58:49:18.1	RRab	0.48485	56257.635	18.046 ±0.074	0.360	17.981 ±0.155	0.603	0.30 ±0.20	1
V21	04:36:12.3	−58:49:24.3	RRab	0.60700	56257.933	17.760 ±0.065	0.292	17.665pm0.089	0.263	−0.05±0.20	0
V22	04:36:13.4	−58:52:32.0	RRab	0.51359	56257.851	17.844±0.072	0.291	17.880 ±0.077	0.351	−0.35 ± 0.22	0
V23-BL	04:36:13.8	−58:51:19.0	RRab	0.46863	56258.153	18.082±0.070	0.244	18.245 ±0.114	0.366	−0.01 ±0.21	0/1
V24	04:36:17.3	−58:51:26.6	RRd	0.34750	56257.864	17.661 ±0.067	0.089	17.780 ± 0.119	-	−0.12 ± 0.19	1
V25	04:36:17.4	−58:53:02.6	RRc	0.32991	56258.020	18.080 ±0.065	0.191	18.073± 0.077	0.242	0.11 ± 0.19	0
V26	04:36:18.5	−58:51:51.8	RRab	0.65696	56257.940	17.653±0.042	0.100	17.720 ±0.087	0.222	−0.11±0.19	0
V27	04:36:18.7	-58:51:44.3	RRab	0.51382	56257.982	17.852±0.052	0.350	17.900±0.071	0.331	−0.31 ± 0.22	0
V28	04:36:19.2	−58:50:15.5	RRc	0.31994	56257.701	17.952 ± 0.065	0.163	18.056 ± 0.141	-	0.23 ± 0.22	1
V29	04:36:20.1	−58:52:33.5	RRab	0.50815	56257.682	17.872 ± 0.067	0.348	17.818 ± 0.078	0.440	0.14 ± 0.20	0
V30	04:36:20.2	−58:52:47.7	RRab	0.53501	56257.725	17.769 ± 0.047	0.242	17.750 ± 0.076	0.301	−0.19 ±0.18	0
V32	04:36:32.0	−58:49:53.2	RRd	0.35230	56257.750	17.903 ± 0.060	0.060	18.083 ± 0.208	-	0.07 ± 0.22	1

Notes. [a]Epoch of maximum light (HJD-2400000) of the 3.6 μm light curve. The epoch of maximum light is the same in the 3.6 μm and 4.5 mum passbands for all sources except for V10. The 4.5 μm data of this star had to be shifted by 0.4 in phase. [b] Magnitudes in the *Spitzer* passbands obtained by fitting a model to the data with the GRATIS software. [c] A "0" in column 12 flags objects which were used to fit the PL relations whereas a "1" flags stars that were discarded. A "0/1" flags V23 because the star was used to fit the the 3.6 μm PL relation, but was automatically rejected by the 3-sigma clipping procedure when fitting the 4.5 μm PL relation. See text for details.

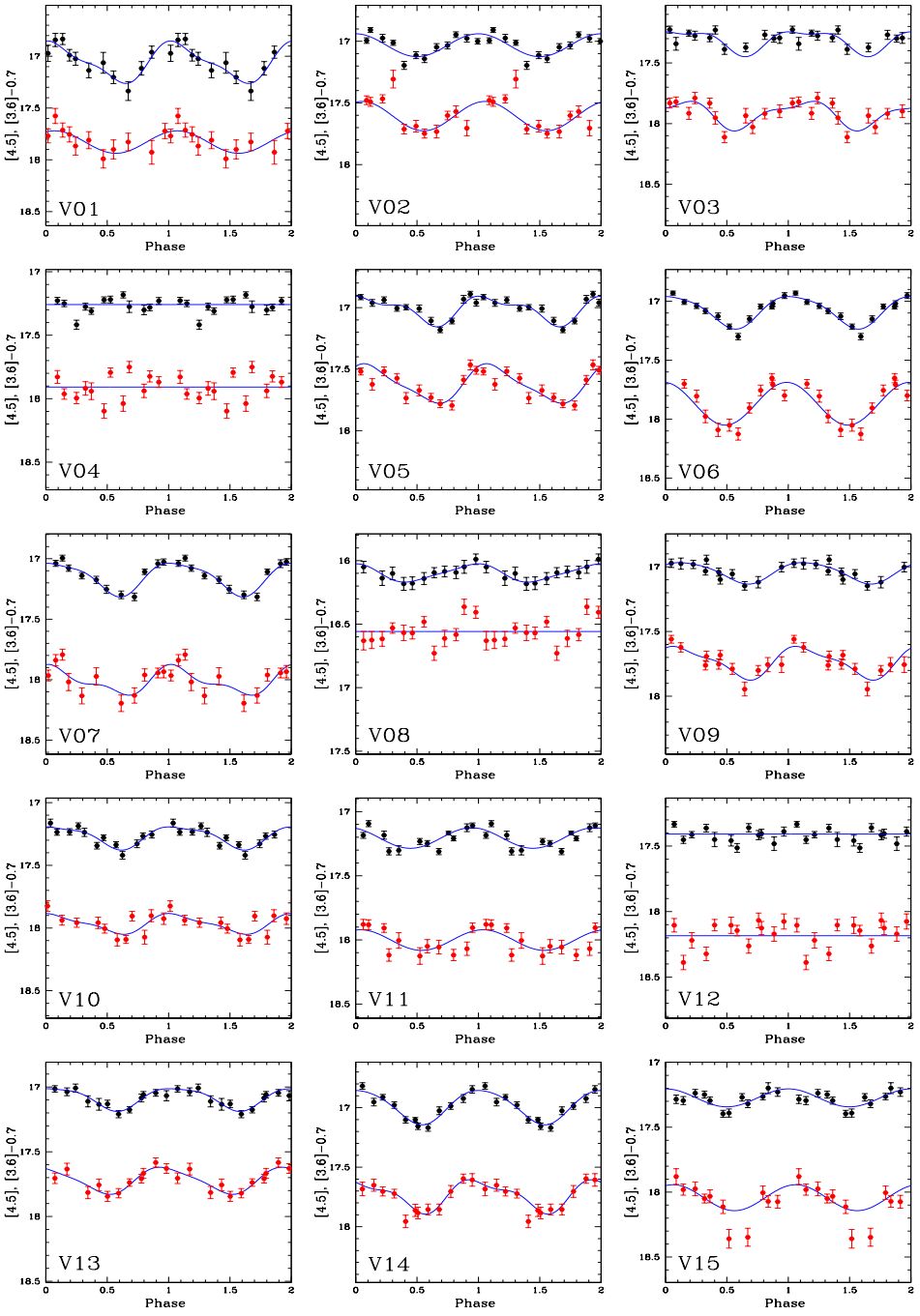

FIGURE 4.4: MIR light curves of the RRLs in Reticulum observed by *Spitzer*-IRAC. Black and red dots represent the [3.6] and [4.5] data points, respectively, with the 3.6 μm shifted by -0.7 mag, for clarity. Blue solid lines show the best fit models obtained with GRATIS. Only data points used in the model fitting are shown. Figure from Muraveva et al. 2018a.

With the aim to clean our sample from blended sources and other contaminants we analysed the position of the RRLs on the CMDs shown in Fig. 4.2 and the light curves (Fig. 4.4) in combination with a visual inspection of the *Spitzer* images. The right panels of Fig. 4.2 show that most of the RRc stars (blue triangles) are, as expected, bluer than

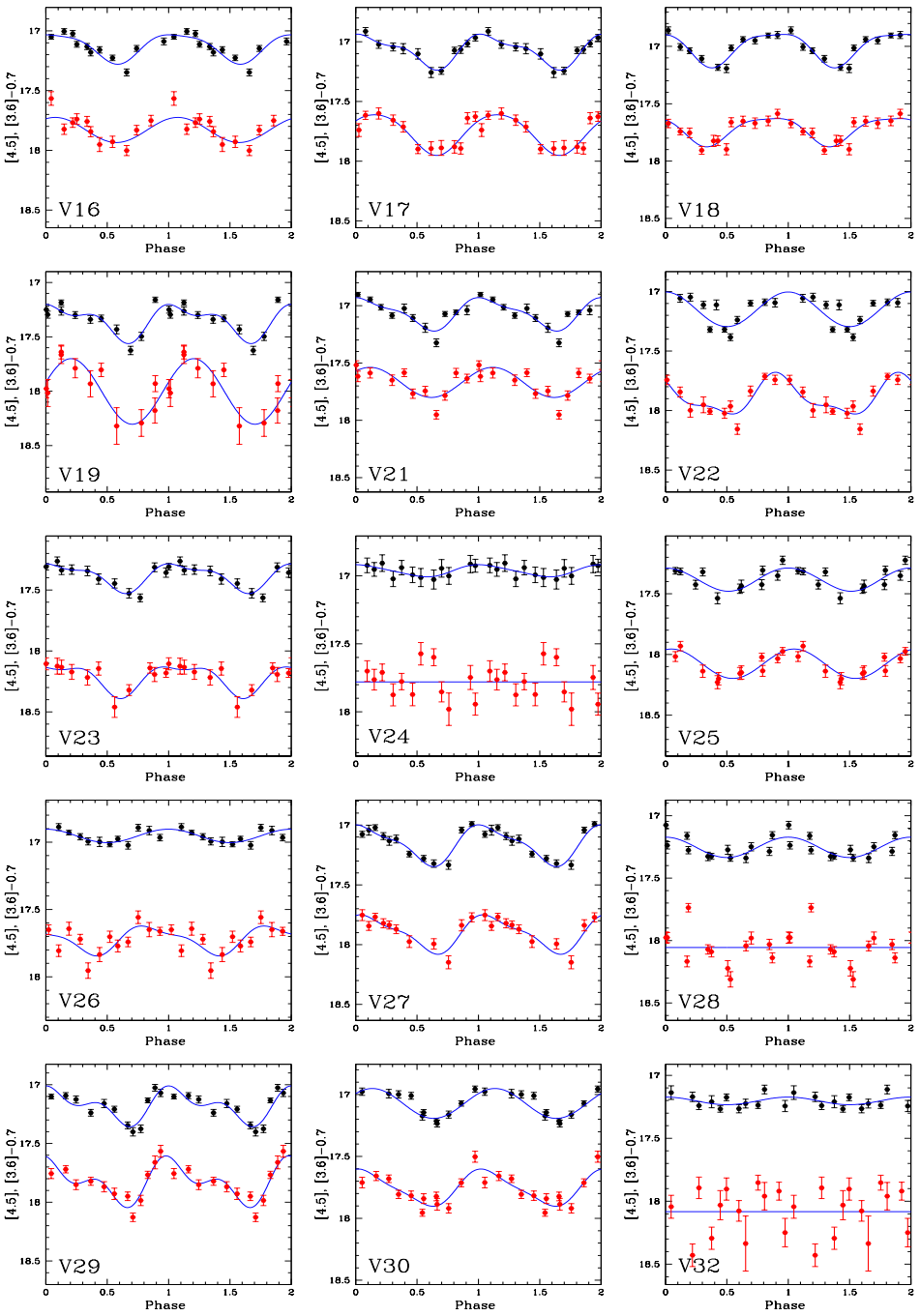
V16
V17
V18
V19
V21
V22
V23
V24
V25
V26
V27
V28
V29
V30
V32
[4.5], [3.6]−0.7
Phase

the RRab variables (red filled circles), and consistently the RRd stars (green squares) are located between RRc and RRab stars. However, for five objects, namely, V01, V08, V19, V23 and V24, the position on the CMD is unusual. Specifically:

- V08 is far too bright and red in colour than the bulk of the RRab stars. The star's light curves are noisy, especially of [4.5] (see Fig. 4.4). Inspection of *Spitzer* images showed that V08 is within an unresolved group of sources.

- V01 is slightly separated from other RRLs in the CMD and has a significantly redder colour than it would be expected for its period (P=0.51 days). The source is located on the upper edge of the [3.6] and [4.5] images and does not have a characteristic stellar shape on the images, hence, its PSF photometry is likely unreliable.

- V23 is potentially a Blažko[2] variable (according to Kuehn et al. 2013) and is slightly fainter than other RRLs, but the [3.6] and [4.5] images and the star light curves do not have particular issues. The faint magnitude of this star may be consistent with its period (0.46863 days) that is the shortest among all the RRab stars in our sample. It is worth noting that V23 has also the faintest V (Kuehn et al. 2013) magnitude among all RRLs in Reticulum, which in combination with the results of this study may prove that V23 is indeed an intrinsically faint star in our sample. While the faint MIR magnitudes can be explained by the shortest period of this star among all the RRab stars in the sample, the reason of the faint visual magnitude is unclear. A high metallicity of V23 could potentially account for its faint V magnitude, however, it would contradict the general picture of Reticulum being a mono-metallic cluster. An alternative possibility is that V23 is a foreground RRL belonging to the field of the LMC.

- V19 has a rather noisy light curve especially in the 4.5 μm band. It also has a colour too blue for an RRab variable. Visual inspection of the images showed that V19 has a companion of $m_{[3.6]}$ $\sim$18 mag at a distance of 0.82 arcsec. The source is also located close to the edge of the [4.5] image. Both these issues may have affected its photometry.

[2] see Sect. 3.6.2

- V24 appears too red in colour for an RRd star and has an extremely noisy light curve. The star is located at a distance of 3.79 arcsec from a 15 mag bright source, with which it is blended in both passbands.

- V28 and V32 have noisy light curves. V28 has a close companion of $\sim$ 19 mag and V32 is blended by a companion of $\sim$ 18 mag located at a distance of 1.87 arcsec.

Finally, images and the position on the CMD of V04 and V12 do not indicate any clear issue despite the fact that these stars have noisy light curves. Specifically, V04 is a double mode pulsator and V12 is the shortest period (and hence faintest) RRL in our sample. This may explain the noisy light curves. To summarise, the following six stars were dropped: V01, V08, V19, V24, V28, V32, while V04 and V12 were retained to avoid biasing our derivation of the PL relations by brighter/longer period stars. Therefore in the following analysis we used a subsample of 24 RRLs consisting of 17 RRab, 3 RRc and 4 RRd stars.

4.1.2.4 MIR PL relations: slopes and zero-points

We need to correct for interstellar absorption the mean apparent 3.6 and 4.5 μm magnitudes of the RRLs in our sample, before fitting the MIR PL relations. The reddening values reported in the literature for the Reticulum cluster are generally low but controversial, covering a range from E(B-V)=0.016 mag (Schlegel et al. 1998) to 0.06 mag (Marconi et al. 2002). Moving to MIR passbands, the situation improves significantly because the absorption is lower and almost negligible compared to optical passbands. For this study we adopt the reddening value E(B-V) = 0.03 $\pm$ 0.02 mag from Walker (1992), who estimated the reddening from the colours of the RRab stars at minimum light and Sturch's method (Sturch 1966, Walker 1990). This value of the reddening is close to the mean of the reddening measurements in the literature. Then we used the following relations to estimate the absorption at 3.6 and 4.5 μm:

$$A_{[3.6]} = 0.203 \times E(B\text{-}V)$$

$$A_{[4.5]} = 0.156 \times E(B\text{-}V)$$

derived by Monson et al. (2012) based on the reddening laws from Cardelli et al. (1989) and Indebetouw et al. (2005). We obtained $A_{[3.6]}$=0.006 and $A_{[4.5]}$=0.005 mag. The [3.6]

and [4.5] RRL mean magnitudes, once absorption-corrected, were used to fit the MIR PL relations. We treated the RRd variables as RRc stars as in Dall'Ora et al. (2004) and periods of both RRc and RRd stars were *fundamentalized* according to the usual relation. We used the weighted least squares method and a 3-sigma clipping procedure to fit the PL relations of 3.6 and 4.5 μm passbands defined by our sample of 24 RRLs. The following relations were derived:

$$[3.6] = (-2.15 \pm 0.23) \times log(P) + (17.23 \pm 0.06) \tag{4.1}$$

with r.m.s.=0.06 mag,

$$[4.5] = (-2.47 \pm 0.32) \times log(P) + (17.14 \pm 0.09) \tag{4.2}$$

with r.m.s.=0.07 mag, where [3.6] and [4.5] are the absorption-corrected apparent magnitudes.

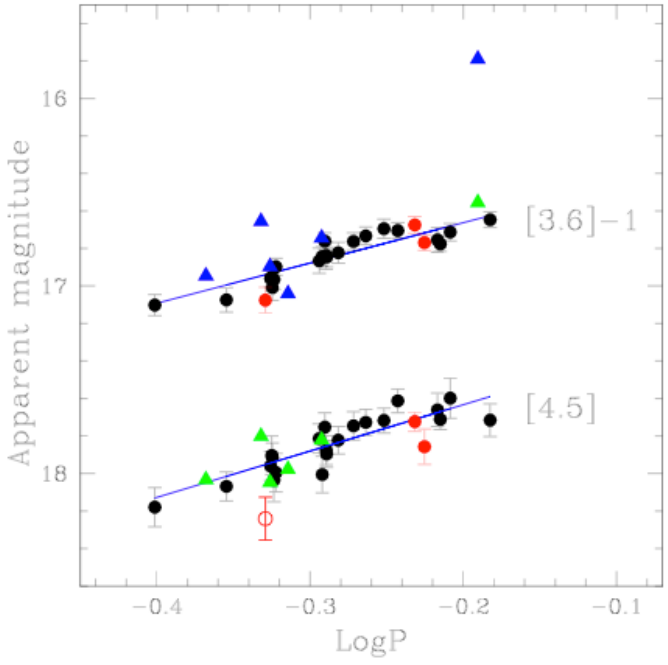

FIGURE 4.5: PL relations at 3.6 and 4.5 μm defined by the Reticulum RRLs. Filled circles represent variables used in the fit, with the Blažko variables (according to Kuehn et al. 2013) highlighted in red. Blue and green triangles show six RRLs that were not used in the fit (see Section 4.1.2.3 for details). Figure from Muraveva et al. (2018a).

The best fit PL relations are shown in Figure 4.5 plotting with filled circles the RRLs

used in the fit and highlighting in red the Blažko variables. Green and blue triangles show instead the six stars that were discarded according to the analysis described in Section 4.1.2.3. Star V23 (marked by an empty red circle) was automatically rejected by the 3-sigma clipping procedure when fitting the PL relation at [4.5], which therefore is based only on 23 RRLs (24 RRLs excluding V23).

To transform the [3.6] and [4.5] apparent magnitudes into absolute magnitudes we have to calibrate the zero points of the PL relation in Eqs. 4.1 and 4.2. Gaia DR2 has published parallaxes for the 30 RRLs of Reticulum analysed here, but due to the large distances and faint magnitudes of the RRLs in Reticulum (mean *Gaia* G-band magnitude ~ 19 mag), 50% of them have negative parallax values and the remaining 15 RRLs have positive parallaxes with large relative uncertainties ($< \sigma_{\varpi}/\varpi > = 2.7$). Consequently, the DR2 parallaxes ($\varpi_D R2$) for the Reticulum RRLs are useless for calibrating the zero points of the MIR PL relations. Therefore we adopt the slope of the MIR PL relations derived with the present study (Eqs. 4.1 and 4.2) and calibrate the zero points using the parallaxes of RRLs in the MW, using the following three datasets: the HST parallaxes of five MW RRLs (RZ Cep, XZ Cyg, SU Dra, RR Lyr and UV Oct) from Benedict et al. (2011), the TGAS parallaxes and *Gaia* DR2 parallaxes for the same stars. We then compared the resulting PL relations with the literature relations. Apparent magnitudes in the *Spitzer* passbands for these variables are published in table 5 of Neeley et al. (2015). The TGAS and *Gaia* DR2 parallaxes are available from the *Gaia* Archive website and are also listed in table 1 of Gaia Collaboration et al. (2017) and table 2 of Muraveva et al. (2018b) respectively, as well as in Tables 3.1 and 3.6 of this Thesis.

The DR2 parallax for RR Lyr (see in Section 3.7.2) has a large negative value (-2.61 ± 0.61 mas) and is clearly wrong, hence for this star we adopt the TGAS parallax instead of the DR2 measure. As widely discussed in Gaia Collaboration et al. (2017) and in Section 3.5.3.1, the direct transformation of parallaxes into absolute magnitudes using equation 3.1 gives rise to biases difficult to manage and thus it is advisable to operate directly in parallax space adopting the ABL method (see Section 3.5.3.1). Hence using equations 3.4 and 3.3, we performed fits in parallax space. Following the usual procedure, the only RRc star in this sample, RZ Cep, was *fundamentalized* before fitting the PL relations. The slopes and zero points of the fits (as given by Eqs. 4.1 and 4.2) are summarised in Table 4.2 (values marked by a yellow band). The parallaxes were then

transformed to absolute magnitudes in order to visualise the data on the PL plane and the resulting 3.6 and 4.5 μm PL fits obtained using the HST, TGAS and DR2 parallaxes of the five calibrators are shown in Fig 4.6, upper, middle and lower panel, respectively.

As discussed earlier (Section 3.7.3.1), we are aware that DR2 parallaxes are systematically smaller with a mean estimated offset of $\delta\varpi = -0.03$ mas (Arenou et al. 2018). Since Arenou et al. (2018) do not recommend to correct individual star parallaxes for this possible parallax offset, we did not apply any correction to the five MW RRLs in our study.

In Table 4.2 we compare the slopes and zero points of the MIR PL relations derived in the present study with the literature values. The $PL_{[3.6]}$ and $PL_{[3.6]}Z$ relations are compared also with PL_{W1} and $PL_{W1}Z$ relations as the 3.6 μm and W1 filters have similar passbands. Similarly, the $PL_{[4.5]}$ and $PL_{[4.5]}Z$ relations are compared also with PL_{W2} and $PL_{W2}Z$ relations.

The slope of our PL relation at 3.6 μm is shallower than values published in previous studies but still consistent with them within the errors. The slope of our PL relation at 4.5 μm is in very good agreement with all previous studies, whereas the absolute magnitudes based on the TGAS and DR2 parallaxes are in very good agreement with each other and generally fainter than those based on the HST parallaxes. Since RRLs in Reticulum share the same metal abundance ([Fe/H]~ -1.66 dex on the Zinn & West (1984) metallicity scale; Mackey & Gilmore 2004) they are not suitable to investigate the effect of metallicity on the MIR PL relations.

4.1.2.5 Distance to Reticulum

Several independent estimates of the distance to Reticulum are available in the literature. Demers & Kunkel (1976), using the mean V magnitudes of the HB stars, derived a distance modulus for Reticulum of $\mu = 18.51$ mag. Walker (1992), Ripepi et al. (2004), Mackey & Gilmore (2004) and Kuehn et al. (2013) derived the distance to Reticulum from optical observations of 32 RRLs in the cluster. Kuehn et al. (2013) also derived a distance modulus for Reticulum using their I-band photometry of the cluster RRL variables, individual metallicities estimated from the Fourier parameters of the light

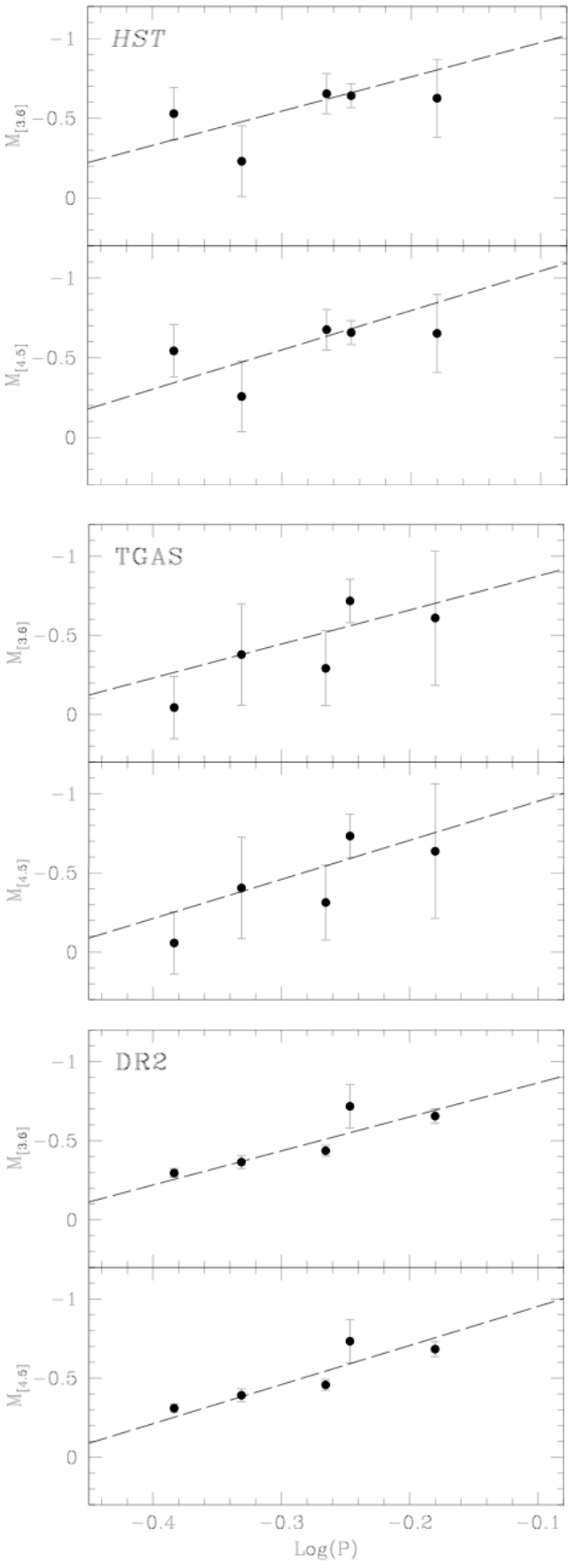

FIGURE 4.6: *PL* relations at [3.6] and [4.5] with slopes derived in the present study (Eq 4.1 and 4.2) and the zero point calibrated using five Galactic RRLs with *HST* parallaxes measured by Benedict et al. (2011) (upper panel), TGAS parallaxes (middle panel), DR2 parallaxes for four sources and TGAS parallax for RR Lyr itself (lower panel). The fits were performed in parallax space. See text for details. Figure from Muraveva et al. (2018a).

TABLE 4.2: Comparison of MIR $PL(Z)$ relations in the form M=$\alpha\times$ log(P) + $\beta\times$ [Fe/H] + ZP

Reference	Band	α	β	ZP from ϖ_{HST}	ZP from ϖ_{TGAS}	ZP from ϖ_{DR2}	ZP others
PL relation W1,[3.6]							
This work	[3.6]	-2.150±0.230	-	-1.190±0.050	-1.190±0.090	-1.080±0.03	-
Madore et al. (2013)	W1	-2.440±0.950	-	-1.260±0.250	-	-	-
Klein et al. (2014) RRab	W1	-2.380±0.200	-	-	-	-	-1.113±0.013[a]
Klein et al. (2014) RRc	W1	-1.640±0.620	-	-	-	-	-1.042±0.031[b]
Neeley et al. (2015)	[3.6]	-2.332±0.106	-	-1.176±0.080	-	-	-1.054±0.020[b]
Neeley et al. (2017)	[3.6]	-2.300±0.110	-	-1.112±0.089	-	-	-
Gaia Collaboration et al. (2017)*	W1	-2.440	-	-	-1.210±.040	-	-
PLZ relation W1,[3.6]							
Dambis et al. (2014)	W1	-2.381±0.097	0.096±0.021	-1.150±0.077	-	-	-0.829±0.093[c]
Neeley et al. (2017)	W1	-2.247±0.018	0.180±0.003	-	-	-	-0.790±0.007[d]
Neeley et al. (2017)	[3.6]	-2.251±0.018	0.180±0.003	-	-	-	-0.793±0.007[d]
Sesar et al. (2017)	W1	$-2.470\pm^{0.74}_{0.73}$	$0.150\pm^{0.09}_{0.08}$	-	$-0.890\pm^{0.12e}_{0.10}$	-	-
Muraveva et al. (2018b)**	W1	$-2.540\pm^{0.60}_{0.58}$	0.150±0.10	-	-	-0.940±0.24	-
PL relation W2,[4.5]							
This work	[4.5]	-2.470±0.320	-	-1.290±0.050	-1.200±0.080	-1.200±0.030	-
Madore et al. (2013)	W2	-2.550±0.890	-	-1.290±0.230	-	-	-
Klein et al. (2014) RRab	W2	-2.390±0.200	-	-	-	-	-1.110±0.013[a]
Klein et al. (2014) RRc	W2	-1.700±0.620	-	-	-	-	-1.057±0.031[b]
Neeley et al. (2015)	[4.5]	-2.33±0.105	-	-1.199±0.080	-	-	-1.091±0.020[b]
Neeley et al. (2017)	[4.5]	-2.340±0.100	-	-1.139±0.089	-	-	-
PLZ relation W2,[4.5]							
Dambis et al. (2014)	W2	-2.269±0.127	0.108±0.021	-1.105±0.077	-	-	-0.776±0.093[c]
Neeley et al. (2017)	W2	-2.237±0.018	0.185±0.003	-	-	-	-0.784±0.007[d]
Neeley et al. (2017)	[4.5]	-2.239±0.018	0.185±0.003	-	-	-	-0.785±0.007[d]
Sesar et al. (2017)	W2	$-2.400\pm^{084}_{0.82}$	$0.170\pm^{0.10}_{0.09}$	-	$-0.947\pm^{0.11e}_{0.10}$	-	-

* see Sect.3.5.4
** see Sect.3.7.3.3
[a] Zero point derived from the M_V-[Fe/H] relation of RR Lyrae stars in combination with the HST parallaxes of RRLs in Benedict et al. (2011).
[b] Zero point calibrated by adopting the distance modulus of the GC M4.
[c] Zero point determined from the statistical-parallax analysis.
[d] Zero point theoretically determined.
[e] Zero point is from table 1 and eq. 4 in Sesar et al. (2017), assuming $P_{ref} = 0.52854$ days and $[Fe/H]_{ref} = -1.4$ dex.

curves and adopting the PLZ relation of Catelan et al. (2004). Jeon et al. (2014) derived the distance to Reticulum by fitting theoretical isochrones to the cluster V, B-V CMD. Distance moduli based on optical photometry agree on a value around μ = 18.40 mag, except Demers & Kunkel (1976)'s that is about 0.1 mag longer.

Dall'Ora et al. (2004) combined the apparent K-band magnitudes of 30 RRLs in Reticulum with the theoretical PLZ relation by Bono et al. (2003) obtaining a distance modulus $\mu = 18.52 \pm 0.005$(random) $\pm$ 0.117(systematic) mag, $\sim$ 0.1 mag longer than that derived from optical photometry. These authors made a detailed analysis of possible systematic uncertainties affecting their analysis and concluded that their distance modulus could be overestimated. Later, Sollima et al. (2008) also confirmed that the distance to Reticulum derived from the K-band photometry of Dall'Ora et al. (2004) is 0.04 mag longer than the distance inferred from the V-band photometry of Walker (1992).

TABLE 4.3: Comparison of distance moduli for Reticulum derived in the present study and literature values.

Reference	Band	E($B-V$) (mag)	Distance modulus (mag)
Demers & Kunkel (1976)	V	0.02	18.51
Walker (1992)	V	0.03	18.38
Ripepi et al. (2004)	V	0.02	18.39±0.12
Mackey & Gilmore (2004)	V	0.05	18.39±0.12
Kuehn et al. (2013)	V	0.016	18.40±0.20
Jeon et al. (2014)	V	0.03	18.40
Sollima et al. (2008)	V	0.03	18.44±0.14
Kuehn et al. (2013)	I	0.016	18.47±0.06
Dall'Ora et al. (2004)	K	0.03	18.52±0.05±0.117
Sollima et al. (2008)	K	0.03	18.48±0.11
This work (HST)	[3.6]	0.03	18.43±0.06
This work (TGAS)	[3.6]	0.03	18.33±0.06
This work (DR2)	[3.6]	0.03	18.32±0.06
This work (HST)	[4.5]	0.03	18.43±0.08
This work (TGAS)	[4.5]	0.03	18.34±0.08
This work (DR2)	[4.5]	0.03	18.34±0.08

Indeed, distance moduli based on K-and I-band photometry are in general longer than those derived from optical photometry as shown in Table 4.3. This could suggest some issues in the zero point calibrations of the two different passbands. Finally we applied our PL relations to estimate individual distances to each of the 24 and 23 RRLs used in our analysis of the 3.6 and 4.5 μm PL relations respectively, and then, we averaged the resulting values. We obtained the following distance moduli for Reticulum: $\mu_{[3.6]} = 18.43 \pm 0.06$ mag and $\mu_{[4.5]} = 18.43 \pm 0.08$ mag from the PL relations calibrated on the HST parallaxes; $\mu_{[3.6]} = 18.33 \pm 0.06$ mag and $\mu_{[4.5]} = 18.34 \pm 0.08$ mag using the TGAS parallaxes; and $\mu_{[3.6]} = 18.32 \pm 0.06$ mag and $\mu_{[4.5]} = 18.34 \pm 0.08$ mag using the DR2 parallaxes. These values are reported in the lower portion of Table 4.3. Errors are the standard deviations from the average. The distance moduli estimated using the PL relations calibrated on the HST parallaxes are in good agreement with the majority of the literature estimates, especially with those based on the V photometry. Distance moduli obtained from the PL relations calibrated on the TGAS and DR2 parallaxes are generally smaller, but still consistent within the errors with the majority of previous estimates.

Adopting for the distance to the LMC the canonical value by Pietrzynski et al. (2013) (D = 49.97 ±0.19 (stat) ± 1.11 (syst) kpc) and taking the mean value of all six LMC distance moduli derived in this study (lower portion of Table 4.3), we conclude that Reticulum is located approximately 3 kpc closer to us than the barycentre of the LMC.

4.1.3 SMHASH: a new mid-infrared RR Lyrae distance determination for the Local Group dwarf spheroidal galaxy Sculptor

4.1.3.1 RR Lyrae stars in Sculptor

Sculptor was the first MW dSph satellite discovered (Shapley 1938) and, consequently, is among the best studied ones. van Agt (1978) identified 602 variables associated with the galaxy, deriving and publishing periods for 64 of these. Kaluzny et al. (1995, hereafter, K95), as part of the Optical Gravitational Lensing Experiment (OGLE) project, has published a catalogue of 229 variables (226 RRL and 3 Anomalous Cepheids) located in the inner part of Sculptor. Using the period distribution of RRab stars, these authors estimated that the bulk of Sculptor RRLs has metallicity $[Fe/H]_{ZW} \leq -1.7$ dex[3]. However, they also note that the colour range spanned by the RGB stars is suggestive of a metallicity spread as large as $-2.2 \lesssim [Fe/H]_{ZW} \lesssim -1.6$ dex. Indeed, Majewski et al. (1999), from an analysis of RGB and HB stars based on optical photometry, found that Sculptor has a bimodal metallicity distribution with a metal-poor stellar component having [Fe/H] ~ -2.3 dex and a more metal-rich component at [Fe/H] ~ -1.5 dex. Combining photometric and high resolution spectroscopic data Tolstoy et al. (2004) confirmed the presence of two stellar populations in Sculptor, one metal-rich, $-1.7 <$ [Fe/H] < -0.9 dex, and one metal-poor, $-2.8 <$ [Fe/H] < -1.7 dex, that are kinematically and spatially separated from each other. Independently, Battaglia et al. (2008, using the velocity dispersion gradient from the calcium triplet lines in spectra of the galaxy's red giant stars) and de Boer et al. (2011, by measuring the age gradient from outer to inner galaxy regions with wide-field photometry) confirmed the existence of multiple components in this dSph. Clementini et al. (2005, hereafter, C05) obtained low resolution spectra for 107 RRLs in Sculptor (about half the sample of RRLs in K95) and measured individual metallicities in the range $-2.40 <$ [Fe/H] < -0.85 dex, with an average value of $[Fe/H]_{ZW} = -1.83 \pm 0.03$ dex ($r.m.s. = 0.26$ dex). C05 remains so

[3]ZW denotes Zinn & West (1984) metallicity scale.

far the only spectroscopic measurement of Sculptor RRL metal abundances. It confirms the existence of a real metallicity spread in this dSph, wider than that found by K95 and consistent with the spread obtained by Geisler et al. (2005) based on high resolution spectra of four RGB stars ($-2.1 \lesssim [\mathrm{Fe/H}]_{\mathrm{ZW}} \lesssim -0.97$ dex). The distance modulus of Sculptor has been measured using several different distance indicators and independent techniques. Over 30 measurements exist in the literature, the majority using RRLs. K95 derived a distance modulus of 19.71 mag based on the average V magnitude of more than 100 RRab stars in their catalogue. Recently, Martínez-Vázquez et al. (2015, 2016a) used archival data spanning 24 years to redouble the known RRL population in Sculptor. They discovered more than 300 new variables spread over $\sim$2 deg^2 from the galaxy's centre. They used the RRL PL relation in the I-band to pin the Sculptor distance modulus down to 19.62 ± 0.04 mag[4]. A detailed comparison of values in the literature for the distance to Sculptor is presented in Section 4.1.3.6. This study is the first in a series dedicated to the results obtained for the four dSph galaxies observed in the SMHASH program. As Sculptor is the dSph with the largest number of previously known RRLs in our sample, we have chosen this galaxy to demonstrate the observational and data reduction methodologies adopted throughout the dwarf satellites, targets of this program. This study serves as a fiducial work for the rest of the SMHASH program on dSphs.

4.1.3.2 Observations and data reduction

The MIR time series photometry presented here was collected on 2014 October 1 - 10 with IRAC on the *Spitzer* Space Telescope as part of the Warm Spitzer Cycle 10 (PI: 61327 K. Johnston). During the Warm *Spitzer* mission, IRAC operates only using two channels simultaneously, at 3.6 μm and 4.5 μm and acquired observations of Sculptor dSph (12, each with exposure time of 140 s) in two adjacent fields. The SMHASH observations of Sculptor were designed to optimise the signal to noise ratio for time-series observations of RRLs in the 3.6 μm channel. As a result the signal to noise ratio of individual 4.5 μm observations is close to the detection limit. Hence, in this study we present only the 3.6 μm observations.

[4]These authors also inferred (semi-theoretical) metallicities for their RRL sample, exploiting the dependence of the I-band PL relation on metallicity (Marconi et al., 2015). Their average metallicity is consistent with the majority of previous spectroscopic measurements.

Our pointing (RA (J2000)= $01^{h}00^{m}02.6^{s}$, DEC (J2000)= $-334'55''$) , about $2''$ South-West direction from the galaxy's centre as published in McConnachie (2012), was selected to maximise the number of RRLs in the IRAC field of view, using the RRL catalogues from K95 and C05 as input. According to the K95 variable star catalogue, there should be 52 RRLs in the $5' \times 5'$ region that our pointing covers. In the process of this work we have found that 3 of these 52 stars (V1926, V2558 and V2559) have identical coordinates to other stars with different ID numbers, and are undoubtedly the same variables (see Table 4.4 for details). These *doubles* had also been noted by Martínez-Vázquez et al. (2015). Therefore we are left with 49 RRL stars (36 fundamental mode, RRab, and 13 first overtone pulsators, RRc stars) that were observed for 12 epochs, non-uniformly spaced over 10 days. Figure 4.7 shows the 49 Sculptor RRLs over-plotted onto the *Spitzer*-IRAC field of view. Blue open circles denote the RRab stars, red filled diamonds denote RRc stars.

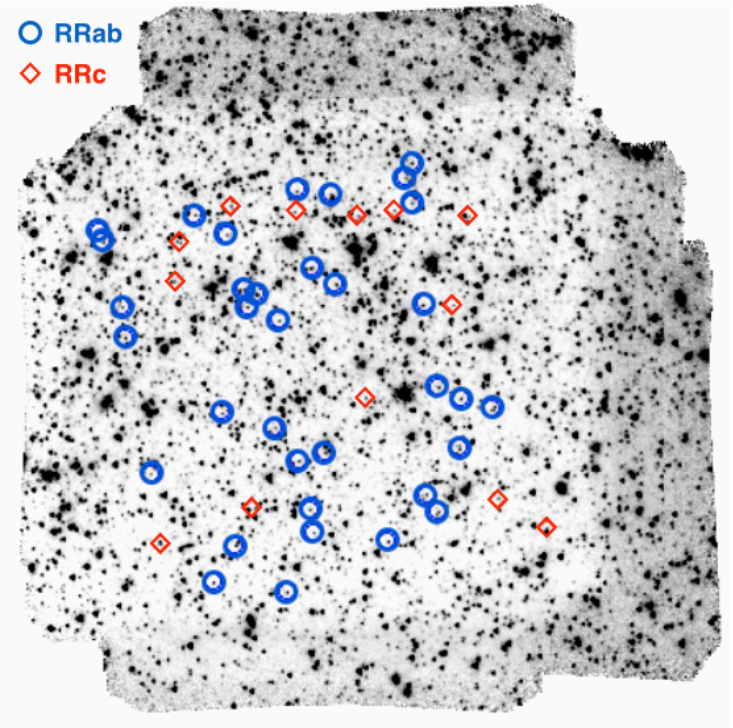

FIGURE 4.7: IRAC-*Spitzer* master mosaic at 3.6 μm that shows the 49 Sculptor RRLs in our sample encircled by blue open circles (RRab stars) or red diamonds (RRc stars). The field of view of the IRAC frame is $5' \times 5'$. North is up and east is to the left. Figure from Garofalo et al. (2018).

Mosaics were created from the *Spitzer* Science Center S19.2 pipeline processed data and the `MOPEX` software package (Makovoz & Khan, 2005). A single mosaic was created for each epoch using the dithered exposures. Additionally, a master mosaic using all exposures for all epochs was made as input for the deep `ALLFRAME` master detection list. Mosaicked location-correction images corresponding to each epoch were also created. Point-spread function (PSF) photometry was then performed using the `DAOPHOT-ALLSTAR-ALLFRAME` packages (Stetson, 1987, 1994). First, the single-epoch mosaics were converted from MJy/sr to counts (DN) using the conversion factor (MJy/sr per DN/sec) and the exposure times provided in the data headers. Then we ran `DAOPHOT`, passing through a sequence of routines to obtain a PSF suitable for all stars of each single-epoch mosaic. Using `ALLSTAR`, we simultaneously applied the PSF to all stars measured on each single-epoch mosaic[5]. The average PSF is built selecting from 50 to 90 isolated and bright stars ($m_{3.6} < 15.5$ mag) uniformly distributed across the whole frame for each single-epoch mosaic. We then ran `ALLFRAME` to obtain the final photometry catalogue of sources. `ALLFRAME` was used to improve the instrumental magnitudes and decrease the photometric uncertainties by fixing the positions of the stars according to the deep reference image and derived translation and rotation of the individual frames, thus reducing the number of free parameters in each PSF fit. The IRAC photometry obtained in this catalogue was calibrated on a zero-point magnitude (zmag) provided in the IRAC handbook[6] in the standard IRAC Vega magnitude system. The *Spitzer* photometric calibration is realized by applying an aperture correction to the list of sources chosen to measure the PSF. This step is implemented using `DAOPHOT` routines in the IRAF[7] environment. A final PSF correction (or calibration) is then calculated from the PSF photometry and the corrected aperture photometry, which is then applied to all stars. This transforms all the IRAC photometry onto the IRAC Vega system. The final step is the application of the array location-dependent correction on to the photometric measurements of the final catalogue using a set of correction images. The corrections depend on the exact position of sources on these images created concurrently with the single-epoch mosaics (detailed information on this process and the creation of

[5]Mosaics have a pixel scale of 0.6 arcsec/pixel where the typical PSF FWHM value for the *Spitzer*-IRAC images at 3.6 μm is 1.66 arcsec, as provided in Section 5 of the IRAC Instrument Handbook (https://irsa.ipac.caltech.edu/data/SPITZER/docs/irac/iracinstrumenthandbook/5).

[6]http://irsa.ipac.caltech.edu/data/SPITZER/docs/irac/iracinstrumenthandbook (Chapter 4).

[7]IRAF is distributed by the National Optical Astronomical Observatory, which is operated by the Association of Universities for Research in Astronomy, Inc., under cooperative agreement with the National Science Foundation.

the correction images are explained in the IRAC handbook[8]). Seven out of the 49 RRL on our frames are very close to other objects, or else have an elongated shape, which makes it difficult to measure their PSF profile accurately, thus making their photometry unreliable. These stars are marked with asterisks in Table 4.4. Such effects are visible in the light curves of these stars (see Section 4.1.3.3) and have repercussions for their positions on the [3.6]-logP plane (see Section 4.1.3.5). We have discarded these seven stars (V59, V1482, V1555, V1558, V1824, V1874, V2021) from our *PL* study. Accordingly, we start our analysis with a sample of 42 RRLs.

4.1.3.3 Light curves

The light curves of the variables were analyzed with the Graphical Analyzer of Time Series software (GRATIS; Clementini et al. 2000). Our data were not optimised for period searches, thus we built the light curves using reference periods and times of maximum light (HJD_{max}) from K95 and C05. All 42 of our variables have been studied by K95 but only 23 are in common with C05, who measured spectroscopic metallicities and remeasured the periods and HJD_{max} from the K95 data. Where available, we use the periods and HJD_{max} from C05, otherwise we use the original values from K95. The K95 periods and those redetermined by C05 differ only at the 4^{th} or 5^{th} decimal digit onward. We consider these changes negligible.

[8] http://irsa.ipac.caltech.edu/data/SPITZER/docs/irac/iracinstrumenthandbook (Section 4.5).

TABLE 4.4: Properties of RRLs in Sculptor observed at 3.6μm.

Name	α (J2000)	δ (J2000)	Type	P[a] (days)	logP	Epoch (max) JD (−2440000)	$\langle V \rangle$ (mag)	Amp_V (mag)	$\langle [3.6] \rangle$[b] (mag)	$\sigma_{\langle [3.6] \rangle}$ (mag)	$Amp_{[3.6]}$ (mag)	[Fe/H][c] (dex)
V59*	0:59:51.31	-33:47:24.1	RRc	0.359681	-0.444	9168.9359	20.176	0.44	18.640	0.037	0.05	-2.14
V377	0:59:51.71	-33:43:14.8	RRc	0.29522	-0.530	9168.9359	20.069	0.50	19.197	0.039	0.22	-
V406	0:59:52.92	-33:45:44.8	RRab	0.55025	-0.259	9168.9359	20.195	0.78	19.171	0.054	0.21	-
V1446	1:00:07.89	-33:47:27.1	RRab	0.77331	-0.111	9168.9359	19.805	0.52	18.496	0.043	0.33	-
V1457	1:00:01.08	-33:47:06.1	RRab	0.717799	-0.144	8827.8527	19.919	0.96	18.808	0.052	0.19	-1.82
V1462	1:00:05.46	-33:46:46.5	RRab	0.56113	-0.251	8827.8527	20.021	1.02	19.029	0.023	0.18	-
V1470	1:00:05.37	-33:46:28.6	RRab	0.50565	-0.296	8827.8527	19.979	0.90	19.115	0.020	0.16	-
V1482*	1:00:09.06	-33:46:18.7	RRc	0.29810	-0.526	8827.8527	20.081	0.70	18.897	0.035	0.06	-
V1546	0:59:59.55	-33:47:14.6	RRab	0.531239	-0.275	9174.9206	20.151	1.00	19.333	0.032	0.10	-2.31
V1553	1:00:10.33	-33:46:42.8	RRab	0.71644	-0.145	9174.9206	20.004	0.54	18.812	0.030	0.20	-
V1555*	0:59:57.76	-33:46:53.5	RRab	0.527243	-0.278	8823.8298	20.089	0.93	18.878	0.021	0.01	-1.84
V1558*	0:59:53.84	-33:46:52.1	RRc/d/Bl	0.243016	-0.614	8833.9116	20.203	0.49	19.061	0.060	0.11	-1.65
V1566	0:59:58.11	-33:46:37.2	RRab	0.570272	-0.244	8809.9982	20.053	0.89	18.987	0.050	0.35	-1.77
V1823	0:59:53.86	-33:44:19.2	RRc	0.298462	-0.525	9189.8649	20.255	0.63	19.567	0.037	0.09/0.12	-1.52
V1824*	0:59:55.72	-33:44:13.8	RRab	0.47550	-0.323	9189.8649	19.963	0.44	18.715	0.025	0.05	-
V1830	1:00:04.61	-33:44:00.9	RRab	0.517855	-0.286	8809.2712	20.224	0.97	19.186	0.028	0.18	-2.09
V1838	1:00:00.66	-33:43:43.5	RRab	0.70752	-0.150	8809.2712	19.926	0.86	18.698	0.050	0.18	-
V1873	0:59:56.13	-33:42:57.7	RRc	0.2923	-0.534	8809.2712	20.157	0.54	19.491	0.059	0.17	-
V1874*	0:59:58.41	-33:42:55.5	RRc	0.26901	-0.570	8809.2712	20.007	0.53	19.101	0.075	0.08	-
V1875	1:00:06.63	-33:42:47.4	RRab	0.499773	-0.301	8823.9437	20.028	1.01	19.137	0.034	0.23	-2.02
V1877	0:59:54.98	-33:42:55.3	RRab	0.56716	-0.246	8823.9437	20.171	0.62	19.166	0.059	0.10/0.15	-
V1899	0:59:55.48	-33:46:08.7	RRab	0.646664	-0.189	9182.9074	19.978	0.84	18.811	0.045	0.27	-2.29
V1910	1:00:05.39	-33:45:50.2	RRab	0.572828	-0.242	9189.9080	20.083	0.87	19.055	0.070	0.31	-2.11
V1914	1:00:03.64	-33:45:48.1	RRab	0.570540	-0.244	8829.8781	20.220	0.71	18.871	0.013	0.23	-1.87
V1926[d]												
V1930	1:00:06.33	-33:45:20.8	RRab	0.611160	-0.214	9188.9162	20.251	0.56	18.980	0.017	0.20	-1.79
V1932	0:59:54.72	-33:45:31.2	RRab	0.506044	-0.296	9174.9206	20.155	1.15	18.894	0.032	0.18	-1.53
V1940	0:59:55.89	-33:45:18.6	RRab	0.692975	-0.159	9224.7748	20.117	0.58	18.827	0.020	0.23	-1.49
V1941	1:00:00.44	-33:45:14.4	RRc	0.365674	-0.437	9166.8670	20.152	0.47	19.161	0.035	0.10	-1.47
V1943	1:00:09.35	-33:45:01.0	RRab	0.551149	-0.259	9169.9100	20.146	0.93	19.048	0.015	0.29	-1.54
V1997	1:00:06.35	-33:43:45.3	RRab	0.626766	-0.203	8823.9437	20.136	0.86	18.879	0.032	0.15	-2.08
V2004	1:00:05.52	-33:43:38.2	RRab	0.58735	-0.231	8823.9437	20.196	1.15	19.024	0.038	0.26	-
V2012	1:00:06.28	-33:43:31.5	RRab	0.71475	-0.146	8823.9437	20.15	0.45	18.766	0.018	0.15	-
V2021*	1:00:01.99	-33:43:26.9	RRab	0.62292	-0.206	8823.9437	20.212	0.52	18.557	0.019	0.16	-
V2048	1:00:02.20	-33:42:41.6	RRc/Bl	0.35836	-0.446	8823.9437	20.150	0.61	19.404	0.065	0.09/0.14	-
V2058	1:00:08.26	-33:42:26.7	RRab	0.503415	-0.298	9226.9053	20.238	0.88	19.081	0.053	0.19	-1.92
V2059	0:59:59.77	-33:42:34.7	RRab	0.49692	-0.304	9226.9053	20.191	1.02	19.267	0.067	0.16	-
V2410	1:00:01.78	-33:42:26.7	RRab	0.53183	-0.274	9226.9053	20.183	0.89	19.180	0.021	0.32	-
V2558[e]												
V2559[f]												
V2562	1:00:05.95	-33:42:26.3	RRc	0.38627	-0.413	9226.9053	20.128	0.54	19.155	0.031	0.08/0.12	-
V2566	0:59:54.99	-33:42:35.0	RRab	0.583517	-0.234	9190.8800	20.234	0.81	18.974	0.052	0.17	-1.38
V2575	0:59:54.42	-33:42:25.0	RRab	0.61108	-0.214	9190.8800	19.984	0.75	18.736	0.075	0.11	-
V3365	1:00:12.18	-33:47:07.2	RRab	0.668088	-0.175	9235.8929	20.105	0.48	18.902	0.040	0.18	-2.01
V3468	1:00:14.87	-33:46:29.1	RRc	0.29382	-0.532	9235.8929	20.120	0.56	19.419	0.051	0.21/0.20	-
V3760	1:00:14.14	-33:43:47.8	RRab	0.54851	-0.261	9235.8929	20.320	0.76	19.012	0.035	0.19	-
V3810	1:00:14.30	-33:42:23.0	RRab	0.66197	-0.179	9235.8929	20.130	0.83	18.836	0.066	0.14	-
V3827	1:00:14.49	-33:45:34.5	RRab	0.587708	-0.231	9226.7339	20.135	0.88	19.017	0.031	0.15	-2.04
V3907	1:00:13.90	-33:43:23.8	RRab	0.583204	-0.234	9169.9000	20.203	0.73	19.053	0.115	0.29	-1.76
V3916	1:00:10.42	-33:43:13.5	RRc	0.305	-0.516	9169.9000	20.153	0.59	19.226	0.034	0.13	-
V3931	1:00:09.52	-33:42:45.3	RRc	0.36016	-0.443	9169.9000	20.248	0.52	19.252	0.058	0.11	-
V3934	1:00:14.17	-33:42:31.6	RRab/Bl	0.5198	-0.284	9169.9000	20.125	0.94	19.163	0.069	0.45	-

Notes. [a]Period, epoch of maximum light and intensity-averaged mean Vmagnitude for stars with metallicities are from C05, who determinated them anew from the light curves based on data from K95. [b] The [3.6] mean magnitudes presented in this work are not reddening corrected (see text for details). [c]Spectroscopic metallicities from C05 on the Zinn & West scale. [d]Same coordinates as V406. [e]Same coordinates as V2058. [f]Same coordinates as V2059. * Most problematic stars.

For one star, V1875, C05's period differs significantly from that derived by K95. C05 classified V1875 as an RRab star while K95 considered it an RRc. We found that the C05 period and classification for V1875 fit our data well (see Figure 4.9), and so we retain the C05 period (and hence classification) for consistency within our analysis. The final sample in our catalogue is as follows: 33 RRab and 9 RRc stars. The light curves of the variable stars are presented in Figure 4.9. The identification and the properties of our sample of RRLs are summarized in Table 4.4. The variables are ordered by increasing ID number, adopting the nomenclature from K95 and C05. Column 1 lists the star identifier, columns 2 and 3 provide the right ascension and declination (J2000 epoch), respectively. The coordinates were obtained from our astrometrized reference image (see Section 4.1.3.2). Column 4 lists the classification of RRLs according to pulsation mode, RRab or RRc, columns 5, 6 and 7 list the pulsation period, its logarithm and HJD_{max} from either K95 or C05 (if a spectroscopic metallicity is available in column 13, then the values in columns 5, 7, 8, and 9 come from C05, otherwise, they are from K95). Columns 8 and 9 list, respectively, the intensity-weighted mean magnitudes and amplitudes of the light variation in the V band from either K95 or C05, while columns 10, 11 and 12 give the intensity-weighted mean magnitudes, the corresponding errors and the amplitudes of the light variation at 3.6 μm. Finally, column 13 provides spectroscopic metallicities from C05, where available. While identifying and classifying the variables, K95 found that some are possibly affected by the Blažko effect. Three of these stars are in our sample: V1558, V2048, V3934. Moreover, we find that V1558 and V2048 are significantly affected by crowding and/or blending. Visual inspection of our imaging also reveals that some of our other stars lie in crowded regions (e.g., V59), or are clearly blended with neighbour stars or diffuse objects. We will discuss these problematical objects in detail in the following section.

4.1.3.4 Comments on individual problematic stars

The following stars are discussed from the most to the least problematic source. The first seven stars (V59, V1482, V1555, V1558, V1824, V1874, V2021), which could be clearly identified as contaminated from the initial visual inspection of the images, are not included in any PL analysis. This is clearer in Figure 4.8 which shows the MIR period-amplitude diagram of the 42 RRLs together with the seven discarded sources, based on light curves at 3.6 μm: most of the RRLs excluded (black crosses) have MIR

amplitude smaller then the RRab (blue open circles) and RRc stars (red diamonds) of the sample. We include the details here for completeness:

V59 - Kovács (2001) classifies star V59 as a suspected double-mode (RRd) with periods of 0.35968/0.4837 d. C05 do not confirm this finding, and instead suggest a classification of a monoperiodic RRc with a noisy light curve. A visual inspection of our images shows it to be completely blended with a nearby star. This is reflected in the time-series as an unnaturally flattened light curve.

V1482 - The star is the second brightest RRc in our sample. The light curve's amplitude is smaller than expected (see Figure 4.8). It is possibly a blended source. The presumed blending is further confirmed by visual inspection of WFC3@HST images (PI:12966 van der Marel) overlapping our IRAC pointing and having higher spatial resolution (0.04 arcsec/pixel).

V1555 - This star is very close to two sources, one of which is brighter than V1555. The bright source may be contaminating the flux measurement of V1555, polluting the light curve periodicity and the mean magnitude (see Figures 4.9, 4.8 and 4.10).

V1558 - Suspected Blažko in K95, whereas C05 suspected it may be an RRd star. In our images V1558 has an elongated shape, which is probably due to the contamination

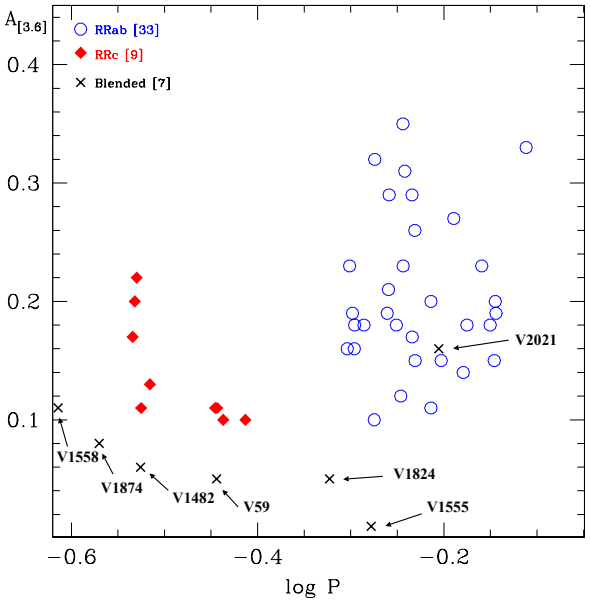

FIGURE 4.8: MIR period-amplitude diagram for all the RRL in our sample based on light curves at 3.6 μm. The blue open circles and the red diamonds mark the RRab and RRc stars, respectively. The RRL affected by crowding/blending and discarded in this study are labelled and marked with crosses. Figure from Garofalo et al. (2018).

from a background source.

V1823 - This is the faintest star of our sample but falls within 1σ of our PL relations and also fits well the PL relations of Neeley et al. (2015) and Madore et al. (2013). One data point was removed from the light curve fit (grey filled squares in Fig. B.1) as it significantly deviated from the fitted light curve model, but is shown in the figure for completeness.

V1824 - Visual inspections of the light curve, images, and log P - luminosity plane show that star is clearly blended with a close diffuse source. The light curve amplitude is reduced (Figures 4.8 and B.1) and the mean magnitude is at least 0.5 mag brighter than expected (Figure 4.10).

V1874 - The light curve is noisy, most likely caused by blending from a close neighbour object indistinguishable on the images.

V2021 - There are not any caveats in the literature regarding this object, but in our images it appears rather extended. This is most likely due to crowding/blending and the reduced resolution of the IRAC images compared to previous studies.

V1877 - The light curve is not sampled between $\phi = 0.9$ and 1.3 (the non-uniform cadence of our observations means that we would never optimally sample the light curve of every star in the field) and, like V1823, has one data point that has been excluded from the fit. However, its mean magnitude plotted on the [3.6]-log P plane follows the PL relations well.

V2048 - According to K95 possibly a Blažko source. Classified by Kovács (2001) as an RRd star.

V2562 - The light curve shows one data point that has been excluded from the fit but this does not affect the star's mean magnitude.

V3931 - K95 considered this star to be an RRc with a period of 0.36016 d. Kovács (2001) classifies this star as an RRd with periods 0.358350/0.48140 d.

V3468 - Adopting the period and HJD_{max} from K95, the light curve is not fully sampled and a couple of data points are significant outliers. Although our data were not optimised for period searches, we attempted to perform a search using GRATIS. The period found using GRATIS (P=0.2733d) was shorter than the one found by K95 (P=0.2938d), and gives a light curve fit with both smaller r.m.s. (0.04 from the GRATIS period compared to 0.06 using the K95 period) and smaller χ^2 (see Fig. B.1). However, because we did not design our observations with a view to perform period searches,

systematics may be present that could affect this measurement. An analysis of such uncertainties is beyond the scope of this work, so rather than trust the new measurement unequivocally we test both values in our analysis.

V1875 - The classifications of both type and period differs significantly between K95 and C05. The formers consider the star to be an RRc affected by the Blažko effect, while C05 considered the star to be an RRab. The periods published by the two studies are aliased ($P_{K95} = 0.66\ P_{C05}$). Our observations are in agreement with the C05 findings.

V3934 - K95 consider this a possible Blažko source. We do confirm their period. The Blažko effect appears generally as a variation of amplitude and period of the light curve typically occurring on time scales from a few tens to a few hundreds of days. This effect has not yet been investigated in detail at MIR wavelengths but it is likely that the amplitude modulation is reduced when going from shorter to longer wavelengths (Klein et al., 2014; Gavrilchenko et al., 2014). Furthermore, the time interval covered by our observations may be too short to reveal the Blažko modulation. These may be the reasons why the amplitude and mean magnitude values we obtain are normal for an RRL with this period.

4.1.3.5 [3.6] PL relations: RRL datasets and slopes

In this work we derived our PL relations using the starting sample of 42 Sculptor RRLs[9] that we divided in various different subsamples as summarised in Table 4.5.

The PL relations are presented in Figures 4.10 and 4.11 for two of these subsamples. In the top panel of each figure the periods of the RRc stars have been *fundamentalised*, by adding 0.127 to the $\log P$, and the RRab and RRc have been fit together using a single PL relation. In the bottom panels we plot the RRab and RRc stars separately and fit them using independent PLs. The grey filled triangles mark the seven most problematic variables (i.e., V59, V1482, V1555, V1558, V1824, V1874, V2021), whose images and light curves reveal signatures of blending and crowding (in some cases confirmed by K95 and C05). The thick black solid line is the least-squares fit calculated by excluding the seven blended stars. The cyan (dashed), orange (thin solid) and green (dot-dashed) lines use the slopes of the empirical PL relations from Madore et al. (2013), Neeley et

[9] Assuming a foreground $E(B-V) = 0.0159$ mag from the Schlafly & Finkbeiner (2011) map and applying the Monson et al. (2012) equation for 3.6 μm [$A_{3.6} = 0.203 \times E(B-V)$], the extinction measured for Sculptor is one order of magnitude smaller than the photometric error (i.e. $A_{3.6} \leq 0.003$ mag) and can be safely neglected for the purposes of this study.

al. (2015) and Neeley et al. (2017), respectively. To avoid overcrowding the figures we only show the $\pm 2\sigma$ deviation lines of Neeley et al. (2017) as an example; dispersions in the other PLs are similar.

Recall from Section 4.1.3.3 that the seven most problematical stars have already been discarded from the sample and are not considered in any of the following analysis. We refer to our starting sample from this point forward as Dataset1 (D1; 42 RRL, 33 RRab + 9 RRc). The scatter from our best-fit model is 0.11 mag, which is smaller than the previous work based on infrared photometry (Pietrzyński et al., 2008, $\sigma_K = 0.22$ mag,

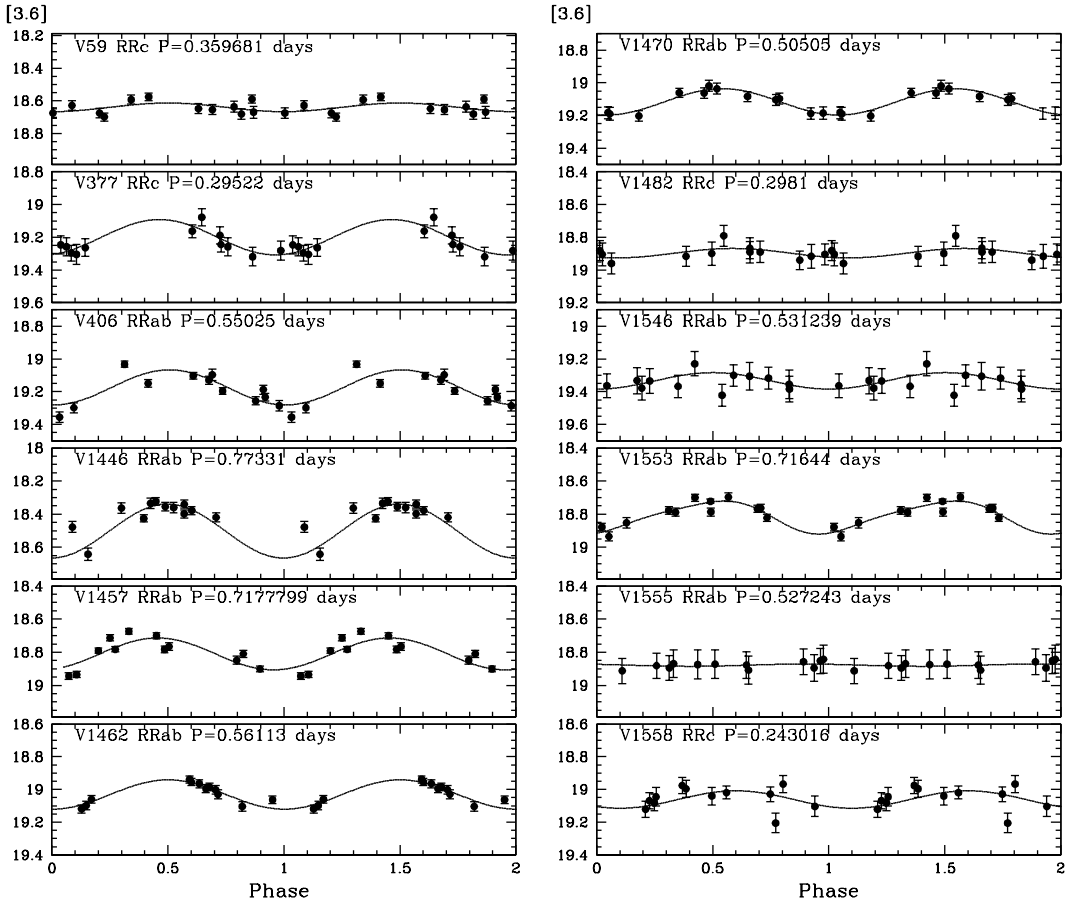

FIGURE 4.9: Light curves in the [3.6]-band for our sample of 49 RRLs in the Sculptor galaxy. The stars are ordered with increasing ID number adopting the nomenclature from K95 and C05. The solid black lines represent the light curve models generated by GRATIS using all phase-points. V59, V1482, V1555 and V1558 are problematic stars not used to fit the PL relations (see Sect. 4.1.3.4 and Table 4.4). The first 12 light curves are shown here, the remaining are plotted in Appendix B. Figure from Garofalo et al. (2018).

TABLE 4.5: Definition of RRL datasets used in this analysis

Sample identifier	Description	No. RRL (RRab+RRc)
D1	Full sample. Original light curves.	42 (33 + 9)
D2	Six partially problematic stars removed (see § 4.1.3.4).	36 (32 + 4)
D3[a]	Full sample. Stars removed in D2 have corrected light curves. V3468 has GRATIS period.	42 (33 + 9)
D3[b]	Full sample. Stars removed in D2 have corrected light curves. V3468 has K95 period.	42 (33 + 9)
D4	Strict selection based on FourStar images.	19 (17 + 2)
DZ[c]	Stars with spectroscopic metallicities from C05.	20 (18 + 2)

Notes: [a]Adopting the GRATIS period for V3468 (P=0.2733d). [b]Adopting the K95 period for V3468 (P=0.2938d). [c] Sample contains 14 RRLs defined as *metal-poor* (with [Fe/H] < -1.7 dex), 6 RRLs defined as *metal-rich* (with [Fe/H] > -1.7 dex).

$\sigma_J = 0.21$ mag). These authors suggest that the single-phase nature of their observations and the metallicity spread of the galaxy might contribute to the large scatter they observe. We will investigate the role played by metallicity later in this section. To determine the quality of our photometry and to see how any systematics arising from blending and/or crowding might affect our results, we subdivided our sample into several datasets (see Table 4.5). This allows us to choose the most accurate sample of RRLs to measure the distance modulus of Sculptor. Dataset2 (D2) contains 36 stars, the "good" variables that remain if we exclude the six partially problematic stars (V1823, V1877, V2048, V2562, V3931 with one or two phase points excluded in the light curve best-fits and V3468 with an ambiguous period, see Section 4.1.3.4). Dataset3 (D3a) comprises 42 stars: 36 "good" variables and the six partially problematic stars with the average magnitude calculated for 5 of them by using only the 10 or 11 phase-points that best fit the light curve model. For V3468 the revised period determined in Section 4.1.3.3 using GRATIS and our data is adopted. Instead Dataset3b (D3b) is the same as in D3a except for V3468's period, which is provided by K95.

Table 4.6 summarizes the slopes of the PL relations for the RRab-only, RRc-only or combined RRab+RRc samples, measured by least squares fitting each of the datasets D1, D2, D3 (columns 2, 3, 4 and 5, respectively). A comparison among datasets shows that the slopes of the RRab+RRc and RRab relations are all compatible within their errors. The RRc stars in our sample exhibit a slope that differs significantly from the slopes of the RRab and RRab+RRc samples and even more so from Neeley et al. (2015)'s slope for RRc stars (Table 4.6 column 8). However, the large uncertainties on our RRc slope results mean that the difference is not statistically significant. Neeley et al. (2015)'s slope for RRc stars also differs from and is steeper than that for RRab stars, but our RRc slopes go in the opposite direction and are shallower. One possible explanation of this finding is the small number and poor distribution in period of the RRc stars in our sample. There are approximately double the number of RRab compared to RRc stars in our

sample. However, because RRc stars are fainter and hence more likely to suffer blending by bright neighbours than RRab stars, after discarding problematical stars the RRc in the D1 sample reduced approximately to one-third the number of RRab stars (and lower still in the D2 sample). In Figure 4.10, bottom panel, it is clear that the RRc do not cover the periods range entirely, but cluster around logP≈ -0.425 and logP≈ -0.525. The poor RRc period distribution means that their PL slopes are less robust than the RRab-only and RRab+RRc slopes. The combination of the non-uniform period distribution with the reduced sample size, results in significantly higher uncertainties for the RRc-only samples. For this reason we exclude the RRc-only samples from further analysis in this work. As a final test on the quality of our sample, we compared our deepest image with a deep ground based H-band image of Sculptor from the FourStar NIR camera on the 6.5 m Magellan telescope (Persson et al., 2013). The image covers a larger area than the *Spitzer*-IRAC field of view, with a resolution of 0.68 arcsec and an exposure time of 1000 s. Comparison with this higher resolution, deeper image allows us to select only those RRL that are perfectly isolated in the *Spitzer* images to measure the distance to Sculptor.

The outcome of this strict selection is our final quality-test subset, D4. It consists of 19 RRLs (17 RRab + 2 RRc). Figure 4.11 shows the PL relations for the D4 sample, colours and symbols are the same as in previous figures. Column 6 of Table 4.6 lists the slopes of the PL relations from D4. Since there are only two RRc stars in the D4 sample we did not attempt to measure an RRc-only slope. There is a perfect agreement between the RRab and RRc+RRab slopes of the PL relations from D4. These slopes are shallower than found from the D1, D2, and D3 datasets and in very good agreement with the slopes found by Muraveva et al. (2018a) from RRLs in the Reticulum cluster. They also agree well within the errors with the slopes in Madore et al. (2013), Neeley et al. (2015) and Neeley et al. (2017).

4.1.3.6 Distance determinations

Since our main aim is to measure the Sculptor distance modulus from our data, we adopt the following MIR PL relations of RRab and RRab+RRc as fiducials:

For RRab+RRc:

$$M_{[3.4]} = -2.44(\pm 0.95)\log(P) - 1.26(\pm 0.25) \tag{4.3}$$

σ[10] = 0.10 mag, eq. 1 of Madore et al. (2013);

$$M_{[3.6]} = -2.332(\pm 0.106)\log(P) - 1.176(\pm 0.080) \tag{4.4}$$

$\sigma = 0.095$ mag, eq. 4 of Neeley et al. (2015);

$$M_{[3.6]} = -2.304(\pm 0.105)\log(P) - 1.112(\pm 0.089) \tag{4.5}$$

$\sigma = 0.055$ mag, from Neeley et al. (2017);

$$M_{[3.6]} = -2.15(\pm 0.23)\log(P) - 1.19(\pm 0.05) \tag{4.6}$$

$\sigma = 0.06$ mag, from Muraveva et al. (2018a) calibrated on the 5 Galactic RRLs with HST parallaxes (see Section 4.1.2.4 and first column of Table 4.2)

$$M_{[3.6]} = -2.15(\pm 0.23)\log(P) - 1.08(\pm 0.03) \tag{4.7}$$

$\sigma = 0.06$ mag, from Muraveva et al. (2018a) calibrated on the same 5 Galactic RRLs but using their TGAS and DR2 parallaxes (see Section 4.1.2.4 and first column of Table 4.2).

For RRab only:

$$M_{[3.6]} = -2.370(\pm 0.139)\log(P) - 1.181 \tag{4.8}$$

from Neeley et al. (2015);

[10] This quantity means the r.m.s deviation, according to the notation adopted so far in this thesis.

$$M_{[3.6]} = -2.342(\pm 0.140)\log(P) - 1.155(\pm 0.089) \tag{4.9}$$

$\sigma = 0.040$ mag, from Neeley et al. (2017).

The Neeley et al. (2017) relations are from a reanalysis of the M4 data in Neeley et al. (2015) using the S19.2 *Spitzer* pipeline reduced data, combined with *HST* parallaxes for zero-point calibration. We include both the old and new Neeley et al. relations here for completeness and for consistency with upcoming SMHASH publications. The PL relations of Muraveva et al. (2018b) are derived for RRc+RRd+RRab whose data were processed with the same *Spitzer* pipeline as in Neeley et al. (2015). Consistently with the other MIR PL relations considered here, as seen in Section 4.1.2.4, the zero point of Muraveva et al. (2018a) PL relation in Eq. 4.6 is calibrated on the *HST* parallaxes while the zero point in Eq. 4.7 on the same 5 Galactic RRLs of Benedict et al. (2011) but using *Gaia* DR2 parallaxes for 4 stars and TGAS parallax for 1 star, RR Lyr itself.

Figures 4.10, 4.11 and 4.12 show the agreement between the PLs published in Madore et al. (2013), Neeley et al. (2015, 2017) and Muraveva et al. (2018a) (Eqs. 4.3, 4.4, 4.5, 4.6 and 4.7, respectively) and our data within 2σ. Only the D1 and D4 sub-samples are shown in the figures, but results for all four sub-samples are summarised in Table 4.6, where our measured RRab+RRc and RRab-only slopes from each dataset are shown to be compatible within the respective errors with those from Madore et al. (2013), Neeley et al. (2015, 2017) and Muraveva et al. (2018a). The results from the D4 dataset are particularly encouraging. The RRab-only and RRab+RRc slopes derived using this sub-sample agree within the uncertainties with those from Neeley et al. and Madore et al. (2013). The agreement of our RRab+RRc slope with that of Muraveva et al. (2018a) is particularly remarkable. Although D4 is a small sample, we are confident that it is free from any contaminating photometric effects. The slopes derived from the four samples all have values in the region predicted from other multi-wavelength analyses (see figure 8 in Neeley et al. 2015, an updated version of Figure 4 in Madore et al. 2013). This adds further weight to the semi-empirical conclusion that the slopes of RRL PLs in the MIR bands are well constrained in a range from -2.2 to -2.6.

The confirmation that our PL slopes are in agreement with published values is an important test of our photometry and of the universality of the RRL PL slope. We adopt the PL slopes from the literature to measure the distance modulus of Sculptor because (a) they are more robustly measured than is possible with our dataset and (b) an independent PL slope measurement allows a more accurate measurement of distance due to fewer free parameters in the fit.

We measured the distance modulus of Sculptor using each of the 4 sub-samples and the various empirical PL relation calibrations finding comparable results for a given fiducial

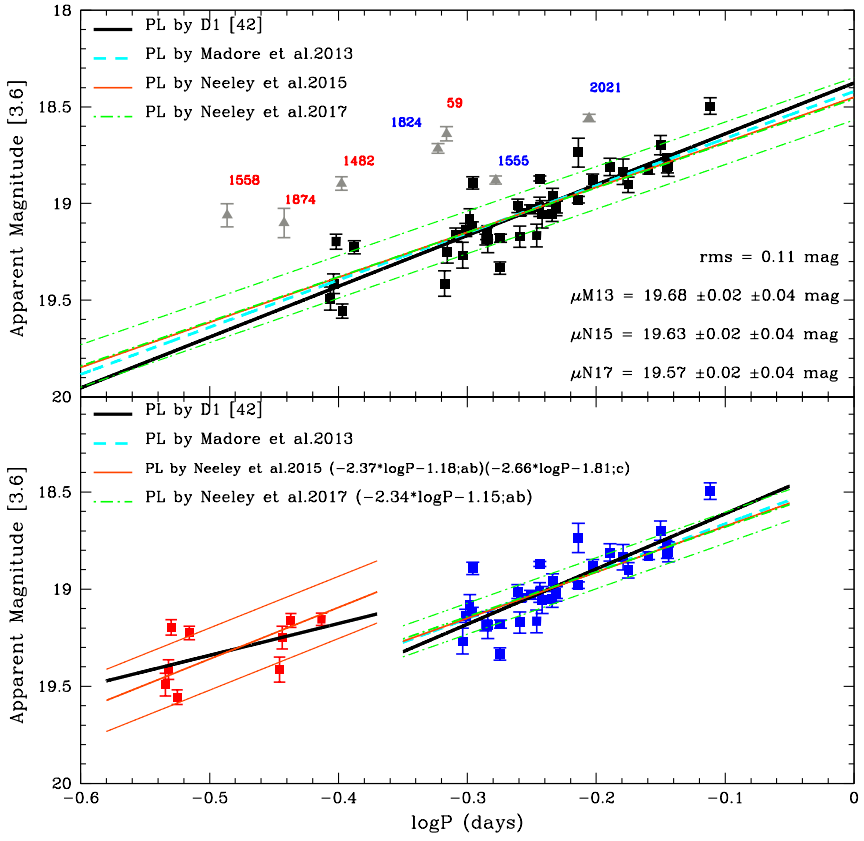

FIGURE 4.10: *Top panel*: 3.6 μm PL relations defined by the 42 RRLs observed in Sculptor (D1 sample). The periods of the RRc stars have been *fundamentalised*. The black solid line represents the least squares fit to the data in Table 4.4. The triangles are the most problematic stars not used in the least square fit. *Bottom panel*: RRab (blue symbols) and RRc (red symbols) stars are plotted in two PL relations that were computed from the fundamental-mode and the first-overtone pulsators separately. In both panels the cyan (dashed), orange (thin solid) and green (dash-dot) lines mark Madore et al. (2013), Neeley et al. (2015) and Neeley et al. (2017) PL relations respectively. We show only $\pm 2\sigma$ the deviation lines of the Neeley et al. (2017)'s PL, the dispersions of the other PL relations are similar or slightly broader. Figure from Garofalo et al. (2018).

PL ($\Delta\mu \leq 0.02$ mag among datasets). They span the range from 19.55 mag for the Neeley et al. (2017) PL relation applied to the D2 sample, to 19.68 mag for the Madore et al. (2013) PL relations and almost any of the Sculptor samples. The results obtained for each sample of RRab-only and RRab+RRc are in complete agreement within both the statistical and the systematic uncertainties using the Madore et al. (2013), Neeley et al. (2015, 2017) and Muraveva et al. (2018a) PL relations. We define the statistical error as the r.m.s. measured by each dataset divided by the square root of the number of RRL in the dataset, $\sigma_{stat} = r.m.s./\sqrt{N_{RRL}}$; the photometric error as the standard deviation of light curve residuals; and the systematic error for each dataset as the propagation of the r.m.s. of the reference PL and dataset; $\sigma_{sys} = \sqrt{(r.m.s._{ref})^2 + (r.m.s._{dataset})^2}$. In Table 4.7 we summarise distance moduli derived using the D1 and D4 datasets and each PL relation calibration. Our preferred values for the Sculptor distance modulus are obtained using the D4 sample along with the Neeley et al. (2017) RRab-only PL relation and the Muraveva et al. (2018a) relations which are valid for RRab+RRc+RRd stars. We consider these PL relations the most accurate as they are the only empirical relations derived so far at 3.6μm using time-resolved Warm-IRAC photometry, and are the most applicable to our data. In addition the relation from Muraveva et al. (2018a, Eq. 4.7 above) is the first MIR PL relation based on *Gaia* parallaxes (DR2 and TGAS, for RR Lyr). We find $\mu = 19.60 \pm 0.02$ (statistical) $\pm$ 0.04 (photometric) mag (with σ_{sys} =0.09 mag), equivalent to a distance of 83 $\pm$1 (statistical) $\pm$ 2 (photometric) kpc (with σ_{sys} =4 kpc) for Sculptor from Neeley et al. (2017) RRab-only PL relation and $\mu = 19.68 \pm 0.02$ (statistical) $\pm$ 0.04 (photometric) mag (with σ_{sys} =0.11 mag), equivalent to a distance of 86 $\pm$ 1 (statistical)$\pm$ 2 (photometric) kpc (with σ_{sys} =5 kpc) and $\mu = 19.57 \pm 0.02$ (statistical) $\pm$ 0.04 (photometric) mag (with σ_{sys} =0.11 mag), equivalent to a distance of 82 $\pm$ 1 (statistical)$\pm$ 2 (photometric) kpc (with σ_{sys} =5 kpc) from the Muraveva et al. (2018b) RRab+RRc+RRd PL relations based on HST and *Gaia* parallaxes, respectively. These results confirm the value found recently in optical bands by Martínez-Vázquez et al. (2015) ($\mu_0 = 19.62 \pm 0.04$ mag from 290 RRLs). Considering the Neeley et al. (2017) RRab+RRc PL relation, the distance modulus becomes $\mu_0 = 19.56 \pm 0.02$ (statistical) $\pm$ 0.04 (photometric) mag (with σ_{sys} =0.10 mag), that is in excellent agreement with the distance inferred from the Muraveva et al. (2018a) PL relation using *Gaia* parallaxes and also agrees with Martínez-Vázquez et al. (2015)'s results within the relative errors.

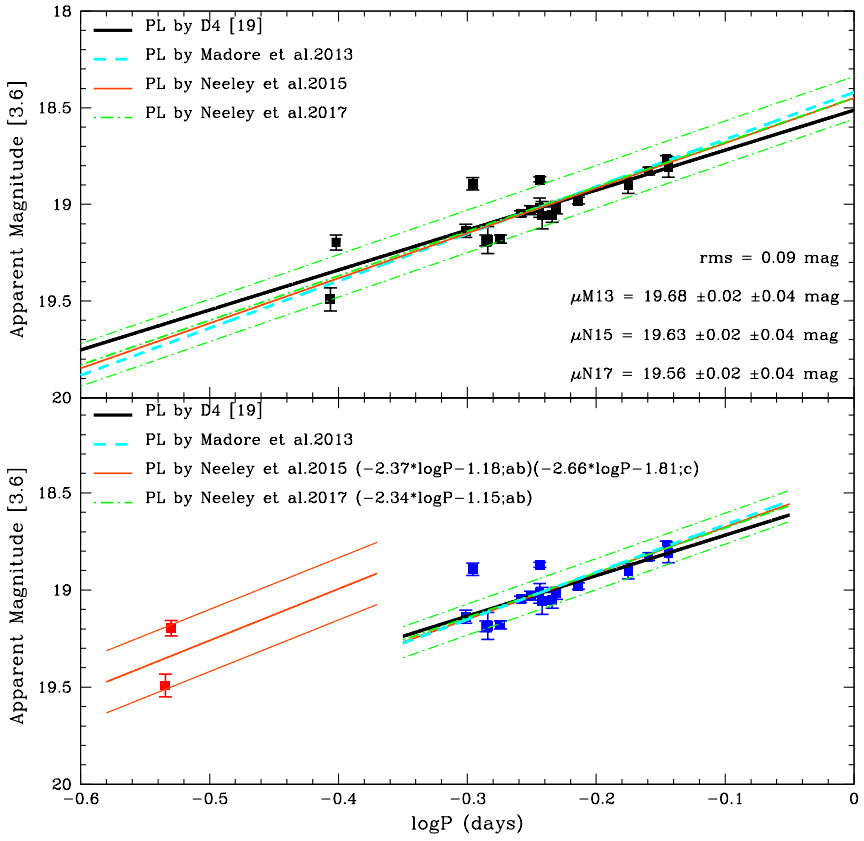

FIGURE 4.11: 3.6 μm *PL* relations defined by the 19 RRLs that compose the D4 sample. Symbols, colours and $\pm 2\sigma$ dispersion lines are as in Figure 4.10. Figure from Garofalo et al. (2018).

TABLE 4.6: Slopes of the [3.6] *PL* relations obtained for different selections of Sculptor RRab+RRc, RRab and RRc stars

Sample	D1 [42]	D2 [36]	D3 [42][a]	D3 [42][b]	D4 [19]	Madore et al. (2013)	Neeley et al. (2015)	Neeley et al. (2017)	Muraveva et al. (2018a)
RRab+RRc									
slope	−2.63	−2.43	−2.57	−2.63	−2.07		−2.33	−2.304	−2.15
$\pm\sigma_{slope}$	±0.22	±0.25	±0.22	±0.23	±0.31		±0.11	±0.105	±0.23
rms	0.11	0.10	0.11	0.11	0.08		0.095	0.055	0.06
RRab									
slope	-2.84	-2.82	-2.85	-2.85	-2.08	-2.44	-2.37	-2.342	
$\pm\sigma_{slope}$	± 0.33	±0.33	± 0.33	± 0.33	± 0.41	± 0.95	± 0.14	± 0.140	
rms	0.10	0.10	0.10	0.10	0.08	0.10		0.040	
RRc									
slope	-1.64	-1.86	-1.63	-1.76	-		-2.66		
$\pm\sigma_{slope}$	± 0.97	± 1.94	±0.89	± 0.97	-		± 0.43		
rms	0.12	0.11	0.12	0.12	-				

Notes. [a]Adopting for V3468 the period found from our data (P=0.2733d); [b]Adopting for V3468 the period from K95 (P=0.2938d).

4.1.3.7 Comparison with the literature

In the literature there are many measurements of the distance to Sculptor obtained using different techniques, such as the tip of the red giant branch (TRGB), the luminosity of the HB and the RRLs. Focussing in particular on distance estimates based on RRLs, results go from the usual optical bands ($\mu_0 = 19.71$ mag from 226 RRL, K95; $\mu_0 = 19.59$ mag from 226 RRLs, Tammann et al. 2008; $\mu_0 = 19.68 \pm 0.08$ mag from 78 RRLs, Pietrzyński et al. 2008) to the near-infrared bands where Pietrzyński et al. (2008) have measured a distance to Sculptor of $19.67 \pm 0.02 \pm 0.12$ mag using 78 RRLs analysed in J and K bands. Figure 4.13 summarizes all the distance measurements to Sculptor derived in various works using independent distance indicators and collected in the NASA/IPAC Extragalactic Database (NED). The green orange and cyan star

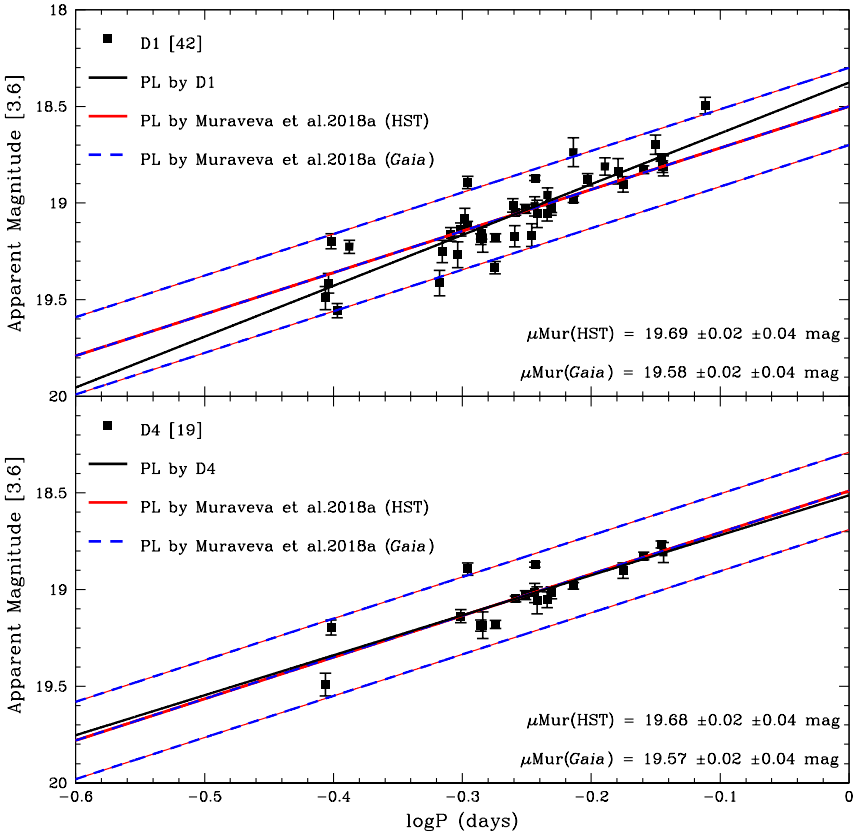

FIGURE 4.12: 3.6 μm PL relations defined by RRab+RRc stars in the D1 and D4 samples (black solid lines), compared with the PL relations by Muraveva et al. (2018a) calibrated on HST and *Gaia* parallaxes (thick solid red and dashed blue lines respectively). The periods of the RRc stars have been *fundamentalised*. Figure from Garofalo et al. (2018).

TABLE 4.7: Distance moduli for Sculptor derived using the D1 and D4 RRLs and different empirical relations

Relation		D1 [42]	D4 [19]
	RRab+RRc		
Madore et al. (2013)	μ $\sigma_{stat} \pm \sigma_{phot}$ (σ_{syst})	19.68 0.02±0.04 (0.15)	19.68 0.02±0.04 (0.14)
Neeley et al. (2015)	μ $\sigma_{stat} \pm \sigma_{phot}$ (σ_{syst})	19.63 0.02±0.04 (0.14)	19.63 0.02±0.04 (0.13)
Neeley et al. (2017)	μ $\sigma_{stat} \pm \sigma_{phot}$ (σ_{syst})	19.57 0.02±0.04 (0.12)	19.56 0.02±0.04 (0.10)
Muraveva et al. (2018a) (HST)	μ $\sigma_{stat} \pm \sigma_{phot}$ (σ_{syst})	19.69 0.02±0.04 (0.12)	19.68 0.02±0.04 (0.11)
Muraveva et al. (2018a) (*Gaia*)	μ $\sigma_{stat} \pm \sigma_{phot}$ (σ_{syst})	19.58 0.02±0.04 (0.12)	19.57 0.02±0.04 (0.11)
	RRab		
Madore et al. (2013)	μ $\sigma_{stat} \pm \sigma_{phot}$ (σ_{syst})	19.68 0.02±0.04 (0.14)	19.68 0.02±0.04 (0.14)
Neeley et al. (2015)	μ $\sigma_{stat} \pm \sigma_{phot}$ (σ_{syst})	19.62 0.02±0.04 (0.10)	19.62 0.02±0.04 (0.08)
Neeley et al. (2017)	μ $\sigma_{stat} \pm \sigma_{phot}$ (σ_{syst})	19.60 0.02±0.04 (0.12)	19.60 0.02±0.04 (0.09)

symbols and bars mark the value and photometric uncertainty obtained in this work adopting Neeley et al. (2017)'s and Muraveva et al. (2018a)'s PL relations for the D4 RRab+RRc sample.

The distance that we provide has a statistical uncertainty of 2.4%. If we also consider the systematic uncertainty, the total uncertainty increases to 4.8%.

We find that all our results are consistent with the modulus estimation provided by Dolphin (2002) (labelled 13 in Figure 4.13) using the colour-magnitude diagram (CMD), thanks to the large error bars of this latter study, while Neeley et al. (2017)'s and only Muraveva et al. (2018a) 's relations based on *Gaia* parallaxes agree with the measurement by Weisz et al. (2014) (labelled 12 in Figure 4.13). Our distance moduli are also in good agreement with the values reported by Pietrzyński et al. (2008), Tammann et al. (2008), Kaluzny et al. (1995), Martínez-Vázquez et al. (2015), Tully et al. (2013), Rizzi et al. (2007) and Górski et al. (2011) that employ the TRGB, different samples of RRL (RRab-only or RRab+RRc) and Huxor & Grebel (2015) *carbon-rich* LPV (labelled 2, 9, 8, 7, 3, 4, 6 and 1 in Figure 4.13). Compared with Huxor & Grebel (2015) which used 2 *carbon-rich* LPV stars only our findings using the Muraveva et al. (2018a)'s relations based on HST parallaxes are in agreement within the photometric errors. Our results overlap with Pietrzyński et al. (2008) (point 2 in Figure 4.13), who adopted the HB magnitude as their distance indicator, but all our measurements are $\sim 0.1 - 0.2$ mag

systematically longer than Webbink (1985)'s and $\sim 0.1-0.2$ mag systematically shorter than Salaris et al. (2013)'s, who both also used the HB (respectively, points 11 and 10 in Figure 4.13). On the other hand, our moduli are always longer than Menzies et al. (2011)'s moduli (labelled 5 in Figure 4.13), which were derived using the Miras and the TRGB. This is because their measurements are based on an LMC modulus of 18.39 mag. This value is shorter than the canonical LMC modulus by Pietrzynski et al. (2013). Indeed, assuming the latter value as reference, all Menzies et al. (2011) measurements are consistent with our results (red points, in Figure 4.13).

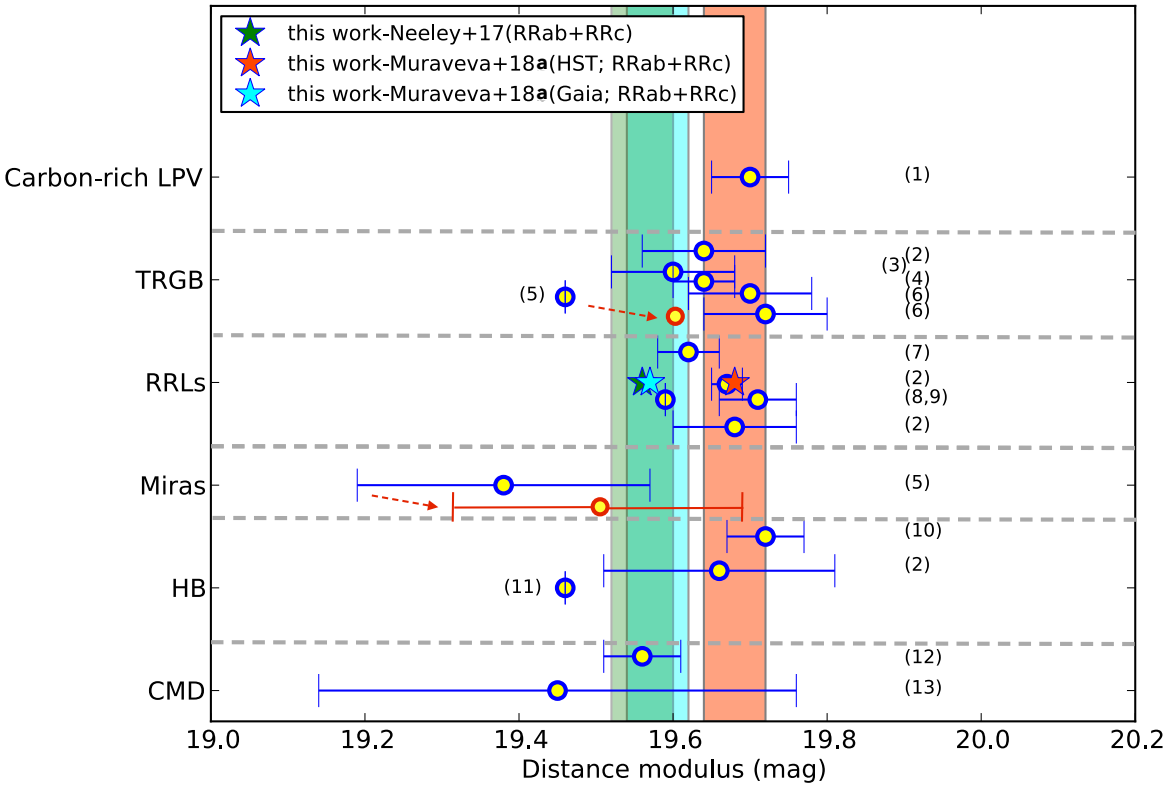

FIGURE 4.13: Sculptor distance modulus estimations derived by different techniques. The green, orange and cyan star symbols and bars mark the values and photometric uncertainties obtained in this work adopting, respectively, the Neeley et al. (2017)'s and Muraveva et al. (2018a)'s *PL* relations for the D4 RRab+RRc sample. (1) Huxor & Grebel (2015); (2) Pietrzyński et al. (2008); (3) Tully et al. (2013); (4) Rizzi et al. (2007); (5) Menzies et al. (2011); (6) Górski et al. (2011); (7) Martínez-Vázquez et al. (2015); (8) Kaluzny et al. (1995); (9) Tammann et al. (2008); (10) Salaris et al. (2013); (11) Webbink (1985); (12) Weisz et al. (2014); (13) Dolphin (2002). Figure from Garofalo et al. (2018).

4.1.3.8 Metallicity

In their spectroscopic study of 107 RRLs in Sculptor, C05 found individual metallicities ranging from −2.40 to −0.85 dex, with a mean value of −1.83 dex and a significant dispersion of ±0.26 dex. This large spread in metallicity makes Sculptor an excellent test bed for investigating potential metallicity effects on the RRL PL relations. We have 20 RRLs (18 RRab, 2 RRc) in common with the C05 catalogue (DZ sample, Table 4.5), covering a metallicity range from −2.31 to −1.38 dex (see Table 4.4, column 11). This range gives a $\Delta[Fe/H] = 0.97$ dex that is smaller than the 1.55 dex value corresponding to the C05 whole sample, but still wide enough to make considerations

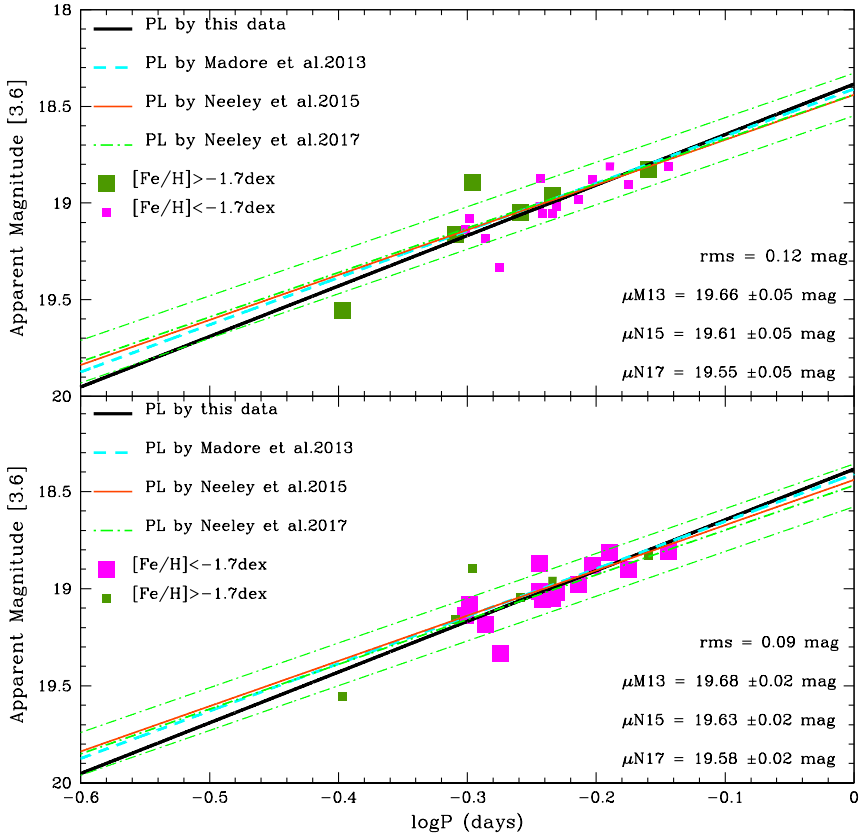

FIGURE 4.14: PL relations for the only 20 RRLs (DZ sample) whose spectroscopic metallicities are known from C05. Green and magenta filled squares mark *metal-rich* and *metal-poor* RRLs, respectively. The black solid line represents the least squares fit to the *metal-rich* (top panel) and *metal-poor* stars (bottom panel), respectively. The green (dash-dot) lines indicate the Neeley et al. (2017) PL relation's $\pm 2\sigma$ deviation. Similarly, the cyan (dashed) and orange (thin solid) lines mark the Madore et al. (2013) and the Neeley et al. (2015) PL relations along with their $\pm 2\sigma$ deviations. The periods of the RRc stars have been *fundamentalised*. Figure from Garofalo et al. (2018).

on *PL*s metallicity effects. In their combined photometric and spectroscopic study, Tolstoy et al. (2004) confirmed what was found by Majewski et al. (1999) only on photometric grounds, i.e., that Sculptor contains two distinct stellar populations: *metal-poor* stars with $[Fe/H]_{ZW} < -1.7$ dex and *metal-rich* stars with $[Fe/H]_{ZW} > -1.7$ dex. This was confirmed in further complementary studies (for example de Boer et al., 2011; Breddels & Helmi, 2014). Following the Tolstoy et al. (2004) scheme, we now split our sample of 20 RRL with individual spectroscopic metallicities from C05 into two groups: *metal-poor* stars with $[Fe/H]_{ZW} < -1.7$ dex (N = 14 stars), and *metal-rich* stars with $[Fe/H]_{ZW} > -1.7$ dex (N = 6 stars).

We show the *PL* relations for these two samples, with the fits defined using the *metal-rich* sample in the top panel and the *metal-poor* sample in the bottom panel (solid black lines) comparing with Madore et al. (2013), Neeley et al. (2015) and Neeley et al.

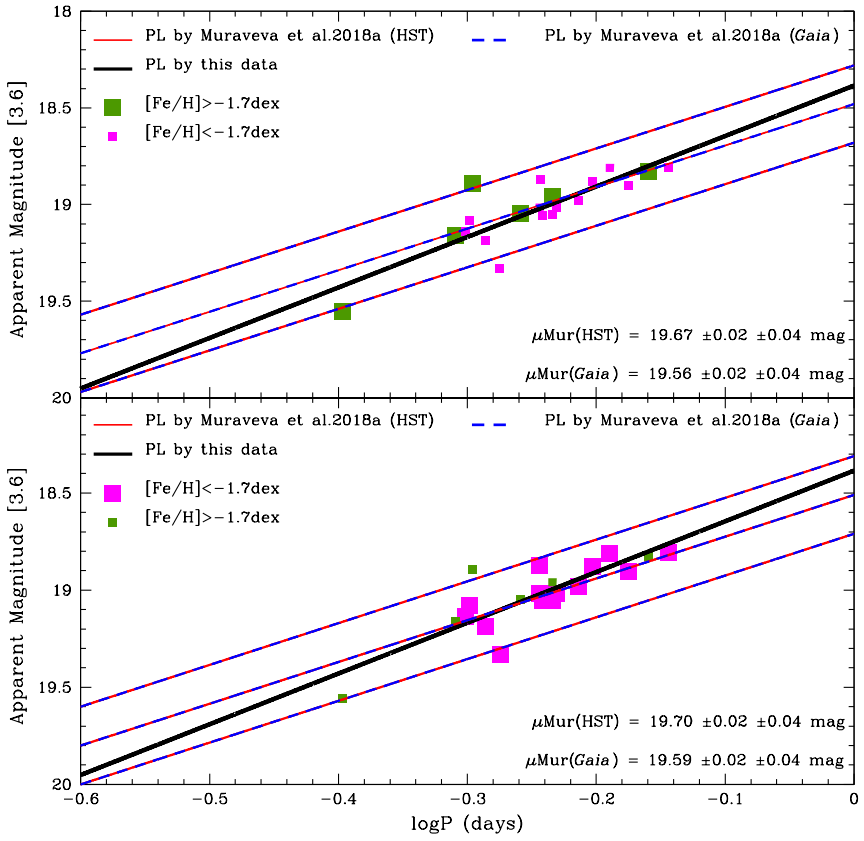

FIGURE 4.15: Same as in Figure 4.14 but with the thick solid red and the dashed blue lines showing the *PL* relations by Muraveva et al. (2018a), calibrated respectively on the HST and *Gaia* parallaxes, $\pm 2\sigma$ deviation. The periods of the RRc stars have been *fundamentalised*. Figure from Garofalo et al. (2018).

(2017) in Fig. 4.14. Figure 4.15 is the same as Fig. 4.14, but compared with the PL relations in Muraveva et al. (2018a). Using the Neeley et al. (2015) PL relation to determine distance moduli, we find $\mu = 19.61$ mag ($\sigma_{stat} = 0.05$ mag) for *metal-rich* stars and $\mu = 19.63$ mag ($\sigma_{stat} = 0.02$ mag) for *metal-poor* stars, in perfect agreement with each other within their respective errors. If we also consider the Madore et al. (2013) PL relations we obtain $\mu = 19.66 \pm 0.05$ mag and $\mu = 19.68 \pm 0.02$ mag for *metal-rich* and *metal-poor* stars, respectively. Adopting the PL relations from Neeley et al. (2017) gives $\mu = 19.55 \pm 0.05$ mag for *metal-rich* and $\mu = 19.58 \pm 0.02$ mag for *metal-poor* stars. Finally, using Muraveva et al. (2018a) PL relations calibrated on HST parallaxes gives $\mu = 19.67 \pm 0.05$ mag and $\mu = 19.70 \pm 0.02$ mag for *metal-rich* and *metal-poor* stars, respectively. These same relations calibrated on *Gaia* parallaxes give: $\mu = 19.56 \pm 0.05$ mag and $\mu = 19.59 \pm 0.02$ mag for *metal-rich* and *metal-poor* stars, respectively. These results suggest that the metallicity dependence, if any, should be very small (Table 4.8). Taking into account the individual spectroscopic metallicity measured for the DZ sample, we used the PLZ relation reported in Table 3 of Neeley et al. (2017) to calculate

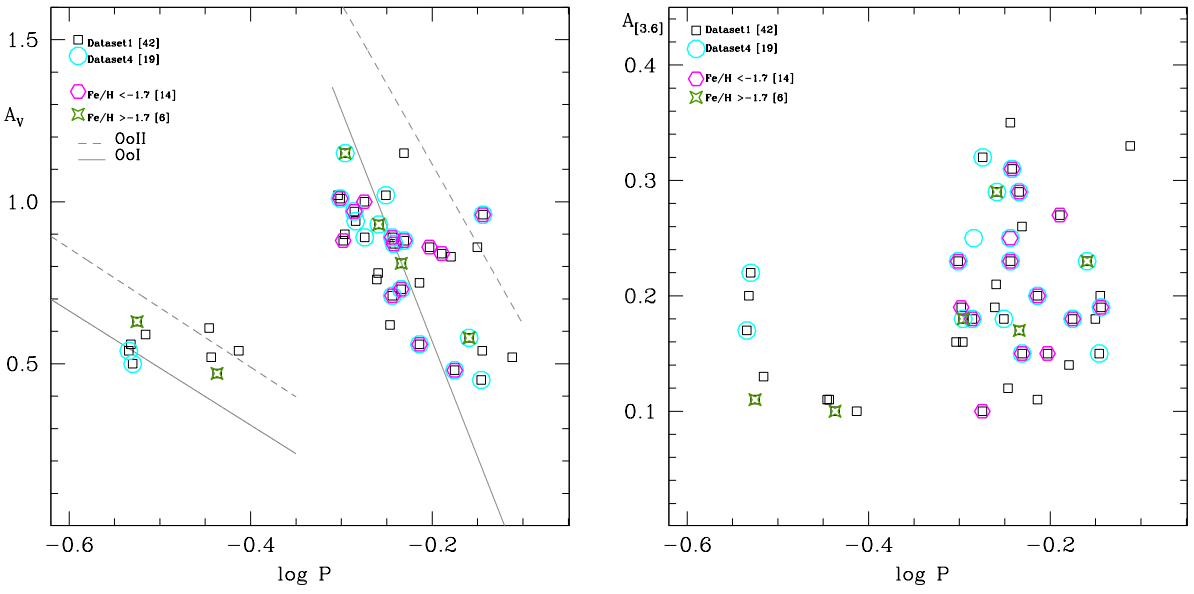

FIGURE 4.16: *Left panel:* V-band period-amplitude diagram for the 42 RRLs of Sculptor, periods and amplitudes are from K95 and C05. The grey lines mark the loci of the OoI (solid) and OoII (dashed) Galactic GCs from Clement & Rowe (2000) where, typically, OoI systems are more metal-rich ([Fe/H] ~ -1.5 dex) than the OoII systems ([Fe/H] ~ -2 dex). Black empty squares are the D1 sample while cyan circles are the D4 sample. Magenta hexagons and green four-pointed stars denote *metal-poor* and *metal-rich* samples, according to C05 metallicities. *Right panel:* MIR period-amplitude diagram, adopting the amplitudes at 3.6 μm derived in this study. Colours and symbols as on the left panel. Figure from Garofalo et al. (2018).

TABLE 4.8: Distance moduli for Sculptor derived using different DZ subsamples and different empirical PL relations

Relation		DZ (metal-rich)	DZ (metal-poor)
	RRab+RRc		
Madore et al. (2013)	μ	19.66	19.68
	$\sigma_{stat} \pm \sigma_{phot}$ (σ_{syst})	0.05±0.03 (0.16)	0.02±0.04 (0.13)
Neeley et al. (2015)	μ	19.61	19.63
	$\sigma_{stat} \pm \sigma_{phot}$ (σ_{syst})	0.05±0.03 (0.15)	0.02±0.04 (0.13)
Neeley et al. (2017)	μ	19.55	19.58
	$\sigma_{stat} \pm \sigma_{phot}$ (σ_{syst})	0.05±0.03 (0.13)	0.02±0.04 (0.10)
Muraveva et al. (2018a) (HST)	μ	19.67	19.70
	$\sigma_{stat} \pm \sigma_{phot}$ (σ_{syst})	0.05±0.03 (0.14)	0.02±0.04 (0.11)
Muraveva et al. (2018a) (*Gaia*)	μ	19.56	19.59
	$\sigma_{stat} \pm \sigma_{phot}$ (σ_{syst})	0.05±0.03 (0.14)	0.02±0.04 (0.11)

Notes. *Metal-rich* are RRLs with [Fe/H] > -1.7 dex (N_{RRL} =6); *metal-poor* are RRLs with [Fe/H] < -1.7 dex (N_{RRL} =14).

the Sculptor distance for *metal-poor* and *metal-rich* stars, getting $\mu = 19.63 \pm 0.02$(stat) ± 0.04(phot) mag (with σ_{sys} =0.11 mag) and $\mu = 19.52 \pm 0.05$(stat) ± 0.03(phot) mag (with σ_{sys} =0.13 mag) respectively and $\mu = 19.59 \pm 0.03$(stat) ± 0.04(phot) mag (with σ_{sys} =0.12 mag) for the whole DZ sample.

Again these distance moduli, in agreement within the systematic errors with the values derived in the previous section, confirm the agreement between empirical and theoretical results.

Admittedly, the number of RRLs with spectroscopic metallicity in our sample is rather small, corresponding to less than a half of our total sample (42 RRLs) and less than 1/10 of the K95 sample (226 RRLs). Furthermore, as it is well known, the RRL population in classical dSphs such as Sculptor does not conform to the Oosterhoff dichotomy observed in the GGCs, but rather have properties intermediate between the two Oosterhoff types (see Chapter 1, Section1.3). Hence, the period-amplitude diagram cannot be used to infer an approximate indication of any metallicity spread for the RRLs in our D4 sample that do not have spectroscopic measurements available. This is clearly shown by Figure 4.16, which in the left panel reports the V-band period-amplitude diagram of the 42 RRLs in our sample, based on the periods and V amplitudes reported in K95 and C05 (Table 4.4 columns 5 and 8, respectively). The grey lines in the left panel define the loci of Oosterhoff properties according to Clement & Rowe (2000), separating the plane into Oo I (solid line) and Oo II (dashed line) regions. There is no sign of a separation between the two Oo types and consequently between the two populations with different

TABLE 4.9: Pulsation properties of each of our datasets compared with K95 RRL sample

Sample	$< P_{ab} >$	fc	$< P_c >$
D1	0.594 ± 0.075	0.21	0.328 ± 0.036
D4	0.587 ± 0.069	0.10	0.294 ± 0.001
DZ	0.586 ± 0.063	0.11	0.332 ± 0.034
DZ[a]	0.586 ± 0.061	-	-
DZ[b]	0.586 ± 0.063	0.33	0.332 ± 0.034
K95	0.587 ± 0.081	0.40	0.336 ± 0.041

[a] Sample contains 14 RRLs defined as *metal-poor* sub-sample.
[b] Sample contains 6 RRLs defined as *metal-rich* sub-sample.

metallicity defined by Tolstoy et al. (2004). Moreover if we separate the RRLs whose metallicities are known from the spectroscopic study of C05 into *metal-poor* and *metal-rich* samples (magenta hexagons and green 4-pointed stars respectively in Figure 4.16) they do not show any significant bimodality.

The Oo-Int nature of Sculptor was clearly established by K95 based on the pulsation properties of over 200 RRLs detected in the galaxy, for which these authors derived $\langle Pab \rangle$ = 0.587 d and $fc{=}N_{RRc}/(N_{RRab} + N_{RRc}){=}0.40$. We reach the same conclusions here if we consider the average pulsation properties of our datasets shown in Figure 4.16. Table 4.9 lists fc, $< P_{ab} >$ and $< P_c >$ values calculated for each dataset: D1, D4 and DZ (split into *metal-poor* and *metal-rich* sub-samples) along with K95 values for comparison. We find, on the one hand, that the fc and $< P_c >$ values suggest an Oo I classification for all datasets. On the other hand, $< P_{ab} >$ places them in an intermediate classification between Oo I and Oo II. Moreover, for all samples, the standard deviation related to the mean period of RRab stars is rather large ($\sigma \sim 0.07$ d), which indicates a mixing of both metal-poor and metal-rich components among Sculptor RRLs that remain indistinguishable irrespective of pulsation properties.
The right panel of Figure 4.16 shows instead the MIR Bailey diagram based on our light curves at 3.6 μm with the same symbols and colours coding as in the left panel. The RRLs distribution is broader in this plane at longer wavelengths than in the V band and it is also much broader than the period-amplitude diagram at 3.6 μm obtained by Muraveva et al. (2018a) for the RRLs in the Reticulum cluster (see upper panel of Fig. 6 in that paper).

As a further test Figure 4.17 shows the individual PL derived distance moduli versus metallicity for each of the 20 RRLs with a spectroscopic metallicity (DZ sample) and

using as a reference the PL relation derived by Neeley et al. (2017) and only the RRab stars in the D4 sample. However, we note that results do not change if a different fiducial PL is adopted. The least squares fit (black line) has been calculated for four different cases: Case A - using the whole sample, case B - removing only V1932, the star with the shortest derived distance modulus (μ =19.384±0.035 mag), case C - removing only V1546, the star with the longest derived distance modulus (μ =19.873±0.032 mag), and case D - excluding both V1932 and V1546. The resultant fits are summarised in Table 4.10. In each case the slopes ($d\mu/d$[Fe/H]) are consistent with zero within 1σ. Again, this strengthens the evidence that any metallicity effect, if it exists, is negligible

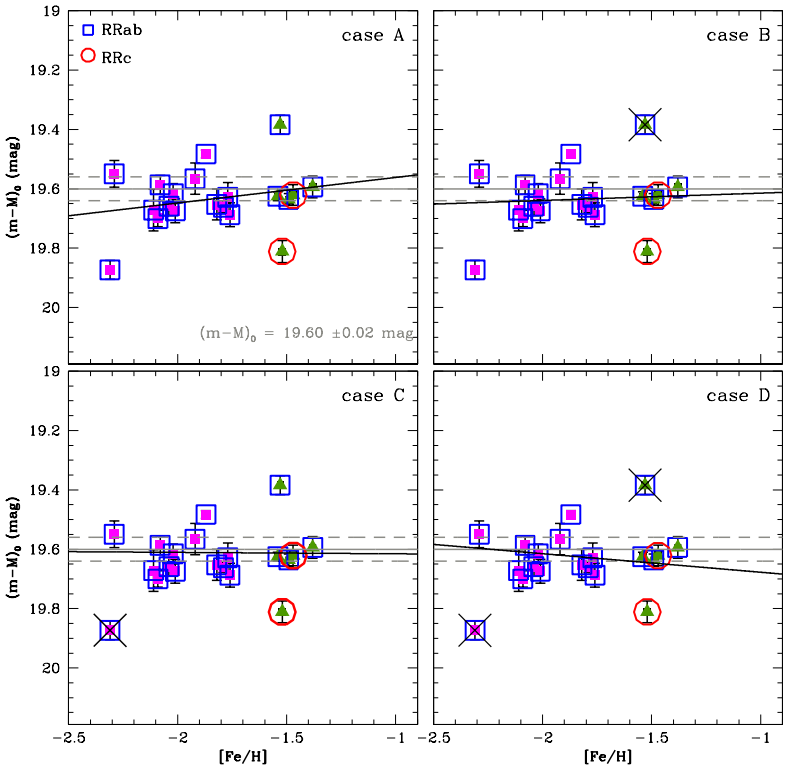

FIGURE 4.17: Distance moduli for the 20 RRLs in our DZ sample as a function of [Fe/H] (spectroscopic metallicities from C05). The solid grey line is the distance modulus $\pm 2\sigma$ (dashed lines) estimated using as a reference the PL relation derived by Neeley et al. (2017) and only the RRab stars in the D4 sample. Metal-poor sources are magenta squares and metal-rich are green triangles. RRab and RRc stars are encircled by blue squares and red circles, respectively. The RRLs marked with a cross are the rejected stars. The least squares fit (black line) has been calculated in four different cases: considering the whole sample (case A, top-left panel), removing the "closest" star (in terms of distance from us; top-right panel, case B), removing the "most distant" star (case C, bottom-left panel) and excluding both (case D, bottom-right panel). In every case the slope ($d\mu/d$[Fe/H]) is consistent with zero within 1σ (see text and Table 4.10 for details. Figure from Garofalo et al. (2018).

TABLE 4.10: $d\mu/d$[Fe/H] derived from the DZ sample

Case	$d\mu/d$[Fe/H]	$\sigma_{d\mu/d\text{[Fe/H]}}$
A	-0.086	$\pm$0.084
B	0.009	$\pm$0.081
C	-0.034	$\pm$0.075
D	0.051	$\pm$0.065

in our sample. Indeed, a direct correlation between distance modulus and metallicity is not observable in our data, neither in this test nor in the analysis for Figs. 4.14 and 4.15 where we looked specifically for differences in the PL relations derived from known *metal-rich* and *metal-poor* stars.

We have also tried to quantify the depth effect set by our data and whether it can affect our distance estimation. The line of sight depth can be measured by subtracting in quadrature the distance scatter we found for Sculptor adopting the D4 sample and the distance scatter that Muraveva et al. (2018a) provide for Reticulum: $[(0.08)^2 - (0.06)^2]^{1/2} \simeq 0.05$ mag, corresponding to $\pm$2 kpc, which is completely within our photometric error. A significant advantage of our study is that we are able to obtain a precise distance estimate of comparable accuracy to the larger studies using an RRL sample that is less than 10% of the size analysed by Martínez-Vázquez et al. (2015) and less than 4% of the total number of Sculptor RRL stars discovered to date. The Sculptor RRL catalogue may not yet be complete, despite having 536 variables identified so far (Martínez-Vázquez et al., 2016b).

4.1.3.9 Metallicity: a newer distance measurement

For the first time it is possible to infer distances from a relation directly calibrated on the trigonometric parallaxes of hundreds of RRLs. Muraveva et al. (2018b) have derived a new RRL PLZ relation whose slope and zero point are based on the *Gaia* DR2 parallaxes of about 400 Galactic RRLs with mean magnitudes in the WISE1 passband (3.4 μm)(Section 3.7.3.3). Since the Muraveva et al. (2018b) manuscript had not yet been published when we completed this work we decided to not include results based on the new PLZ relation in Garofalo et al. (2018). However, we had envisaged re-deriving the distance modulus of Sculptor with this new PLZ once the Muraveva et al. (2018b) paper was accepted for publication. Accordingly, we applied the Muraveva et al. (2018b) PLZ ($PM_{W1}Z$ in the lower part of Table A.4; table 4 in Muraveva et al. 2018b)

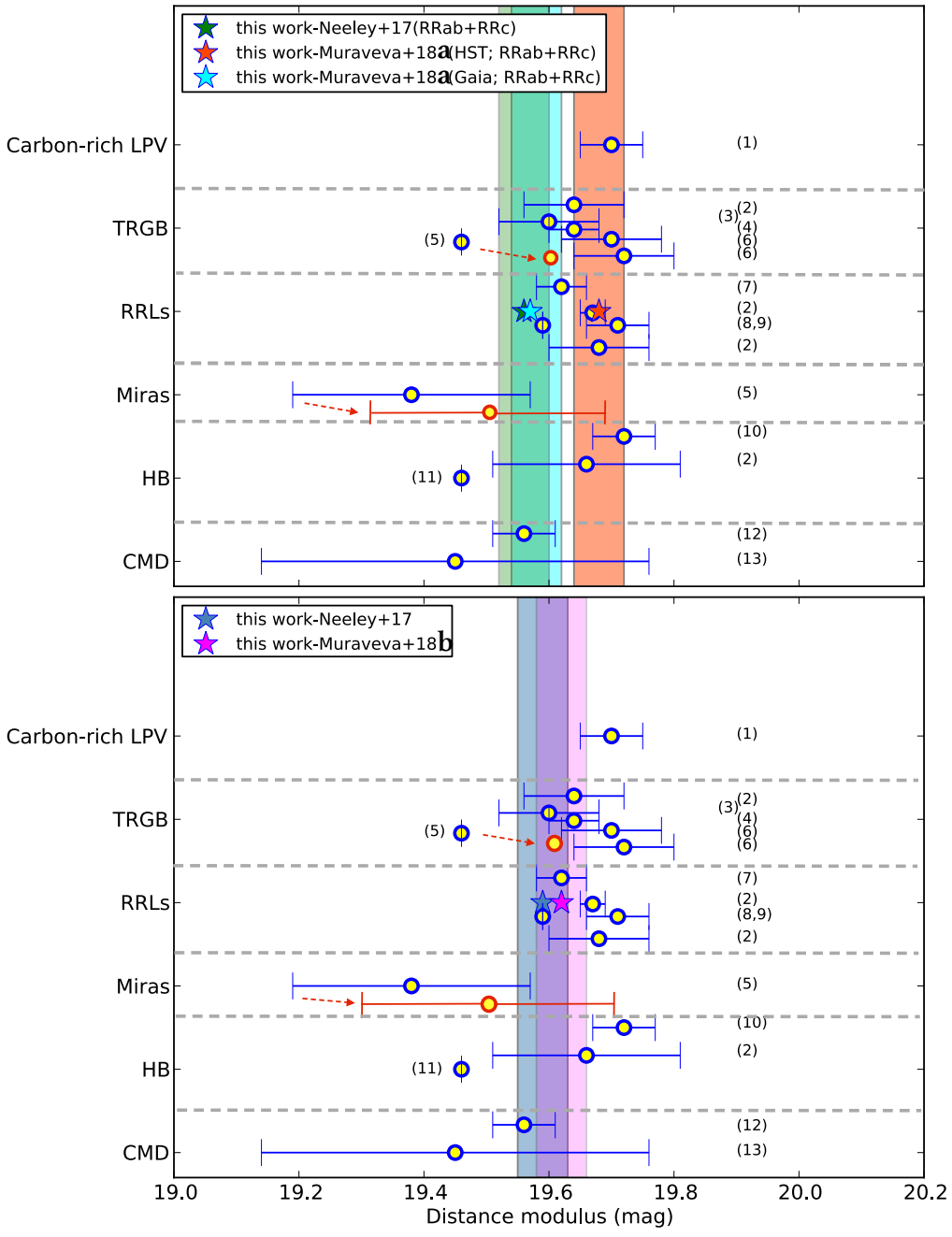

FIGURE 4.18: *Top panel*: Figure 4.13 is replotted here to facilitate the comparison with the bottom panel. *Bottom panel*: Same as in the top panel but for the DZ sample. The magenta and steel-blue star symbols and bars mark the values and photometric uncertainties obtained in this work adopting, respectively, the Neeley et al. (2017) and the Muraveva et al. (2018b) *PLZ* relations.

relation to our DZ sample and we obtained $\mu = 19.62 \pm 0.03$(stat) ± 0.04(phot) mag (with σ_{sys} =0.22 mag) for the whole DZ sample and $\mu = 19.52 \pm 0.05$(stat) ± 0.04(phot) mag (with σ_{sys} =0.22 mag) and $\mu = 19.67 \pm 0.03$(stat) ± 0.04(phot) mag (with σ_{sys} =0.21 mag) for the *metal-rich* and *metal-poor* subsamples, respectively. These values are in very good agreement with the distance moduli derived in previous sections (see Tables 4.7 and 4.8). Figure 4.18 summarizes all the distance measurements to Sculptor derived in various works using independent techniques showing our results divided in two panels: the bottom panel of Figure 4.18 shows with the magenta and steel-blue star symbols and bars the values and the photometric uncertainties we obtained adopting Neeley et al. (2017) and Muraveva et al. (2018b) PLZ relations for the DZ sample; the top panel of Figure 4.18, to make the comparison of results easier, displays, once again, Figure 4.13 with star symbols and bars indicating the values and photometric uncertainties obtained in this work adopting Neeley et al. (2017) and Muraveva et al. (2018a) PL relations for the D4 RRab+RRc sample. The distance moduli derived from Neeley et al. (2017) and Muraveva et al. (2018b) PLZ relations, besides being in full agreement to each other, also agree with almost all the values reported in the literature. The only exceptions are the Salaris et al. (2013) value that is still longer than our findings and the Webbink (1985) result that does not agree with the distance modulus obtained using the Neeley et al. (2017) relation but, within the errors, overlaps our value from the Muraveva et al. (2018b) relation.

Chapter 5

Summary and Future Developments

In this thesis we have exploited the variable stars of RR Lyrae type (RRLs), in their dual role of standard candles for the measurement of distances, and tracers of the old stellar populations of the stellar systems where they are hosted. To this end, we have studied the RRL population in a number of different environments: the field of our Galaxy, globular clusters (GCs), ultra-faint dwarf (UFD) and dwarf spheroidal (dSph) satellites of the Milky Way (MW) and M31, based on different datasets which include multiband photometry from visual to (near/mid) infrared passands and astrometry (parallax measurements), collected at three world-leading international facilities: the Large Binocular Telescope (LBT), the *Spitzer* space telescope, and the European Space Agency (ESA) astrometric mission *Gaia*.

1. For the study of the MW UFD Pisces II (Psc II) and the M31 dSph satellites Andromeda XXV (And XXV) and XXVII (And XXVII), presented in Chapter 2, we have collected B,V time series photometry with the Large Binocular Cameras (LBCs) of the LBT. We obtained detailed information on the properties (distance, age, metallicity, Oosterhoff types and structure) of these 3 stellar systems, that allowed us to compare them with other satellites around the MW and M31.

1a In Psc II we have identified 3 variable stars: an RRab star (V1) with P $\sim$ 0.56 d, an SX Phoenicis star (V3; P $\sim$ 0.06 d) both lying within the Psc II half-light radius

(r_h), and a third variable, V4, outside the galaxy's r_h, with uncertain classification and about 0.25 mag brighter than V1. We classify Psc II as an Oosterhoff I (Oo I) system, based on the period of V1, from which we also measured the galaxy distance modulus: 21.22 ± 0.14 mag, placing Psc II at 175 ± 11 kpc from us, in good agreement with the literature and at the same distance of Pegasus III (Peg III). V4 could either be an RRab star with P = 0.72 d or a first overtone anomalous Cepheids (AC) with P = 0.42 d. Based on the comparison with the period-luminosity (PL) and period-Wesenheit (PW) relations for ACs and classical Cepheids (CCs) and theoretical isochrones overlaid on the galaxy colour-magnitude diagram (CMD) we concluded that V1 is likely an Oosterhoff II (Oo II) metal poor ([Fe/H] $\gtrsim -2.4$ dex) RRab star belonging to Psc II. The CMD suggests the presence of a dominant old stellar population (t > 10 Gyr) with metallicity [Fe/H] > -1.8 dex in Psc II along with, possibly, a minor, more metal poor component traced by V4.

Results from this work are presented in:

"Born in a pair(?): Pisces II and Pegasus III" by A. Garofalo, M. Tantalo, F. Cusano et al. (2018), in preparation.

1b And XXV was found to host 62 variable stars: 58 RRLs, 3 ACs, one eclipsing binary (ECL) and an unclassified variable. The average period of the RRab stars ($\langle P_{ab} \rangle$=0.60±0.04 days) qualifies And XXV as an Oosterhoff-intermediate (Oo Int) dSph. From the average luminosity of the RRLs we derive a distance modulus of $(m\text{-}M)_0$ = 24.63 ± 0.17 mag. The properties of the RRLs and the comparison of the galaxy CMD with stellar isochrones both suggest that a single, old (10-12 Gyr) and metal poor ([Fe/H]~ -1.8 dex) stellar generation is the dominant component of And XXV. We detected a spherical concentration of stars (Gep 1) near the centre of And XXV which could either be a candidate globular cluster or the nucleus of this dSph galaxy. And XXV is the first of the M31 satellites we have investigated to lay ON the Great plane of Andromeda (GPoA) defined by Ibata et al. (2013).

A comprehensive description of this study has been published in:

"Variable stars and stellar populations in Andromeda XXV: III. A central cluster or the galaxy nucleus?" by F. Cusano, A. Garofalo, G. Clementini et al. 2016,

ApJ, 829, 26.

1c In the field of And XXVII we discovered a total of 90 variable stars: 89 RRLs and one AC. The average period of the RRab stars $\langle P_{\rm ab} \rangle$ =0.59 ± 0.05 d and the period-amplitude diagram place And XXVII in the class of Oo I/Oo Int systems. Combining information from the CMD and the variable stars, we conclude that And XXVII hosts a single, t∼13 Gyr old and metal-poor ([Fe/H]∼ − 1.8 dex) stellar population. The spatial distributions of RRLs and RGB stars and the large spread in distance of the RRLs along the line of sight reveal that And XXVII is a completely disrupted system, significantly contributing its stars to the building of the M31 halo. The highest concentration of RGB and RRL stars is found in a circular area of 4 arcmin in radius, about 0.2° off-centred from Richardson et al. (2011) centre coordinates of And XXVII, which we suggest to be the true centre of this dSph. The pulsation properties (average period of the RRab stars, fraction of RRc stars over total number of RRLs) of the RRL population in the eleven M31 satellites studied so far for variability are not found to vary depending on whether the host systems are ON or OFF the GPoA. Conversely, the number of ACs detected in the OFF-plane dSphs is about 5 times larger than found in the ON-plane systems. Although statistics is at present still rather poor, this may indicate that only OFF-plane satellites were able to retain enough gas to give rise to an intermediate-age stellar generation (1-2 Gyr old) producing ACs.

Results from this work have been published in:

"Variable stars and stellar populations in Andromeda XXVII: IV. An off-centered, disrupted galaxy" by F. Cusano, A. Garofalo, G. Clementini, et al. 2017, ApJ 851, 9.

2. *Gaia*, the European Space Agency (ESA) cornerstone mission in scientific operations since July 2014, is repeatedly monitoring the whole sky by measuring positions, trigonometric parallaxes, proper motions and multi-band time-series photometry for over a billion sources, down to a limiting magnitude $V \sim 21.0$ mag. Among them are hundreds of thousands of RRLs as well as thousands of Cepheids. As detailed in Chapter 3, we have tested the *Gaia* parallaxes of RRLs and Cepheids (CCs and Type II Cepheids –T2Cs) published in the 2016 and 2018

data releases (*Gaia* Data Release 1 –DR1 and Data Release –DR2, respectively) by building PL, PW and LZ relations calibrated on the *Gaia* astrometry, and have validated the results on all-sky RRLs published in DR2 by comparison with RRLs in GGCs and dwarf galaxies (UFDs and dSphs) known in the literature.

2a *Gaia* DR1 published parallaxes for more than 700 Galactic Cepheids and RRLs, computed as part of the Tycho-*Gaia* Astrometric Solution (TGAS). We tested the TGAS parallaxes of RRLs, CCs and T2Cs by comparing them with literature estimates from *Hipparcos* and the HST, then we derived new PL, PW relations for CCs and T2Cs, and infrared PL, PLZ and optical LZ relations for RRLs, with zero points calibrated on TGAS parallaxes. The new relations were computed using literature multi-band $(V, I, J, K_S, W1)$ photometry and spectroscopic metal abundances, and adopting three different approaches: i) by linear least squares fitting the absolute magnitudes inferred from direct transformation of the TGAS parallaxes, (ii) by adopting astrometric-based luminosities, and (iii) using a Bayesian fitting approach. The latter two methods work in parallax space where parallaxes are used directly, thus maintaining symmetrical errors and allowing negative parallaxes to be used. The PL relations show the significant improvement of the TGAS parallaxes for RRLs and Cepheids with respect to the *Hipparcos* measurements. This is particularly true for the RRLs for which improvement in quality and statistics is impressive. The TGAS-based PL, PW, PLZ and LZ relations defined from samples comprising 200 RRLs, 102 CCs and 26 T2Cs were finally tested by comparing the distance to the Large Magellanic Cloud (LMC) provided by different types of pulsating stars and alternative fitting methods.

Results from this study have been presented in the papers:

"*Gaia* Data Release 1, Validating the parallaxes with local Cepheids and RR Lyrae stars", by Gaia Collaboration, Clementini, G., Eyer, L., Ripepi, V., Marconi, M., Muraveva, T., Garofalo, A., et al. (+576 co-authors) 2017, A&A, 605, A79;

"A hierarchical Bayesian model to infer PL(Z) relations using *Gaia* parallaxes" Delgado, H. E., Sarro, L. M., Clementini, G., Muraveva, T., Garofalo, A., 2018, A&A, (re-submitted after revision according to referee's review), arXiv:1803.01162.

2b On 25 April 2018, with the publication of *Gaia* DR2, parallaxes based only on *Gaia* astrometry and G-band time-series photometry have become available for

more than 400 RRLs in the field of the MW. We compared the DR2 parallaxes with estimates from HST, TGAS and *Hipparcos*, finding general good agreement with the former two and a further significant improvement with respect to the latter. Using a Bayesian fitting approach we have derived new near- and mid-infrared PLZ relations and new LZ relations in the V and G passbands with slope and zero-point based on the *Gaia* DR2 parallaxes. We find the dependence of the luminosity on metallicity (LZ relation) to be higher than usually derived in the literature. We show that this high metallicity dependence likely arises from the actual distribution of the data and the presence of a zero-point offset in the *Gaia* parallaxes of -0.057 mas, with the *Gaia* DR2 parallaxes being systematically smaller, confirming previous findings by Arenou et al. (2018). Based on the *Gaia* DR2 parallaxes we estimate the RRL absolute magnitude in the V, G, K_S and $W1$ bands, at metallicity of [Fe/H]=-1.5 dex and period of P = 0.5238 d, to be: $M_V = 0.66 \pm 0.06$ mag, $M_G = 0.63 \pm 0.08$ mag, $M_{Ks} = -0.37 \pm 0.11$ mag and $M_{W1} = -0.41 \pm 0.11$ mag, respectively. Our study demonstrates the effectiveness of the *Gaia* parallax measurements to establish the cosmic distance ladder by recovering the canonical distance modulus of the LMC ($\sim$ 18.5 mag), once the DR2 parallax offset is properly corrected for.

Results from this study have been published in:

"RR Lyrae stars as standard candles in the *Gaia* Data Release 2 Era" by T. Muraveva, H.E. Delgado, G. Clementini, L.M. Sarro & A. Garofalo 2018, MNRAS, 481, 1195.

2c Along with the first *Gaia*-only parallaxes, *Gaia* DR2 published a first mapping of full-sky RRLs and Cepheids observed by the satellite during the first 22 months of science operations. The Specific Object Study (SOS) pipeline, developed within the *Gaia* Processing and Analysis Consortium (DPAC) to validate and fully characterise Cepheids and RRLs (SOS Cep&RRL) observed by *Gaia*, confirmed the classification and measured the pulsation characteristics (periodicities, mean magnitudes, amplitudes and Fourier parameters of the light curves) for 140,784 RRLs, then estimated the G-band interstellar absorption and the photometric metallicity for 54,272 and 64,932 of them, respectively. We have built a catalogue of more than 4,000 known RRLs belonging to 150 GCs and 54 ("classical" and ultra-faint) dwarf spheroidals with which we have tested the RRL results provided by the *Gaia*

SOS Cep&RRL pipeline, in order to establish its performance in fields with different crowding degree and the reliability of the derived pulsation characteristics and stellar parameters on systems (GGCs in particular) for which these quantities are generally well known in the literature. Among the 140,784 RRLs released in DR2, 1,986 turned out to be known RRLs in GGCs and dwarf galaxies. Agreement between the RRLs pulsation characteristics estimated by the SOS Cep&RRL pipeline and the literature values is satisfactory in most cases (10 GGCs and 4 dSphs) and excellent in the case of the GGC M3 and the Sculptor dSph.

A comprehensive description of this work has been published in:

"Gaia Data Release 2: Specific characterisation and validation of all-sky Cepheids and RR Lyrae stars", by G. Clementini, V. Ripepi, R. Molinaro, A. Garofalo, T. Muraveva et al. 2018, A&A, in press, arXiv:1805.02079.

3. *Gaia* DR1 and DR2 published largely improved parallax measurements for significant numbers of Galactic RRLs that allowed us to recalibrate the zero point (with the DR1 measurements) and determine new values for both slope and zero point (with the DR2 measurements) of the RRL LZ and infrared PL, PLZ relations. In Chapter 4, in the framework of the Carnegie RR Lyrae Project (CRRP) and the *Spitzer* Merger History And Shape of the Galactic Halo (SMHASH) project, we have exploited these new relations to measure the distance to the LMC globular cluster Reticulum and the Sculptor dSph galaxy.

3a As part of CRRP, we have analysed a sample of 30 RRLs in the LMC cluster Reticulum, that we observed at 3.6 and 4.5 μm with IRAC-*Spitzer*. Based on our analysis of the light curves, the position on the CMD and the appearance on the frames, we selected a sub-sample of 24 RRLs to fit new mid-infrared (MIR) PL relations, for which we obtained slopes of -2.15 ± 0.23 and -2.47 ± 0.32 at 3.6 and 4.5 μm, respectively. The new slopes are consistent, within their errors, with values published in the literature. The zero points of the PL relations were estimated using the trigonometric parallaxes of five bright MW RRLs measured with the Hubble Space Telescope (HST) and, as an alternative, the TGAS and *Gaia* DR2 parallaxes of the same stars. We obtained the following distance moduli for Reticulum: $\mu_{[3.6]} = 18.43 \pm 0.06$ mag, $\mu_{[4.5]} = 18.43 \pm 0.08$ mag from the PL

relations calibrated on the HST parallaxes; and $\mu_{[3.6]}$ = 18.32 ± 0.06 mag, $\mu_{[4.5]}$ = 18.34 ± 0.08 mag using the DR2 parallaxes. These distance moduli are in good agreement with the literature estimates based on visual photometry and the optical LZ relation. The agreement with the literature is less pronounced in the case of the PL relations at I and K passbands. The average of the distance moduli derived in this study places Reticulum ∼ 3 kpc closer to us than the barycentre of the LMC.

Results from this work have been published in:

"The Carnegie RR Lyrae Program: Mid-infrared Period-Luminosity relations of RR Lyrae stars in Reticulum" by T. Muraveva, A. Garofalo, V. Scowcroft, G. Clementini, W.L. Freedman, B.F. Madore & A.J. Monson 2018, MNRAS, 480, 4138.

3b In the framework of the SMHASH project, using IRAC-*Spitzer* data we have determined a new distance modulus for the Sculptor dSph using RRLs located in the inner region of the galaxy. Based on mid-infrared (3.6 μm) light curves for 42 RRLs we measured the Sculptor distance modulus: μ = 19.60 ± 0.02 (statistical) ± 0.04 (photometric) mag (with σ_{sys} = 0.09 mag), using 3.6 μm literature empirical PL relations derived for the GGC M4, or μ = 19.57 ± 0.02 (statistical) ± 0.04 (photometric) mag (with σ_{sys} = 0.11 mag), using the empirical relations we had derived for Reticulum (see section 3a above). Both measurements are in good agreement with literature estimates based on RRLs observed at optical passbands, and are also consistent with recent literature near-infrared results. Best agreement with the literature is found for the latter modulus which corresponds to a distance: d = 82 ± 1 (statistical) ± 2 (photometric) kpc (with σ_{sys} = 4 kpc). In addition, using a subsample of 20 RRLs in Sculptor with individual spectroscopic metallicities available in the literature we showed that our distance estimates are not affected by metallicity effects.

Finally, adopting the new PLZ in the WISE1 passband we derived from Galactic RRLs with *Gaia* DR2 parallax measurements (see section 2b in the summary of Chapter 2) we measure for Sculptor a distance modulus of μ = 19.62 ± 0.03 (statistical) ± 0.04 (photometric) mag (with σ_{sys} =0.22 mag), corresponding to

84 ± 1 (statistical) ± 2 (photometric) kpc (with σ_{sys} =8 kpc), in very good agreement with the vast majority of distance determinations in the literature and consistently with results obtained in this work using different fiducial PL and PLZ relations.

A comprehensive presentation of this study has been published in:

"SMHASH: a new mid-infrared RR Lyrae distance determination for the Local Group dwarf spheroidal galaxy Sculptor" by Garofalo, A. et al. 2018, MNRAS, 481, 578.

We end this Chapter by briefly describing future developments of the work presented in this Thesis, in the context of on-going and future missions/surveys we are directly involved in.

Undoubtedly, to reach a step forward in the exploitation of RRLs as standard candles and stellar population tracers, wide-area coverage, deep and very accurate photometry, astrometry (positions, parallaxes and proper motions) and radial velocities are crucial. This is the harvest being provided by on-going surveys like *Gaia* and, in the near future, by the Large Synoptic Survey Telescope (LSST).

* With *Gaia* DR2 parallaxes it has for the first time been possible, with such accuracy, to determine the coefficients (slopes and zero-points) of the fundamental relations (LZ, infrared PL and PLZ relations) that the RRLs conform to.

* At the same time, the number of new RRLs discovered by *Gaia* that were released in DR2 along with those already known in the literature provide the largest ever census of RRLs in our Galaxy and its close companions. This number will increase with further *Gaia* releases as the number of observations per source increases, as it is also expected to increase the number of the parameters (positions, parallaxes and proper motions) and their accuracy (parallaxes, in particular) derived for these sources. For *Gaia* Data Release 3 (DR3), currently foreseen for the first half of 2021, time series radial velocities of RRLs will also be processed besides the multiband photometry. This will improve the RRL characterisation and will also open the path for the derivation of additional stellar parameters such as gravities, temperatures and absolute magnitudes independent of parallaxes.

* Starting operations in 2020, LSST will become *Gaia*'s deep complement in the southern hemisphere, as it will provide parallaxes, proper-motions, and multiband photometry with similar uncertainties at *Gaia* faint end ($V \sim$ 20.5-21 mag), but up to about five magnitudes fainter than with *Gaia*.

As an active member of the Coordination Unit 7 (CU7, variability) in the *Gaia* Data Processing and Analysis Consortium (DPAC) and one of the 5 team members of the LSST project "The *Gaia*-LSST synergy: from pulsating stars and star formation history to WD planets" (PI: G. Clementini), which is specifically tasked with enlarging *Gaia*'s horizon for pulsating variable stars as standard candles and stellar population tracers into the space/time domain of LSST, I am in an optimum position to fully take advantage of a deep knowledge of virtues and shortcomings of the data (parallaxes, proper motions, photometry and characterisation of the variable stars) that these projects deliver.

However, in the short time scale, follow-up of two of the studies described in this Thesis is already possible and will take most of my time in the next few months.

1 The complex structure of the M31 halo in the And XXVII neighbourhood and the possible connection of this dSph with the M31 North-West (NW) stream will be investigated with our recently obtained new B, V time series LBT imaging, to study the variable stars and the resolved stellar populations in 5 fields along both the arc-path described by the NW stream and the M31 halo (Cusano, F., Garofalo, A. et al., in prep).

2 To further investigate the metallicity dependence of the RRL LZ and PLZ relations a step forward will be to study the relations defined by large samples of RRLs in GGCs for which the metallicity is known from high resolution spectroscopic studies. This is addressed in a work in progress (Garofalo et al. 2018, in preparation) in which we apply the same Bayesian approach we used to study the relations of the MW field RRLs, to the RRLs in 20 GGCs spanning a range of about 2 dex in metal abundance, for a total of about $\sim$ 1000 RRLs, and derive new LZ relations in the V and G passbands and a new PLZ relation in the I-band, based on DR2 parallaxes.

Appendix A

Additional tables

TABLE A.1: Photometric and pulsation properties of the variable stars identified in And XXV

Name	α (2000)	δ (2000)	Type	P (days)	Epoch (max) HJD (−2455000)	$\langle B \rangle$ (mag)	$\langle V \rangle$ (mag)	Amp_B (mag)	Amp_V (mag)
V1	00:30:10.688	+46:51:21.71	RRab	0.6078	852.561	25.90	25.42	1.10	0.86
V2	00:30:09.937	+46:51:34.93	RRab	0.5459	851.356	25.77	25.38	1.42	0.87
V3	00:30:09.306	+46:51:43.73	RRab	0.6147	852.048	25.80	25.43	1.42	0.86
V4	00:30:12.324	+46:50:58.88	AC	1.355	854.800	24.23	23.79	0.68	0.56
V5	00:30:05.194	+46:50:48.71	RRc	0.3858	851.920	25.82	25.41	0.72	0.36
V6	00:30:11.050	+46:51:58.73	RRab	0.609	854.732	25.58	25.23	0.98	0.76
V7	00:30:05.122	+46:50:27.28	RRab	0.6116	857.708	25.80	25.39	1.00	0.72
V8	00:30:05.122	+46:50:27.28	RRc	0.3457	851.164	25.53	25.17	0.73	0.70
V9	00:30:14.345	+46:50:47.45	RRab	0.5742	856.642	25.57	25.15	1.41	1.10
V10	00:30:04.745	+46:50:06.57	RRab	0.72	854.705	25.71	25.32	0.76	0.49
V11	00:30:14.186	+46:50:17.44	RRab	0.5963	856.705	25.68	25.33	1.06	0.98
V12	00:30:12.939	+46:52:22.79	RRab	0.5466	854.795	25.73	25.39	1.44	1.10
V13	00:30:02.642	+46:50:12.32	RRab	0.7254	852.133	25.80	25.38	1.00	0.78
V14	00:30:02.612	+46:52:23.61	RRab	0.576	854.804	25.72	25.33	1.36	1.06
V15	00:30:14.464	+46:49:28.74	RRab	0.591	856.663	25.63	25.20	1.01	0.79
V16	00:30:17.886	+46:51:58.24	RRab	0.610	851.573	25.95	25.53	0.90	0.56
V17	00:30:18.136	+46:50:05.58	RRab	0.5675	855.784	25.68	25.31	1.36	1.18
V18	00:30:02.457	+46:48:57.10	RRc	0.375	854.810	25.64	25.31	0.74	0.33
V19	00:30:13.024	+46:48:31.33	RRab	0.577	855.587	25.66	25.28	1.22	0.95
V20	00:29:59.216	+46:52:40.02	RRc	0.3085	852.695	25.43	25.16	0.53	0.36
V21	00:30:21.242	+46:51:02.77	RRab	0.562	854.804	25.41	25.07	1.60	1.25
V22	00:29:58.666	+46:53:04.62	RRab	0.655	857.894	25.69	25.31	0.71	0.65
V23	00:30:21.905	+46:51:36.72	RRc	0.3668	858.900	25.49	25.15	0.81	0.61
V24	00:30:18.610	+46:53:37.02	RRab	0.537	854.816	25.66	25.29	1.89	1.28
V25	00:30:15.060	+46:47:56.28	RRab	0.637	856.670	25.73	25.27	0.80	0.51
V26	00:30:23.121	+46:51:10.67	RRc	0.405	856.782	25.61	25.26	0.70	0.47
V27	00:30:21.141	+46:49:12.98	RRab	0.547	857.652	25.60	25.22	1.25	0.97
V28	00:30:17.693	+46:48:10.12	RRab	0.565	856.747	25.62	25.25	1.42	1.12
V29	00:29:55.136	+46:49:28.51	RRab	0.632	856.860	25.73	25.26	0.781	0.56
V30	00:30:03.691	+46:47:25.31	RRc	0.368	856.767	25.55	25.20	0.452	0.41
V31	00:30:13.107	+46:47:15.13	RRab	0.669	856.780	25.50	24.88	0.845	0.51
V32	00:30:11.748	+46:55:04.50	RRc	0.378	856.677	25.60	25.34	0.66	0.59
V33	00:29:58.771	+46:47:48.94	RRab	0.577	856.850	25.61	25.24	0.87	0.72
V34	00:30:26.025	+46:51:13.58	RRab	0.5575	858.894	25.65	25.30	1.16	0.81
V35	00:30:19.772	+46:47:45.21	RRab	0.579	854.780	25.64	25.17	1.50	1.17
V36	00:30:26.764	+46:50:36.83	RRab	0.5678	858.615	25.47	25.14	1.71	1.32
V37	00:30:02.239	+46:46:45.76	RRab	0.6992	857.747	25.64	25.23	0.80	0.62
V38	00:30:18.484	+46:47:02.00	RRab	0.67	856.802	25.63	25.30	0.72	0.47
V39	00:30:22.544	+46:54:27.27	RRab	0.5766	858.601	25.54	25.22	1.21	1.00
V40	00:30:18.502	+46:46:50.06	RRab	0.621	858.638	25.66	25.27	1.37	0.82
V41	00:29:55.859	+46:47:19.20	RRab	0.618	856.664	25.66	25.29	0.82	0.67
V43	00:29:48.512	+46:51:50.74	RRc	0.37	855.660	25.59	25.17	0.64	0.34
V44	00:29:48.589	+46:49:46.67	RRab	0.615	858.598	25.59	25.25	0.92	0.69
V45	00:30:04.316	+46:44:45.19	RRab	0.5867	855.842	25.59	25.33	1.13	0.93
V46	00:29:42.803	+46:51:51.83	AC/CC?	1.213	852.697	23.82	23.38	0.62	0.40
V47	00:30:08.635	+46:44:29.81	RRab	0.6322	854.715	25.65	25.36	1.02	0.81
V48	00:29:57.962	+46:44:56.31	RRab	0.6325	857.792	25.74	25.36	0.81	0.70
V49	00:30:25.549	+46:56:26.38	RRab	0.592	855.790	25.65	25.33	1.05	0.92
V50	00:29:41.661	+46:50:24.07	RRab	0.579	856.863	25.65	25.45	0.81	0.67
V51	00:30:17.641	+46:57:49.18	RRab	0.6371	855.593	25.43	25.08	1.13	0.93
V52	00:30:09.862	+46:43:59.74	RRab	0.6243	856.652	25.58	25.20	0.97	0.71
V53	00:30:20.789	+46:44:32.70	RRc?	0.3934	854.826	25.54	25.26	0.56	0.42
V54	00:30:24.470	+46:57:13.95	RRab	0.635	855.580	25.66	25.20	0.80	0.65
V55	00:30:37.347	+46:52:57.46	RRab	0.681	851.572	25.61	25.231	0.80	0.66
V56	00:29:50.346	+46:44:58.80	RRc	0.299	858.907	25.66	25.39	0.67	0.53
V57	00:30:16.060	+46:42:25.70	RRab	0.57	856.764	25.77	25.38	0.97	0.72
V58	00:29:32.588	+46:49:37.73	AC	0.531	855.810	24.53	24.24	0.90	0.76
V59	00:29:56.648	+46:42:10.13	RRab	0.642	856.847	25.45	25.22	1.201	1.087
V60*	00:30:13.652	+46:41:30.72	uncl	0.848	854.595	21.48	19.96	0.239	0.197
V61*	00:30:06.316	+46:41:26.44	ECL	0.25677	856.760	24.24	23.22	1.39	0.886
V62	00:30:14.030	+46:41:22.26	RRab	0.5337	856.732	25.67	25.22	1.58	1.233
V63*	00:29:49.898	+46:49:07.68	RRab	0.5486	855.629	25.55	25.16	1.483	1.157

*Field variable stars

Notes: Solid lines separate variable stars within an area enclosed within once and twice the galaxy r_h. Column 1 lists the star identifier, Columns 2 and 3 give right ascension and declination (J2000 epoch), obtained from our astrometrized catalogs. Column 4 provides the type of variability. A question mark identifies stars whose classification is uncertain. Columns 5 and 6 list the period and the Heliocentric Julian Day of maximum light, respectively. Columns 7 and 8 give the intensity-weighted mean B and V magnitudes, while Columns 9 and 10 list the corresponding amplitudes of the light variation.

TABLE A.2: Photometric and pulsation properties of the variable stars identified in And XXVII

Name	α (2000)	δ (2000)	Type	P (days)	Epoch (max) HJD (−2455000)	$\langle B \rangle$ (mag)	Amp_B (mag)	$\langle V \rangle$ (mag)	Amp_V (mag)
V1	00:37:31.893	+45:23:54.12	RRab	0.6171	53.792	25.38	0.62	24.94	0.49
V2	00:37:32.950	+45:22:58.27	AC	1.2502	53.085	23.79	1.73	23.48	1.43
V3	00:37:33.655	+45:24:40.61	RRc	0.3091	53.633	25.19	0.74	24.91	0.53
V4	00:37:19.667	+45:24:27.33	RRc	0.3857	53.272	25.38	0.82	25.08	0.59
V5	00:37:36.643	+45:22:58.03	RRab	0.6048	54.080	25.72	1.05	25.37	0.82
V6	00:37:19.271	+45:21:17.88	RRc	0.3642	53.600	25.61	0.59	25.32	0.46
V7	00:37:28.721	+45:26:12.74	RRab	0.5798	53.762	25.78	1.04	25.25	0.55
V8	00:37:25.769	+45:19:50.86	RRab	0.5999	53.421	25.55	0.94	25.14	0.62
V9	00:37:22.045	+45:26:39.96	RRab	0.6910	53.292	25.56	0.66	25.19	0.66
V10	00:37:23.724	+45:19:30.90	RRab	0.6226	53.817	25.74	0.52	25.33	0.37
V11	00:37:16.889	+45:26:08.05	RRc	0.3552	53.428	25.41	0.69	25.06	0.42
V12	00:37:19.295	+45:19:31.97	RRc	0.2432	53.856	25.30	0.69	25.05	0.57
V13	00:37:37.243	+45:27:03.68	RRc	0.3635	53.735	25.38	0.72	24.99	0.53
V14	00:37:38.799	+45:26:48.76	RRab	0.6710	53.271	25.22	0.94	24.76	0.70
V15	00:37:44.006	+45:21:10.15	RRab	0.5645	53.783	25.78	0.97	25.53	0.85
V16	00:37:21.577	+45:18:40.74	RRab	0.5881	53.459	25.72	1.16	25.35	0.78
V17	00:37:46.582	+45:23:51.84	RRab	0.6586	53.390	25.64	0.67	25.30	0.59
V18	00:37:29.435	+45:28:15.86	RRab	0.5793	53.425	25.57	1.09	25.21	0.89
V19	00:37:30.249	+45:18:03.82	RRab	0.6181	53.987	25.33	1.30	25.05	1.18
V20	00:37:07.677	+45:26:04.87	RRab	0.5612	53.679	25.30	1.49	24.92	0.99
V21	00:37:40.518	+45:27:58.79	RRc	0.4357	53.691	25.42	0.46	24.99	0.31
V22	00:37:12.966	+45:18:22.55	RRc	0.2925	53.985	25.33	0.67	25.12	0.57
V23	00:37:38.962	+45:28:28.95	RRab	0.5570	53.857	25.11	1.14	24.70	0.96
V24	00:37:06.459	+45:19:45.37	RRab	0.5746	53.559	25.41	1.19	25.10	0.96
V25	00:37:45.060	+45:18:43.87	RRab	0.7150	53.391	25.52	0.71	25.11	0.70
V26	00:37:01.535	+45:24:21.95	RRab	0.5535	53.588	25.66	1.00	25.26	1.03
V27	00:37:45.003	+45:28:36.34	RRc	0.3938	53.147	25.52	0.56	25.10	0.35
V28	00:37:52.395	+45:19:57.61	RRab	0.5870	53.910	25.58	0.95	25.13	0.87
V29	00:37:17.317	+45:30:03.48	RRc	0.3601	54.076	25.34	0.44	24.88	0.38
V30	00:36:59.737	+45:25:39.13	RRab	0.5541	53.887	25.50	1.04	25.14	0.69
V31	00:37:56.368	+45:25:06.03	RRab	0.5408	53.803	25.56	1.05	25.25	0.98
V32	00:37:57.393	+45:21:23.21	RRc?	0.2793	53.931	25.44	0.47	25.27	0.47
V33	00:37:56.332	+45:20:25.79	RRab	0.5492	53.824	25.50	0.82	25.23	0.50
V34	00:37:00.936	+45:18:26.79	RRab	0.5579	53.875	25.54	1.46	25.18	1.00
V35	00:37:58.868	+45:20:16.64	RRc	0.3579	53.544	25.67	0.58	25.30	0.43
V36	00:38:00.070	+45:21:13.33	RRc	0.3641	53.781	25.60	0.66	25.21	0.67
V37	00:38:00.481	+45:24:46.02	RRab	0.5996	53.525	25.35	1.31	24.99	0.96
V38	00:37:52.645	+45:17:32.73	RRc	0.3987	53.928	25.27	0.63	24.92	0.45
V39	00:36:55.883	+45:27:09.36	RRc	0.3534	53.504	25.51	0.82	25.14	0.56
V40	00:38:02.723	+45:24:46.06	RRc	0.3395	53.616	25.50	0.72	25.28	0.59
V41	00:37:13.142	+45:14:50.52	RRab	0.5888	53.486	25.50	1.05	25.20	1.02
V42	00:36:51.394	+45:25:50.83	RRc	0.3550	53.660	25.55	0.57	25.27	0.56
V43	00:37:56.003	+45:29:09.95	RRab	0.6087	53.686	25.66	0.97	25.24	0.72
V44	00:37:25.859	+45:32:50.55	RRab?	0.6312	53.322	25.37	0.45	25.12	0.53
V45	00:36:49.108	+45:20:47.83	RRab	0.5315	53.758	25.37	1.28	25.03	1.18
V46	00:37:24.064	+45:13:16.69	RRab	0.5855	54.116	25.78	0.82	25.46	0.90
V47	00:38:02.920	+45:18:20.73	RRab	0.5293	53.342	25.67	1.14	25.29	0.70
V48	00:38:06.624	+45:20:36.47	RRc	0.3501	53.816	25.58	0.54	25.26	0.45
V49	00:38:05.333	+45:19:20.00	RRc	0.3541	53.015	25.54	0.50	25.21	0.31
V50	00:36:48.952	+45:19:02.07	RRab	0.6451	53.359	25.56	1.17	25.14	0.76
V51	00:37:13.308	+45:13:20.85	RRc	0.3558	53.410	25.53	0.61	25.28	0.51
V52	00:36:47.422	+45:27:31.80	RRab	0.5627	53.761	25.20	1.21	24.84	0.85
V53	00:36:52.857	+45:30:18.98	RRab	0.5980	53.706	25.42	0.78	25.06	0.69
V54	00:38:11.223	+45:21:26.58	RRab	0.5754	54.079	25.41	1.10	25.12	1.02
V55	00:37:09.934	+45:12:53.19	RRab	0.6226	53.920	25.53	0.79	25.24	0.57
V56	00:38:02.164	+45:30:14.28	RRab	0.5794	53.853	25.60	0.95	25.26	0.84
V57	00:36:42.634	+45:21:18.38	RRab	0.5357	53.638	25.49	1.18	25.29	0.96
V58	00:38:10.002	+45:18:59.73	RRab	0.5395	53.369	25.62	1.00	25.25	0.79
V59	00:37:43.102	+45:34:14.31	RRab	0.6000	53.707	25.42	1.19	25.04	0.92
V60	00:36:39.192	+45:23:25.77	RRab	0.5788	53.866	25.47	0.94	25.09	0.94
V61	00:38:16.025	+45:24:01.56	RRc?	0.3830	53.841	25.43	0.75	25.20	0.76
V62	00:36:37.523	+45:23:46.74	RRc	0.4281	53.797	25.41	0.58	24.95	0.22
V63	00:38:15.170	+45:19:44.42	RRab	0.6023	53.829	25.10	0.87	24.73	0.71
V64	00:36:42.559	+45:17:17.99	RRab	0.5537	53.877	25.41	1.19	25.10	0.96
V65	00:38:07.107	+45:31:17.21	RRab	0.6035	53.411	25.57	0.87	25.16	0.53
V66	00:38:17.987	+45:21:20.02	RRab	0.7383	53.309	25.34	0.52	24.77	0.35
V67	00:38:14.697	+45:17:42.86	RRab	0.5621	53.544	25.76	0.90	25.45	0.68
V68	00:36:45.329	+45:14:56.17	RRc	0.3682	53.304	25.49	0.67	25.21	0.50
V69	00:38:13.766	+45:16:28.40	RRab	0.5715	53.933	25.70	0.90	25.33	0.98
V70	00:36:33.155	+45:24:24.17	RRc	0.3547	53.748	25.54	0.58	25.15	0.37
V71	00:38:20.719	+45:20:47.63	RRc	0.3594	53.929	25.45	0.66	25.15	0.58
V72	00:38:18.355	+45:27:54.69	RRab	0.6236	53.679	25.64	0.84	25.25	0.71
V73	00:38:06.155	+45:32:45.88	RRab	0.6524	53.969	25.57	1.22	25.27	1.16
V74	00:38:12.060	+45:15:24.61	RRab	0.5616	53.699	25.56	0.96	25.12	0.56
V75	00:38:05.872	+45:13:29.96	RRc	0.3487	53.877	25.50	0.64	25.20	0.56
V76	00:36:35.681	+45:28:17.18	RRc	0.3642	53.833	25.53	0.65	25.20	0.48
V77	00:38:23.292	+45:22:27.00	RRab	0.5306	53.267	25.65	1.15	25.30	0.96
V78	00:38:14.075	+45:15:18.82	RRc	0.3333	53.837	25.50	0.68	25.24	0.65
V79	00:36:29.952	+45:23:43.59	RRc?	0.2924	53.494	25.37	0.70	25.19	0.48
V80	00:38:23.752	+45:20:48.11	RRc	0.3648	53.352	25.61	0.74	25.31	0.64
V81	00:36:30.046	+45:25:46.60	RRab	0.5595	53.968	25.26	1.01	24.89	0.82
V82	00:38:09.009	+45:12:59.08	RRc	0.2547	53.786	25.49	0.69	25.24	0.38
V83	00:38:27.464	+45:23:03.51	RRab	0.5628	53.780	25.50	1.15	25.16	0.92
V84	00:36:31.312	+45:28:59.64	RRab	0.6628	53.385	25.33	1.00	24.83	0.71
V85	00:38:20.435	+45:15:59.67	RRab	0.5575	53.929	25.87	1.38	25.48	1.11
V86	00:38:28.400	+45:20:51.17	RRab	0.5453	54.120	25.73	1.10	25.29	0.99
V87	00:36:28.323	+45:15:54.01	RRab	0.7117	53.641	25.45	0.77	25.10	0.56
V88	00:38:32.760	+45:26:30.92	RRab	0.6063	53.786	25.47	0.73	25.07	0.56
V89	00:36:19.903	+45:21:49.53	RRab	0.5905	53.809	25.29	1.68	25.01	1.47
V90	00:36:21.505	+45:18:27.19	RRab	0.5959	53.657	25.41	1.03	25.15	0.64

Notes: Columns content as Table A.1.

TABLE A.3: Dataset for 364 RRLs with ϖ_{TGAS}

Name	ID_{Gaia}	$ID_{Hipparcos}$	ID_{Tycho2}	ϖ_{Hip} (mas)	$\sigma\varpi_{Hip}$ (mas)	ϖ_{TGAS} (mas)	$\sigma\varpi_{TGAS}$ (mas)	P (days)	Type	G_{Gaia} (mag)	σ_G (mag)	$\langle V \rangle$ (mag)	$\langle K_s \rangle$ (mag)	A_V (mag)	[Fe/H] (dex)
AA CMi	3111925220109675136	35281	164-182-1	2.84	3.47	0.82	0.23	0.4764	AB	11.513	0.022	11.552	10.287	0.257	−0.55
AB UMa	1546016668386865792	59411	3455-362-1	0.14	1.94	0.93	0.27	0.5996	AB	10.733	0.010	10.899	9.623	0.068	−0.72
AE Boo	1234729395962169216	72342	1478-225-1	0.32	2.00	1.21	0.26	0.3150	C	10.526	0.015	10.664	9.730	0.07	−1.47
AF Vel	5360400626025377536	53213	8207-1400-1	1.45	2.18	1.16	0.25	0.5275	AB	11.394	0.010	11.389	10.042	0.407	−1.64
AL CMi	3143813565573130880		192-43-1	-	-	1.12	0.40	0.5506	AB	11.840	0.012	11.931	10.767	0.024	−0.85
AM Tuc	4692528057537147136	6115	9136-229-1	0.46	1.87	0.85	0.26	0.4058	C	11.539	0.013	11.619	10.610	0.069	−1.54
AM Vir	3604450388616968576	65344	6120-430-1	−3.22	2.84	0.59	0.41	0.6151	AB	11.402	0.017	11.525	10.197	0.205	−1.37
AN Leo	3817504852675061888		270-519-1	-	-	1.16	0.97	0.5721	AB	12.401	0.012	12.528	11.041	0.186	−1.14
AN Ser	1191509999055192960	77830	951-213-1	−1.71	2.93	0.77	0.29	0.5221	AB	10.985	0.018	10.961	9.831	0.124	−0.04
AO Tuc	4918030711207756032		8470-493-1	-	-	0.70	0.24	0.3333	C	11.168	0.009	11.107	10.364	0.031	−1.25
AR Her	1398766016745955584	78417	3491-487-1	1.70	1.95	0.45	0.24	0.4700	AB	11.303	0.027	11.241	10.406	0.038	−1.4
AR Per	234108359386230784	19993	3332-1444-1	0.93	1.45	1.99	0.24	0.4256	AB	10.286	0.017	10.470	8.659	0.97	−0.43
AS Vir	3626569264033312896		5538-115-1	-	-	0.88	0.78	0.5535	AB	11.874	0.020	11.982	10.773	0.112	−1.49
AT Ser	4454183795247850880	77997	943-703-1	−0.74	3.41	0.51	0.30	0.7465	AB	11.419	0.015	11.492	10.214	0.114	−2.03
AT Vir	3677686040644104320	63054	4956-24-1	1.08	2.28	0.15	0.38	0.5258	AB	11.393	0.016	11.335	10.337	0.092	−1.91
AU Vir	3631453500841926272	65445	4965-401-1	−1.09	3.73	0.65	0.43	0.3433	C	11.531	0.022	11.602	10.770	0.085	−1.55
AV Peg	1793460110951463424	107935	2202-1379-1	2.28	1.72	1.53	0.23	0.3904	AB	10.418	0.029	10.485	9.377	0.303	−0.44
AV Ser	4410058469479744000		366-711-1	-	-	0.78	0.38	0.4876	AB	11.505	0.015	11.484	10.014	0.514	−1.2
AV Vir	3731723085779316992	65063	891-239-1	2.84	2.73	0.14	0.27	0.6570	AB	11.724	0.012	11.812	10.566	0.086	−1.32
BB Eri	2976126944141674240	22750	5907-1032-1	4.35	2.80	0.67	0.30	0.5701	AB	11.420	0.023	11.498	10.047	0.148	−1.51
BB Vir	3720468828354785024	67653	315-1326-1	−0.19	2.47	−0.25	0.35	0.4712	AB	11.052	0.036	11.111	10.301	0.076	−1.61
BC Dra	2269585754295172608	89372	4570-56-1	3.09	1.48	0.54	0.23	0.7196	AB	11.424	0.009	11.588	10.088	0.208	−2.0
BC Vir	3717352881121133568		306-647-1	-	-	0.60	0.51	0.5646	AB	12.098	0.027	12.121	11.125	0.104	−1.5
BH Aur	182142003881848832	24226	2397-244-1	9.29	3.26	1.00	0.29	0.4561	AB	11.502	0.013	11.797	9.881	1.182	−0.34
BH Pav	6437477681110756736		9077-2070-1	-	-	0.45	0.26	0.4770	AB	12.469	0.016	12.480	11.285	0.306	−1.6
BH Peg	2828497064068310784	112994	1698-111-1	0.31	1.82	1.40	0.22	0.6419	AB	10.364	0.014	10.446	9.084	0.236	−1.38
BI Cen	5335614747719701632		8642-1380-1	-	-	0.32	0.28	0.4532	AB	11.900	0.023	11.955	10.513	0.626	−0.83
BK Dra	2254942458436117120	94869	4229-1189-1	1.09	1.24	0.70	0.43	0.5921	AB	11.274	0.012	11.169	10.069	0.097	−2.12
BK Tuc	6380659524390970752		9345-132-1	-	-	0.42	0.24	0.5501	AB	12.784	0.016	12.789	11.721	0.076	−1.82
BN Pav	6445351283875384064	96581	9084-1868-1	6.22	4.47	0.67	0.38	0.5672	AB	12.415	0.032	12.560	11.269	0.223	−1.32
BN Vul	2022835519452349184	95702	2125-1630-1	6.09	2.24	1.45	0.23	0.5942	AB	10.722	0.021	10.985	8.665	1.283	−1.52
BO Aqr	2603947377740412800		5816-616-1	-	-	1.16	0.81	0.6941	AB	12.057	0.037	12.157	10.898	0.118	−1.8
BP Pav	6428374137148505984	98265	9097-1105-1	−1.70	4.53	1.02	0.28	0.5272	AB	12.467	0.015	12.493	11.366	0.182	−1.48
BR Aqr	2438710605654285312	116664	5829-1043-1	−1.97	2.61	0.82	0.28	0.4819	AB	11.450	0.017	11.450	10.369	0.083	−0.84
BS Aps	5806921712636471040		9281-1742-1	-	-	0.53	0.23	0.5826	AB	12.039	0.012	12.196	10.885	0.244	−1.33
BT Dra	1617474891148520960	72691	4180-1364-1	1.19	1.65	0.32	0.23	0.5886	AB	11.613	0.013	11.628	10.399	0.031	−1.55
BV Aqr	6820039248616386688	108839	6383-1552-1	3.87	2.36	0.92	0.26	0.3638	C	10.885	0.022	10.888	10.010	0.103	−1.49
BX Leo	3972712532526824448	56742	1438-1575-1	4.15	3.12	0.53	0.28	0.3629	C	11.476	0.015	11.598	10.605	0.07	−1.39
CG Lib	6238435083998634240	76313	6764-290-1	−3.40	3.44	0.70	0.44	0.3068	C	11.427	0.016	11.511	10.224	0.914	−1.32
CG Peg	1797739513285655808	107078	2193-904-1	1.98	2.07	1.44	0.67	0.4672	AB	11.059	0.026	11.168	9.986	0.261	−0.48
CH Aql	6908369683465862912	101453	5188-1517-1	27.73	22.97	0.47	0.38	0.3892	AB	13.560	0.017	13.466	12.418	0.1	−0.88
CI And	349612811796499584	8939	2828-830-1	0.89	4.69	0.38	0.27	0.4848	AB	12.033	0.030	12.244	10.929	0.211	−0.83
CN Lyr	4539434120069033856	91634	2119-755-1	−1.44	1.95	1.02	0.24	0.4115	AB	11.271	0.009	11.468	9.935	0.686	−0.26
CQ Lac	1956961303931536384		3204-359-1	-	-	1.62	0.42	0.6200	AB	12.359	0.029	12.447	11.091	0.282	−2.04
CS Eri	4947090013255935616	12199	7558-414-1	2.71	1.10	2.16	0.23	0.3114	C	8.974	0.012	9.009	8.121	0.057	−1.48
CW Her	1327053634999596160		2597-581-1	-	-	0.45	0.23	0.6239	AB	12.478	0.016	12.540	11.393	0.057	−2.09
DD Hya	3090871393500268416	40186	199-1667-1	−2.99	3.97	0.39	0.40	0.6482	AB	12.362	0.014	12.202	11.210	0.0	−1.0
DM And	1912453760434108928		2773-253-1	-	-	1.11	0.33	0.5916	AB	11.818	0.012	11.943	10.575	0.439	−2.32
DM Cyg	1853751143864356736		2707-757-1	-	-	0.74	0.47	0.6304	AB	11.522	0.011	11.530	10.287	0.3	−0.14
DN Aqr	2381771777534596864	115135	6973-1111-1	1.82	2.11	0.53	0.25	0.4199	AB	11.087	0.020	11.182	9.901	0.077	−1.63
DQ Lyn	905055196743761152		2482-5-1	-	-	0.99	0.54	0.4949	C	11.336	0.008	11.412	10.440	0.138	−1.58
DR And	3150283263793733760		2286-352-1	-	-	0.19	0.35	0.5328	AB	12.451	0.018	12.431	11.332	0.122	−1.48
DX Cep	2299963989259501056		4650-982-1	-	-	0.96	0.37	0.5261	AB	12.160	0.018	12.370	10.427	1.097	−1.83

Continued in the next page

Name	ID$_{Gaia}$	ID$_{\rm Hipparcos}$	ID$_{Tycho2}$	ϖ_{Hip} (mas)	$\sigma\varpi_{Hip}$ (mas)	$\varpi_{\rm TGAS}$ (mas)	$\sigma\varpi_{\rm TGAS}$ (mas)	P (days)	Type	G_{Gaia} (mag)	σ_G (mag)	$\langle V\rangle$ (mag)	$\langle K_{\rm s}\rangle$ (mag)	A$_V$ (mag)	[Fe/H] (dex)
DX Del	1760981190300823808	102593	1097-846-1	0.77	1.38	1.66	0.22	0.4727	AB	9.904	0.008	9.945	8.542	0.248	−0.56
DZ Peg	2817589255885467520		1713-1366-1	-	-	1.41	0.88	0.6075	AB	11.948	0.024	11.955	10.890	0.117	−1.52
EL Aps	5801111515236622336		9444-2849-1	-	-	0.71	0.22	0.5798	AB	11.729	0.010	11.896	10.193	0.659	−1.56
EZ Cep	568205137966212096	18548	4521-107-1	−0.46	6.13	0.65	0.26	0.3790	C	12.655	0.018	12.887	11.612	0.391	−0.45
EZ Lyr	2093443098171439104	92221	2650-506-1	12.27	5.61	0.69	0.21	0.5253	AB	11.101	0.002	11.558	10.430	0.071	−1.56
FS Vel	5390917846133815040		7735-975-1	-	-	0.86	0.29	0.4758	AB	11.941	0.024	12.097	10.429	0.805	−1.17
FW Lup	6005656893165960704	75234	7839-1841-1	1.57	1.18	2.74	0.24	0.4842	AB	8.893	0.012	9.020	7.659	0.295	−0.59
GY Her	1328420087434496896		3063-1333-1	-	-	0.32	0.35	0.5243	AB	12.701	0.020	12.640	11.864	0.039	−1.92
HH Pup	5510293232308723712	35584	8120-896-1	2.52	1.87	1.19	0.21	0.3908	AB	11.343	0.025	11.282	9.953	0.577	−0.69
HH Tel	6660781552043047424		8389-1466-1	-	-	0.43	0.24	0.4821	AB	12.157	0.016	12.297	11.074	0.192	−1.02
HK Pup	3030561875047012352	37779	5418-876-1	0.70	2.52	0.53	0.26	0.7343	AB	11.265	0.015	11.334	9.928	0.067	−1.26
HY Tel	6472840586399564032		8780-192-1	-	-	0.41	0.26	0.4028	AB	12.473	0.028	12.668	11.587	0.137	−0.17
IK Hya	3486473753028871808	58907	6675-28-1	2.11	1.32	1.25	0.29	0.6504	AB	10.025	0.011	10.113	8.758	0.186	−1.36
IN Ara	6653158053812911616	88802	8747-2167-1	−22.38	25.3	0.19	0.23	0.6315	AB	13.190	0.015	13.153	11.857	0.202	−1.75
IO Lyr	4593112037219674368	90053	2627-1159-1	0.01	2.07	0.59	0.22	0.5771	AB	11.639	0.020	11.838	10.536	0.219	−1.52
IU Car	5480600096166907776		8548-1214-1	-	-	0.37	0.32	0.7371	AB	11.881	0.021	11.935	10.483	0.259	−1.85
LU Aps	5810083117803121152		9293-1598-1	-	-	0.53	0.26	0.7551	AB	12.703	0.011	12.920	11.458	0.139	−2.06
MS Ara	6701723997807118464	88402	8743-2210-1	12.43	3.90	0.74	0.47	0.5250	AB	11.909	0.032	12.047	10.662	0.435	−1.48
MT Tel	6662886601414152448	93476	8374-757-1	1.16	1.46	1.43	0.31	0.3170	C	8.946	0.017	8.969	8.076	0.173	−1.81
RR Gem	886793511196722432	35667	2452-1683-1	−5.01	2.86	0.74	0.26	0.3973	AB	11.068	0.040	11.369	10.279	0.238	−0.35
RR Gru	6565527904791301504		7992-369-1	-	-	0.39	0.28	0.5525	AB	12.364	0.013	12.438	11.349	0.066	−0.45
RR Lyr	2125982595039626368	95497	3142-494-1	3.46	0.64	3.64	0.23	0.5669	AB	7.641	0.031	7.755	6.519	0.16	−1.37
RS Boo	1286188051969685632	71186	2553-1108-1	0.11	1.40	1.52	0.28	0.3774	AB	10.398	0.025	10.374	9.522	0.036	−0.32
RU Cet	2371321778506174976	4725	5848-2292-1	2.67	3.78	0.73	0.25	0.5863	AB	11.647	0.017	11.638	10.501	0.071	−1.6
RU Psc	294072906063827072	5803	1747-1336-1	1.71	1.68	1.44	0.30	0.3903	C	10.169	0.017	10.176	9.107	0.132	−1.73
RU Scl	2336550169954917376	226	6412-619-1	−0.11	1.42	1.52	0.30	0.4934	AB	10.329	0.014	10.218	9.222	0.055	−1.25
RV Cap	6883653108749373568	103755	6345-376-1	−2.00	2.51	0.28	0.27	0.4478	AB	11.152	0.023	11.040	9.789	0.126	−1.72
RV Cet	5151789460253603968	10491	5281-1037-1	2.03	2.12	0.95	0.32	0.6235	AB	10.682	0.021	10.886	9.468	0.073	−1.32
RV CrB	1317846462066886272	79974	2054-5-1	3.97	2.34	0.50	0.28	0.3317	C	11.360	0.013	11.424	10.514	0.118	−1.69
RV Oct	5769986333917619968	67227	9512-1029-1	1.32	1.32	1.13	0.23	0.5712	AB	10.633	0.024	10.978	9.516	0.395	−1.34
RV Phe	6526559494716694272	115870	8455-21-1	0.24	3.09	0.64	0.24	0.5965	AB	11.832	0.012	11.882	10.766	0.023	−1.6
RV UMa	1561928422706459264	66122	3850-662-1	−0.66	1.34	0.74	0.23	0.4681	AB	10.771	0.020	10.782	9.841	0.054	−1.19
RW Ari	80556921999940096		1217-1508-1	-	-	0.54	0.47	0.3544	C	12.130	0.009	12.359	11.176	0.257	−1.11
RW Cnc	695655337537044864	45709	1958-774-1	−7.11	2.98	0.74	0.93	0.5473	AB	11.795	0.028	11.838	10.692	0.062	−1.52
RW Col	2890929498956531072	28699	7071-298-1	2.35	6.20	0.03	0.22	0.5457	AB	13.082	0.018	13.316	12.039	0.172	−1.03
RW Dra	1431291700999242112	81238	3884-2060-1	−0.88	2.02	0.58	0.23	0.4429	AB	11.694	0.020	11.659	10.585	0.035	−1.4
RW TrA	5815008826813850368	83244	9051-1868-1	3.12	2.31	0.96	0.27	0.3741	AB	11.225	0.011	11.347	10.058	0.416	0.07
RX Cet	2373827050109860992	2655	5847-1684-1	7.20	2.83	1.00	0.32	0.5735	AB	11.357	0.017	11.428	10.277	0.075	−1.46
RX Col	2884776803686161920	29528	7084-453-1	−2.56	3.15	0.42	0.23	0.5938	AB	12.510	0.012	12.688	11.316	0.338	−1.7
RX Eri	2981136559635823744	22442	5899-580-1	1.50	1.12	1.83	0.28	0.5873	AB	9.656	0.015	9.690	8.424	0.174	−1.33
RX For	5073412491854346880		6442-690-1	-	-	0.39	0.28	0.5971	AB	12.002	0.015	11.959	10.929	0.043	−1.26
RX Leo	3994645453038686464		1983-539-1	-	-	0.64	0.56	0.6534	AB	11.786	0.011	11.948	10.741	0.051	−1.38
RY Col	4818854968540980608	24471	7591-1523-1	1.36	1.34	1.54	0.40	0.4789	AB	10.776	0.034	10.906	9.737	0.079	−1.11
RY Com	3944929145003343616		1993-2658-1	-	-	0.33	0.43	0.4690	AB	12.478	0.023	12.385	11.427	0.041	−1.65
RY Oct	6356371759209904512	106649	9478-890-1	−0.95	3.36	0.44	0.27	0.5635	AB	11.884	0.039	12.047	10.864	0.345	−1.83
RY Psc	2544592853854602496		4664-143-1	-	-	−0.15	0.67	0.5298	AB	12.240	0.018	12.342	11.143	0.094	−1.39
RZ CVn	1458363360901873152	67087	2540-1136-1	−3.16	2.25	0.65	0.26	0.5675	AB	11.623	0.011	11.519	10.480	0.042	−1.92
RZ Cep	2211629018927324288	111839	4273-949-1	0.59	1.48	2.65	0.24	0.3087	C	9.194	0.015	9.459	7.923	0.907	−1.75
RZ Cet	5176548537965653120	11517	5282-84-1	−0.45	4.25	0.46	0.29	0.5107	AB	11.875	0.018	11.836	10.828	0.09	−1.5
RZ Lyr	2090986686116693504		2641-1678-1	-	-	0.40	0.31	0.5114	AB	11.708	0.021	11.558	10.464	0.265	−2.13
S Com	3960906320265637888	61225	1991-1486-1	−1.05	2.33	0.43	0.32	0.5867	AB	11.727	0.022	11.609	10.665	0.059	−2.0
SS CVn	1497236182185018880	67354	3027-152-1	1.25	2.61	0.38	0.23	0.4786	AB	11.843	0.016	11.889	10.938	0.02	−1.52
SS Cnc	680218812758449280		1927-426-1	-	-	0.42	0.34	0.3674	AB	12.143	0.027	12.220	11.212	0.136	−0.07
SS For	5117708894760403328	9932	6432-1585-1	2.96	1.51	1.69	0.45	0.4955	AB	10.299	0.029	10.158	9.235	0.044	−1.35
SS Leo	3797319365376869632	56409	4930-316-1	−0.13	2.79	1.13	0.72	0.6264	AB	11.103	0.019	11.074	9.947	0.054	−1.83
SS Oct	6345324587928571648	108057	9524-1884-1	4.29	2.70	0.90	0.28	0.6219	AB	11.740	0.017	11.898	9.787	0.872	−1.6

Continued in the next page

Name	ID$_{Gaia}$	ID$_{\rm Hipparcos}$	ID$_{Tycho2}$	ϖ_{Hip} (mas)	$\sigma\varpi_{Hip}$ (mas)	$\varpi_{\rm TGAS}$ (mas)	$\sigma\varpi_{\rm TGAS}$ (mas)	P (days)	Type	G_{Gaia} (mag)	σ_G (mag)	$\langle V\rangle$ (mag)	$\langle K_{\rm s}\rangle$ (mag)	A$_V$ (mag)	[Fe/H] (dex)
SS Psc	2896620433703043 84	6301	1203-549-1	5.26	1.99	1.11	0.51	0.2879	C	10.865	0.016	10.979	10.048	0.149	−0.82
ST Boo	1374971554328855424	75942	2570-206-1	1.19	1.61	0.69	0.33	0.6223	AB	11.001	0.016	11.014	9.933	0.065	−1.86
ST CVn	1453674734083793152	68188	2012-893-1	−0.11	2.82	0.22	0.36	0.3291	C	11.281	0.010	11.334	10.415	0.038	−1.23
ST Com	3940418398550912512	64875	1457-102-1	−5.10	2.46	0.37	0.30	0.5990	AB	11.390	0.015	11.438	10.191	0.072	−1.26
ST Leo	3915998554534971136	56785	860-138-1	−1.19	2.30	0.72	0.32	0.4780	AB	11.566	0.019	11.516	10.290	0.115	−1.29
ST Vir	3652665554042358144	70702	4977-480-1	−2.81	3.67	0.87	0.61	0.4109	AB	11.716	0.010	11.551	10.670	0.119	−0.88
SU Dra	1058066258521694464	56734	4159-532-1	0.20	1.13	1.43	0.28	0.6603	AB	9.718	0.024	9.815	8.617	0.031	−1.74
SV Eri	5165898383172441216	14856	5297-700-1	1.48	1.67	1.34	0.26	0.7139	AB	9.832	0.020	9.948	8.637	0.261	−2.04
SV Hya	3499611302073156736	61031	6686-81-1	4.49	1.76	1.32	0.24	0.4786	AB	10.541	0.022	10.512	9.372	0.245	−1.7
SV Scl	5022411782439031936	8163	7003-95-1	5.43	1.88	0.44	0.32	0.3774	C	11.297	0.014	11.380	10.524	0.043	−1.75
SW And	2857456207478683776	1878	1737-1702-1	1.48	1.21	1.77	0.26	0.4423	AB	9.629	0.032	9.712	8.509	0.113	−0.38
SW Aqr	2689556486950807040	104930	528-1261-1	−0.73	2.39	0.76	0.23	0.4594	AB	11.207	0.042	11.176	10.056	0.233	−1.24
SW Dra	1683444626742055168	59946	4394-761-1	−0.46	1.29	1.01	0.23	0.5697	AB	10.436	0.018	10.499	9.316	0.044	−1.24
SW For	5045760839567585152		7560-526-1	-	-	0.16	0.26	0.8038	AB	12.193	0.011	12.341	11.059	0.048	−1.95
SX Aqr	2697816774212075904	106645	546-661-1	0.01	2.86	0.64	0.28	0.5357	AB	11.846	0.013	11.754	10.639	0.148	−1.83
SX For	4860671835287027584	16321	7027-701-1	−2.52	1.70	0.77	0.27	0.6054	AB	11.077	0.011	11.099	9.778	0.035	−1.62
SX UMa	1565435486842373632	65547	3853-589-1	1.11	1.29	0.42	0.34	0.3072	C	10.902	0.017	10.859	10.066	0.03	−1.78
SZ Gem	670266858138317440	38561	1371-838-1	1.40	3.11	0.71	0.29	0.5012	AB	11.824	0.020	11.738	10.715	0.157	−1.81
SZ Hya	5743059534671356416	45292	5458-44-1	−5.30	4.95	1.66	0.42	0.5374	AB	11.276	0.019	11.277	10.255	0.114	−1.75
TT Cnc	603291103764056960	41936	808-590-1	−0.66	2.81	0.80	0.40	0.5635	AB	11.210	0.022	11.341	9.973	0.13	−1.58
TT Lyn	1009665138191506432	44428	2989-1709-1	−1.48	1.74	1.53	0.40	0.5986	AB	9.781	0.011	9.848	8.610	0.052	−1.59
TU UMa	4022618712476736896	56088	2523-441-1	−0.53	1.28	1.47	0.31	0.5569	AB	9.447	0.019	9.828	8.662	0.066	−1.44
TV Boo	1492230552420859776	69759	3038-699-1	−0.07	1.60	0.76	0.23	0.3126	C	10.909	0.011	10.999	10.210	0.03	−2.24
TV CrB	1270551003758183680	75225	2028-1124-1	−0.36	3.68	0.53	0.25	0.5847	AB	11.953	0.012	11.875	10.792	0.101	−2.33
TW Boo	1489614951696832512	72115	3046-992-1	−0.28	1.63	0.72	0.24	0.5323	AB	11.258	0.020	11.264	10.176	0.041	−1.41
TW Her	4596935588904631040	87681	2608-2414-1	−1.37	1.66	0.65	0.31	0.3996	AB	11.317	0.024	11.274	10.238	0.172	−0.67
TW Lyn	924355886418231680	37805	2967-176-1	−2.98	3.96	0.50	0.29	0.4819	AB	11.840	0.019	11.979	10.776	0.157	−1.23
TY Aps	5797234602876902272	72444	9266-2648-1	2.24	2.39	0.76	0.26	0.5017	AB	11.709	0.018	11.870	10.451	0.52	−1.21
TY Pav	5909759310058062208		9058-2328-1	-	-	0.34	0.28	0.7104	AB	12.433	0.014	12.604	11.253	0.297	−2.31
TZ Aur	949205983077666944	34743	2948-760-1	−2.14	4.13	0.84	0.31	0.3917	AB	11.904	0.015	11.909	10.669	0.301	−0.8
U Cae	4818348918314107264		7586-270-1	-	-	0.29	0.26	0.4198	AB	12.254	0.017	12.145	11.180	0.041	−1.11
U Com	3962473193054146944	61809	1992-1477-1	3.51	2.94	0.46	0.28	0.2928	C	11.770	0.009	11.737	10.937	0.044	−1.36
U Lep	2973463342863091456	22952	5912-332-1	1.71	1.93	1.16	0.24	0.5816	AB	10.670	0.020	10.602	9.569	0.083	−1.93
U Pic	4784552714015117312	22466	8083-387-1	−0.57	1.83	0.77	0.36	0.4404	AB	11.479	0.014	11.352	10.386	0.027	−0.73
UU Boo	1290953129206046592		2569-519-1	-	-	0.47	0.26	0.4570	AB	12.332	0.016	12.280	11.302	0.051	−1.92
UU Cet	2414817599507403008	320	5838-661-1	5.30	4.06	0.54	0.26	0.6059	AB	11.905	0.012	12.045	10.841	0.064	−1.32
UU Vir	3698725333080479104	59208	4939-145-1	0.70	2.17	1.35	0.32	0.4756	AB	10.686	0.022	10.588	9.276	0.054	−0.82
UV Oct	5768557209320424320	80990	9522-447-1	2.44	0.81	2.02	0.23	0.5426	AB	9.511	0.011	9.498	8.296	0.295	−1.61
UV Vir	3699778115464435456		282-632-1	-	-	−0.01	0.84	0.5872	AB	11.809	0.020	11.919	10.865	0.075	−1.19
UW Gru	6508563375587983232		8822-225-1	-	-	0.07	0.23	0.5483	AB	13.232	0.014	13.248	12.175	0.064	−1.68
UW Oct	6354668581338232576		9482-15-1	-	-	0.95	0.48	0.4445	AB	11.712	0.017	11.825	10.382	0.516	−0.49
UY Boo	3727833391597367424	68292	907-1037-1	1.00	1.80	0.21	0.26	0.6509	AB	10.886	0.025	10.923	9.820	0.1	−2.56
UY Cam	1134921880785295872	39009	4369-1129-1	0.18	1.99	1.16	0.65	0.2671	C	11.463	0.013	11.534	10.803	0.069	−1.42
UZ CVn	1533880980593444352	61029	3018-255-1	3.38	4.24	0.41	0.25	0.6979	AB	12.025	0.018	12.099	10.889	0.057	−1.89
UZ Scl	2329707050101123712		7507-715-1	-	-	1.16	0.95	0.4492	AB	12.112	0.044	12.318	11.367	0.044	−1.14
V Ind	6483680327939151488	104613	8422-875-1	1.57	1.47	1.10	0.27	0.4797	AB	10.043	0.023	9.957	8.992	0.132	−1.5
V0338 Pup	5555745531172521344	31400	8104-1448-1	2.10	0.86	1.78	0.23	0.7974	AB	9.034	0.004	9.143	7.826	0.035	−2.16
V0341 Aql	4229920119381310080	101356	510-1223-1	2.80	2.59	0.75	0.25	0.5782	AB	10.841	0.046	10.865	9.733	0.045	−1.37
V0413 CrA	6730211038418525056	92244	7915-350-1	−0.62	2.11	0.86	0.27	0.5894	AB	10.436	0.017	10.581	9.156	0.295	−1.21
V0440 Sgr	6771307450164337920	96101	6889-1242-1	−0.22	2.55	1.28	0.42	0.4775	AB	10.394	0.023	10.322	9.090	0.346	−1.47
V0445 Oph	4352084485521550720	80402	5047-712-1	1.69	3.79	1.90	0.46	0.3972	AB	10.850	0.019	11.015	9.264	0.865	−0.23
V0455 Oph	4484858348599494912	89450	1017-263-1	0.76	5.06	0.67	0.80	0.4539	AB	12.237	0.021	12.316	11.093	0.498	−1.42
V0494 Sco	4055098870077726976	86512	7376-369-1	6.14	4.68	1.06	0.30	0.4273	AB	11.350	0.019	11.330	10.330	0.588	−1.01
V0499 Cen	6108774866054295168	67976	7802-553-1	0.35	2.10	0.80	0.73	0.5213	AB	10.980	0.052	11.101	9.926	0.249	−1.56
V0671 Cen	6163494948428593280		7278-390-1	-	-	0.47	0.45	0.7791	AB	12.308	0.013	12.378	11.063	0.0	−1.4
V0690 Sco	4035521825030647552	87922	7890-1497-1	−3.10	3.87	0.86	0.24	0.4923	AB	11.245	0.022	11.419	10.168	0.375	−1.11
V0796 Sgr	6688967566980810752		7937-1579-1	-	-	1.18	0.87	0.6255	AB	11.903	0.021	12.141	10.772	0.201	−1.87

Continued in the next page

Name	ID$_{Gaia}$	ID$_{\rm Hipparcos}$	ID$_{Tycho2}$	ϖ_{Hip} (mas)	$\sigma\varpi_{Hip}$ (mas)	$\varpi_{\rm TGAS}$ (mas)	$\sigma\varpi_{\rm TGAS}$ (mas)	P (days)	Type	G_{Gaia} (mag)	σ_G (mag)	$\langle V\rangle$ (mag)	$\langle K_{\rm s}\rangle$ (mag)	A$_V$ (mag)	[Fe/H] (dex)
V1645 Sgr	6680420204104678272		7953-1362-1	-	-	0.26	0.42	0.5530	AB	11.328	0.024	11.378	10.258	0.173	−1.74
V1646 Sgr	6796320308904070016		7442-1549-1	-	-	0.23	0.38	0.5445	AB	11.973	0.024	12.083	10.781	0.204	−1.41
V363 Cas	429162271910068352	1222	4014-1751-1	0.55	1.71	0.76	0.23	0.5465	AB	10.165	0.010	10.548	8.283	1.133	−0.72
VW Dor	5283957629860435072	29055	8905-975-1	5.11	2.58	0.73	0.22	0.5706	AB	11.784	0.010	11.770	10.581	0.199	−1.24
VW Scl	4985455994038393088	6094	7534-870-1	1.45	2.11	1.11	0.33	0.5110	AB	11.181	0.014	11.029	10.109	0.048	−1.06
VX Her	4467433013440949376	80853	1510-178-1	−2.55	2.00	0.90	0.24	0.4554	AB	10.840	0.021	10.687	9.576	0.135	−1.52
VX Scl	5011834343140631040	7398	7005-642-1	0.87	2.80	0.70	0.24	0.6371	AB	11.896	0.013	11.999	10.911	0.044	−2.25
VY Lib	6262626676272369280	77663	6186-22-1	1.80	3.05	1.09	0.34	0.5340	AB	11.616	0.010	11.724	10.030	0.588	−1.32
VZ Her	1338388088052805888	84233	2603-1830-1	4.80	1.61	0.81	0.35	0.4404	AB	11.577	0.022	11.479	10.499	0.084	−1.03
VZ Peg	2852346261548304896	116942	2251-527-1	−1.67	2.82	−0.08	0.34	0.3065	C	11.811	0.007	11.869	11.039	0.137	−1.77
W CVn	1483653708889398656	68908	3034-976-1	0.66	1.60	1.28	0.24	0.5518	AB	10.502	0.019	10.548	9.380	0.015	−1.21
W Crt	3546458297076978944	55825	6088-1749-1	−3.59	2.91	0.91	0.28	0.4115	AB	11.567	0.017	11.536	10.533	0.123	−0.5
W Tuc	4709830419187537920	4541	8845-285-1	3.33	1.53	0.72	0.25	0.6423	AB	11.639	0.008	11.433	10.340	0.063	−1.64
WW CrA	6723991376017059200		7911-1078-1	-	-	0.44	0.25	0.5595	AB	11.799	0.021	12.110	10.782	0.325	−1.38
WY Ant	5461994297841116160	50289	6630-1689-1	−0.24	1.61	0.83	0.23	0.5744	AB	10.778	0.013	10.862	9.625	0.223	−1.66
WY Pav	5918501423941085824	87804	8750-727-1	−2.54	4.38	0.42	0.26	0.5886	AB	11.746	0.013	12.141	10.552	0.398	−0.98
WZ Hya	3765574712337027456	50073	5496-429-1	0.62	2.72	0.59	0.34	0.5377	AB	10.834	0.022	10.880	9.613	0.229	−1.39
X Ari	15489404416044288	14601	651-83-1	0.88	1.32	2.02	0.22	0.6512	AB	9.538	0.015	9.551	7.938	0.537	−2.4
X Crt	3587566356779832448	57625	5520-554-1	−1.47	2.80	0.63	0.47	0.7328	AB	11.378	0.013	11.465	10.148	0.083	−1.75
X LMi	803407442699793920		3000-744-1	-	-	−0.84	0.80	0.6844	AB	12.297	0.019	12.355	11.205	0.046	−1.68
X Ret	4672142012446071040		8866-1496-1	-	-	0.44	0.34	0.4921	AB	11.714	0.016	11.728	10.631	0.136	−1.32
XX Pup	5721192378699544960	39849	5996-727-1	−0.74	2.43	0.77	0.26	0.5172	AB	11.399	0.014	11.237	10.084	0.192	−1.42
XZ Aps	5773390387558186624	72721	9436-1635-1	3.43	3.28	0.71	0.30	0.5874	AB	12.297	0.015	12.332	10.919	0.382	−1.57
XZ Cyg	2142052885197472000	96112	3929-1961-1	2.29	0.84	1.56	0.23	0.4667	AB	9.851	0.022	9.697	8.747	0.166	−1.52
XZ Dra	2254366864099297024	94134	4225-305-1	2.26	0.88	1.43	0.21	0.4766	AB	10.249	0.015	10.244	9.155	0.136	−0.87
Y Oct	5764934181067920256		9521-425-1	-	-	0.65	0.32	0.6466	AB	12.115	0.017	12.302	10.909	0.383	−1.52
YY Tuc	6492356127518044800		8837-411-1	-	-	0.47	0.29	0.6350	AB	12.032	0.013	11.993	10.912	0.05	−1.82
YZ Cap	6884361743993904768	105285	6347-974-1	4.11	2.39	0.53	0.29	0.2735	C	11.204	0.017	11.297	10.392	0.192	−1.22
Z CVn	1528760795461189888		3023-942-1	-	-	0.75	0.28	0.6540	AB	11.793	0.011	11.980	10.704	0.043	−1.98
Z Mic	6787617914888746368	105026	7472-67-1	−1.43	2.86	1.05	0.26	0.5870	AB	11.427	0.015	11.612	10.113	0.286	−1.28
AH Cam	468529083148554752		3722-351-1	-	-	1.24	0.24	0.3687	AB	11.684	0.012	-	-	-	-
AO Lep	2985023161440929920		5344-793-1	-	-	0.40	0.37	0.5601	AB	12.216	0.021	-	-	-	-
AQ CrB	1319786344176190208		2040-1369-1	-	-	0.56	0.27	0.6654	AB	12.268	0.014	-	-	-	-
AR Ser	4427066402532783744	76172	354-1216-1	−5.43	4.06	0.67	0.28	0.5751	AB	11.847	0.020	-	-	-	-
AW Mic	6782827480165128448	105249	7481-15-1	0.61	1.05	1.92	0.25	0.4790	C	8.993	0.001	-	-	-	-
BB CMi	3137525080616559488	38361	188-1483-1	−0.26	1.84	2.05	0.27	0.3964	C	10.211	0.011	-	-	-	-
BB Lep	2971190068212939136		5917-198-1	-	-	0.58	0.27	0.5389	AB	12.275	0.020	-	-	-	-
BI Hya	5403461865055509888		7205-1078-1	-	-	0.72	0.30	0.5265	-	11.550	0.013	-	-	-	-
BK Ant	5431789682636192256		7697-594-1	-	-	0.93	0.24	0.5166	AB	11.944	0.008	-	-	-	-
BL Cap	6861426343755648384	102217	6335-1160-1	4.63	0.65	4.22	0.31	-	-	7.261	0.002	-	-	-	-
BN CVn	1543912168771411584		3456-533-1	-	-	0.42	0.24	-	-	12.384	0.006	-	-	-	-
BN CrB	1376147275855922176		2577-679-1	-	-	0.43	0.23	0.5120	AB	13.033	0.021	-	-	-	-
BO Leo	4000636863697454592		1443-1405-1	-	-	1.56	0.59	0.5472	AB	11.684	0.018	-	-	-	-
BQ Pup	5613411823676887424		6542-1690-1	-	-	0.45	0.23	0.6823	AB	11.619	0.012	-	-	-	-
BS Com	1444657948461630080		1997-754-1	-	-	0.57	0.26	0.3635	AB	12.645	0.008	-	-	-	-
BT Ant	5455339812952094848		7185-14-1	-	-	0.99	0.43	0.3304	-	11.786	0.009	-	-	-	-
BW Tri	326383086038685952		2318-978-1	-	-	0.92	0.52	0.2225	C	12.463	0.005	-	-	-	-
BX Dra	1629262755310203776	78891	4192-448-1	4.34	1.15	2.17	0.23	0.5612	-	10.667	0.014	-	-	-	-
CD Ari	115744249026519552		1790-244-1	-	-	0.58	0.29	0.3283	C	11.498	0.009	-	-	-	-
CD Vel	5412243355193801216	47796	8168-1670-1	11.27	3.60	0.81	0.24	0.5735	AB	11.925	0.014	-	-	-	-
CF Leo	3924834676652911872		1441-1539-1	-	-	0.69	0.46	0.7389	AB	12.026	0.010	-	-	-	-
CL Cet	2367323129593788032	2274	5840-121-1	3.91	1.46	3.14	0.25	-	C	9.739	0.003	-	-	-	-
CN Cam	1133454135841004800		4556-251-1	-	-	1.81	0.36	-	AB	9.519	0.008	-	-	-	-
CU Scl	5022005134935583744		7003-434-1	-	-	0.59	0.31	0.3773	C	12.249	0.012	-	-	-	-
CW Cet	2455527636001382144	6501	5276-1411-1	5.27	0.97	5.06	0.77	-	-	8.138	0.002	-	-	-	-
CW Lup	6096455216226834432		7817-118-1	-	-	0.70	0.32	0.3774	-	11.746	0.020	-	-	-	-
CY Dra	2235895000033046912		3946-531-1	-	-	0.78	0.34	-	-	12.681	0.013	-	-	-	-
CZ Lac	2000976541097427200	110213	3619-3987-1	−2.60	12.91	0.85	0.25	0.4322	AB	11.604	0.016	-	-	-	-

Continued in the next page

Name	ID$_{Gaia}$	ID$_{\rm Hipparcos}$	ID$_{Tycho2}$	ϖ_{Hip} (mas)	$\sigma\varpi_{Hip}$ (mas)	$\varpi_{\rm TGAS}$ (mas)	$\sigma\varpi_{\rm TGAS}$ (mas)	P (days)	Type	G_{Gaia} (mag)	σ_G (mag)	$\langle V\rangle$ (mag)	$\langle K_{\rm s}\rangle$ (mag)	A$_V$ (mag)	[Fe/H] (dex)
DE Ind	6458861945318808064		8815-869-1	-	-	0.63	0.36	0.4808	AB	12.645	0.026	-	-	-	-
DE Oct	6363526624969220608	100187	9460-1453-1	4.42	0.99	4.21	0.28	-	C	9.049	0.003	-	-	-	-
DG Boo	1587711214463492736		3482-1589-1	-	-	0.42	0.27	0.4587	AB	12.515	0.022	-	-	-	-
DQ CMi	3141172160686908928		176-2290-1	-	-	0.31	0.35	0.6158	AB	11.951	0.015	-	-	-	-
EP Gru	6501050653153411712		8831-796-1	-	-	0.32	0.27	0.3697	C	12.660	0.009	-	-	-	-
ES Peg	1888524229885625600		2735-326-1	-	-	0.80	0.32	0.5387	AB	12.319	0.017	-	-	-	-
EV Psc	2642479659656205952		587-376-1	-	-	1.26	0.39	0.3063	C	10.469	0.011	-	-	-	-
EW Cam	1111846052295620864	36213	4368-739-1	2.13	1.10	1.69	0.23	-	AB	9.367	0.011	-	-	-	-
EX UMa	1031239720991986560		3801-1644-1	-	-	1.25	0.30	-	AB	10.982	0.014	-	-	-	-
FO CVn	1501038293393870720		3029-738-1	-	-	3.15	0.25	0.2845	C	10.774	0.003	-	-	-	-
FT UMa	1016919337954459392	43738	3423-1606-1	6.88	1.28	4.36	0.27	-	C	9.164	0.004	-	-	-	-
GN Cnc	636073901939515264	45483	1408-3-1	5.35	0.93	4.55	0.27	-	-	8.643	0.003	-	-	-	-
HI Dra	2157403476266324096	90972	3917-2301-1	3.92	0.68	3.44	0.23	-	C	8.986	0.005	-	-	-	-
HL Cet	2491648104802033920		4688-1104-1	-	-	0.63	0.33	0.3015	C	11.903	0.010	-	-	-	-
HN Cet	23769173650192512		631-147-1	-	-	0.11	0.31	0.4627	AB	12.585	0.028	-	-	-	-
HN Dra	2154012616765216896	91983	3926-291-1	5.33	0.53	3.88	0.23	-	-	8.030	0.003	-	-	-	-
HU Cas	413542059967823744		3677-1213-1	-	-	0.64	0.23	0.4116	AB	12.335	0.020	-	-	-	-
HV UMa	774558834567373184	58157	3452-457-1	5.18	1.01	4.01	0.32	-	C	8.624	0.008	-	-	-	-
HW Lib	6338829085548027648	73465	5008-210-1	2.09	1.22	4.99	0.28	-	-	8.858	0.003	-	-	-	-
HY Com	3946316419440162432	59995	1445-215-1	1.61	1.80	0.81	0.56	-	C	10.328	0.018	-	-	-	-
IN Lib	6319127142848360832	74825	5585-789-1	13.89	0.53	13.13	0.44	-	-	7.216	0.003	-	-	-	-
IU Pup	5539433039226900352		7668-2873-1	-	-	0.93	0.33	-	-	9.841	0.003	-	-	-	-
IV Pav	6373510637226413952	101545	9316-114-1	0.60	1.98	3.35	0.23	-	-	10.616	0.009	-	-	-	-
IW Lib	6234240515858059008	76694	6785-269-1	1.81	1.66	3.34	0.25	-	-	9.137	0.003	-	-	-	-
KN Per	236411320847848320	15726	2869-2543-1	5.35	4.26	1.24	0.23	0.4332	C	11.419	0.016	-	-	-	-
KT UMa	856816804134137344		3827-104-1	-	-	0.51	0.42	-	AB	11.251	0.010	-	-	-	-
KV Cnc	703542443680915328		1948-1733-1	-	-	1.22	0.70	0.5020	AB	12.453	0.016	-	-	-	-
KZ Pup	5717854261396705920	38441	5986-18-1	1.81	3.30	0.25	0.23	-	-	12.023	0.023	-	-	-	-
LP Cam	476292459874275840		4068-447-1	-	-	1.32	0.35	-	AB	11.148	0.011	-	-	-	-
LS Her	1199539148357125248	78539	1507-924-1	6.17	2.54	0.50	0.28	0.2308	C	10.866	0.011	-	-	-	-
MO UMa	765390900456068992		3010-1290-1	-	-	0.85	0.73	0.3180	C	11.461	0.018	-	-	-	-
MU UMa	766938634870850432		3013-1988-1	-	-	0.28	0.91	0.2679	C	11.701	0.018	-	-	-	-
MU Vul	1833093725559996288		2141-2569-1	-	-	1.09	0.35	0.5000	-	12.2696	0.0003	-	-	-	-
NO Cas	428893303878673408		4015-1454-1	-	-	0.43	0.31	0.7195	AB	10.893	0.007	-	-	-	-
NS UMa	1093345635287502208		4133-560-1	-	-	0.84	0.25	0.5991	AB	11.063	0.009	-	-	-	-
OP Pup	3027132189042054400		5984-2147-1	-	-	0.27	0.25	-	-	10.727	0.010	-	-	-	-
OQ Vel	5318418935624519040	43071	8569-825-1	5.25	0.51	4.51	0.27	-	C	7.673	0.001	-	-	-	-
OW Dra	1686384274158206208		4404-1105-1	-	-	0.77	0.32	0.3330	C	10.215	0.010	-	-	-	-
OW UMa	1026974887186753408		3419-959-1	-	-	0.23	0.36	0.3113	C	12.084	0.014	-	-	-	-
OZ UMa	1036978862451366272		3801-1162-1	-	-	1.28	0.29	0.3453	C	11.268	0.009	-	-	-	-
QW UMa	1063808835955123456		4139-289-1	-	-	0.98	0.28	0.2985	C	10.871	0.011	-	-	-	-
QY UMa	827975308467743488		3439-1005-1	-	-	0.33	0.27	0.5721	AB	12.972	0.014	-	-	-	-
RV Men	5265153816361777920		9176-1136-1	-	-	4.45	0.90	0.5423	AB	11.346	0.018	-	-	-	-
ST Pic	5481339586456220800	29583	8893-454-1	1.46	0.83	2.12	0.30	0.4857	-	9.407	0.010	-	-	-	-
SU Col	4825302298567969280	23868	7050-299-1	4.11	4.55	0.43	0.30	-	AB	12.478	0.022	-	-	-	-
SX Hyi	4633341277893887360		9353-88-1	-	-	0.05	0.67	0.3107	-	12.561	0.015	-	-	-	-
TV Lyn	975895390891334656	36750	3409-1947-1	0.15	2.84	1.06	0.29	0.2407	C	11.408	0.014	-	-	-	-
TX Scl	2334529748619150592		6985-559-1	-	-	0.72	0.47	0.7278	-	12.337	0.013	-	-	-	-
UU Cam	550622641368680064		4339-474-1	-	-	1.49	0.22	0.3413	C	11.540	0.011	-	-	-	-
UV Mon	3113029267219306624		162-3042-1	-	-	1.92	0.34	0.4157	-	12.527	0.016	-	-	-	-
UY Scl	4998159957544145408	1182	7524-154-1	7.29	3.45	5.52	0.23	-	C	11.585	0.025	-	-	-	-
UZ Eri	5155339748939697664		5300-438-1	-	-	0.33	0.24	0.6486	-	12.865	0.021	-	-	-	-
V0350 Mus	5791008171609343360		9254-1886-1	-	-	5.68	0.36	0.3691	C	8.115	0.006	-	-	-	-
V0351 Peg	2814517254757092224	115627	1713-1187-1	6.67	0.71	6.28	0.31		C	7.958	0.011	-	-	-	-
V0363 Aps	5818849592729664896		9277-2756-1	-	-	0.61	0.29	0.7286	AB	11.607	0.012	-	-	-	-
V0372 Lyr	2102256645943577344		3129-1562-1	-	-	3.22	0.29	-	-	11.8977	0.0007	-	-	-	-
V0372 Ser	4415594270007206016		5002-629-1	-	-	0.86	0.29	-	D?	11.225	0.013	-	-	-	-

Continued in the next page

Name	ID_{Gaia}	$ID_{Hipparcos}$	ID_{Tycho2}	ϖ_{Hip} (mas)	$\sigma\varpi_{Hip}$ (mas)	ϖ_{TGAS} (mas)	$\sigma\varpi_{TGAS}$ (mas)	P (days)	Type	G_{Gaia} (mag)	σ_G (mag)	$\langle V \rangle$ (mag)	$\langle K_s \rangle$ (mag)	A_V (mag)	[Fe/H] (dex)
V0381 Tel	6666950671268333440		8403-647-1	-	-	0.12	0.28	0.3478	D?	12.640	0.012	-	-	-	-
V0387 Dra	1367619154434071552		3523-274-1	-	-	0.43	0.49	0.5459	AB	11.983	0.020	-	-	-	-
V0388 Vir	3700131608452399360		282-743-1	-	-	2.20	0.82	0.5430	AB	12.582	0.019	-	-	-	-
V0391 Mon	3058799154715133952		4824-1986-1	-	-	1.75	0.57	0.4643	AB	11.9311	0.0006	-	-	-	-
V0394 Dra	2152712238106970240		4201-1737-1	-	-	0.84	0.62	0.5785	AB	12.046	0.017	-	-	-	-
V0414 Dra	2253188840469314816		4224-890-1	-	-	1.28	0.31	0.3481	C	11.198	0.005	-	-	-	-
V0417 Dra	2131968508140833920		3545-35-1	-	-	0.44	0.28	0.6132	AB	11.706	0.014	-	-	-	-
V0420 Dra	2254703039779410432		4225-125-1	-	-	1.09	0.45	0.3296	C	12.330	0.007	-	-	-	-
V0429 Ori	3224778097149020800	22943	4741-1272-1	−0.03	1.98	0.69	0.23	0.5017	AB	9.810	0.001	-	-	-	-
V0447 Dra	2298500504923153408		4597-1249-1	-	-	0.73	0.29	0.3283	C	11.554	0.010	-	-	-	-
V0456 Ser	4403909038384950656		5017-674-1	-	-	0.42	0.93	0.5176	AB	12.594	0.016	-	-	-	-
V0459 Nor	5834468533360206848		8722-769-1	-	-	0.85	0.24	0.3754	C	11.658	0.011	-	-	-	-
V0468 Hya	3089817958282262656		195-658-1	-	-	0.73	0.71	0.4677	C	11.301	0.021	-	-	-	-
V0476 Vir	3631923988738868096		4965-617-1	-	-	0.28	0.47	0.5763	AB	11.594	0.025	-	-	-	-
V0487 Sco	4053550654626346496		7384-434-1	-	-	1.97	0.38	0.3291	C	11.137	0.022	-	-	-	-
V0491 Cam	1142428762063953024		4539-694-1	-	-	0.78	0.27	0.3928	C	11.593	0.004	-	-	-	-
V0507 Vul	1842509530824560128		2171-89-1	-	-	0.53	0.81	0.3361	C	11.635	0.016	-	-	-	-
V0516 And	363101689164595584		2285-18-1	-	-	0.49	0.50	0.4287	C	11.482	0.014	-	-	-	-
V0535 Mon	3114440833992409216		163-1482-1	-	-	0.87	0.30	0.3329	C	11.587	0.010	-	-	-	-
V0542 Ser	4476806350068793344		445-1218-1	-	-	0.38	0.28	0.2854	C	12.506	0.005	-	-	-	-
V0556 Hya	6190268571961010944		6722-1540-1	-	-	0.47	0.27	0.5961	AB	11.525	0.015	-	-	-	-
V0559 Hya	6276259520943508608		6730-109-1	-	-	0.62	0.35	0.4479	AB	12.474	0.018	-	-	-	-
V0568 Cas	535903101250396928		4309-238-1	-	-	1.48	0.50	0.6230	-	12.417	0.022	-	-	-	-
V0590 Cen	5397395618886854912		7213-1978-1	-	-	0.90	0.32	-	-	12.080	0.019	-	-	-	-
V0595 Cen	5398731869112363520		7214-1559-1	-	-	0.72	0.33	-	-	12.206	0.012	-	-	-	-
V0600 Sco	5973272908473041024		7869-2268-1	-	-	1.15	0.87	0.4553	AB	12.106	0.022	-	-	-	-
V0618 Peg	2765589159119818880		1174-352-1	-	-	1.23	0.41	0.5624	AB	11.991	0.016	-	-	-	-
V0653 Aur	896914447011316096		2460-101-1	-	-	0.59	0.27	0.5793	AB	12.512	0.027	-	-	-	-
V0660 And	1937447240281971840		3242-507-1	-	-	1.48	0.35	0.3854	C	11.958	0.003	-	-	-	-
V0672 Aql	4298086473054704896		1057-1390-1	-	-	0.71	0.35	0.5298	AB	11.932	0.014	-	-	-	-
V0680 Ara	5830535648986454912		9038-1209-1	-	-	0.96	0.27	0.3038	C	11.841	0.006	-	-	-	-
V0680 Mon	3157882744563883264		748-218-1	-	-	2.51	0.85	-	-	10.032	0.011	-	-	-	-
V0701 Pup	5696434675375951232		6556-609-1	-	-	0.47	0.36	0.2857	C	10.505	0.009	-	-	-	-
V0713 And	2874897657350964608		2772-1010-1	-	-	1.52	0.46	0.3185	C	11.904	0.004	-	-	-	-
V0753 Cen	5343850742643949824	57812	8635-711-1	1.86	1.94	1.59	0.23	0.2213	C	10.395	0.009	-	-	-	-
V0764 Mon	3054054555882018688	37126	5397-921-1	4.21	0.61	3.91	0.66	-	C	7.0287	0.0006	-	-	-	-
V0795 Cep	573712179393014272		4619-1292-1	-	-	1.81	0.41	0.3670	C	11.305	0.007	-	-	-	-
V0819 Cen	6062302426560552192		8661-387-1	-	-	2.87	0.33	0.6755	-	8.949	0.003	-	-	-	-
V0893 Her	1385661075093558528	80020	3492-1292-1	2.75	0.72	2.59	0.22	-	-	9.115	0.004	-	-	-	-
V0924 Mon	3158082031047116288		752-542-1	-	-	0.21	0.35	0.7124	AB	11.856	0.008	-	-	-	-
V1022 Cen	6004817416038315520	73595	7829-2386-1	3.21	0.96	3.71	0.27	-	-	8.120	0.002	-	-	-	-
V1035 Cas	391221046211708160		3256-1394-1	-	-	0.94	0.69	0.3920	C	12.052	0.013	-	-	-	-
V1047 Cas	417906777531618432		3655-151-1	0.00	-0.0	−0.08	0.73	0.3344	C	11.032	0.017	-	-	-	-
V1057 Cas	524535422331664640		4025-131-1	-	-	2.20	0.31	0.4233	C	10.032	0.006	-	-	-	-
V1059 Cas	538832097147911296		4308-485-1	-	-	1.12	0.25	0.6497	AB	10.218	0.007	-	-	-	-
V1141 Her	1384578159218816256		3060-1159-1	-	-	0.75	0.24	0.3172	C	11.137	0.008	-	-	-	-
V1176 Sgr	4090995244663875840		6278-1906-1	-	-	1.21	0.25	0.3548	AB	11.477	0.021	-	-	-	-
V1195 Her	1411345391840760320		3502-2020-1	-	-	0.52	0.25	0.6097	AB	11.738	0.010	-	-	-	-
V1203 Her	1411773514180605056		3505-602-1	-	-	0.52	0.34	0.3179	C	12.406	0.009	-	-	-	-
V1283 Her	1342550323680165888		3087-2079-1	-	-	1.04	0.31	0.2727	C	10.370	0.014	-	-	-	-
V1305 Her	4581071766422018176		2094-1921-1	-	-	0.60	0.25	0.2914	C	12.350	0.009	-	-	-	-
V1319 Sco	6246499211515591808		6199-755-1	-	-	1.18	0.26	0.2541	C	11.433	0.009	-	-	-	-
V1330 Her	4606912282538897280		2634-1102-1	-	-	0.60	0.27	0.2703	C	11.875	0.012	-	-	-	-
V1344 Cen	5891984983039411712		8686-406-1	-	-	1.19	0.27	0.4183	AB	11.629	0.019	-	-	-	-
V1345 Cen	5891108156878546816		8690-2031-1	-	-	0.56	0.25	0.6313	AB	11.170	0.008	-	-	-	-
V1348 Her	4528944298105649024		1581-1784-1	-	-	0.71	0.35	0.5911	AB	11.808	0.014	-	-	-	-
V1464 Aql	4195401467225441152	97600	5725-2399-1	5.24	1.13	4.12	0.48	-	C	8.574	0.003	-	-	-	-

Continued in the next page

Name	ID$_{Gaia}$	ID$_{\rm Hipparcos}$	ID$_{Tycho2}$	ϖ_{Hip} (mas)	$\sigma\varpi_{Hip}$ (mas)	$\varpi_{\rm TGAS}$ (mas)	$\sigma\varpi_{\rm TGAS}$ (mas)	P (days)	Type	G_{Gaia} (mag)	σ_G (mag)	$\langle V\rangle$ (mag)	$\langle K_{\rm s}\rangle$ (mag)	A$_V$ (mag)	[Fe/H] (dex)
V1719 Cyg	2169337231878673664	104029	3600-2-1	3.79	0.58	2.54	0.23	0.2673	C	7.919	0.008	-	-	-	-
V1815 Cyg	1976149602904391680		3609-2052-1	-	-	2.59	0.37	-	C	11.157	0.010	-	-	-	-
V1821 Aql	4299563701280764800		1076-281-1	-	-	1.46	0.60	0.3297	C	11.713	0.009	-	-	-	-
V1823 Cyg	2055744074276141184		2679-1740-1	-	-	1.06	0.27	-	AB	12.038	0.018	-	-	-	-
V1829 Aql	4228943684336361344		5163-1582-1	-	-	1.20	0.82	0.7248	AB	11.503	0.019	-	-	-	-
V1962 Cyg	1966406143173474688		3187-1992-1	-	-	0.69	0.34	-	AB	9.004	0.001	-	-	-	-
V2232 Sgr	6673750910168700800	99126	7959-1377-1	13.52	12.20	0.26	0.33	-	-	13.267	0.021	-	-	-	-
V2369 Cyg	2052128914398060672		3135-673-1	-	-	0.95	0.41	0.2972	C	10.786	0.010	-	-	-	-
V2709 Oph	4113122950532563840		6811-414-1	-	-	1.01	0.24	0.4614	AB	11.542	0.016	-	-	-	-
V2725 Oph	4387211133249913088		401-204-1	-	-	0.74	0.35	0.7377	AB	11.953	0.011	-	-	-	-
V4424 Sgr	6750122644237157248	97923	7439-1920-1	0.92	1.94	1.66	0.25	-	AB	10.135	0.010	-	-	-	-
VY Dor	4777034665821217408		8510-1671-1	-	-	1.36	0.58	-	-	12.250	0.021	-	-	-	-
VY Nor	5930524652301541120	80931	8712-3621-1	−7.08	10.38	0.27	0.24	0.3753	AB	12.955	0.021	-	-	-	-
VZ Dra	1623839242406860672	80102	3884-1671-1	0.54	2.88	0.17	0.48	0.3210	C	12.704	0.016	-	-	-	-
XX Boo	1282118725076064640		2022-180-1	-	-	0.41	0.35	0.5814	AB	11.815	0.011	-	-	-	-
XX Dor	4655250352747062784		9165-722-1	-	-	0.18	0.32	0.3289	C	11.300	0.010	-	-	-	-
XY UMi	1699041955096306560		4406-241-1	-	-	0.68	0.29	0.6525	AB	13.093	0.017	-	-	-	-
XZ Cet	5141890213471060480	9361	5856-1883-1	2.73	1.46	0.85	0.31	0.8231	AB	9.205	0.009	-	-	-	-
XZ Gru	6547228904569342208	112532	8004-149-1	1.89	1.94	1.01	0.25	0.3474	C	10.485	0.015	-	-	-	-
XZ UMi	1701333887084708352		4416-214-1	-	-	1.02	0.26	0.5851	AB	11.832	0.016	-	-	-	-
YZ PsA	6811546930041062912		6944-710-1	-	-	0.69	0.77	0.3169	C	11.538	0.015	-	-	-	-
Z For	5075767886279322112		6440-701-1	-	-	0.21	0.24	0.3704	-	12.638	0.016	-	-	-	-

TABLE A.4: RRL $M_V - [\mathrm{Fe/H}]$, $M_G - [\mathrm{Fe/H}]$ and PMZ relations based on *Gaia* DR2 parallaxes: (1) relation; (2) number of RRLs used in the fit; (3) mathematical form; (4) intrinsic dispersion; (5) parallax zero-point offset; (6) absolute magnitude in the corresponding passband; (7) distance modulus of the LMC.

Relation	No. stars	Mathematical form	w (mag)	$\Delta\varpi_0$ (mas)	M* (mag)	$\mu_{\rm LMC}$ (mag)
Standard bands						
Lin. $M_V - [\mathrm{Fe/H}]$	381	$M_V = \left(0.34^{+0.03}_{-0.03}\right)[\mathrm{Fe/H}] + \left(1.17^{+0.04}_{-0.04}\right)$	$0.14^{+0.01}_{-0.01}$	$-0.062^{+0.006}_{-0.006}$	0.66 ± 0.06	18.50 ± 0.16
Quad. $M_V - [\mathrm{Fe/H}]$	381	$M_V = \left(0.02^{+0.04}_{+0.04}\right)[\mathrm{Fe/H}]^2 + \left(0.39^{+0.10}_{-0.09}\right)[\mathrm{Fe/H}] + \left(1.19^{+0.06}_{-0.06}\right)$	$0.14^{+0.01}_{-0.01}$	$-0.062^{+0.006}_{-0.006}$	0.65 ± 0.18	18.50 ± 0.15
$PM_{K_s}Z$	400	$M_{K_s} = \left(-2.58^{+0.20}_{-0.20}\right)\log(P) + \left(0.17^{+0.03}_{-0.03}\right)[\mathrm{Fe/H}] + \left(-0.84^{+0.09}_{-0.09}\right)$	$0.16^{+0.01}_{-0.01}$	$-0.054^{+0.005}_{-0.006}$	-0.37 ± 0.11	18.55 ± 0.11
$PM_{W1}Z$	397	$M_{W1} = \left(-2.56^{+0.19}_{-0.19}\right)\log(P) + \left(0.17^{+0.03}_{-0.03}\right)[\mathrm{Fe/H}] + \left(-0.87^{+0.09}_{-0.09}\right)$	$0.14^{+0.01}_{-0.01}$	$-0.056^{+0.006}_{-0.006}$	-0.41 ± 0.11	–
Lin. $M_V - [\mathrm{Fe/H}]$	23	$M_V = \left(0.25^{+0.05}_{-0.05}\right)[\mathrm{Fe/H}] + \left(1.18^{+0.12}_{-0.12}\right)$	$0.13^{+0.04}_{-0.03}$	$-0.142^{+0.058}_{-0.064}$	0.80 ± 0.14	18.34 ± 0.16
Quad. $M_V - [\mathrm{Fe/H}]$	23	$M_V = \left(0.07^{+0.07}_{-0.08}\right)[\mathrm{Fe/H}]^2 + \left(0.41^{+0.18}_{-0.18}\right)[\mathrm{Fe/H}] + \left(1.21^{+0.13}_{-0.13}\right)$	$0.13^{+0.04}_{-0.03}$	$-0.127^{+0.060}_{-0.066}$	0.75 ± 0.35	18.39 ± 0.15
$PM_{K_s}Z$	23	$M_{K_s} = \left(-2.65^{+0.63}_{-0.61}\right)\log(P) + \left(0.11^{+0.07}_{-0.07}\right)[\mathrm{Fe/H}] + \left(-0.81^{+0.26}_{-0.24}\right)$	$0.12^{+0.04}_{-0.03}$	$-0.135^{+0.053}_{-0.063}$	-0.23 ± 0.33	18.40 ± 0.10
$PM_{W1}Z$	23	$M_{W1} = \left(-2.72^{+0.61}_{-0.58}\right)\log(P) + \left(0.12^{+0.07}_{-0.06}\right)[\mathrm{Fe/H}] + \left(-0.87^{+0.25}_{-0.23}\right)$	$0.11^{+0.04}_{-0.03}$	$-0.141^{+0.053}_{-0.062}$	-0.29 ± 0.32	–
Lin. $M_V - [\mathrm{Fe/H}]$	23	$M_V = \left(0.26^{+0.05}_{-0.05}\right)[\mathrm{Fe/H}] + \left(1.04^{+0.07}_{-0.07}\right)$	$0.13^{+0.04}_{-0.03}$	-0.057	0.65 ± 0.10	18.49 ± 0.15
Quad. $M_V - [\mathrm{Fe/H}]$	23	$M_V = \left(0.09^{+0.07}_{+0.07}\right)[\mathrm{Fe/H}]^2 + \left(0.47^{+0.17}_{-0.16}\right)[\mathrm{Fe/H}] + \left(1.11^{+0.09}_{-0.09}\right)$	$0.12^{+0.04}_{-0.03}$	-0.057	0.61 ± 0.31	18.53 ± 0.14
$PM_{K_s}Z$	23	$M_{K_s} = \left(-2.49^{+0.61}_{-0.64}\right)\log(P) + \left(0.14^{+0.07}_{-0.07}\right)[\mathrm{Fe/H}] + \left(-0.88^{+0.25}_{-0.26}\right)$	$0.12^{+0.04}_{-0.03}$	-0.057	-0.39 ± 0.33	18.55 ± 0.10
$PM_{W1}Z$	23	$M_{W1} = \left(-2.54^{+0.60}_{-0.58}\right)\log(P) + \left(0.15^{+0.06}_{-0.06}\right)[\mathrm{Fe/H}] + \left(-0.94^{+0.24}_{-0.24}\right)$	$0.11^{+0.04}_{-0.03}$	-0.057	-0.45 ± 0.31	
Gaia bands						
$M_G - [\mathrm{Fe/H}]$	160	$M_G = \left(0.32^{+0.04}_{-0.04}\right)[\mathrm{Fe/H}] + \left(1.11^{+0.06}_{-0.06}\right)$	$0.17^{+0.02}_{-0.02}$	-0.057	0.63 ± 0.08	–

* Absolute magnitudes of RRLs in different passbands calculated adopting the metallicity [Fe/H]=−1.5 dex and period P=0.5238 days.

Appendix B

Additional figures

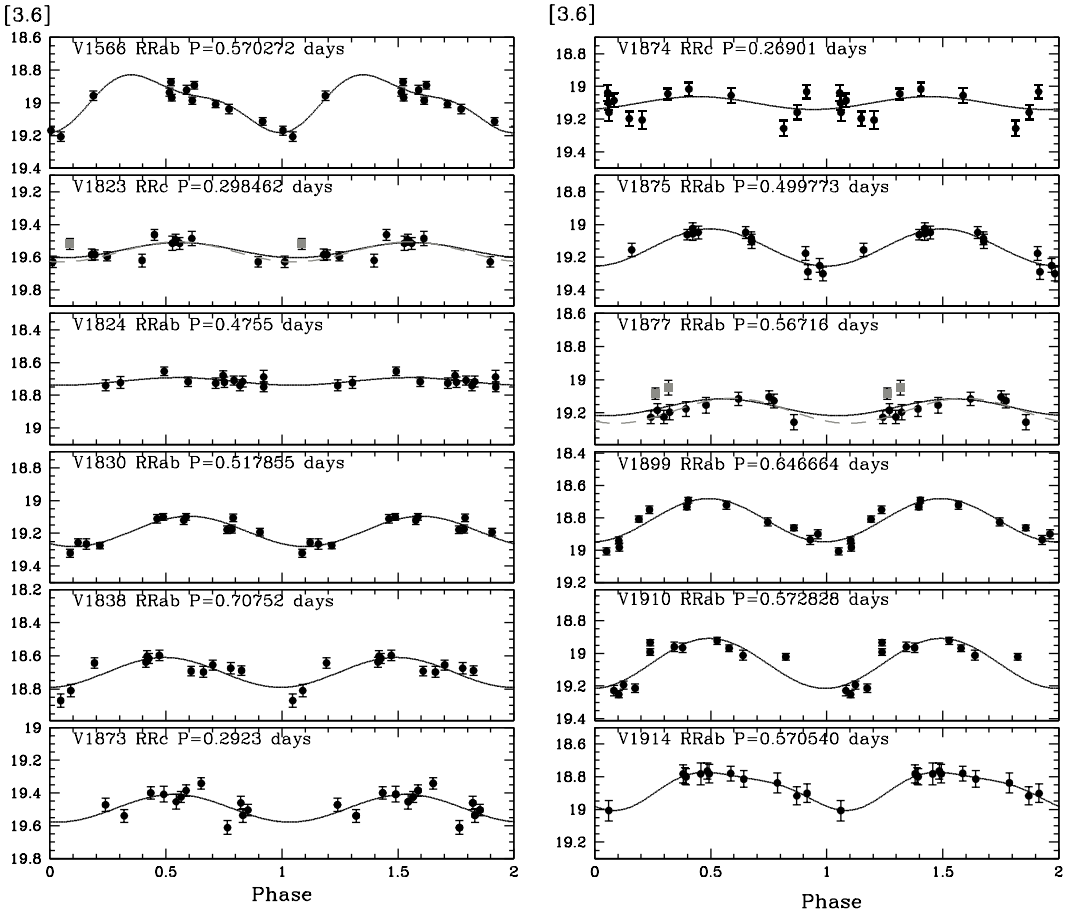

FIGURE B.1: Light curves at 3.6 μm for our sample of 49 RRLs in Sculptor. Stars are ordered with increasing ID number adopting the nomenclature from K95 and C05. This figure is the continuation of Fig. 4.9 in the main text. The solid black lines represent the light curve models generated by GRATIS using all phase-points while the grey dashed lines are the light curve models discarding points marked by grey filled squares. V1824 and V1874 are problematic stars not used to fit the *PL* relations (see Sect. 4.1.3.4 and Table 4.4). Figure from Garofalo et al. (2018).

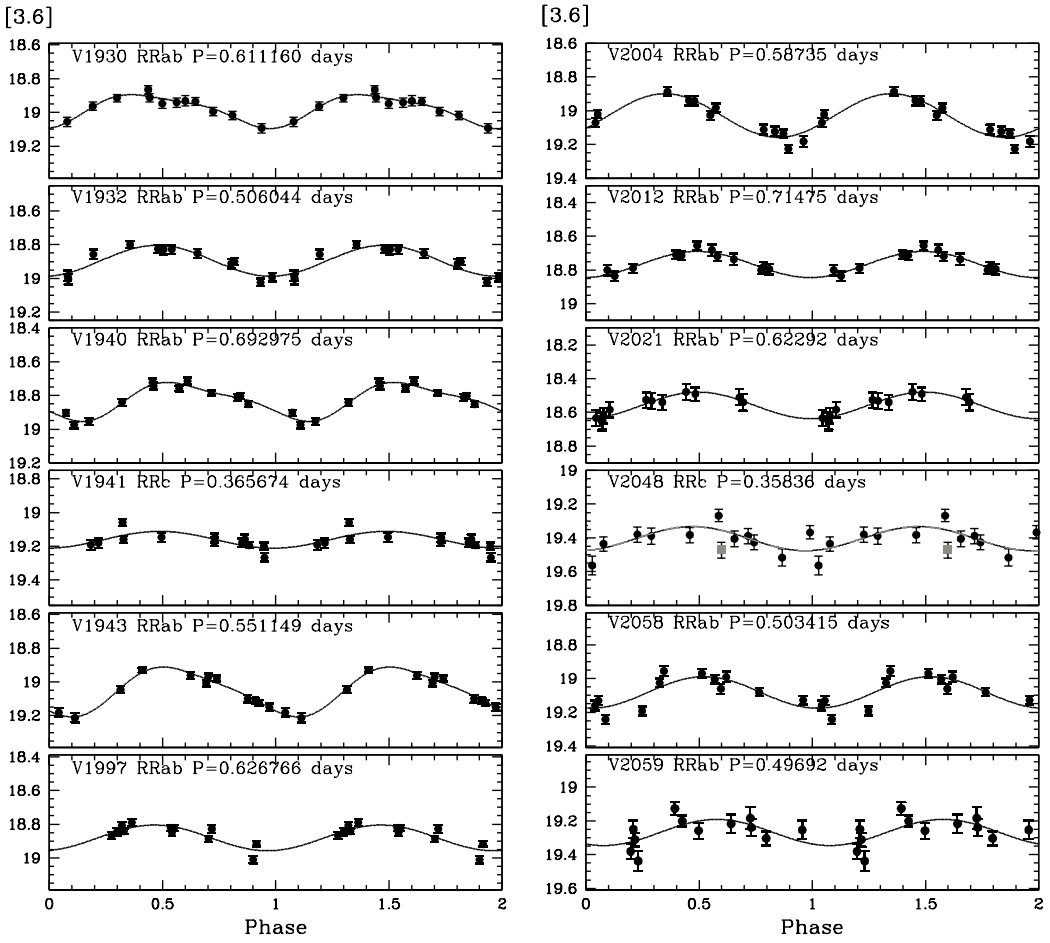

(Continued).V2021 is a problematic star not used to fit the PL relations (see Sect. 4.1.3.4 and Table 4.4). Figure from Garofalo et al. (2018).

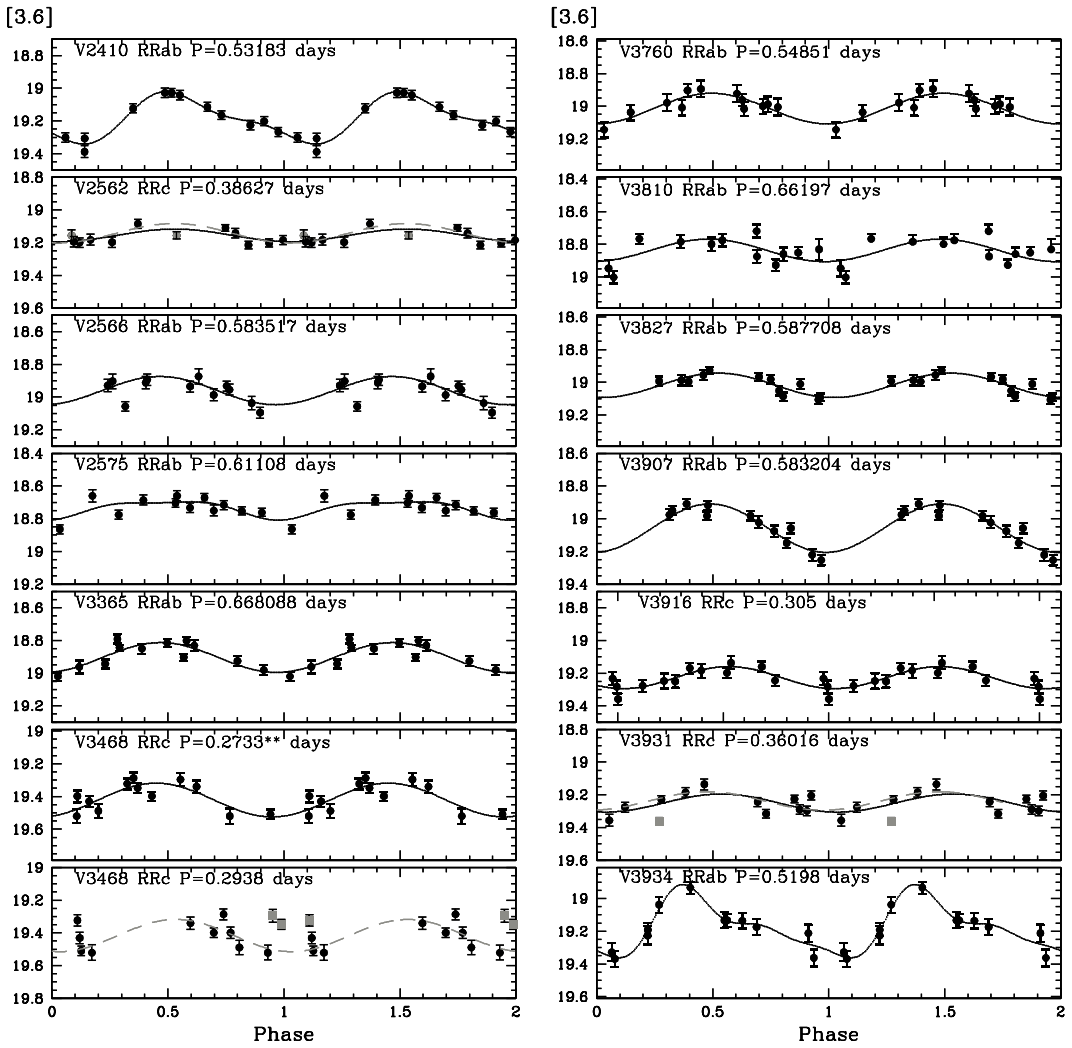

(Continued). Both the period derived from the analysis of our data with GRATIS and the original period from K95 were used to fold the light curve of V3468 in the bottom-left two panels (see Sect. 4.1.3.4 for details). Figure from Garofalo et al. (2018).

Appendix C

Pulsating variable stars of other types

C.1 Classical Cepheids

Classical Cepheids (CCs) are perhaps the best known type of pulsating variable stars, with pulsation periods typically in the range from below 1 to 100 d[1] and large amplitudes (from 0.5 up to 2 mag). They are bright ($-2 \leqslant M_V \leqslant -7$) and numerous (in the *Gaia* DR2 catalogue there are about 9,000 candidate CCs of which about 7,000 are in the MCs Clementini et al. 2018). The CCs are young objects (ages $\leqslant$ 50-200 Myr), tracers of the young stellar populations in the systems where they reside, mainly, the MW disk, open clusters and young stellar associations. After Henrietta Leavitt in 1914 discovered the relation existing between their pulsation period and the luminosity, the characteristic PL relation or Leavitt-Law, as it was recently re-named to honour its discoverer, the CCs have become backbones of the extragalactic distance ladder (Freedman et al. 2001; Saha et al. 2006) and primary tools for the calibration of secondary distance indicators allowing to measure the Hubble constant (H_0) with a few % uncertainty (see, e.g. Riess et al. 2016 and references therein). CCs are intermediate-mass giant stars (masses between 3.5 and 15 $M_\odot$), going through the stage of helium-burning. They ignite helium (He) in a non electron-degenerate He-core but develop an electron

[1]CCs pulsating in the first overtone mode can have periods shorter than 1 d. Recently, a few CCs with periods exceeding 100 d, hence named ultra-long period (ULP) Cepheids, have been detected in star forming galaxies (Bird et al. 2009).

degenerate carbon-oxygen core at the end of central Helium-burning. The evolutionary track of intermediate-mass stars can cross the classical IS up to three times (see fig.4.4 in Catelan & Smith 2015). A CC behaviour can be observed only for those stars that experience a blue-loop phase extended enough to cross the IS. Since the theory of stellar evolution predicts a mass-luminosity (ML) relation for intermediate mass stars during the central helium-burning phase, for each fixed chemical composition, the Cepheid luminosity is expected to be a function of period and effective temperature that, in the observational plane, translates into a Period-Luminosity-Colour (PLC) relation. The PL relation is the projection of the PLC relation onto the PL plane. The PL relation is a statistical relation with an intrinsic dispersion due to the finite width of the instability strip. The dispersion of the PL relation is particularly significant at optical passbands where it is on the order of ~ 0.25 mag, but decreases steadily moving towards longer wavelengths to less than ~ 0.1 mag in the NIR and MIR passbands. One of the main open problems concerning the use of the CC PL and (PLC) relations for extragalactic distance determinations is the dependence of these relations on chemical composition. The extragalactic distance scale is traditionally anchored on CCs in the LMC or, more recently, on CCs in NGC4258 (Riess et al. 2011), hence, when applied to galaxies with different chemical composition this may introduce a systematic error that may bias the calibration of secondary distance indicators and the estimate of the H_0, in turn. So far, no general consensus has been reached yet on the metallicity dependence of the CC pulsation properties, as observational tests (Groenewegen 2013 and references therein) and non linear convective hydrodynamical models (Marconi et al. 2005 and references therein) suggest opposite behaviours.

A further open issue is the linearity of the CC PL relations. Some authors find evidence for a non linearity in the form of a break around 10 days, with a clear corresponding change of the PL slope in B, V, R and I (see e.g. Ngeow & Kanbur 2006; Tammann et al. 2003). Both the metallicity dependence, the linearity effect, as well as the effect of the finite intrinsic width of the instability strip, decrease when moving from optical to NIR and MIR bands (see e.g. Madore & Freedman 1991; Caputo et al. 2000; Marconi et al. 2005; Ngeow et al. 2012; Ripepi et al. 2012; Inno et al. 2013 and references therein). The reddening-free formulation of the PL relation is called Period-Wesenheit (PW) relation and it is based on the Wesenheit function[2] (Madore 1982; Caputo et al. 2000;

[2] A linearly independent combination of colours and magnitudes that it is itself independent of reddening

Ripepi et al. 2012). The PW relations include a colour term, the so-called Wesenheit index, that takes into account and partially corrects for the finite colour width of the instability strip (thus reducing the associated uncertainty on distance determinations) with a coefficient corresponding to the ratio between total to selective extinction in the filter pair used for the observations. The Wesenheit relation in the V, I bands $PW(V, I)$ is often adopted to derive precise extragalactic distances as it is widely recognized to be little dependent on metallicity (see e.g. Bono et al. 2010 and references therein). Other filter combinations, extending to the NIR, are also commonly used in the literature (see Riess et al. 2011, 2016; Fiorentino et al. 2013; Ripepi et al. 2012, 2016). Figure C.1 shows the $PW(V, I)$ relations for classical, Type-II (Sect. C.2) and anomalous Cepheids (Sect. C.3) in the LMC, from Soszyński et al. (2008).

C.2 Type II Cepheids

Like RRLs, the Type II Cepheids (T2Cs) are Population II pulsating variable stars. They are usually divided in three subclasses of different evolutionary stage: BL Herculis (BL Her) with periods between 1 and 4 d, W Virginis (W Vir) with periods from 4 to 20 d and RV Tauri (RV Tau) with periods from 20 to 150 d. The shape of the BL Her and W Vir light curves can range from almost sinusoidal to highly non-sinusoidal, whereas the RV Tau stars can show light curves with alternating minima. The BL Her stars are low-mass stars (0.5-0.6 $M_{\odot}$) that start the central He burning on the blue side of the RRL IS, and cross the IS at about 0.5-1.5 mag brighter than the RRLs (hence the longer periods). The W Vir variables, instead, cross the IS during their blue-loop excursions from the asymptotic giant branch (AGB) during helium-shell flashes. They are ∼2-4 mag brighter than the RRLs. Both the BL Her and the W Vir stars are thought to pulsate in the fundamental radial mode (see, e.g., Lemasle et al. 2015, and references therein). The RV Tau variables are post AGB stars that cross the IS at high luminosity during their evolution toward the white dwarf cooling sequence. Since the RV Tau stars have a different evolutionary history, it is not clear whether it is appropriate to include them in the same class as BL Her and W Vir stars (Wallerstein 2002). In addition to the three types described above, Soszyński et al. (2008) suggested the existence of the so-called peculiar W Vir (pW Vir) stars, which exhibit peculiar light curves and, at constant period, are generally brighter than normal T2Cs. Although their true nature

remains uncertain, likely the pW Vir stars are part of binary systems. It has been known since a long time that T2Cs follow their own PL relations, which differs from the CC PL relations, being T2Cs older and having lower masses than CCs. Nemec et al. (1994) first derived the T2C PL relation in optical bands. Kubiak & Udalski (2003) then found that T2Cs with periods from 0.7 to 10 d in the OGLE II (Udalski et al., 1992) sample follow the same PL relation as later confirmed by Pritzl et al. (2003) and Matsunaga et al. (2006) for T2Cs in GGCs, by Groenewegen et al. (2008) for T2Cs in the Galactic bulge, and by Soszyński et al. (2008) for the LMC sample, using OGLE III data (see Fig. C.1). Matsunaga et al. (2011), using single-epoch data, showed that T2Cs follow quite tight PL relations in the $J, H, K_{\rm s}$ passbands. This result has been confirmed by Ripepi et al. (2015) on the basis of multi-epoch $J, K_{\rm s}$ photometry for 130 T2Cs observed in the LMC by the *VISTA survey of the Magellanic Clouds system, VMC* (Cioni et al. 2011). They found that unique PL and PW relations hold both for BL Her and W Vir variables, whereas the RV Tau stars follow different and more dispersed relationships (see Fig. C.1). Ripepi et al. (2015) also found that the metallicity dependence of the T2C PL and PW relations is small, if any. The T2C PL and PW relations, calibrated on T2Cs with parallax measured by the HST and applied to the LMC and to GGCs hosting T2Cs, provide distance moduli for the host systems which are in excellent agreement with those inferred by RRLs, but about 0.1 mag longer than those estimated based on CCs with HST parallaxes (Ripepi et al. 2015).

C.3 Anomalous Cepheids

Anomalous Cepheids (ACs) are pulsating variables that belong to the Cepheid class. Like RRLs, they are central He-burning stars with low metal abundances, but are more massive (typically, 1-2 $M_{\odot}$) and at least 1 magnitude brighter than RRLs. Their pulsation periods range from 0.3 to 2 d, hence, shorter than typical CCs. The ACs are observed in metal-poor ([Fe/H]$\leqslant -1.4$ dex) stellar systems like the LG dSphs, a few GGCs and the MW halo, and are generally considered to trace an intermediate-age population (1-2 Gyr) with low metallicity (Z $\leqslant$ 0.0004).

ACs were explained theoretically by Bono et al. (1997) according to an evolutionary scenario where stars of $\sim$1-1.2 $M_{\odot}$ produce a ZAHB crossing the IS at brighter luminosities than the RRLs. Later, Caputo et al. (2004) revealed that the ACs are indeed

post-He flash stars with mass ∼1.9-2.2 $M_{\odot}$ and likely the extension of the CCs to lower metallicities (Z ∼ 0.0004, according to Marconi et al. 2004), fainter luminosities and shorter periods. There is a further scenario trying to explain the apparent youth of the ACs (compared to RRLs), according to which they would be the evolved counterpart of the MS blue stragglers. In this scenario, they would not trace a recent star formation episode, but rather they would be the result of mass transfer occurred in a close binary system about 1 Gyr ago. These two scenarios can both produce ACs, however, perhaps a distinction can be made between the few ACs generally found in old stellar systems like the GGCs and MW UFDs (i.e. Hercules, Musella et al. 2012; Canes Venatici I, Kuehn et al. 2008), that likely originated from merged binaries, and the larger numbers of ACs found in galaxies with gas and recent star formation episodes like Leo T among the UFDs (Clementini et al. 2012) or Carina (Dall'Ora et al. 2003) and Leo I (Weisz et al. 2014, Stetson et al. 2014) among the "classical" MW dSphs, which indeed hosts much more ACs than all other MW UFDs and several of the "classical" dSphs. A similar distinction can be made perhaps among the M31 satellites, where many ACs have been identified in the OFF-GPoA satellites (e.g., And XIX, And XXI and And VI), whereas much less or none have been found among the ON-GPoA systems (e.g., And I, And III, And XI, And XIII, And XXV and And XXVII; see Sections 2.2.5, 2.3.4 and Table 2.5). Therefore, depending on the formation channel, the presence of ACs may indicate that some of the MW and M31 satellites have had a more complex star formation history than expected.

Like CCs and T2Cs, the ACs follow their own PL and PW relations, which differ from those followed by CCs. We recall that use of the PW relation (Madore 1982) in place of the PL relation is preferred, because the PW relation[3] has the advantage of being reddening free (see Section C.1).

[3]The PW relation includes a colour term, the Wesenheit index, with a coefficient corresponding to the ratio between total to selective extinction in the filter pair used in the observations. For the B, V passbands, used in this thesis, the Wesenheit index is defined as $W(B,V) = M_V - 3.1 \times (B-V)$, where M_V is the absolute visual magnitude, namely, the stars V apparent magnitude corrected for the distance modulus.

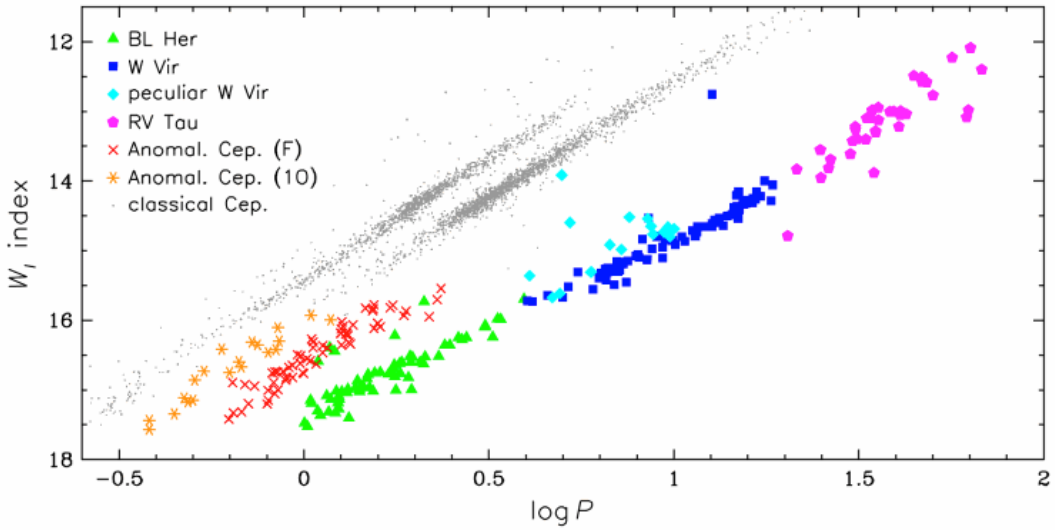

FIGURE C.1: $PW(V,I)$ relations for Cepheids in the LMC. Green, blue, cyan and magenta symbols show T2Cs (BL Her, W Vir, pW Vir and RV Tau respectively); red and orange crosses are the ACs (fundamental and first overtone, respectively), grey points represent CCs. Figure from Soszyński et al. (2008).

Bibliography

Ahn, C. P., Alexandroff, R., Allende Prieto, C., et al. 2014, Astrop. J. Supp., 211, 17

Alcock, C., Allsman, R. A., Alves, D. R. et al. 2000, AJ, 119, 2194

Anderson, R.I., Casertano, S., Riess, A.G., et al. 2016, Astrop. J. Supp., 226, 18

Andrae, R., Fouesneau, M., Creevey, O., et al. 2018, A&A, 616, A8

Arellano Ferro, A., Figuera Jaimes, R., Giridhar, S., et al. 2011, MNRAS, 416, 2265

Arellano Ferro, A., Bramich, D. M., Giridhar, S., et al. 2013, Acta Astron., 63, 429

Arellano Ferro, A., Ahumada, J. A., Calderón, J. H., & Kains, N. 2014, Rev. Mexicana Astron. Astrofis., 50, 307

Arellano Ferro, A., Rojas Galindo, F. C., Muneer, S., & Giridhar, S. 2018, Rev. Mexicana Astron. Astrofis., 54, 325

Arenou, F., & Luri, X. 1999, ASPC, 167, 13

Arenou, F., Luri, X., Babusiaux, S., et al. 2017, A&A, 599, A50

Arenou, F., Luri, X., Babusiaux, C., et al. 2018, A&A, 616, A17

Bailey, S. I. 1902, Annals of Harvard College Observatory, 38, 1

Bailey, S. I., & Pickering, E. C. 1913, Annals of Harvard College Observatory, 78, 1

Bailey, S. I., Leland, E. F., Woods, I. E., & Pickering, E. C. 1919, Annals of Harvard College Observatory, 78, 195

Battaglia, G., Helmi, A., Tolstoy, E., et al. 2008, ApJL, 681, L13

Beaton, R. L., Freedman, W. L., Madore, B. F., et al. 2016, ApJ, 832, 210

Bell, E. F., Slater, C. T., & Martin, N. F. 2011, ApJL, 742, L15

Bellazzini, M., Beccari, G., Oosterloo, T. A., et al. 2011, A&A, 527, A58

Bellini, A., Bedin, L. R., Piotto, G., et al. 2010, AJ, 140, 631

Belokurov, V., Walker, M. G., Evans, N. W., et al. 2010, ApJL, 712, L103

Benedict, G. F., McArthur, B. E., Fredrick, L. W., et al. 2002, AJ, 123, 473

Benedict, G. F., McArthur, B. E., Feast, M. W., et al. 2007, AJ, 133, 1810

Benedict, G. F., McArthur, B. E., Feast, M. W., et al. 2011, AJ, 142,187

Benkő, J. M., Bakos, G. Á., & Nuspl, J. 2006, MNRAS, 372, 1657

Berdnikov , L. N., Dambis, A. K., & Vozyakova, O. V. 2000, A&AS, 143, 211

Bica, E. L. D., Schmitt, H. R., Dutra, C. M., & Oliveira, H. L. 1999, AJ, 117, 238

Bingham, E. A., Cacciari, C., Dickens, R. J., & Pecci, F. F. 1984, MNRAS, 209, 765

Bird, J. C., Stanek, K. Z., & Prieto, J. L. 2009, ApJ, 695, 874

Blazhko, S. 1907, Astr. Nachr., 175, 325

Boettcher, E., Willman, B., Fadely, R., et al. 2013, AJ, 146, 94

Bono, G., Caputo, F., Santolamazza, P., Cassisi, S., & Piersimoni, A. 1997, AJ, 113, 2209

Bono, G., Caputo, F., Castellani, V., Marconi, M., & Storm, J. 2001, MNRAS, 326, 1183

Bono, G., Caputo, F., Castellani, V., et al. 2003, MNRAS, 344, 1097

Bono, G., Caputo, F., Marconi, M., & Musella, I. 2010, ApJ, 715, 277

Borissova, J., Rejkuba, M., Minniti, D., Catelan, M. and Ivanov, V. D. 2009, A&A, 502, 505

Braga, V. F., Dall'Ora, M., Bono, G., et al. 2015, ApJ, 799, 165

Braga, V. F., Stetson, P. B., Bono, G., et al. 2016, AJ, 152, 170

Breddels, M. A., & Helmi, A. 2014, ApJL, 791, L3

Bressan, A., Marigo, P., Girardi, et al. 2012, MNRAS, 427, 127

Brown, T. M., Ferguson, H. C., Smith, E., et al. 2004, AJ, 127, 2738

Bullock, J. S., Kravtsov, A. V., & Weinberg, D. H. 2001, ApJ, 548, 33

Bullock, J. S., & Johnston, K. V. 2005, ApJ, 635, 931

Cacciari, C., & Clementini, G. 2003, in Lecture Notes in Physics, Berlin Springer Verlag, Vol. 635, Stellar Candles for the Extragalactic Distance Scale, ed. D. Alloin & W. Gieren, 105-122

Cacciari, C., Corwin, T. M., & Carney, B. W. 2005, AJ, 129, 267

Caputo, F., Marconi, M., Musella, I., & Santolamazza, P. 2000, A&A, 359, 1059

Caputo, F., Castellani, V., Degl'Innocenti, S., Fiorentino, G., & Marconi, M. 2004, A&A, 424, 927

Cardelli, J. A., Clayton, C., & Mathis, J. S. 1989, AJ, 345, 245

Carrasco, J. M., Evans, D. W., Montegriffo, P., et al. 2016, A&A, 595, A7

Carretta, E., & Gratton, R. G. 1997, A&A Supp., 121, 95

Carretta, E., Gratton, R. G., Clementini, G., & Fusi Pecci, F. 2000, ApJ, 533, 215

Carretta, E., Bragaglia, A., Gratton, R. G., et al. 2009, A&A, 505, 117

Casertano, S., Riess, A. G., Anderson, J., et al. 2016, ApJ, 825, 11

Casertano, S., Riess, A. G., Bucciarelli, B., & Lattanzi, M. G. 2017, A&A, 599, A67

Cassisi, S., Castellani, V., degl'Innocenti, S., & Weiss, A. 1998, A&A Supp., 129, 267

Coppola, G., Dall'Ora, M., Ripepi, V., et al. 2011, MNRAS, 416, 1056

Catelan, M., Pritzl, B. J., & Smith, H. A. 2004, Astrop. J. Supp., 154, 633

Catelan, M., & Cortés, C. 2008, ApJL, 676, L135

Catelan, M. 2009, Ap& SS, 320, 261

Catelan, M., & Smith, H. A. 2015, Pulsating Stars (Wiley-VCH)

Chambers, K. C., Magnier, E. A., Metcalfe, N., et al. 2016, arXiv:1612.05560

Cioni, M.-R. L., Clementini, G., Girardi, L., et al. 2011, A&A, 527, A116

Clement, C. M., & Rowe, J. 2000, AJ, 120, 2579

Clement, C. M., Muzzin, A., Dufton, Q., et al. 2001, AJ, 122, 2587

Clementini, G., Carretta, E., Gratton, R., et al. 1995, AJ, 110, 2319

Clementini, G., Di Tomaso, S., Di Fabrizio, L., et al. 2000, AJ, 120, 2054

Clementini, G., Gratton, R. G., Bragaglia, A., et al. 2003, AJ, 125, 1309

Clementini, G., Ripepi, V., Bragaglia, A., et al. 2005, MNRAS, 363, 734

Clementini, G., Contreras, R., Federici, L., et al. 2009, ApJL, 704, L103

Clementini, G. 2010, in Variable Stars, the Galactic halo and Galaxy Formation, ed. C. Sterken, N. Samus, & L. Szabados (Moscow: Sternberg Astronomical Institute of Moscow Univ.), 107

Clementini, G., Cignoni, M., Contreras Ramos, R., et al. 2012, ApJ, 756, 108

Clementini, G., Ripepi, V., Leccia, S., et al. 2016, A&A, 595, A133

Clementini, G., Garofalo, A., Muraveva, T., & Ripepi, V. 2018, arXiv:1804.09575

Clementini, G., Ripepi, V., Molinaro, R., et al. 2018, arXiv:1805.02079

Collins, M. L. M., Chapman, S. C., Rich, R. M., et al. 2013, ApJ, 768, 172

Collins, M. L. M., Chapman, S. C., Rich, R. M., et al. 2014, ApJ, 783, 7

Conn, A. R., Ibata, R. A., Lewis, G. F., et al. 2012, ApJ, 758, 11

Contreras, R., Catelan, M., Smith, H. A., et al. 2010, AJ, 140, 1766

Contreras Ramos, R., Clementini, G., Federici, L., et al. 2013, ApJ, 765, 71

Corwin, T. M., Borissova, J., Stetson, P. B., et al. 2008, AJ, 135, 1459

Crnojević, D., Sand, D. J., Zaritsky, D., et al. 2016, ApJ, 824L, 14

Cropper, M., Katz, D., Sartoretti, P., et al. 2018, arXiv:1804.09369

Cuffey, J. 1966, AJ, 71, 514

Cusano, F., Clementini, G., Garofalo, A., et al. 2013, ApJ, 779, 7

Cusano, F., Garofalo, A., Clementini, G., et al. 2015, ApJ, 806, 200

Cusano, F., Garofalo, A., Clementini, G., et al. 2016, ApJ, 829, 26

Cusano, F., Garofalo, A., Clementini, G., et al. 2017, ApJ, 851, 9

Cutri, R., et al. 2003, University of Massachusetts and Infrared Processing and Analysis Centre (IPAC/California Institute of Technology)

Dall'Ora, M., Ripepi, V., Caputo, F., et al. 2003, AJ, 126, 197

Dall'Ora, M., Storm, J., Bono, G., et al. 2004, ApJ, 610, 269

Dall'Ora, M., Clementini, G., Kinemuchi, K., et al. 2006, ApJL, 653, L109

Dall'Ora, M., Kinemuchi, K., Ripepi, V., et al. 2012, ApJ, 752, 42

Dambis, A. K., Berdnikov, L. N., Kniazev, A. Y., et al. 2013, MNRAS, 435, 3206

Dambis, A. K., Rastorguev, A. S., & Zabolotskikh, M. V. 2014, MNRAS, 439, 3765

de Boer, T. J. L., Tolstoy, E., Saha, A., et al. 2011, A&A, 528, A119

De Grijs, R., Wicker J. E., & Bono, G., 2014, AJ, 147, 122

de Jong, J. T. A., Martin, N. F., Rix, H.-W., et al. 2010, ApJ, 710, 1664

Delgado, H. E., Sarro, L. M., Clementini, G., Muraveva, T., & Garofalo, A. 2018, arXiv:1803.01162

Del Principe, M., Piersimoni, A. M., Storm, J., et al. 2006, AJ, 652, 362

Demers, S., & Kunkel, W. E. 1976, ApJ, 208, 932

Di Criscienzo, M., Marconi, M., & Caputo, F., 2004, ApJ, 612, 1092

di Tullio, G. A. 1979, A&AS, 37, 591

Dolphin, A. E. 2002, MNRAS, 332, 91

Drimmel, R., Cabrera-Lavers, A., & Lopez-Corredoira, M. 2003, A&A, 409, 205

Drlica-Wagner, A., Bechtol, K., Rykoff, E. S., et al. 2015, ApJ, 813, 109

Eyer, L., Mowlavi, N., Evans, D. W., et al. 2017, arXiv:1702.03295

Evans, N. R. 1994, ApJ, 436, 273

Evans, D. W., Riello, M., De Angeli, F., et al. 2017, A&A, 600, A51

Evans, D. W., Riello, M., De Angeli, F., et al. 2018, A&A, 616, A4

Fazio, G. G., Hora, J. L., Allen, L. E., et al. 2004, Astrop. J. Supp., 154, 10

Feast, M. W. 1997, MNRAS, 284, 761

Feast, M. W., Clifton, D. L., Kinman, T. D., van Leeuwen, F. & Whitelock, P. A. 2008, MNRAS, 386, 2115

Feast, M. W. 2017, European Physical Journal Web of Conferences, 152, 08001

Fernie, J. D., Evans, N. R., Beattie, B., & Seager, S. 1995, Information Bulletin on Variable Stars, 4148, 1

Fernie, J. D. 2000, AJ, 120, 978

Fiorentino, G., Musella, I.,& Marconi, M. 2013, MNRAS, 434, 2866

Fouqué, P., Arriagada, P., Storm, J., et al. 2007, A&A, 476, 73

Freedman, W. L., Madore, B. F., Gibson, B. K., et al. 2001, ApJ, 553, 47

Freedman, W. L., Madore, B. F., Scowcroft, V., et al. 2011, AJ, 142, 192

Freedman, W. L., Madore, B. F., Scowcroft, V., et al. 2012, ApJ, 758, 24

Fusi Pecci, F., Buonanno, R., Cacciari, C., et al. 1996, AJ, 112, 1461

Gaia Collaboration, Brown, A. G. A., Vallenari, A., et al. 2016, A&A, 595, A2

Gaia Collaboration, Prusti, T., de Bruijne, J. H. J., et al. 2016, A&A, 595, A1

Gaia Collaboration, Clementini, G., Eyer, L., et al. 2017, A&A, 605, A79

Gaia Collaboration, Brown, A. G. A., Vallenari, A., et al. 2018, A&A, 616, A1

Gaia Collaboration, Spoto, F., Tanga, P., et al. 2018, A&A, 616, A13

Gaia Collaboration, Helmi, A., van Leeuwen, F., et al. 2018, A&A, 616, A12

Gallenne, A., Kervella, P., Mérand, A., et al. 2012, A&A, 541, A8

Galleti, S., Federici, L., Bellazzini, M., Fusi Pecci, F., & Macrina, S. 2004, A&A, 416, 917

Garofalo, A., Cusano, F., Clementini, G., et al. 2013, ApJ, 767, 62

Garofalo, A., Scowcroft, V., Clementini, G., et al. 2018, MNRAS, 481, 578

Gavrilchenko, T., Klein, C. R., Bloom, J. S., & Richards, J. W. 2014, MNRAS, 441, 715

Geisler, D., Smith, V. V., Wallerstein, G., Gonzalez, G., & Charbonnel, C. 2005, AJ, 129, 1428

Genovali, K., Lemasle, B., Bono, G., et al. 2014, A&A, 566, A37

Gibson, B. K. 2000, MmSAIt, 71, 693

Girardi, L., Grebel, E. K., Odenkirchen, M., & Chiosi, C. 2004, A&A, 422, 205

Goranskij, V. P. 1976, Peremennye Zvezdy Prilozhenie, 3, 1

Górski, M., Pietrzyński, G., & Gieren, W. 2011, AJ, 141, 194

Gratton, R. G., Fusi Pecci, F., Carretta, E., et al. 1997, ApJ, 491, 749

Gratton, R. G., Carretta, E., & Clementini, G. 1999, Post-Hipparcos Cosmic Candles, 237, 89

Gratton, R. G., Bragaglia, A., Clementini, G., et al. 2004, A&A, 421, 937

Greco, C., Dall'Ora, M., Clementini, G., et al. 2008, ApJL, 675, L73

Groenewegen, M. A. T. 1999, A&AS, 139, 245

Groenewegen, M. A. T., Udalski, A., & Bono, G. 2008, A&A, 481, 441

Groenewegen, M. A. T. 2013, A&A, 550, A70

Harris, W. E. 1996, AJ, 112, 1487

Hendel, D., Scowcroft, V., Johnston, K. V., et al. 2018, MNRAS, 479, 570

Hill, J. M., Green, R. F., Ashby, D. S., et al. 2010, Proceedings of the SPIE, 7733, 77330C

Høg, E., Fabricius, C., Makarov, V. V., et al. 2000, A&A, 355, L27

Holl, B., Audard, M., Nienartowicz, K., et al. 2018, arXiv:1804.09373

Huxor, A. P., Ferguson, A. M. N., Tanvir, N. R., et al. 2011, MNRAS, 414, 770

Huxor, A. P., & Grebel, E. K. 2015, MNRAS, 453, 2653

Ibata, R. A., Lewis, G. F., Conn, A. R., et al. 2013, Nature, 493, 62

Ibata, R. A., Lewis, G. F., McConnachie, A. W., et al. 2014, ApJ, 780, 128

Iben, I., Jr. 1974, ARA&A, 12, 215

Indebetouw, R., Mathis, J. S., Babler, B. L., et al. 2005, ApJ, 619, 931

Inno, L., Matsunaga, N., Bono, G., et al. 2013, ApJ, 764, 84

Inno, L., Matsunaga, N., Romaniello, M., et al. 2015, A&A, 576, A30

Jacyszyn-Dobrzeniecka, A. M., Skowron, D. M., Mróz, P., et al. 2016, Acta Astronomica, 66, 149

Jeffery, E. J., Smith, E., Brown, T. M., et al. 2011, AJ, 141, 171

Jeon, Y.-B., Nemec, J. M., Walker, A. R., & Kunder, A. M. 2014, AJ, 147, 155

Jones, R. V., Carney, B. W., & Fulbright, J. P. 1996, PASP, 108, 877

Johnston, K. V., Choi, P. I., & Guhathakurta, P. 2002, AJ, 124, 127

Jordi, C., Gebran, M., Carrasco, J. M., et al. 2010, A&A, 523, A48

Jurcsik, J. 1995, Acta Astronomica, 45, 653

Jurcsik, J., & Kovacs, G. 1996, A&A, 312, 111

Kaluzny, J., Kubiak, M., Szymanski, M., et al. 1995, A&A Supp., 112, 407

Kapakos, E., Hatzidimitriou, D., & Soszyński, I. 2011, MNRAS, 415, 1366

Kerp, J., Kalberla, P. M. W., Ben Bekhti, N., et al. 2016, A&A, 589A, 120

Kim, D., Jerjen, H., Mackey, D., Da Costa, G. S., & Milone, A. P. 2015, ApJL, 804, L44

Kim, D., Jerjen, H., Geha, M., et al. 2016, ApJ, 833, 16

Kinemuchi, K., Harris, H. C., Smith, H. A., et al. 2008, AJ, 136, 1921

Kirby, E. N., Simon, J. D., Geha, M., Guhathakurta, P., & Frebel, A. 2008, ApJL, 685, L43

Kirby, E. N., Lanfranchi, G. A., Simon, J. D., Cohen, J. G., & Guhathakurta, P. 2011, ApJ, 727, 78

Kirby, E. N., Simon, J. D., & Cohen, J. G. 2015, ApJ, 810, 56

Klagyivik, P., & Szabados, L. 2009, A&A, 504, 959

Klein, C. R., Richards, J. W., Butler, N. R., & Bloom, J. S. 2014, MNRAS, 440, L96

Koch, D. G., Borucki, W. J., Basri, G., et al. 2010, ApJL, 713, L79

Kovács, G. 2001, A&A, 375, 469

Kubiak, M., & Udalski, A. 2003, Acta Astronomica, 53, 117

Kuehn, C., Kinemuchi, K., Ripepi, V., et al. 2008, ApJL, 674, L81

Kuehn, C. A., Dame, K., Smith, H. A., et al. 2013, AJ, 145, 160

Laevens, B. P. M., Martin, N. F., Bernard, E. J., et al. 2015, ApJ, 813, 44

Lambert, D. L., Heath, J. E., Lemke, M., & Drake, J. 1996, Astrop. J. Supp., 103, 183

Landolt, A. U. 1992, AJ, 104, 340

Layden, A. C., & Sarajedini, A. 2003, AJ, 125, 208

Lee, Y.-W., Demarque, P., & Zinn, R. 1990, ApJ, 350, 155

Lemasle, B., Kovtyukh, V., Bono, G., et al. 2015, A&A, 579, A47

Lindegren, L., & Bastian, U. 2010, EAS Publications Series, 45, 109

Lindegren, L., Lammers, U., Hobbs, D., et al. 2012, A&A, 538, A78

Lindegren, L., Lammers, U., Bastian, U., et al. 2016, A&A, 595, A4

Lindegren, L., Hernández, J., Bombrun, A., et al. 2018, A&A, 616, A2

Longmore, A. J., Fernley, J. A., & Jameson, R. F. 1986, MNRAS, 220, 279

Longmore, A. J., Dixon, R., Skillen, I., Jameson, R. F., & Fernley, J. A. 1990, MNRAS, 247, 684

Luri, X., Gomez, A. E., Torra, J., Figueras, F., & Mennessier, M. O. 1998, A&A, 335, L81

Luri, X., Brown, A. G. A., Sarro, L. M., et al. 2018, A&A, 616, A9

Mackey, A. D., & Gilmore, G. F. 2004, MNRAS, 355, 504

Mackey, A. D., & van den Bergh, S. 2005, MNRAS, 360, 631

Madore, B. F. 1982, ApJ, 253, 575

Madore, B. F., & Freedman, W. L. 1991, PASP, 103, 933

Madore, B. F., Hoffman, D., Freedman, W. L., et al. 2013, ApJ, 776, 135

Maintz, G. 2005, A&A, 442, 381

Majewski, S. R., Siegel, M. H., Patterson, R. J., & Rood, R. T. 1999, ApJL, 520, L33

Makovoz, D., & Khan, I. 2005, Astronomical Data Analysis Software and Systems XIV, 347, 81

Mancone, C., & Sarajedini, A. 2008, AJ, 136, 1913

Marconi, G., Ripepi, V., Andreuzzi, G., et al. 2002, Extragalactic Star Clusters, 207, 193

Marconi, M., Fiorentino, G., & Caputo, F. 2004, A&A, 417, 1101

Marconi, M., & Clementini, G. 2005, AJ, 129, 2257

Marconi, M., Musella, I., & Fiorentino, G. 2005, ApJ, 632, 590

Marconi, M., Coppola, G., Bono, G., et al. 2015, ApJ, 808, 50

Marigo, P., Girardi, L., Bressan, A., et al. 2017, ApJ, 835, 77

Martin, N. F., de Jong, J. T. A., & Rix, H.-W. 2008, ApJ, 684, 1075

Martin, N. F., Ibata, R. A., McConnachie, A. W., et al. 2013, ApJ, 776, 80

Martin, N. F., Ibata, R. A., Lewis, G. F., et al. 2016, ApJ, 833, 167

Martínez-Vázquez, C. E., Monelli, M., Bono, G., et al. 2015, MNRAS, 454, 1509

Martínez-Vázquez, C. E., Monelli, M., Gallart, C., et al. 2016a, MNRAS, 461, L41

Martínez-Vázquez, C. E., Stetson, P. B., Monelli, M., et al. 2016b, MNRAS, 462, 4349

Martínez-Vázquez, C. E., Monelli, M., Bernard, E. J., et al. 2017, ApJ, 850, 137

Mateo, M., Fischer, P., & Krzeminski, W. 1995, AJ, 110, 2166

Mateo, M. L. 1998, Annual Review of A&A, 36, 435

Matsunaga, N., Fukushi, H., Nakada, Y., et al. 2006, MNRAS, 370, 1979

Matsunaga, N., Feast, M. W., & Soszyński, I. 2011, MNRAS, 413, 223

McConnachie, A. W. 2012, AJ, 144, 4

McConnachie, A. W., Ibata, R., Martin, N., et al. 2018, arXiv:1810.08234

Menzies, J. W., Feast, M. W., Whitelock, P. A., & Matsunaga, N. 2011, MNRAS, 414, 3492

Michalik, D., Lindegren, L., & Hobbs, D. 2015, A&A, 574, A115

Molnár, L., & Szabados, L. 2014, MNRAS, 442, 3222

Monaco, L., Bellazzini, M., Ferraro, F. R., Pancino, E. 2005, MNRAS, 356, 1396

Monelli, M., Martínez-Vázquez, C. E., Bernard, E. J. et al. 2016, ApJ, 819, 147

Monson, A. J., Freedman, W. L., Madore, B. F., et al. 2012, ApJ, 759, 146

Monson, A. J., Beaton, R. L., Scowcroft, V., et al. 2017, AJ, 153, 96

Moretti, M. I., Dall'Ora, M., Ripepi, V., et al. 2009, ApJL, 699, L125

Morgan, S. M., Wahl, J. N., & Wieckhorst, R. M. 2007, MNRAS, 374, 1421

Muraveva, T., Palmer, M., Clementini, G., et al. 2015, ApJ, 807, 127

Muraveva, T., Garofalo, A., Scowcroft, V., et al. 2018, MNRAS, 480, 4138

Muraveva, T., Delgado, H. E., Clementini, G., Sarro, L. M., & Garofalo, A. 2018, MNRAS, 481, 1195

Musella, I., Ripepi, V., Clementini, G., et al. 2009, ApJL, 695, L83

Musella, I., Ripepi, V., Marconi, M., et al. 2012, ApJ, 756, 121

Ngeow, C., & Kanbur, S. M. 2006, ApJ, 650, 180

Ngeow, C.-C. 2012, ApJ, 747, 50

Ngeow, C.-C., Kanbur, S. M., Bellinger, E. P., et al. 2012, Ap&SS, 341, 105

Neeley, J. R., Marengo, M., Bono, G., et al. 2015, ApJ, 808, 11

Neeley, J. R., Marengo, M., Bono, G., et al. 2017, ApJ, 841, 84

Nemec, J. M., Nemec, A. F. L., & Lutz, T. E. 1994, AJ, 108, 222

Nemec, J. M., Cohen, J. G., Ripepi, V., et al. 2013, ApJ, 773, 181

Norris, J. E., Wyse, R. F. G., Gilmore, G., et al. 2010, ApJ, 723, 1632

Oosterhoff, P. T. 1939, The Observatory, 62, 104

Pawlowski, M. S., Kroupa, P., Jerjen, H., et al. 2013, MNRAS, 435, 1928

Pawlowski, M. S. 2016, MNRAS, 456, 448

Pejcha, O., & Kochanek, C. S. 2012, ApJ, 748, 107

Perryman, M. 2009, Planetary and Space Science, 57, 105

Persson, S. E., Murphy, D. C., Smee, S., et al. 2013, PASP, 125, 654

Piersimoni, A. M., Bono, G., & Ripepi, V. 2002, AJ, 124, 1528

Pietrinferni, A., Cassisi, S., Salaris, M., & Castelli, F. 2004, ApJ, 612, 168

Pietrzyński, G., Gieren, W., Szewczyk, O., et al. 2008, AJ, 135, 1993

Pietrzynski, G., Graczyk, D., Gieren, W., et al. 2013, Nature, 495, 76

Piotto, G., King, I. R., Djorgovski, S. G., et al. 2002, A&A, 391, 945

Pojmanski, G. 2002, Acta Astron., 52, 397

Preston, G. W. 1959, ApJ, 130, 507

Pritzl, B. J., Armandroff, T. E., Jacoby, G. H., & Da Costa, G. S. 2002, AJ, 124, 1464

Pritzl, B. J., Smith, H. A., Stetson, P. B., et al. 2003, AJ, 126, 1381

Pritzl, B. J., Armandroff, T. E., Jacoby, G. H., & Da Costa, G. S. 2004, AJ, 127, 318

Pritzl, B. J., Armandroff, T. E., Jacoby, G. H., & Da Costa, G. S. 2005, AJ, 129, 2232

Richardson, J. C., Irwin, M. J., McConnachie, A. W., et al. 2011, ApJ, 732, 76

Riello, M., De Angeli, F., Evans, D. W., et al. 2018, A&A, 616, A3

Riess, A. G., Macri, L., Casertano, S., et al. 2011, ApJ, 730, 119

Riess, A. G., Casertano, S., Anderson, J., MacKenty, J., & Filippenko, A. V. 2014, ApJ, 785, 161

Riess, A. G., Macri, L. M., Hoffmann, S. L., et al. 2016, ApJ, 826, 56

Riess, A. G., Casertano, S., Yuan, W., et al. 2018, ApJ, 861, 126

Rimoldini, L., Holl, B., Audard, M., et al. 2018 submitted to A&A

Ripepi, V., Monelli, M., Dall'Ora, M., et al. 2004, Communications in Asteroseismology, 145, 24

Ripepi, V., Moretti, M. I., Marconi, M., et al. 2012, MNRAS, 424, 1807

Ripepi, V., Marconi, M., Moretti, M. I., et al. 2014, MNRAS, 437, 2307

Ripepi, V., Moretti, M.-I., Marconi, M., et al. 2015, MNRAS, 446, 3034

Ripepi, V., Marconi, M., Moretti, M. I., et al. 2016, Astrop. J. Supp., 224, 21

Rizzi, L., Tully, R. B., Makarov, D., et al. 2007, ApJ, 661, 815

Saha, A., Thim, F., Tammann, G. A., Reindl, B., & Sandage, A. 2006, Astrop. J. Supp., 165, 108

Salaris, M., de Boer, T., Tolstoy, E., Fiorentino, G., & Cassisi, S. 2013, A&A, 559, A57

Sales, L. V., Navarro, J. F., Abadi, M. G., & Steinmetz, M. 2007, MNRAS, 379, 1464

Salinas, R., Contreras Ramos, R., Strader, J., et al. 2016, AJ, 152, 55

Samus', N. N., Kazarovets, E. V., Durlevich, O. V., Kireeva, N. N., & Pastukhova, E. N. 2017, Astronomy Reports, 61, 80

Sand, D. J., Strader, J., Willman, B., et al. 2012, ApJ, 756, 79

Sandage, A., Katem, B., & Sandage, M. 1981, Astrop. J. Supp., 46, 41

Sandage, A. 1993, AJ, 106, 703

Sarajedini, A., Mancone, C. L., Lauer, T. R., et al. 2009, AJ, 138, 184

Sarajedini, A. 2011, RR Lyrae Stars, Metal-Poor Stars, and the Galaxy, 5, 181

Schaefer, B. E. 2008, AJ, 135, 112

Schlafly, E. F. & Finkbeiner D. P. 2011, ApJ, 737, 103

Schlegel, D. J., Finkbeiner, D. P., & Davis, M. 1998, ApJ, 500, 525

Sesar, B., Banholzer, S. R., Cohen, J. G., et al. 2014, ApJ, 793, 135

Sesar, B., Fouesneau, M., Price-Whelan, A. M., et al. 2017, ApJ, 838, 107

Shanks, T., Metcalfe, N., Chehade, B., et al. 2015, MNRAS, 451, 4238

Shapley, H. 1938, Harvard College Observatory Bulletin, 908, 1

Simon, N. R., & Teays, T. J. 1982, ApJ, 261, 586

Simon, J. D., & Geha, M. 2007, ApJ, 670, 313

Simon, J. D., Geha, M., Minor, Q. E., et al. 2011, ApJ, 733, 46

Smith, H. A. 1995, RR Lyrae stars (Cambridge University Press)

Sollima, A., Borissova, J., Catelan, M., et al. 2006, ApJL, 640, L43

Sollima, A., Cacciari, C., Arkharov, A. A. H., et al. 2008, MNRAS, 384, 1583

Soszyński, I., Udalski, A., Szymański, M. K., et al. 2008, Acta Astronomica, 58, 293

Stetson, P. B. 1987, PASP, 99, 191

Stetson, P. B. 1994, PASP, 106, 250

Stetson, P. B., Fiorentino, G., Bono, G., et al. 2014, PASP, 126, 616

Stierwalt, S., Liss, S. E., Johnson, K. E., et al. 2017, Nature Astronomy, 1, 0025

Strigari, L. E., Koushiappas, S. M., Bullock, J. S., et al. 2008, ApJ, 678, 614

Sturch, C. 1966, ApJ, 143, 774

Szabados, L. 1997, in 'Hipparcos - Venice '97', ESA SP-402, p. 657

Szabados, L. 2003, IBVS, 5394

Sziládi, K., Vinkó, J., Poretti, E., Szabados, L., & Kun, M. 2007, A&A, 473, 579

Tammann, G. A., Sandage, A., & Reindl, B. 2003, A&A, 404, 423

Tammann, G. A., Sandage, A., & Reindl, B. 2008, ApJ, 679, 52

The Dark Energy Survey Collaboration 2005, arXiv:astro-ph/0510346

Tolstoy, E., Irwin, M. J., Helmi, A., et al. 2004, ApJL, 617, L119

Tolstoy, E., Hill, V., & Tosi, M. 2009, ARA&A, 47, 371

Torrealba, G., Koposov, S. E., Belokurov, V., & Irwin, M. 2016, MNRAS, 459, 2370

Tully, R. B., Courtois, H. M., Dolphin, A. E., et al. 2013, AJ, 146, 86

Turner, D. G., Billings, G. W., & Berdnikov, L. N. 2001, PASP, 113, 715

Udalski, A., M., Kaluzny, J., Kubiak, M., & Mateo, M. 1992, Acta Astronomica, 42, 253

Udalski, A., Soszynski, I., Szymanski, M., et al. 1999, Acta Astron., 49, 45

Wade, R. A., Donley, J., Fried, R., White, R. E., & Saha, A. 1999, AJ, 118, 2442

Walker, A. R. 1990, AJ, 100, 1532

Walker, A. R. 1992, AJ, 103, 1166

Walker, A. R., & Nemec, J. M. 1996, AJ, 112, 2026

Walker, A. R. 1998, AJ, 116, 220

Wallerstein, G. 2002, PASP, 114, 689

Webbink, R. F. 1985, Dynamics of Star Clusters, 113, 541

Weisz, D. R., Dolphin, A. E., Skillman, E. D., et al. 2014, ApJ, 789, 147

Wenger, M., Ochsenbein, F., Egret, D., et al. 2000, A&A Supp., 143, 9

van Agt, S. L. T. J. 1978, Publications of the David Dunlap Observatory, 3, 205

VandenBerg, D. A., Denissenkov, P. A., & Catelan, M. 2016, ApJ, 827, 2

van Leeuwen, F. 2007, Astrophysics and Space Science Library, 350

van Leeuwen, F. 2007, A&A, 474, 653

Yang, S.-C. & Sarajedini, A. 2012,MNRAS, 419, 1362

Yanny, B., Rockosi, C., Newberg, H. J., et al. 2009, AJ, 137, 4377

York, D. G., Adelman, J., Anderson, J. E., Jr., et al. 2000, AJ, 120, 1579

Veljanoski, J., Mackey, A. D., Ferguson, A. M. N., et al. 2014, MNRAS, 442, 2929

Zaritsky, D., Crnojević, D., & Sand, D. J. 2016, arXiv:1604.08594

Zinn, R., & West, M. J. 1984, Astrop. J. Supp., 55, 45

Zorotovic, M., Catelan, M., Smith, H. A., et al. 2010, AJ, 139, 357